



HAL
open science

Bio-inspired strategies for the catalytic reduction and valorization of carbon dioxide

Philipp Gotico

► **To cite this version:**

Philipp Gotico. Bio-inspired strategies for the catalytic reduction and valorization of carbon dioxide. Catalysis. Université Paris Saclay (COMUE), 2019. English. NNT : 2019SACLS283 . tel-02310759

HAL Id: tel-02310759

<https://theses.hal.science/tel-02310759v1>

Submitted on 10 Oct 2019

HAL is a multi-disciplinary open access archive for the deposit and dissemination of scientific research documents, whether they are published or not. The documents may come from teaching and research institutions in France or abroad, or from public or private research centers.

L'archive ouverte pluridisciplinaire **HAL**, est destinée au dépôt et à la diffusion de documents scientifiques de niveau recherche, publiés ou non, émanant des établissements d'enseignement et de recherche français ou étrangers, des laboratoires publics ou privés.

Stratégies bio-inspirées pour la réduction catalytique et la valorisation du dioxyde de carbone

Thèse de doctorat de l'Université Paris-Saclay
préparée à l'Université Paris Sud

École doctorale n°571 sciences chimiques : molécules, matériaux,
instrumentation et biosystèmes (2MIB)
Spécialité de doctorat: Chimie

Thèse présentée et soutenue à Orsay, le 20 Septembre 2019 par

Philipp Gotico

Composition du Jury :

Marc Fontecave Professeur, Collège de France	Président du Jury
Marc Robert Professeur, Université Paris Diderot	Rapporteur
Fabrice Odobel Professeur, Université de Nantes	Rapporteur
Sylvie Chardon-Noblat Directrice de Recherche, Université Joseph Fourier Grenoble 1	Examinatrice
Clifford Kubiak Professeur, University of California, San Diego	Examineur
Ally Aukauloo Professeur, Université Paris Sud	Examineur
Winfried Leibl Directeur de Recherche, CEA Saclay	Directeur de thèse

Acknowledgments

I am forever grateful for this journey. I still could not believe that someone who initially did not plan to do PhD studies due to fear and anxiety of the challenges that science can give is now a full-pledged doctor. PhD life is tough, but I learned a lot. It sparked a great interest in answering fundamental questions and even more in asking trivial things. I am truly humbled that I have achieved this feat with great support from a lot of people in so many ways.

First and foremost, I would like to thank my supervisors Winfried Leibl and Ally Aukauloo for picking up a lost soul, for motivating me to stand up on my feet, and for guiding me all the way. Since I started my M2 internship with them, their continuous support and encouragement is remarkable. I want to also extend my gratitude to my co-supervisors Zakaria Halime and Annamaria Quaranta, who supplemented a much-needed guidance. I consider these people as my second family here in France. They are always there answering my random curiosities and taking care of me from all the (mis)adventures during my stay: from breaking my arm in a ski strip, to having a worsened slip disk needing an epidural injection, to having a retinal detachment just after coming from a conference abroad, to losing my passport in Barcelona during a vacation, and to all the other surprises that I bring. These are stories that I will always remember and tell.

I am honored and grateful for all the distinguished scientists in my defense jury: Marc Fontecave, Marc Robert, Fabrice Odobel, Clifford Kubiak, and Sylvie Chardon-Noblat, for taking their time to evaluate my work and for a very insightful three-hour discussion.

I want to thank all the people who I collaborated with during my PhD and without whom I could not have published the papers that I needed to graduate: Davide Audisio, Antonio del Vecchio, and Serena Monticelli from *Laboratoire de Marquage au Carbone 14* (CEA Saclay) for the two-chamber experiments; Bernard Boitrel from *Université Rennes 1* for providing the porphyrin precursors, which made the synthesis of the catalysts less complicated; Marie Sircoglou and Vincent Gandon from *Institut de Chimie Moléculaire et des Matériaux d'Orsay* (ICMMO) for the DFT calculations; Dooshaye Moonshiram from *IMDEA Nanociencia* in Spain for the time-resolved X-ray absorption spectroscopy measurements; and Trần Thu Trang, Minh Huong Ha Thi and Thomas Pino from *Institut des Sciences Moléculaires d'Orsay* for the double flash photolysis experiments.

I thank all the people in ICMMO who I constantly interact with to characterize the complexes I synthesized and to set-up some needed experiments: Regis Guillot (XRD), Christian Herrero (EPR), Tanya Inceoglou (MS), Jean Pierre Baltaze and Amandine Dos Santos (NMR), Emilie Kolodziej (GC-MS), and Eric Riviere (SQUID). I want to also thank Essyllt Louarn from *Laboratoire de Chimie Physique* for the attempts we had for characterizing the “mysterious gas” produced by one of my catalysts using a membrane inlet mass spectrometry.

I thank all my colleagues in *Service de Bioénergétique, Biologie Structurale et Mécanismes* (CEA Saclay): Sandra Andrianambinintsoa, Anja Krieger-Liszkay, Klaus Brettel, Pavel Muller, Sun Un, Diana Kirilovsky, Pierre Setif and Alberto Mezzetti for the informal discussions during coffee sessions or randomly in the hallway and cafeteria. I would like to extend my appreciation to my friends Simona, Fernando, Pablo, Alex and the whole gang in the CEA groups’ “Sushi Fridays” and “Beauty and The Beer” for keeping me sane all these years.

I thank the interns Edouard, Max, Lei, Mewenn, and Yen who I supervised in the laboratory and the SERP Chem Batch of 2018 who I taught a three-hour inorganic chem course, for giving me the opportunity to share my knowledge and experiences. I thank the postdocs Maria, Jully, Khaled, Tania and Rajaa, the alumni Stephanie, Clem, Linh, Antoine and Yiting, and the current PhD students Ju, Asma, Adel, Yiting, Amanda, Laura, Adama, Axel, Nico, Sophie, Riya, Arthur, Gabriel, and Jeremy, to whom I have shared some random questions, jokes, and stories. I especially thank Dr. Tam, my running mate in this PhD journey – we finally did it!

To some extent, I want to thank again my SERP-Chem family headed by our program director Sandrine Lacombe, for giving me the chance to be in Europe in the first place during my master studies and for opening a lot of opportunities from then on. I thank our ever-supportive Eva and Kali who is always there to answer to my needs. I thank my professors Hynd Remita, Thomas Gustavsson, Benedikt Lasalle, Rachel Meallet-Renault, Remi Metivier, and Andrew Mayne for the chance encounters during conferences and some catch-up discussions. I want to extend my gratitude to Laure Catala for agreeing to be on my *comité de suivi de thèse*, for being there to listen and for giving me advices on how to clear up all the confusions and worries I had over the years.

Lastly, I offer all my achievements to my family: Mi, Di, Kuya Van, Kuya Mark, and El, for all your sacrifices and efforts to provide everything in my life.

Taos puso akong nagagalak at nagpapasalamat!

Abstract

Heavy reliance on fossil fuels as a dominant energy resource and a key industrial carbon feedstock has caused alarming concentrations of carbon dioxide (CO₂) in the atmosphere. The anthropogenic accumulation of this greenhouse gas has instigated critical effects on climate change and global warming. This necessitated a global consensus not just in decarbonizing the current energy mix by venturing on renewable energy resources but also in capturing and reducing current CO₂ emissions. A look on the natural carbon cycle reveals an important role that plants play in sequestering CO₂ just by using the renewable solar energy resource. This inspired the strategies employed by the field of artificial photosynthesis in harnessing solar energy while addressing the current greenhouse problem. At the heart of this challenge, is the development of sustainable catalysts that can help capture, activate, reduce, and eventually valorize CO₂.

This PhD project was focused on the design and characterization of molecular catalysts, inspired by natural systems, to understand how to efficiently harness solar energy and use it to drive CO₂ reduction and transformative reactions. An initial investigation was done on rhenium triscarbonyl bipyridyl complexes, photo-activating it with ruthenium trisbipyridine photosensitizers to perform a visible-light driven reduction of CO₂ to CO. The photocatalytic activity of the system was optimized, and key processes were studied by spectroscopy, electrochemistry, and single flash photolysis to track the electron transfer reactions. Because of the need to accumulate photo-induced electrons on the catalyst to perform CO₂ reduction, double flash photolysis and photo-accumulation studies were employed. Such investigations allowed to disentangle productive and deleterious reaction pathways upon multiple excitations, and these fundamental insights are crucial to improve the efficiency of charge accumulation in order to optimize the photocatalytic systems.

In search for more efficient and stable catalysts, synthesis of novel complexes employing earth-abundant metals was pursued. New mimics of the Ni-centered active site of the CO dehydrogenase (CODH), the only enzyme known to reversibly reduce CO₂ to CO, have been synthesized and investigated towards CO₂ reduction activity. Our catalyst design strategy included consideration of an unsaturated coordination sphere of the metal complexes by employing penta-coordinated ligands, multi-point hydrogen bonding pillars, and a substrate-activating

environment on the second coordination sphere. We have successfully engineered a series of modified iron porphyrins employing urea and imidazolium functions in a meticulous 3D pre-arrangement which significantly lowered the overpotential for CO₂ reduction while maintaining good turnover frequency and selectivity.

Further inspiration from functional features of the CODH enzyme led us to establish a proof-of-concept for direct valorization of the CO produced by our photocatalytic system. The photocatalytic system was utilized to transform isotopically labeled ¹³CO₂ into isotopically labeled ¹³CO and immediately use this product in aminocarbonylation reaction to produce isotopically labeled amide groups, a common motif in pharmaceutical drugs. This application shows the capability of our system for light-driven transformation of CO₂ into valorized products, further opening opportunities on renewable energy utilization not only for energy but also for transformative chemistry.

Résumé

La forte dépendance vis-à-vis des combustibles fossiles en tant que source d'énergie dominante et en tant que matière première industrielle de carbone a entraîné des concentrations alarmantes de dioxyde de carbone (CO₂) dans l'atmosphère. L'accumulation anthropique de ce gaz à effet de serre a provoqué des effets critiques sur le changement climatique et le réchauffement de la planète. Cela a nécessité un consensus mondial sur non seulement la décarbonisation du bouquet énergétique actuel en exploitant des sources d'énergie renouvelables, mais également sur la captation et la réduction des émissions actuelles de CO₂. Un regard sur le cycle naturel du carbone révèle le rôle important que jouent les plantes dans la séquestration du CO₂ simplement en utilisant de l'énergie solaire. Cela a inspiré les stratégies employées dans le domaine de la photosynthèse artificielle pour l'exploitation de l'énergie solaire tout en s'attaquant au problème actuel de l'effet de serre. Le développement de catalyseurs pouvant aider à capturer, activer, réduire et valoriser le CO₂ est au cœur de ce défi.

Cette thèse portait sur la conception et la caractérisation de catalyseurs moléculaires, inspirés de la Nature, pour comprendre comment exploiter efficacement l'énergie solaire et l'utiliser pour des réactions de réduction et de transformation du CO₂. Une première étude a été réalisée sur les complexes de rhénium triscarbonyl bipyridyle, photo-activés par des photosensibilisateurs de type ruthénium trisbipyridine afin d'effectuer une réduction du CO₂ en CO induite par la lumière visible. L'activité photocatalytique du système a été optimisée et les processus clés étudiés par spectroscopie, électrochimie, et photolyse éclair pour suivre les réactions de transfert d'électrons. En raison de la nécessité d'accumuler des électrons photo-induits sur le catalyseur pour réaliser la réduction du CO₂, des études de photolyse à double flash et de photo-accumulation ont été entreprises. De telles investigations ont permis de démêler des voies de réaction productives et délétères lors des excitations multiples, et ces informations fondamentales sont essentielles pour améliorer l'efficacité de l'accumulation de charges afin d'optimiser les systèmes photocatalytiques.

Dans cette quête de catalyseurs plus performants pour la réduction du CO₂, les recherches se sont également orientées vers le développement de nouveaux complexes à base de métaux abondants comme catalyseurs. De nouveaux mimiques du site actif centré sur le Ni de la CO déshydrogénase (CODH), la seule

enzyme connue pour réduire le CO_2 en CO , ont été synthétisées et étudiées en vue d'une activité de réduction du CO_2 . Notre stratégie de conception de catalyseur comprenait la prise en compte d'une sphère de coordination non saturée des complexes métalliques en utilisant des ligands penta-coordonnés, ou encore des piliers de liaisons hydrogènes multiples et un environnement de type liquide ionique dans la seconde sphère de coordination. Nous avons mis au point avec succès une série de porphyrines à fer modifiées utilisant les fonctions urée et imidazolium dans un arrangement en 3D méticuleux, ce qui a considérablement réduit le potentiel de réduction du CO_2 tout en maintenant une bonne fréquence de cycle catalytique et une bonne sélectivité.

Une autre inspiration des caractéristiques fonctionnelles de l'enzyme CODH nous a amené à établir une preuve de concept pour la valorisation directe du CO produit par notre système photocatalytique. Le système photocatalytique a été utilisé pour transformer du $^{13}\text{CO}_2$ marqué isotopiquement en ^{13}CO et d'utiliser directement ce produit dans une réaction d'aminocarbonylation pour produire des fonctions amides marquées isotopiquement, un motif courant dans les molécules à intérêt thérapeutique. Cette application montre la capacité de notre système à transformer le CO_2 en produits valorisés, ouvrant aussi de nouvelles possibilités d'utilisation de l'énergie renouvelable, non seulement pour l'énergie, mais également pour la chimie de transformation.

Table of Abbreviations

ACN	acetonitrile
ACS	acetyl CoA synthase
ATR	attenuated total reflectance
BNAH	1-benzyl-1,4-dihydronicotinamide
BIH	1,3-dimethyl-2-phenyl-2,3-dihydro-1H-benzimidazole
bpy	2,2'-bipyridine
Cat	catalyst
CoA	coenzyme A
CODH	CO dehydrogenase
CV	cyclic voltammetry
DABCO	1,4-diazabicyclo[2.2.2]octane
DMA	dimethylacetamide
DMF	dimethylformamide
DFT	density functional theory
ED	electron donor
EXAFS	Extended X-Ray Absorption Fine Structure
Fc	ferrocene
FDH	formate dehydrogenase
FE	Faradaic efficiency
GC	gas chromatography
GHG	greenhouse gas
IR	infrared
LED	light emitting diode
LFP	laser flash photolysis
Me	methyl
MLCT	metal-to-ligand charge transfer
MS	mass spectrometry
NaAsc	sodium ascorbate
NHE	normal hydrogen electrode
nm	nanometer
NMR	nuclear magnetic resonance
OER	one-electron reduced species
Ph	phenyl
PhOH	phenol
PS	photosensitizer
SHE	standard hydrogen electrode
TBAP	tertbutylammonium hexafluorophosphate
TEA	triethylamine
TEOA	triethanolamine
TFE	trifluoroethanol
TOF	turnover frequency
TON	turnover number
TPP	tetraphenylporphyrin
UV-Vis	ultraviolet-visible
XAS	X-ray absorption spectroscopy
XANES	X-ray absorption near edge structure
XRD	X-ray diffraction

Table of Contents

Acknowledgments	iii
Abstract	v
Résumé	vii
Table of Abbreviations	ix
Table of Contents	xi
Chapter 1. Introduction	1
1.1. The Great Concern	3
1.2. Transforming Carbon Dioxide	5
1.3. Artificial Photosynthesis as an Innovative Solution	7
1.4. Enzymatic Conversion of CO ₂	9
1.5. Bio-inspired Strategy	14
1.6. State-of-the-Art	15
1.6.0. Evaluating Catalyst Performance	15
1.6.1. Photosensitizers and Electron Donors	17
1.6.2. Structural Motifs of Functional CO ₂ Reduction Catalysts	22
1.6.3. Catalysts Employing Second Coordination Sphere Effects	32
1.7. Thesis Objectives and Scope	43
Bibliography	44
Chapter 2. Understanding Photocatalysis: <i>How can visible light be used to reduce CO₂ to CO?</i>	49
2.1. Introduction	51
2.2. Objectives	52
2.3. Electrochemistry	53
2.4. Mechanistic Analysis by IR Spectroelectrochemistry	55
2.5. Tracking the First Photo-Induced Electron Transfer	58
2.6. Optimization of Photocatalytic Performance	62
2.7. Tracking Electron Accumulation in the Re Catalyst	67
2.8. Conclusions	72
Bibliography	73
Chapter 3. Designing Catalysts: <i>First Coordination Sphere Modifications</i>	75
3.1. Introduction	77
3.2. Objectives	80
3.3. Syntheses and Structural Characterization	81
3.4. Electrochemical Characterization	83
3.5. Photocatalytic Activity	87
3.6. Tracking the First Photo-Induced Electron Transfer	89
3.7. X-ray Absorption Spectroscopy Measurements	95
3.8. Conclusions	100
Bibliography	100

Table of Contents

Chapter 4. Designing Catalysts: Second Coordination Sphere Effect	103
4.1. Introduction	105
4.2. Objectives	109
4.3. Implications of Proximal Amines	110
4.4. Urea and Amide Moieties as Hydrogen-Bond Relays	118
4.5. Cationic Imidazolium Moieties as Intermediate Stabilizers	129
4.6. Conclusions	136
Bibliography	137
Chapter 5. Valorizing CO₂ Waste: Going beyond CO	141
5.1. Introduction	143
5.2. Carbon Monoxide Valorization	145
5.3. Objectives	147
5.4. Upscaling Optimized Photocatalytic CO ₂ Reduction	148
5.5. Screening and Optimizing CO Valorization	150
5.6. A Change of Criterion	151
5.7. Isotopic Labeling	153
5.8. Conclusions	156
Bibliography	157
Chapter 6. Conclusions and Perspectives	159
Annex: Supplementary Information	167

Chapter 1

Introduction

1.1. The Great Concern

Everything comes with a price. The desire to search for a better life through advancement of economic and industrial sectors has inevitably caused a great dependence on energy sources. Indeed, energy is critical for providing life sustainability needs, basic social services, and income-generating opportunities. Through the years, energy consumption has increased substantially, as shown in Figure 1-1, due to industrial revolution and the large increase in population. With the continuing increase in population and the goal of increasing global standard of living, it is expected that energy consumption will continue to increase.^[1]

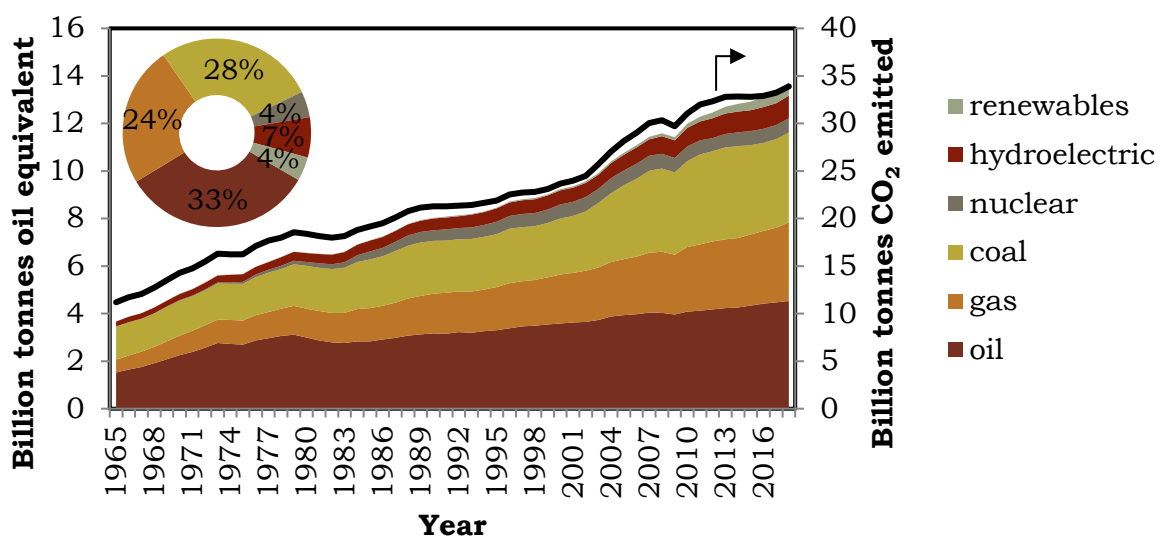


Figure 1-1. Global energy consumption by fuel source type from 1965 to 2011, with the inset showing percent contribution of each fuel type. Black solid line shows the related CO₂ emission from the combustion of oil, coal, and gas. Data from BP Statistical Review of 2019 World Energy.^[1]

The global energy demands are still primarily met by fossil fuels, such as coal, natural gas, and oil/petroleum, at a total of 85% contribution to global energy consumption, as shown in the inset of Figure 1-1. Fossil fuels are products of natural photosynthesis and took millions of years to build up. They contain reduced carbon material with low (coal), average (oil), or high (natural gas) hydrogen content. Burning the C-C and C-H bonds from these hydrocarbons in an exothermic reaction with oxygen releases the stored energy, and as such these products serve as energy carriers^[2] Heavy reliance on such energy sources however presents a critical global concern as fossil fuels are finite and humans are using them at an alarming rate. Further exhaustion of these resources not only concerns the growing energy crisis,

but also the shortage of carbon sources to produce various synthetic organic compounds, polymers, and carbon materials, which are critical inputs for the industrial sector.

A much bigger concern is the emission of carbon dioxide, a dominant greenhouse gas, accompanied when using such energy carriers. As shown in the solid black line in Figure 1-1, for every billion ton of oil equivalent of fossil fuel consumed, around 2-3 billion tons of CO₂ are emitted. What is worrying is that the rate at which human activities emit CO₂ exceeds the rate at which natural photosynthetic systems are able to sequester CO₂ leading to increasing mean concentrations in the atmosphere, as shown in Figure 1-2.^[3] As CO₂ is acting as a greenhouse gas, there is a high correlation between cumulative emissions of CO₂ with global mean surface warming. The current atmospheric concentration of 411.57 ppm (as of June 2019) has already caused around 1 °C temperature increase compared to pre-industrial base temperatures (blue curve in Figure 1-2). The 2014 Fifth Assessment Report of the Intergovernmental Panel on Climate Change (IPCC) indicates that the unprecedented increase of such anthropogenic greenhouse gas emissions have critically disrupted the climatic system causing impacts on both natural and human systems in all continents and across the oceans. Some of these impacts include a decrease in cold temperature extremes, an increase in warm temperature extremes, an increase in extreme high sea levels and an increase in the number of heavy precipitation events in several regions.^[4]

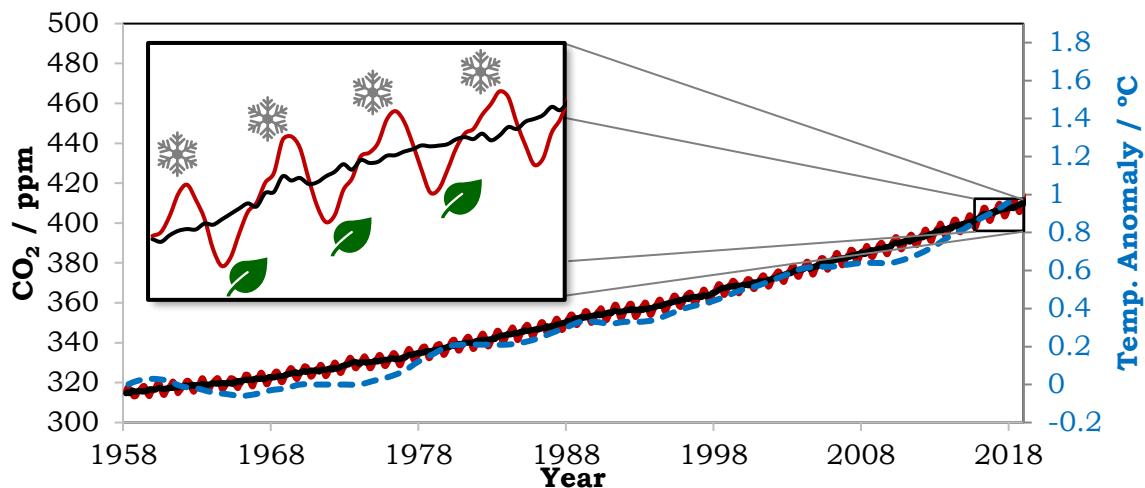


Figure 1-2. Monthly mean carbon dioxide measured at Mauna Loa Observatory, Hawaii from 1958 to 2019, with the red curve showing mole fraction in dry air and the black curve showing mean values after correction for seasonal cycle magnified in the inset. Blue dashed lines correspond to the global surface temperature change from the base period of 1951-1980. Data from NOAA Earth System Research Laboratory.^[3,5]

Continued emission of such greenhouse gas will cause further warming by the end of the 21st century leading to a very high risk of severe, pervasive and irreversible global impacts. The report suggests that mitigation measures would be more cost-effective if used in an integrated approach that combines actions to reduce energy use and the greenhouse gas intensity of end-use sectors, decarbonize energy supply, reduce net emissions, and enhance carbon sinks in land-based sectors.^[4] As such, the Paris Agreement was then adopted by 195 nations to the United Nations Framework Convention on Climate Change in December 2015 that aimed at strengthening the global response to the threat of climate change by “holding the increase in the global average temperature to well below 2°C above pre-industrial levels and pursuing efforts to limit the temperature increase to 1.5°C above pre-industrial levels.”^[6] This in part accelerated the global research and implementation of carbon capture, storage, and utilization strategies.

1.2. Transforming Carbon Dioxide

Carbon dioxide is an extremely stable molecule generally produced by fossil fuel combustion and respiration. Returning CO₂ to a useful state by activation is a scientifically challenging problem, requiring appropriate catalyst and energy input. The initial step to activate CO₂ involves an electron transfer (reduction process) that occupies the σ^* anti-bonding lowest unoccupied molecular orbital (LUMO). This causes the increase in the C-O distance, manifested in the bending of the molecule, as shown in Figure 1-3.^[7] This bent molecule can then interact with electrophiles and nucleophiles through its frontier orbitals.

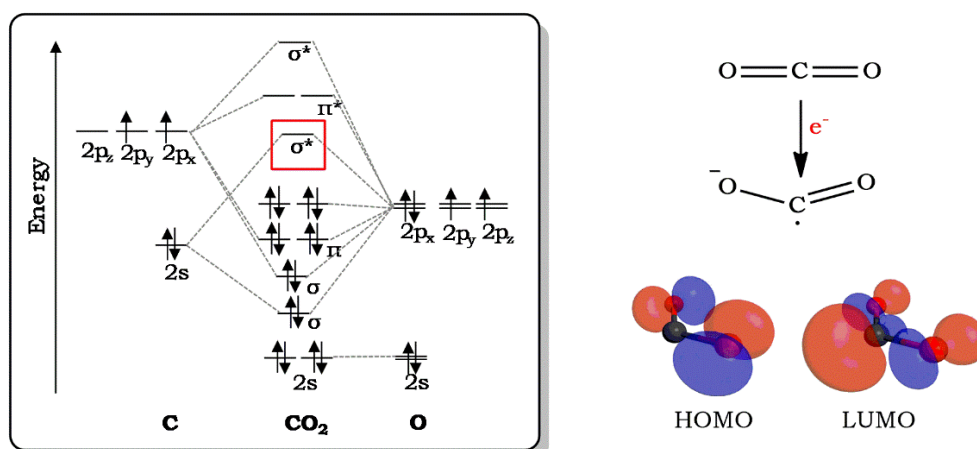


Figure 1-3. Initial activation of the linear molecule requires an electron transfer that makes the linear molecule bent. The bent CO₂ shows strong charge localization associated with the frontier orbitals.^[7]

Table 1-1. Reduction potentials of various reduction reactions of CO₂.

Reaction	E° / V vs SHE
CO ₂ + e ⁻ → CO ₂ ^{•-}	-1.90
CO ₂ + 2e ⁻ + 2H ⁺ → CO + H ₂ O	-0.53
CO ₂ + 2e ⁻ + 2H ⁺ → HCOOH	-0.61
CO ₂ + 4e ⁻ + 4H ⁺ → H ₂ CO + H ₂ O	-0.48
CO ₂ + 6e ⁻ + 6H ⁺ → H ₃ COH + H ₂ O	-0.38
CO ₂ + 8e ⁻ + 8H ⁺ → CH ₄	-0.24

This one-electron reduction of CO₂ to CO₂^{•-} however, is a highly endergonic reaction occurring at a reduction potential of E° = -1.90 V vs SHE, due to a large reorganizational barrier between the linear molecule and bent radical anion. Multi-proton and multi-electron steps are more favorable than single electron reductions because they can lead to thermodynamically more stable molecules like carbon monoxide (CO), formic acid (HCOOH), formaldehyde (H₂CO), methanol (H₃COH), and methane (CH₄) as products (Table 1-1). This thermodynamic ease comes however with a kinetic cost of bringing together all the protons and electrons in appropriate pathways to result in the desired reaction. As such, to transform CO₂ by overcoming the thermodynamic and kinetic barriers of its reduction, catalysts are needed to stabilize intermediate transition states. In addition, energy is still needed to be introduced into the reaction mixture to drive the reduction reactions because of the intrinsic overpotential of catalytic systems. Ideally, the energy for this process will be supplied by a renewable source such as solar energy. The energy-rich reduction products then may serve as energy source in a closed carbon-neutral cycle.

Though products such as methanol and methane are more readily useful as fuels, direct reduction of CO₂ to such products necessitates multiple electron and proton transfer and the kinetic barriers associated with these are very high. In comparison, the “considerably easier” strategy of 2-electron, 2-proton coupled reduction of CO₂ to CO is equally valuable as CO can then be used in the well-proven d-metal catalyzed Fischer-Tropsch technologies to convert synthesis gas (CO and H₂) to liquid hydrocarbons such as diesel fuel and gasoline.^[8] Carbon monoxide also has a significant fuel value (ΔH_c⁰ = -283 kJ/mol) and can readily be converted into methanol (e.g., by the CuO/ZnO/Al₂O₃-catalyzed process) for use as a liquid

fuel. Furthermore, CO serves as an important feedstock in industrial processes such as the production of acetic acid by Cativa-Monsanto processes,^[9] purification of nickel in the Mond process,^[10] and the production of phosgene,^[11] useful for preparing isocyanates, polycarbonates, and polyurethanes. Indeed, in a techno-economic perspective, the transformation of CO₂ molecules to short-chain simple building blocks is currently the most economically compelling target because of the current efficiencies and selectivities of catalytic systems.^[12]

1.3. Artificial Photosynthesis as an Innovative Solution

A deeper look in the CO₂ concentration trends in Figure 1-2 already reveals the potential of natural systems for sequestering CO₂. The high concentrations during winter are significantly lowered when the first signs of spring arrive due to the process of photosynthesis. Plants, algae, and most autotroph bacteria are known to use free and sustainable resources such as solar energy and water to capture and store CO₂ in the form of carbohydrates thereby providing essentially all energy input into the biosphere. This biological process provides an interesting strategy by employing sustainable solar energy to transform CO₂ into an energy vector, closing the carbon cycle and alleviating global warming.^[13] This process is also the basis of the field of artificial photosynthesis. By learning and mimicking the natural photosynthetic systems, artificial technologies can be designed to produce renewable solar fuels and synthetic building blocks from CO₂ as a feedstock and as such, address at the same time the intermittency and storage concerns of solar energy harnessing, as envisioned in Figure 1-4.

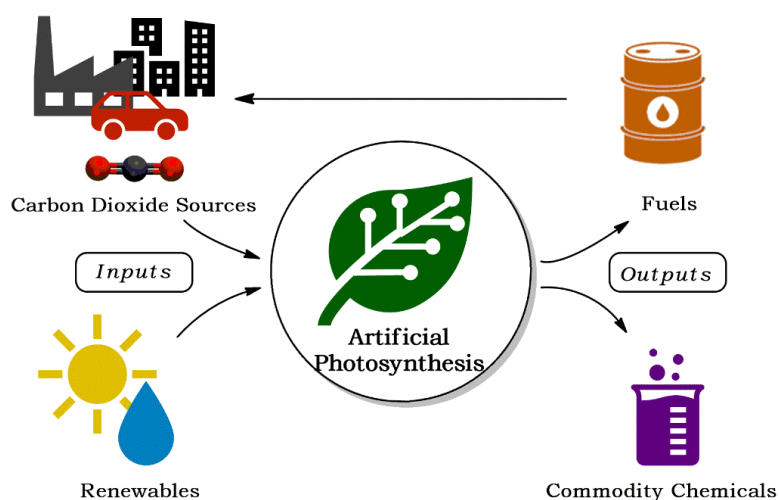


Figure 1-4. Strategy of artificial photosynthesis in harnessing renewable solar energy while reducing carbon dioxide.

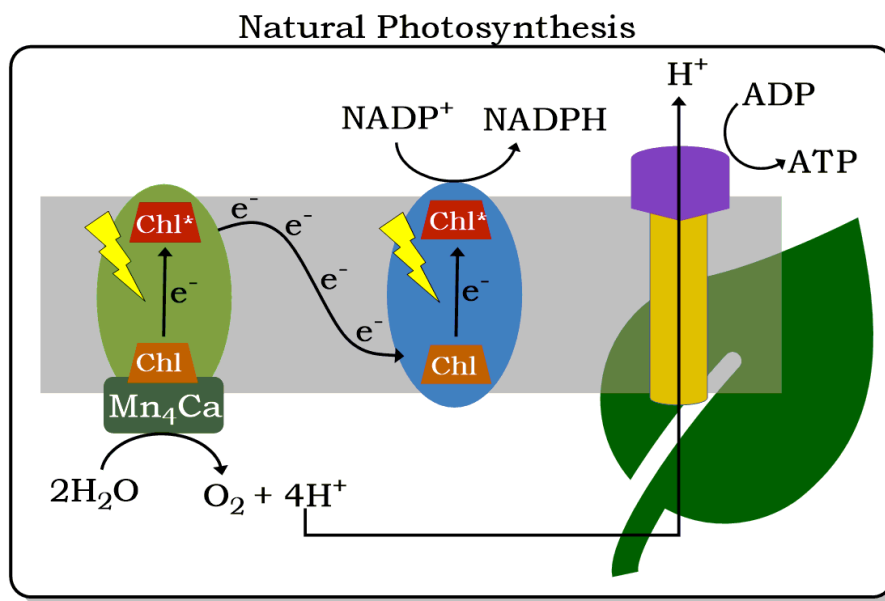


Figure 1-5. General schematic process involved in natural photosynthesis in harnessing solar energy and transforming CO_2 to carbohydrates.

In natural photosynthesis, solar energy is absorbed by light harvesters which transfer this energy to the reaction center where reduction-oxidation (redox) reactions occur, as shown in Figure 1-5. To maximize the entire visible spectrum of the solar irradiation, green plants use a variety of light harvesters: chlorophyll a, the main pigment, absorbs in the blue-violet, orange-red spectral regions while the accessory pigments like xanthophylls, carotenoids, and chlorophyll b, absorb in the intermediate yellow-green-orange part. These light harvesters are specifically arranged in an antenna-array configuration to efficiently capture solar energy and relaying them to the reaction centers.^[14] The reaction centers use this excitation energy to transfer electrons from donors to acceptors, creating energetic charge-separated states that resist recombination long enough to allow migration of the oxidizing and reducing equivalents to the catalytic sites. Water oxidation to molecular oxygen occurs in the manganese-calcium complex of the photosystem II (PS II) reactions while the electrons are delivered through a series of uphill and downhill steps to generate energy-rich intermediates in the photosystem I (PS I) reactions. The process results in the synthesis of the biological two-electron reducing agent nicotinamide adenine dinucleotide phosphate (NADPH) and generates a transmembrane proton gradient that drives the production of adenosine triphosphate (ATP).^[15] Both NADPH and ATP are then used in a series of light-independent reactions to form C-C covalent bonds of carbohydrates.



Figure 1-6. General schematic process involved in artificial photosynthesis in harnessing solar energy and transforming CO_2 into high-energy chemicals.

In the artificial system, the goal is to design a photochemical cell that similarly contains a photosensitizer that captures solar energy, creating charged separated states. The holes are used by an oxidation catalyst to oxidize water to molecular oxygen producing electrons and protons which are then utilized by a reduction catalyst to reduce protons to dihydrogen gas or reduce carbon dioxide to produce high-energy chemicals called solar fuels, as shown in Figure 1-6. At the core of this strategy is the fundamental understanding on how the energy of a photon of light is transformed and leveraged to drive redox reactions that are otherwise endergonic in the absence of light. As such, this presents an interesting way of harnessing and storing the intermittent renewable solar energy as chemical energy which can be exploited at the later part of the process chain.

1.4. Enzymatic Conversions of CO_2

In nature, there are six pathways known to fix carbon dioxide as organic material for biomass. The involved enzymes perform carboxylation of various sugars, coenzyme-A (CoA) esters and carboxylic acid, and reduction of CO_2 (to CO or formate).^[7] The dominant process is the reductive pentose phosphate (Calvin-Benson-Bassham) cycle which involves the ribulose biphosphate carboxylase/oxygenase (RuBisCO) catalyzing the reaction of CO_2 with a five-carbon

sugar 1,5-ribulose biphosphate to form two molecules of 3-phosphoglycerate (a precursor for a series of interconversions to form the six-carbon sugar fructose-1,6-biphosphate).^[16] The other five pathways all involve net reactions of producing acetyl-CoA from CO₂ for anabolic (biosynthesis) and catabolic (energy) purposes: reductive acetyl-CoA pathway, reductive citric acid cycle, dicarboxylate/4-hydroxybutyrate cycle, 3-hydroxypropionate/4-hydroxybutyrate cycle, and 3-hydroxypropionate bi-cycle.^[17]

Though the thermodynamically favorable multi-electron reductions of CO₂ are very important reactions, they are surprisingly not observed in natural systems, which instead use discrete two-electron reduction steps. For example, the Wood-Ljungdahl pathway for autotrophic growth and acetate synthesis involves initial two-electron reduction steps: the CO dehydrogenase (CODH)-catalyzed reduction of CO₂ to CO and the formate dehydrogenase (FDH)-catalyzed reduction of CO₂ to formate. Similar discrete two-electron steps are involved in the eight-electron reduction reactions observed for methanogenic archaea catalyzing CO₂ to methane and for acetogenic bacteria catalyzing reduction of CO₂ to acetic acid. Reasons for this strategy include (i) the versatility of these two-electron reduced intermediates to branch off into various pathways for the synthesis of cellular metabolites, and (ii) the final products (e. g. methane, acetic acid) are usually just by-products in the overall energy conservation scheme.^[18] As such, fundamental learnings from the biological two-electron reduction of CO₂ to CO and formate would be particularly interesting in designing synthetic CO₂ reduction catalysts.

CO-dehydrogenase (CODH) catalyzes the two-electron, two-proton interconversion between CO₂ and CO. Two types of CODH exist: one is from anaerobic microorganisms such as *Moorella thermoacetica*, *Carboxydotherrmus hydrogenoformans*, and *Methanosarcina barkerii* with a [NiFe] active site, and another from aerobic organisms such as *Oligotropha carboxidovorans* with a [MoCu] active site.^[7] The [NiFe]-centered active site catalyzes the reversible reduction of CO₂ to CO with turnover frequency (TOF) of 45 s⁻¹ for CO₂ reduction and TOF of 40,000 s⁻¹ for CO oxidation.^[19] Crystallographic studies of the oxidized form of this [NiFe] C cluster site shows a Ni center bridged by an Fe₃S₄ electronic buffer that rigidly positions the Ni metal in close proximity to an Fe metal (structure **1** in Figure 1-7). The Ni species is coordinatively unsaturated binding three sulfur ligands in a distorted T-shaped configuration. In its reduced form (reaction with Ti^{III} citrate) and in the presence of CO₂ substrate (through bicarbonate ion source), CO₂ is observed

to bridge the Ni and Fe metals, as shown by structure **3** in Figure 1-7. CO₂ is bound to the reduced, formally Ni⁰ metal by the C atom completing the square planar coordination of Ni while the carboxylate oxygen atom is bound to the pendant Fe atom, as well as forming hydrogen bond with a lysine (Lys) residue. In addition, the second carboxylate oxygen atom seems to be within a hydrogen bonding distance from a protonated histidine (His) residue. This bifunctional activation, reminiscent of a frustrated Lewis acid-base pair, works in synergy with the second coordination sphere activation to cause only minor changes from the T-shaped coordination geometry to square planar.^[20] This structure promotes the heterolytic cleavage of the C-O bond, resulting in a CO coordinated to the Ni metal and a hydroxide coordinated to the Fe metal. The CO is then released from this Ni center to form back the oxidized state, completing the proposed mechanism in Figure 1-7.^[7] The low reorganizational energy observed from these experimentally-determined intermediate structures explains the high turnover rates of the enzyme.

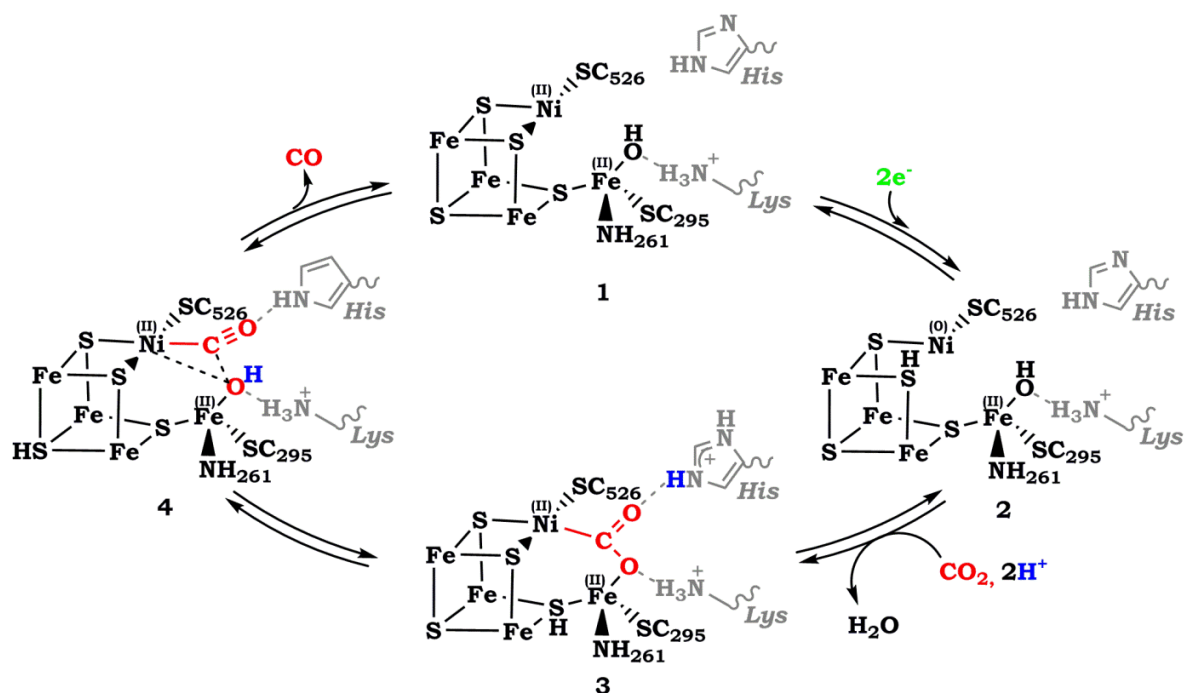


Figure 1-7. Proposed structure-based mechanism for the catalytic cycle of [NiFe] CODH towards reversible reduction of CO₂ to CO.^[20]

[MoCu] CODH has similar structure to that of the [NiFe]-centered CODH with the presence of heterobimetallic metal centers in the active site though it is observed to only catalyze the oxidation of CO to CO₂ at a much lower TOF of 100 s⁻¹.^[21,22] The oxidized form of the active site shows a Mo metal with an apical oxo

group linked to two sulfur atoms of the molybdopterin cytosine dinucleotide cofactor, as shown in structure **5** in Figure 1-8. The second coordination sphere similarly contains amino acid residues such as glutamine and glutamate that are within hydrogen bonding distances from the oxo and hydroxyl ligands, respectively. Based on *n*-butylisonitrile-inhibited enzyme studies,^[22] the reaction of a Mo^{VI} oxo/hydroxy species with CO leads to the formation of the reduced Mo^{IV} state with a thiocarbonate insertion product, structure **6**. This is a distinct difference with the [NiFe] CODH as the carbon atom of the carboxylate-like intermediate is bound to the ligated sulfido group acting as the Lewis base, instead of the reduced Mo metal center.^[7]

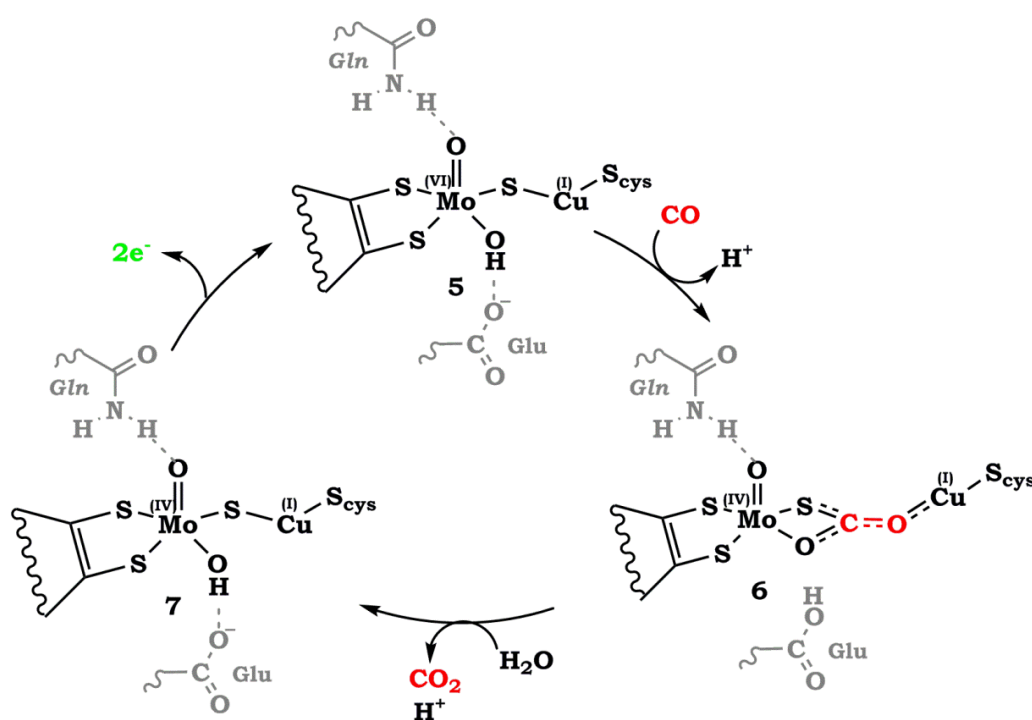


Figure 1-8. Proposed structure-based mechanism for [MoCu] CODH towards oxidation of CO to CO₂.^[22]

A similar sulfur-rich Mo-centered active site is found in the air-sensitive formate dehydrogenase (FDH). These enzymes catalyze both the reduction of CO₂ to formate with a TOF of 280 s⁻¹ and the oxidation of formate with TOF of 3400 s⁻¹.^[23] The oxidized form of the active site contains a Mo^{VI} metal center in a distorted trigonal prismatic geometry with four S atoms from two pyranopterin ligands, a selenium atom from a selenocysteine residue, and a sulfur atom in the sixth coordination site, as shown in structure **8** in Figure 1-9. In its reduced form, a square pyramidal coordination is produced with an apical sulfur atom and

decoordinated selenocysteine ligand. Based from nitrite-inhibited enzyme studies, one oxygen atom of the CO_2 substrate is bound to the Mo metal while the other oxygen atom is in close contact with an arginine (Arg) residue assisting to orient the intermediate for proton delivery by the protonated histidine (His) residue, as shown in structure **11**.^[24] After this protonation step, the formate product is released, producing back the oxidized form and completing the proposed catalytic cycle in Figure 1-9.

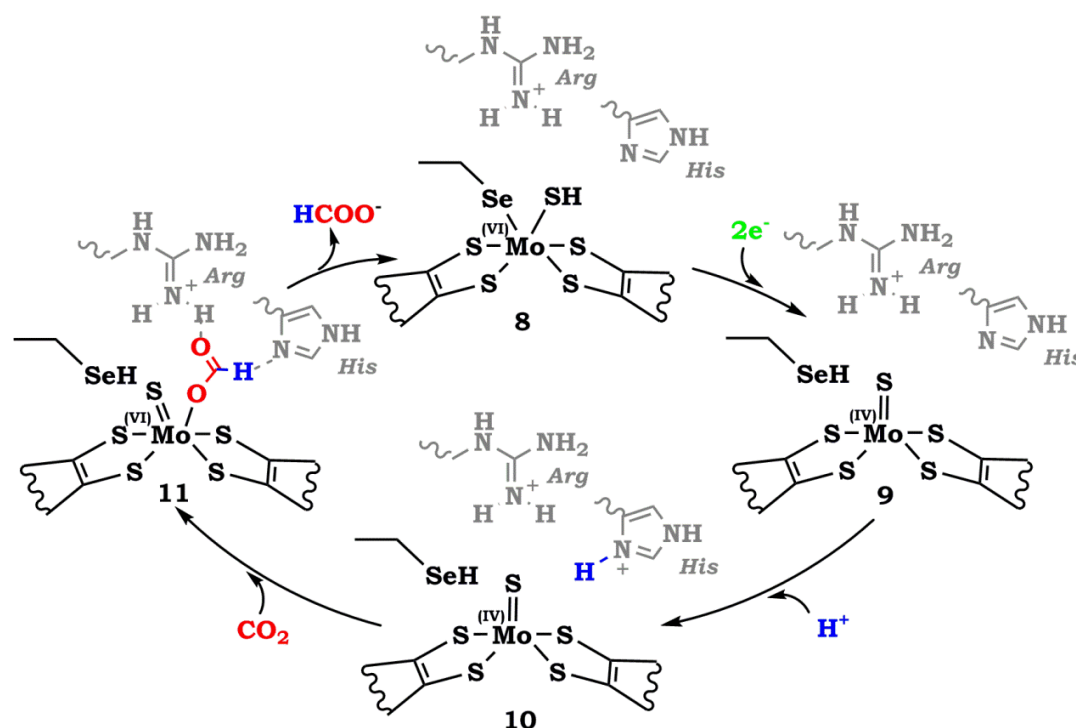


Figure 1-9. Proposed structure-based mechanism of formate dehydrogenase towards reduction of CO_2 to formate.^[7,24]

These enzymes that catalyze the two-electron and two-proton reduction to either CO or formate seemingly contain similar features. First, they consist of sulfur-rich ligand structures that can store and supply electrons (Fe_3S_4 cluster, and pterin-like cofactors). Second, they employ a substrate-activating environment either by bifunctional Lewis acid-base pair or second coordination sphere activation by nearby amino acid residues. Third, they promote good CO_2 binding in meticulously pre-arranged active sites with minimal changes in the geometry, resulting in low reorganizational energies. Lastly, they take leverage of the flexibility of their aqueous environment to manage the proton supply, and promote proton-coupled electron transfer steps, significantly helping in the thermodynamic requirement of the reduction reactions.

1.5. Bio-inspired Strategy

Inspired by the ingenious scheme of natural photosynthesis in harnessing solar energy and the efficiency of enzymes in selectively performing discrete two-electron CO_2 reduction steps, we envisioned a bio-inspired strategy taking into account key insights from these natural systems. A modular molecular approach strategy was chosen to systematically design and investigate photo- and electro-catalysts for CO_2 reduction. As shown by the general scheme in Figure 1-10, the photo-catalytic system consists of a photosensitizer (**PS**) capable of absorbing light and creating charge separated states. The holes are replenished by an electron donor (**ED**), which ideally performs the oxidation of water in the final photo-electrochemical cell, and the electrons are used to activate a reduction catalyst (**Cat**) for CO_2 reduction. On the other hand, an electro-catalytic system takes leverage of photovoltaics to deliver the necessary electrons to the catalyst. Central to both these approaches is the design of homogenous molecular catalysts taking into account a ligand framework able to accumulate charges, a metal-centered catalyst able to capture and bind CO_2 , and a second coordination environment able to activate the substrate, all working in synergy to efficiently reduce CO_2 . Such strategy would not only provide fundamental understanding of transforming solar energy into chemical energy but also important information for the development of efficient bio-inspired catalysts.

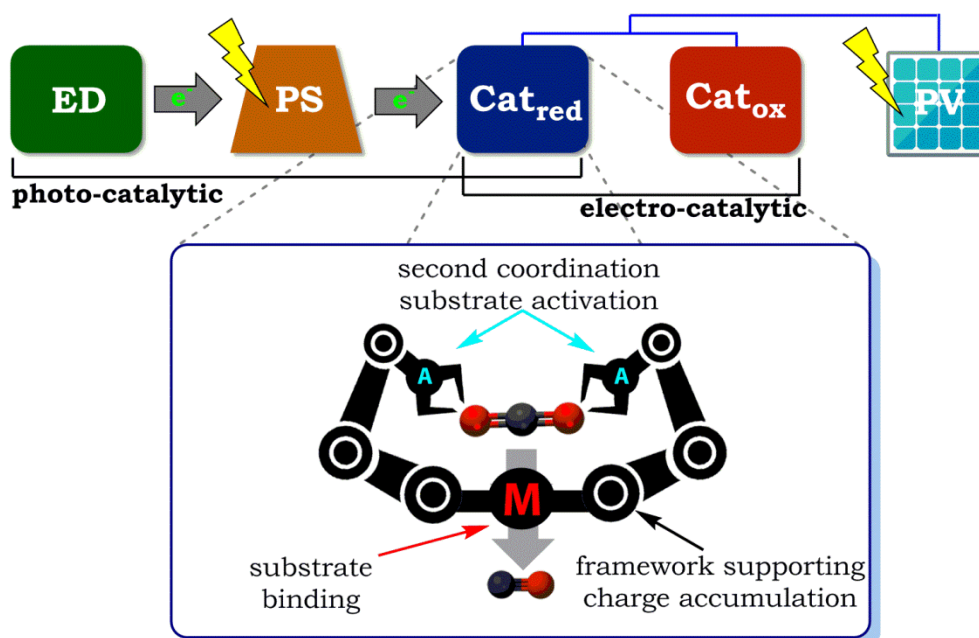


Figure 1-10. Bio-inspired strategy employing a modular molecular approach in developing photo- and electro-catalytic systems for CO_2 reduction. (ED = electron donor, PS = photosensitizer, Cat_{red} = reduction catalyst, Cat_{ox} = oxidation catalyst PV = photovoltaics).

1.6. State-of-the-Art

Following the bio-inspired strategy, a look on the current state-of-the art on both photo- and electro-catalytic systems would provide a background on where our approach will commence. Extensive reviews^[25–27] have been published in the literature but here it will be limited to the following: i) summary of photosensitizers and electron donors used in photo-catalytic systems, ii) summary of common structural motifs of CO₂ reduction catalysts, and iii) summary on catalysts employing second coordination effects.

1.6.0. Evaluating Catalyst Performance

The difference in the photo- and electro-catalytic approach requires a look on the different criteria used to compare catalysts performance. Generally, a better performing catalyst should have high activity, high energetic efficiency, high stability, and high selectivity,

The activity of the catalyst is often reported by calculating the rate of the catalytic reaction in the form of turnover frequency (TOF) with a unit of s⁻¹. In a photo-catalytic system, this is measured by the initial linear slope of the plot between amount of products normalized by the amount of catalyst in the solution and the irradiation time. In an electro-catalytic system, a reaction layer is considered because not all of the bulk concentration of the catalyst participates in the reaction. The catalytic rate is measured based on the amount of active catalysts in the vicinity of the electrode that participates in the catalytic cycle at given point in time. This is determined by foot-of-the wave analysis of the cyclic voltammogram of the catalyst in a catalytic condition (presence of CO₂ substrate and proton source). This is described in detail in the Supplementary Information in the Annex. The higher the TOF, the more products are formed per unit of time.

The stability of the catalyst strongly depends on a variety of deactivation pathways such as decomposition, deleterious side reactions, and product inhibition, but the overall performance is usually evaluated in terms of turnover number (TON). In a photo-catalytic system, this is simply determined by dividing the maximum amount of products formed by the amount of catalyst in the solution. In an electro-catalytic system, the TON is determined from the calculated TOF but more accurately described by the trend in the current as a function of bulk electrolysis time.

The energetic efficiency refers to how a source of energy (either by a photon for photo-catalytic systems or an electrical energy for electro-catalytic system) is efficiently utilized to perform the reduction of CO₂. In a photocatalytic system, it is reported in the form of quantum efficiency calculated by dividing the equivalent amount of electrons from the amount of product formed by the amount of photons absorbed by the system. The higher the quantum efficiency, the more efficiently a photon of light is utilized to form the product. In an electro-catalytic system, it is reported in terms of Faradaic efficiency and overpotential. Faradaic efficiency is calculated by dividing the equivalent amount of electrons from the amount of product formed by the total amount of charge passed during bulk electrolysis. The higher the Faradaic efficiency, the more efficient is the charge utilized to form the product. Overpotential is similarly calculated as it refers to the additional potential needed to be applied to the system past the thermodynamic potential of the reaction. A lower overpotential indicates a less energetic requirement to perform the reaction.

Lastly, selectivity is as important as the other criteria because it refers to how a preferred reaction is being followed and it would be indicative of the additional steps necessary to perform the separation of other undesired products. In the photo-catalytic system, it is calculated by dividing the amount of the desired product by the total amount of products formed. It is similarly determined for the electro-catalytic system, but the calculated Faradaic efficiency would already give a hint on the product selectivity of the system.

These criteria are often used for catalyst performance comparison but when considering scalability and industrial applications, the cost of the catalyst is as well important. The choice of the metal for metal-centered catalysts is usually related to its abundance, with first row transition elements appearing to be cheaper choices. There should be a balance of choice however, as the complexity of the ligand framework (indicating expensive synthetic routes) could counterbalance the cost of the metal. In the end, as long as the catalyst is stable and efficiently performing, it almost translates to upscaling with some cost modifications, which is beyond the scope of this comparison.

1.6.1. Photosensitizers and Electron Donors

The first step in the photo-catalytic system is the harvesting of solar energy creating charge-separated states. As such, photosensitizers should i) absorb in the solar irradiation spectrum (preferentially with high absorption coefficient in the visible region), ii) have a long-lived excited state for efficient quenching process, and iii) provide the necessary redox power (either in the excited state or one-electron reduced species) matched for an electron transfer to the catalyst.^[25]

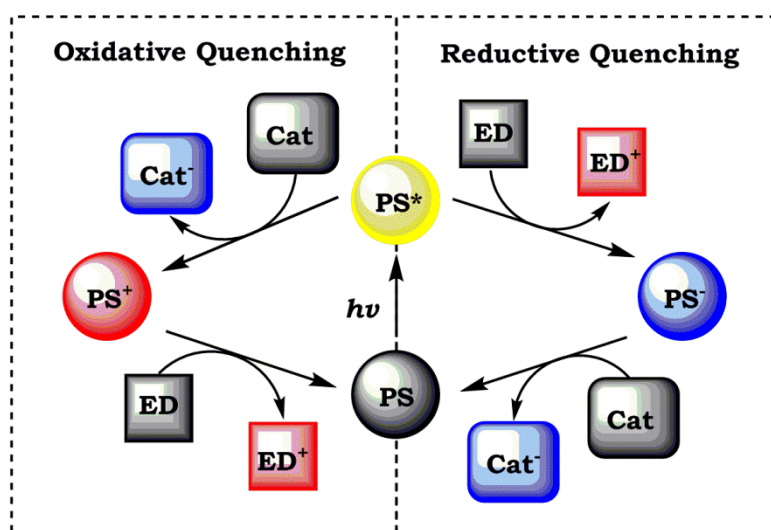


Figure 1-11. Possible electron transfer quenching mechanisms of an excited photosensitizer (PS = photosensitizer, Cat = catalyst, ED = electron donor).

After absorption of light, the excited state of the photosensitizer can either be quenched by energy transfer or electron transfer reactions. Energy transfer usually occurs between two light-sensitive complexes through radiative or radiationless transition between two excited states. As in general excited states have at the same time reducing and oxidizing power, electron transfer occurs either by reductive or oxidative quenching, as shown in Figure 1-11. Reductive quenching occurs when the excited photosensitizer **PS*** reacts with the electron donor forming a one-electron reduced species (OER) of the photosensitizer, denoted **PS-**, and an oxidized donor **ED+**. This **PS-** can then reduce and transfer the electron to the catalyst, **Cat**. On the other hand, oxidative quenching occurs when **PS*** is reducing enough to already reduce the **Cat** forming **Cat-** and oxidized **PS+**. The **ED** then reduces this **PS+** to form back the original **PS**. Which quenching mechanism is followed depends first on the relative concentrations of **ED** and **Cat** if these bimolecular interactions of

both with **PS** are diffusion controlled. But importantly the occurrence of both quenching mechanisms depends on the thermodynamic drive between the intermediates, and as such the following parameters are determined: oxidation potential (reducing power) of the excited photosensitizer (E_{ox}^* of $\text{PS}^* \rightarrow \text{PS}^+$), reduction potential of catalyst (E_{red} for $\text{Cat}^0 \rightarrow \text{Cat}^-$), reduction potential (oxidizing power) of the excited photosensitizer (E_{red}^* of $\text{PS}^* \rightarrow \text{PS}^-$), and oxidation potential of the electron donor (E_{ox} for $\text{D}^0 \rightarrow \text{D}^+$). The excited state potentials are determined by the Rehm-Weller equation: $E_{\text{red}}^* = E_{\text{red}} + E_{00}$ and $E_{\text{ox}}^* = E_{\text{ox}} - E_{00}$, where $E_{\text{red/ox}}$ refers to the ground state potentials for reduction and oxidation of the photosensitizer measured by cyclic voltammetry, and E_{00} represents the difference in energy between the zeroth vibrational states of the ground and excited states, experimentally determined from the intersection between the absorption and emission spectra, often just approximated by the emission energy of the PS at 77 K.^[28,29] Some common and notable photosensitizers utilized for the photocatalytic reduction of CO_2 are listed in Table 1-2 with the structures shown in Figure 1-12.

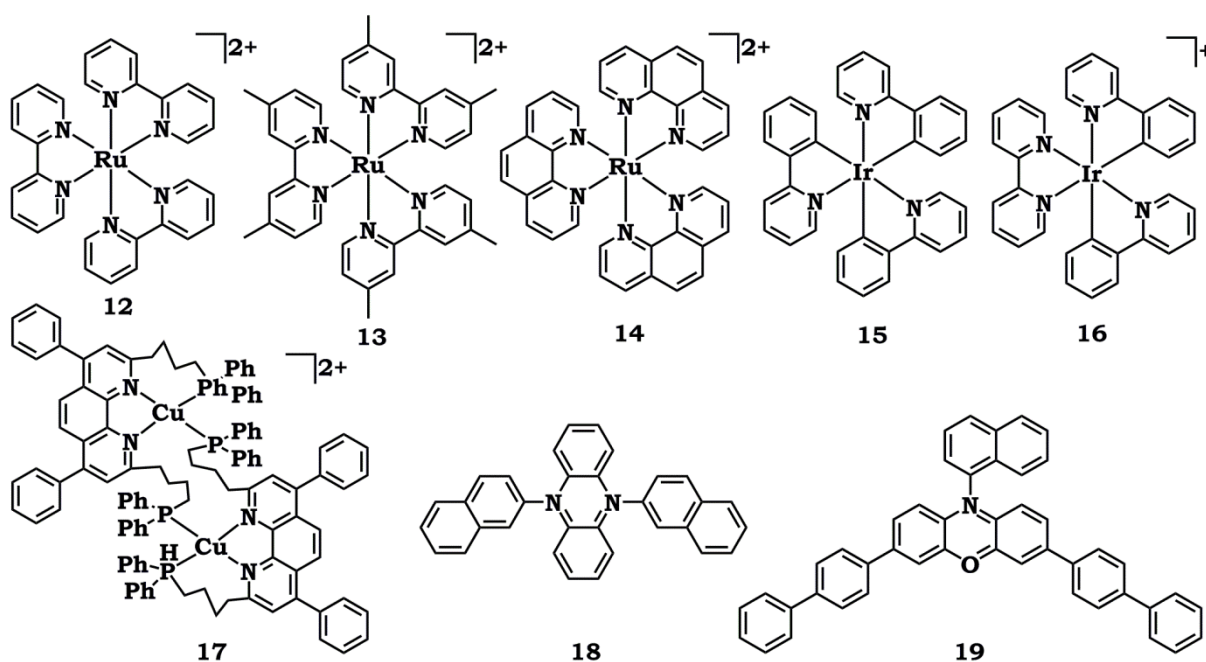


Figure 1-12. Some common and notable photosensitizers used for the photocatalytic CO_2 reduction.

One of the most common photosensitizers used is the ruthenium (II) trisbipyridine, denoted as $[\text{Ru}(\text{bpy})_3]^{2+}$ shown in structure **12**. This complex shows strong absorption in the visible region, attributed to the singlet metal-to-ligand charge transfer ($^1\text{MLCT}$). After the absorption of light, there is a fast intersystem

crossing (change of spin state) to a triplet MLCT ($^3\text{MLCT}$) with quantum efficiency near unity due to the strong spin-orbit coupling from the heavy metal center. Because of the forbidden nature of transition from $^3\text{MLCT}$ to the singlet ground state, this results in a long-lived emission with typical lifetimes from 600 to 1000 ns. This excited state lifetime is long enough to allow chemical interactions with other components in the solution. In photocatalytic CO_2 reduction, this excited state is usually reductively quenched by an electron donor to form the bipyridine-centered one-electron-reduced (OER) species, formally denoted as Ru^{I} . From Table 1-2, the typical $[\text{Ru}(\text{bpy})_3]^{2+}$ has a reducing potential of $-1.71 \text{ V vs Fc}^{+/0}$,^[30] thermodynamically sufficient to transfer an electron to some CO_2 reduction catalysts. Modifying this photosensitizer by introducing methyl donors in the 4,4'-position (structure **13**) increases the reducing power to $-1.83 \text{ V vs Fc}^{+/0}$ ^[31] or replacing the bipyridine ligands with phenanthroline ligands (structure **14**) increases the potential to $-1.79 \text{ V vs Fc}^{+/0}$,^[32] showing the versatility of this class of complexes in driving the photo-induced electron transfer to CO_2 reduction catalysts. In addition, this class of photosensitizers has spectrally defined characteristics that permit tracking of electron transfer steps in the system by time-resolved absorption measurements.

Table 1-2. Photophysical and electrochemical characteristics of some photosensitizers used for photocatalytic CO_2 reduction, with labels and structures shown in Figure 1-12. Shaded region corresponds to the reducing power sought from these **PS**. Potentials are all reported versus the $\text{Fc}^{+/0}$ reference couple.

PS	$\lambda_{\text{max}}^{\text{abs}}$	$\lambda_{\text{max}}^{\text{em}}$	$\tau^{[\text{d}]}$ / μs	E_{red} / V	E_{ox} / V	E_{red}^* / V	E_{ox}^* / V	Ref.
12 ^[a]	452 nm	615 nm	1.10	-1.71	0.91	0.39	-1.19	[30]
13 ^[b]	462 nm	639 nm	0.88	-1.83	0.73	0.21	-1.31	[31]
14 ^[a]	477 nm	608 nm	0.60	-1.79	1.02	0.43	-1.20	[32]
15 ^[a]	375 nm	494 nm	1.90	-2.57	0.39	-0.07	-2.11	[33]
16 ^[a]	310 nm	606 nm	0.34	-1.78	0.88	0.55	-1.45	[34]
17 ^[a]	375 nm	624 nm	3.19	-2.04	0.80	-0.02	-1.19	[35]
18 ^[c]	343 nm	654 nm	4.30	-	-0.17	-	-2.07	[36]
19 ^[c]	388 nm	506 nm	480	-	0.27	-	-2.18	[36]

^[a] acetonitrile, ^[b] dimethylformamide, ^[c] dimethylacetamide, ^[d] from the triplet state

Catalysts that operate at more negative potentials (i.e. more negative than -1.9 V) require the use of cyclometalated iridium (III) tris-2-phenylpyridine, denoted as $[\text{Ir}(\text{ppy})_3]$ shown in structure **15**. Once excited in the near UV region (375 nm), it

possesses a sufficiently long-lived excited state (-1.90 μs) with a very reducing potential of -2.11 $\text{V vs Fc}^{+/0}$ which can reduce most CO_2 reduction catalysts.^[33] It can also be reductively quenched to form a more reducing OER with a potential of -2.57 $\text{V vs Fc}^{+/0}$. Equally important is the reducing power of the modified **[Ir(ppy)₂(bpy)]⁺** (structure **16**) which possesses a spectrally well-defined bpy-centered OER once the excited state is reductively quenched.

There is a current exploration of cheaper alternatives for photosensitizers for the photocatalytic CO_2 reduction and some have emerged as promising alternatives for the Ru and Ir-based ones. Notable examples include the heteroleptic copper (I) complex possessing diimine and phosphine ligands (structure **17**) which possesses a long-lived excited state (3.19 μs) and a sufficiently reducing power of -2.04 $\text{V vs Fc}^{+/0}$ for the OER once reductively quenched by an electron donor. Organic dyes were also considered as potential **PSs** because of their long-lived excited state but most do not possess sufficiently reducing potentials. Recent advancements show the promise of N,N-5,10-di(2-naphthalene)-5,10-dihydrophenazine (structure **18**) and 3,7-(4-biphenyl)-1-naphthalene-10-phenoxazine (structure **19**) which access a long-lived triplet excited state (4.3 μs and 480 μs for **18** and **19**, respectively) and at the same time possessing very reducing excited state potentials comparable with the Ir-based **PSs** (-2.07 V and -2.18 V for **18** and **19**, respectively).^[36] It can be noticed however from Table 1-2, that **PSs** possessing more reducing power have absorptions only at the shorter wavelengths of the visible region. As such, a choice of **PS** should balance the need to maximize the solar irradiation spectrum and the thermodynamic matching with the CO_2 reduction catalyst.

The modular molecular approach for CO_2 reduction requires the use of appropriate electron donors to either reductively quench the excited **PS** to produce the OER species of the **PS** or to reduce the oxidized **PS⁺** (formed from the oxidative quenching with the catalyst) to generate back **PS** (Figure 1-11). As such, it should possess the necessary thermodynamic potential (E_{ox} of ED < E_{red}^* of **PS^{*}** or E_{ox} of ED > E_{ox} of **PS⁺**) and efficient quenching rate. Equally important in the long durations of photocatalytic conditions are the reaction pathways of the oxidized **ED** as it may play some non-innocent roles in the system.^[25,37] Some of the commonly used **EDs** for photocatalytic CO_2 reduction are shown in Figure 1-13.

Ascorbate, or monodeprotonated ascorbic acid, denoted as **Asc** in Figure 1-13, possesses a sufficient potential to reductively quench the excited state of

[Ru(bpy)₃]²⁺ and is often used as a reversible electron donor^[38] in time-resolved photophysical measurements. It is not very often used in the longer durations of photocatalytic CO₂ conditions as its use as **ED** does not efficiently translate to good photocatalytic activity. It is reported that the oxidized species of **Asc** can disproportionate to generate dehydroascorbic acid, which is a mild oxidant that can thermodynamically oxidize the reduced **PS^{•-}** or the reduced **Cat⁻**, i.e. a short-circuit reaction.^[38,39]

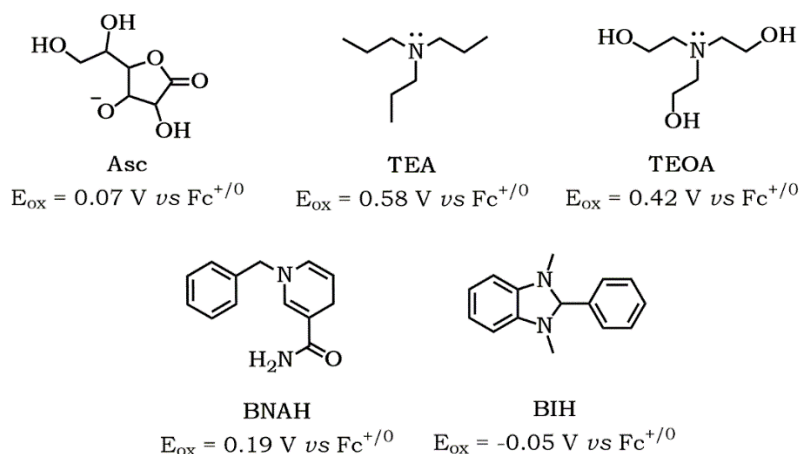


Figure 1-13. Electron donors (**EDs**) used in the photocatalytic CO₂ reduction.^[25,37]

More efficient catalytic activities are achieved with amine-based **EDs** such as trimethylamine (**TEA**), triethanolamine (**TEOA**), 1-benzyl-1,4-dihydronicotinamide (**BNAH**), and 1,3-dimethyl-2-phenyl-2,3-dihydro-1H-benzo[d]imidazole (**BIH**). The low reducing power of **TEA** and **TEOA** makes them useful in reducing an oxidized **PS⁺** such as from Ir-based **PSs** which go through oxidative quenching mechanism. These aliphatic amines are sometimes considered two-electron and one-proton donors, as the radical formed after deprotonation of the one-electron oxidized species has a more reducing power than the starting amine themselves. On the other hand, **BNAH** and **BIH** possess higher reducing power able to effectively quench the excited **PS^{*}** (as such involved in most reductive quenching pathways). **BNAH** is not as effective as **BIH** however because of the rapid dimerization of the deprotonated oxidized radical, and as such, it only acts as a one-electron one-proton donor.^[40] **BIH** has been recently widely utilized in most photocatalytic systems because of the highly reducing nature of the deprotonated one-electron oxidized radical **BI^{•-}** ($-2.06 \text{ V vs Fc}^{+/0}$), making it an effective two-electron one-proton donor.^[41] This is adventitiously used to drive catalysts whose thermodynamic potentials are not matched for a photo-induced electron transfer (and accumulation) from a photosensitizer.

1.6.2. Structural Motifs of Functional CO₂ Reduction Catalysts

Both photo- and electro-catalytic systems rely on the design and the optimized performance of the catalyst. As such, it is central to review the common structural motifs found in functional CO₂ reduction catalysts. Most of the catalysts contain a central transition metal atom that is supported by a coordinated ligand framework, as shown in Figure 1-14. The metal center usually acts as the point of binding for the CO₂ substrate and it is typically responsible for transferring the electrons to the substrate to perform reduction reactions. The metal can range from the initially reported better performances with the use of second (*4d*) d-block series metals such as Ru, Rh, & Pd, and third (*5d*) d-block series metals such as Re, Os, Ir, & Pt. There is a recent trend in exploring first (*3d*) d-block series metals such as Fe, Mn, Co, Ni, and Cu because of their relative abundance and the observation that Nature uses such metals in performing efficient catalytic reactions. Equally important as the redox active metal is the ligand framework which supports and stabilizes the reduced metal and/or accumulate charges in its framework allowing the storage of multiple reducing equivalents across the molecule. There is a vast literature on the ligand frameworks and they are generally categorized into the following family: polypyridyl complexes (e.g. bipyridines, phenanthrolines, terpyridines, quaterpyridines, etc.), porphyrins & similar macrocyclic complexes, cyclams & other aza-macrocyclic complexes, and phosphines.^[26,42,43] In this work, we will review only some notable catalysts relevant to our employed experimental strategies, deeply investigating the rhenium-based bipyridine catalysts and iron porphyrin catalysts.

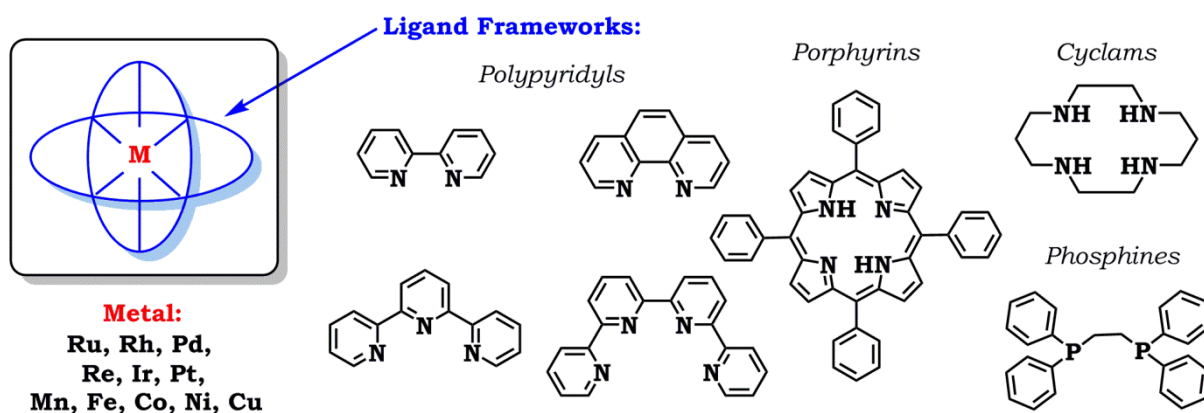


Figure 1-14. Common structural motifs of CO₂ reduction catalysts containing a central metal atom and a ligand framework.

Rhenium tricarbonyl bipyridine complexes

Pioneering work by the group Lehn in 1980s have shown both electro- and photo-catalytic activity of $\text{Re}(\text{bpy})(\text{CO})_3\text{Cl}$ for the reduction of CO_2 to CO .^[44,45] The catalysts possess two reduction potentials: a reversible first reduction at $-1.68\text{ V vs Fc}^{+/0}$ attributed to a bpy-centered reduction and a second irreversible reduction at $-1.98\text{ V vs Fc}^{+/0}$ attributed to a $\text{Re}^{\text{I}/0}$ metal centered-reduction. Initial reports have shown the possibility of a one-electron and two-electrons pathway mechanisms for the reduction of CO_2 to CO by this type of catalyst, depending on the applied potential^[46] and solvent conditions^[47–49]. In the one-electron reduction pathway (left cycle of Figure 1-15), after the first reduction of the catalyst and halide loss, it was proposed that a $[\text{Re}(\text{bpy})(\text{CO})_3]^\bullet$ radical reacts with two CO_2 substrates to form CO and CO_3^{2-} . Later studies confirmed the formation of a CO_2 -bridged dimer intermediate,^[50] in the absence of proton source, and proposed a bimetallic disproportionation with another CO_2 molecule leading to CO and CO_3^{2-} .^[48,51]

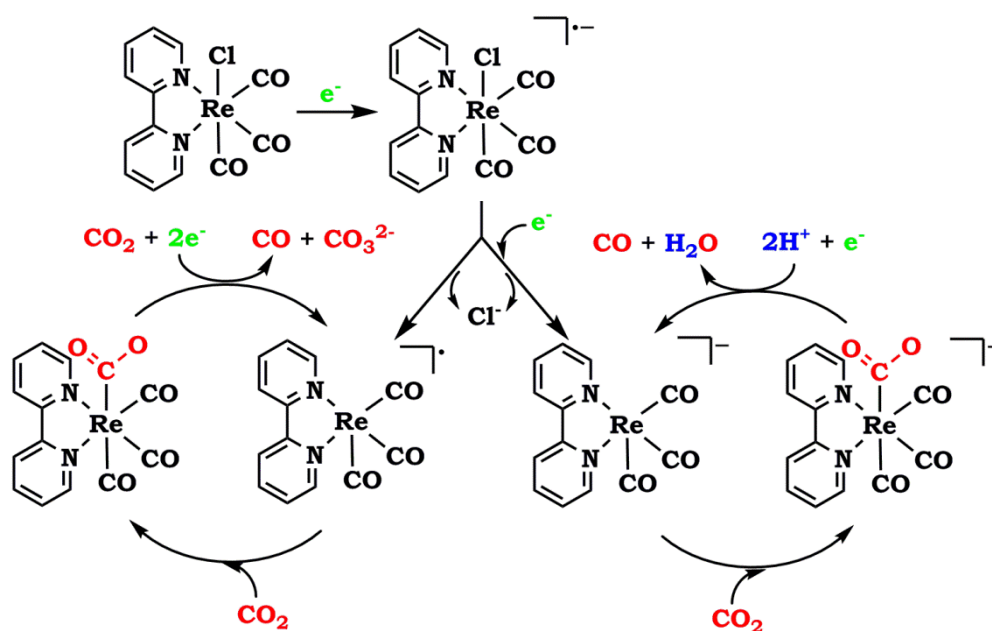


Figure 1-15. Proposed one-electron and two-electron pathway mechanisms for the reduction of CO_2 by $\text{Re}(\text{bpy})(\text{CO})_3\text{Cl}$.^[46–49]

On the other hand, the two-electron reduction pathway (right cycle of Figure 1-15) is accompanied by a fast loss of the halide ligand, producing a doubly-reduced $[\text{Re}^0(\text{bpy}^\bullet)(\text{CO})_3]^-$ intermediate which is active towards the reduction of CO_2 to CO .^[46] This was later confirmed by IR spectroelectrochemistry and it was reported that such intermediate was necessary for the interaction with CO_2 in acetonitrile.^[47] Indeed the initial electrolysis experiments were done on the second

reduction peak to produce higher current densities and high Faradaic efficiency for CO.^[45] It was further confirmed by the group of Kubiak that such a doubly-reduced intermediate showed higher affinity for a CO₂ substrate even in the presence of excess protons in the solution, resulting in a highly selective reduction towards CO, preventing the competing proton reduction.^[49,52]

Since then, many studies have utilized such rhenium-based catalysts and implemented a variety of modifications in the bipyridine ligand, the halide ligand and the metal center. The group of Alberto in 2006^[53] have systematically changed the diimine ligand from bipyridine (bpy) to phenanthroline (phen), dipyridoquinoxaline (dpq), and dipyridophenazine (dppz), and showed that increasing the aromaticity of the diimine significantly lowered the first reduction potential, as shown in Figure 1-16. This stabilization is due to the delocalization of the electron in the extended aromatic rings, helping to stabilize electron accumulation. This did not translate however to better photocatalytic activity towards CO₂ to CO, as shown by the lowered TON, indicating that indeed the catalytic activity is not significantly dependent on the bpy-centered reduction.

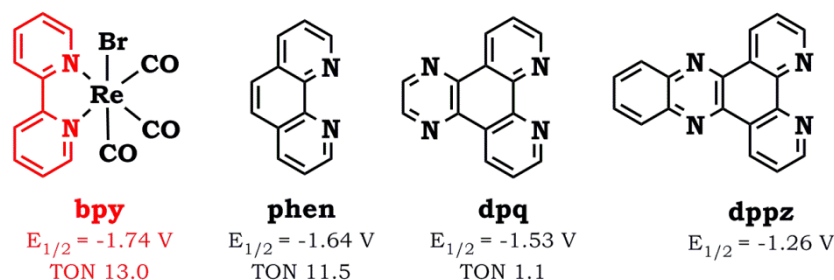


Figure 1-16. Effect of modifying the diimine ligand on the first reduction potential (V vs Fc^{+/0}) of the Re catalyst and the photocatalytic turnover number for CO₂ to CO in DMF with TEOA as ED.^[53]

The group of Kubiak recently published another systematic study investigating the effect of 4,4'-substitutions in the bipyridine ligand of the Re catalyst.^[54] The electronic effects of the nature of the *para* substituents, such as methoxy, methyl, *tert*-butyl, trifluoromethyl, and cyano groups, on the bipyridine ligand is clearly reflected in the linear relationship between the first reduction potential and the Hammett parameter as shown in Figure 1-17a. This indicates that the electronic character of the bpy ligand indeed affects the bpy-centered reduction potential. However, this electronic character does not necessarily translate to improved electrocatalytic activity which occurs at more negative potentials. It can

be observed from the linearity of the plot of the catalytic overpotential *vs* log TOF in Figure 1-17b, that the improvements observed in the TOF are mainly dependent on the linear free energy relationship with the overpotential. The substituent effects do not correspond to the same trend observed for the electronic effects on the first reduction potential, indicating again that catalytic activity goes beyond the bpy-based reduction. Though the tert-butyl substituted Re catalyst was initially reported as the most active^[55] because of the steric bulkiness preventing deactivation by catalyst dimerization, it seems from the plot that this effect is mainly due to the electron donating ability of the group. The observed increase of the TOF comes with the cost of the higher overpotential. It was interesting to note that though CF₃ and CN substituents follow this linearity, they are not stable and quickly deactivate during bulk electrolysis. This was reasoned out to be due to the highly destabilizing state of the extra electron density in the bipyridine ligand, leading to catalyst degradation.^[54] In addition, their Faradaic efficiencies for CO production are very low (3%) compared to the high Faradaic efficiencies of the unsubstituted Re catalyst (100%), indicating mechanistic deviations for the typical product formation, e.g. cyano groups react with CO₂ to form carboxyamides.^[56]

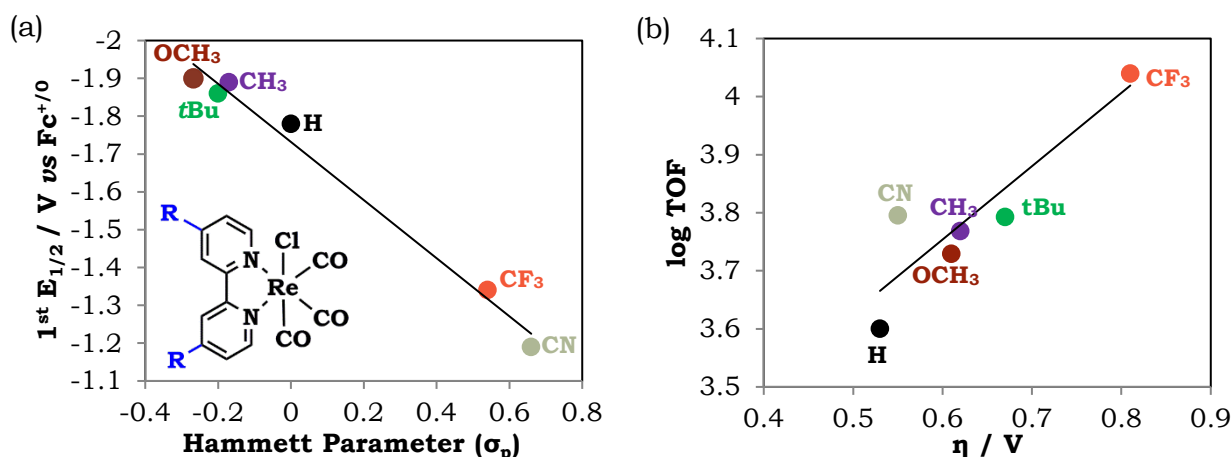

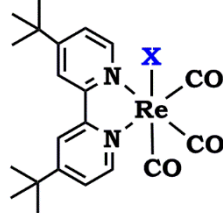


Figure 1-17. (a) Trend between electron donating character of 4,4'-bpy substituent and 1st reduction potential of the Re catalyst in ACN. (b) Trend between electrocatalytic overpotential and log TOF in CO₂-saturated ACN with 1 M PhOH. Data from ^[54].

The axial ligand was also systematically studied using Cl, Br, H₂O, SCN, CN, P(OEt)₃, CH₃CN, and pyridine ligands as shown in Table 1-3.^[53,54,57,58] Replacing the halide ligand with a H₂O ligand results in a cationic complex, and as such, this complex shows the most anodically shifted first reduction potential (-1.55 V *vs* Fc^{+/0}). This does not translate however to an improved photocatalytic activity as

shown by the lower photocatalytic TON (1.8). A much better improvement was noted with a SCN ligand due to the long-term stability of the resulting complex. This enhanced stability was reasoned to be coming from the suppression of the formation of a catalytically inefficient formate complex $[\text{Re}(\text{HCOO})(\text{bpy})(\text{CO})_3]$ as an undesired side product in the halide-coordinated Re catalyst.^[53] Recently, the group of Kubiak showed that the cationic complexes with CH_3CN or pyridine as labile ligands made it also easier to reduce the modified bpy ligand compared to neutral complexes. This didn't significantly improve the catalytic overpotential nor the electrocatalytic TOF, concluding that the ligand loss does not determine such described parameters. This is in contrast to the photocatalytic reactions where the loss of the halide ligand is key to the reactivity.^[59]

Table 1-3. Effect of changing the nature of the axial ligand on the first reduction potential of the catalyst and the corresponding changes in the photocatalytic TON or the electrocatalytic TOF.

Re Complex	X	$E_{1/2} / \text{V vs Fc}^{+/0}$	TON	Log TOF	Ref
	Cl	-1.68	8.2	-	[53]
	Br	-1.74	13.0	-	[53]
	H_2O	-1.55	1.8	-	[53]
	SCN	-1.57	26.4	-	[53]
	CN	-1.58	4.5	-	[53]
	$\text{P}(\text{OEt})_3$	-1.59	7.5	-	[57,60]
	Cl	-1.86	-	3.79	[54]
	Br	-1.86	-	3.78	[54]
	CH_3CN	-1.73	-	3.92	[54]
	pyridine	-1.68	-	3.90	[54]

The effect of the metal center was also studied by substituting the Re metal with the isoelectronic Mn^[61-63], as shown in Figure 1-18. The Mn alternatives was first reported by the group of Deronzier^[62] with $\text{Mn}(\text{bpy})(\text{CO})_3\text{Br}$ and $\text{Mn}(\text{dmbpy})(\text{CO})_3\text{Br}$ and showed reasonable efficiencies and selectivities, with lower overpotential compared to the Re analogue.^[64] Various modifications were similarly performed in the bipyridine ligands^[61,63,65,66] to improve the catalytic activity of the

Mn catalyst. The best performing catalyst so far (in terms of TOF and overpotential) is the Mn complex possessing bulky mesityl groups in the 6,6' position of the bipyridine ligand that prevents dimer formation.^[61] A systematic study was also done investigating W- and Mo-centered complexes with (*t*Bu-bpy)(CO)₄ ligand structures,^[67] as shown in Figure 1-18. These group 6 transition metals are often observed in natural systems and the dianionic forms of these complexes are formally isoelectronic to the pentacoordinated active form of the group 7 (Mn and Re) catalysts. These complexes were shown to be active towards reduction of CO₂ to CO but suffered from low TOF mainly attributed to the stronger back donation to CO compared to the group 7 counterparts.

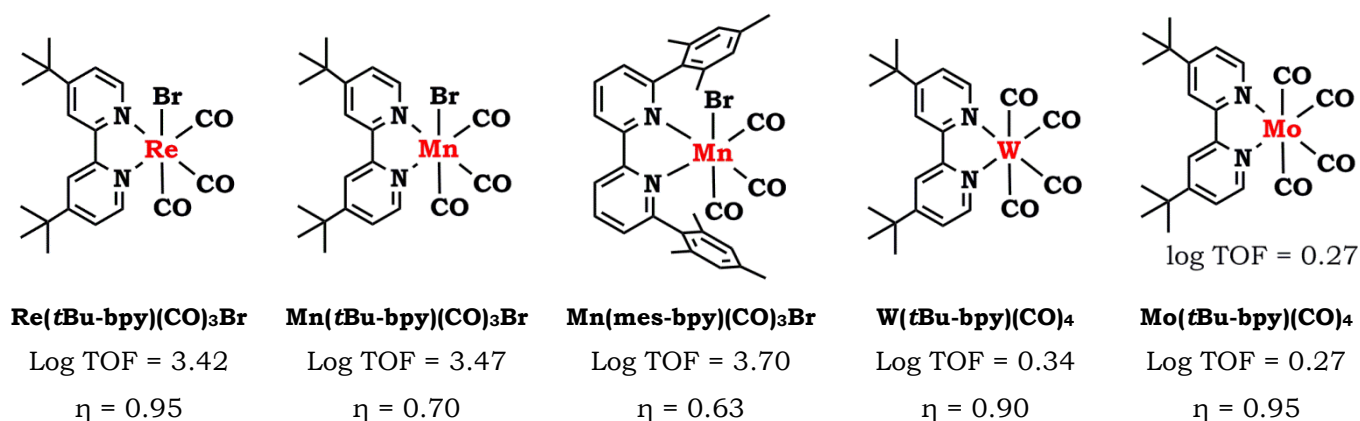


Figure 1-18. Effect of changing the metal center in bipyridine carbonyl-based complexes on the electrocatalytic TOF and overpotential towards CO₂ reduction to CO in ACN.

The photocatalytic activity of the Re catalyst has been greatly improved when photosensitized in the visible region through the construction of supramolecular catalysts with a Ru-based photosensitizer unit.^[25,31,43,68-72] This has been extensively investigated by the group of Ishitani who has shown that these supramolecular photocatalysts are performing much better compared to separate bimolecular units.^[31] From TON of 5-20 when the photocatalytic activity was first published, current improvements show TONs of ca. 3000, as shown in Table 1-4.^[73] These systematic studies have arrived at some important conclusions concerning the molecular architecture for better catalytic activity. First is the establishment of directionality of electron flow by having the π* orbital energy of the peripheral ligand of the PS to be equal or higher than that of the bridging ligand.^[68] Second is the establishment of a sufficiently high π* orbital energy of the bridging ligand to maintain the high reducing power of the catalyst towards CO₂ reduction. As such,

establishment of conjugated ligands, which anodically shifts and stabilizes the potential of the catalyst, are not recommended as it consequently lowers the reducing power of the catalyst.^[72] Most improved systems involve the use of short aliphatic bridges^[31,68,70,73] and the highly efficient two-electron one-proton donor **BIH**.^[73]

Table 1-4. Photocatalytic performances of supramolecular catalysts.^[25,43]

Structure	R	Z	L	L'	ED	TON	Ref
1		X = (4dmbpy) ₂ Ru, Y = Re(CO) ₃ Cl			BNAH	14	[68]
1		X = Re(CO) ₃ Cl, Y = (4dmbpy) ₂ Ru,			BNAH	28	[68]
2	H	CH ₂ CH(OH)CH ₂	Cl	CO	BNAH	50	[68]
2	H	(CH ₂) ₂	Cl	CO	Asc	1	[69]
2	CF ₃	(CH ₂) ₂	Cl	CO	BNAH	3	[68]
2	CH ₃	(CH ₂) ₂	Cl	CO	BNAH	180	[70]
2	CH ₃	CH=CH	Cl	CO	BNAH	50	[72]
2	CH ₃	(CH ₂) ₄	Cl	CO	BNAH	120	[70]
2	CH ₃	(CH ₂) ₆	Cl	CO	BNAH	120	[70]
2	CH ₃	CH ₂ CH(OH)CH ₂	Cl	CO	BNAH	170	[68]
3	CH ₃	none	P(<i>p</i> F-Ph) ₃	P(<i>p</i> F-Ph) ₃	BNAH	48	[31]
2	CH ₃	(CH ₂) ₂	P(<i>p</i> F-Ph) ₃	P(<i>p</i> F-Ph) ₃	BNAH	207	[31]
2	CH ₃	(CH ₂) ₂	P(<i>p</i> F-Ph) ₃	P(<i>p</i> F-Ph) ₃	BIH	3029	[73]
3	CH ₃	none	PPh ₃	PPh ₃	BNAH	24	[31]
2	CH ₃	(CH ₂) ₂	PPh ₃	PPh ₃	BNAH	144	[31]
3	CH ₃	none	P(OEt) ₃	P(OEt) ₃	BNAH	3	[31]
2	CH ₃	(CH ₂) ₂	P(OEt) ₃	P(OEt) ₃	BNAH	22	[31]
2	CH ₃	CH ₂ OCH ₂	P(OEt) ₃	P(OEt) ₃	BNAH	253	[71]
2	CH ₃	(CH ₂) ₃	P(OEt) ₃	P(OEt) ₃	BNAH	178	[71]
2	CH ₃	CH ₂ SCH ₂	P(OEt) ₃	P(OEt) ₃	BNAH	73	[71]

The synthetic tunability and mechanistic flexibility (either through electro- or photo-catalytic pathways) of the Re polypyridyl-type complexes has indeed resulted in vast investigations and optimizations. Some mechanistic studies have been provided both experimentally and theoretically but the sensitivity of mechanistic pathways on various modification strategies has made it difficult to generalize certain criteria for the improvement of catalytic activities. In addition, there is a lack of bridge between the trends observed and optimized in electro-catalytic measurements with that of the photo-catalytic measurements, possibly because of the intrinsic differences of catalyst activation. This might indicate an interesting point for further understanding and investigation.

Iron porphyrin complexes

Another well-studied and efficient CO₂-to-CO reduction catalyst is the class of iron porphyrins, pioneered and extensively investigated by the group of Savéant.^[74] Addition of weak Brønsted acids such as water, trifluoroethanol, and phenol^[75] or addition of any Lewis acids like magnesium cations,^[76] have shown to greatly improve the catalytic activity. In a general proposed mechanism, the iron (III) tetraphenylporphyrin chloride, shown in Figure 1-19, undergoes three reversible reductions as evidenced by three reversible peaks in its cyclic voltammetry. This corresponds to the formal reductions from **Fe^{III}** to **Fe^{II}** to **Fe^I** and finally to the active form of **Fe⁰**. Recent studies have suggested that the last two additional electrons reside in the π* orbitals of the porphyrin ligand.^[77] As such, the last two reductions can be formulated as **[Fe^{II}TPP]/[Fe^{II}(TPP•)]⁻** and **[Fe^{II}(TPP•)]⁻/[Fe^{II}(TPP••)]²⁻**. Since these electrons are delocalized in the conjugated macrocycle, the corresponding electron transfer will involve marginal geometric distortions of the ligand, and hence a low reorganizational energy. The formal Fe⁰ reacts with the CO₂ substrate producing two mesomeric forms: **[Fe^I(CO₂•)]²⁻** and **[Fe^{II}(CO₂••)]²⁻**. DFT calculations have shown that reaction goes through the **Fe^I** asymmetrical adduct rather than the **Fe^{II}** symmetrical adduct because of the asymmetrical roles of the carbon-oxygen bond.^[75] This adduct is stabilized by a hydrogen bond donor such as weak acids and further protonation from a second acid molecule leads to C–O bond cleavage. CO is then released after homogeneous one-electron reduction of the **Fe^{II}–CO** adduct by a **Fe⁰** species. Recent studies have confirmed such mechanism by employing resonance Raman spectroscopy at low temperature.^[78]

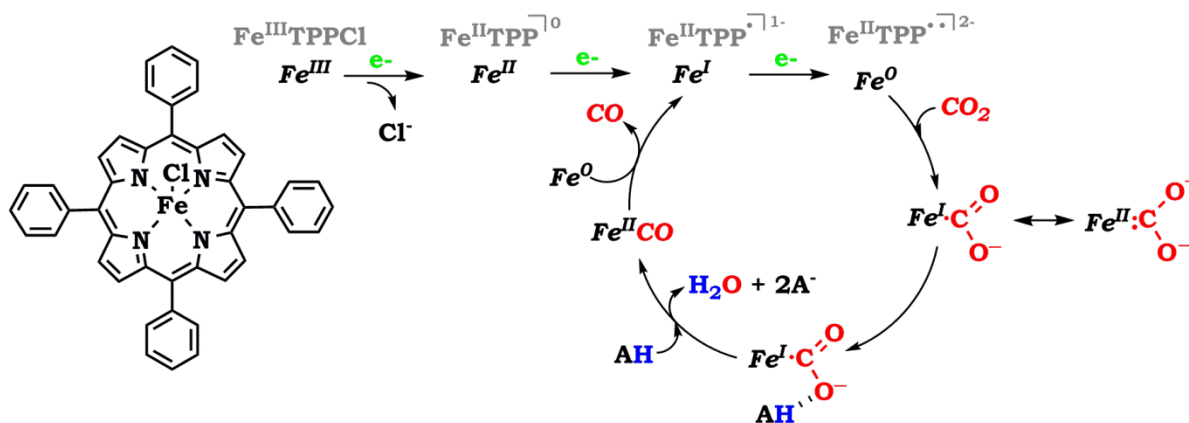


Figure 1-19. Proposed mechanism for the CO₂ to CO reduction by iron porphyrins in the presence of a proton source.

The group has also developed benchmarking strategies to critically compare electrocatalytic CO₂ reduction performance by a simple technique of cyclic voltammetry (CV) and the corresponding analysis of catalytic Tafel plots from the foot-of-the-wave of the CV.^[75,79–81] This provided a quick estimation of catalyst performance independent of the side phenomena that interfere at high current densities.^[79] Catalytic Tafel plots correlate the turnover frequency to the overpotential as shown in Figure 1-20a with a corresponding linear correlation in Figure 1-20b.^[82] For example, the modification of the porphyrin ligand by through-structure substituents affects the electronic structure of the catalyst, resulting in correlated changes with respect to both the overpotential and TOF. The addition of electron withdrawing groups such as fluorine atoms is expected to lower the overpotential because it lowers the electron density near the metal active site. Thus, it is easier to inject an electron into the catalyst, shifting the reduction potential anodically, resulting in a lower overpotential. This can be observed for the addition of increasing number of fluorine atoms from 5 to 10 to 20, resulting in a lower overpotential compared to the nonfunctionalized **FeTPP**.^[82,83] This comes however, with a decrease in the catalytic activity due to the decrease in the affinity between the active catalyst (now with decreased Lewis basicity) and the substrate in the framework of an electronic-push-pull mechanism. On the other hand, putting electron donating group, increases the Lewis basicity of the active site able to efficiently transfer electrons to the CO₂ substrate. This comes however with cost of more negative catalytic potentials. This implicates that substituents that alter the electronic structure of the catalyst favor one parameter but disfavors another one.

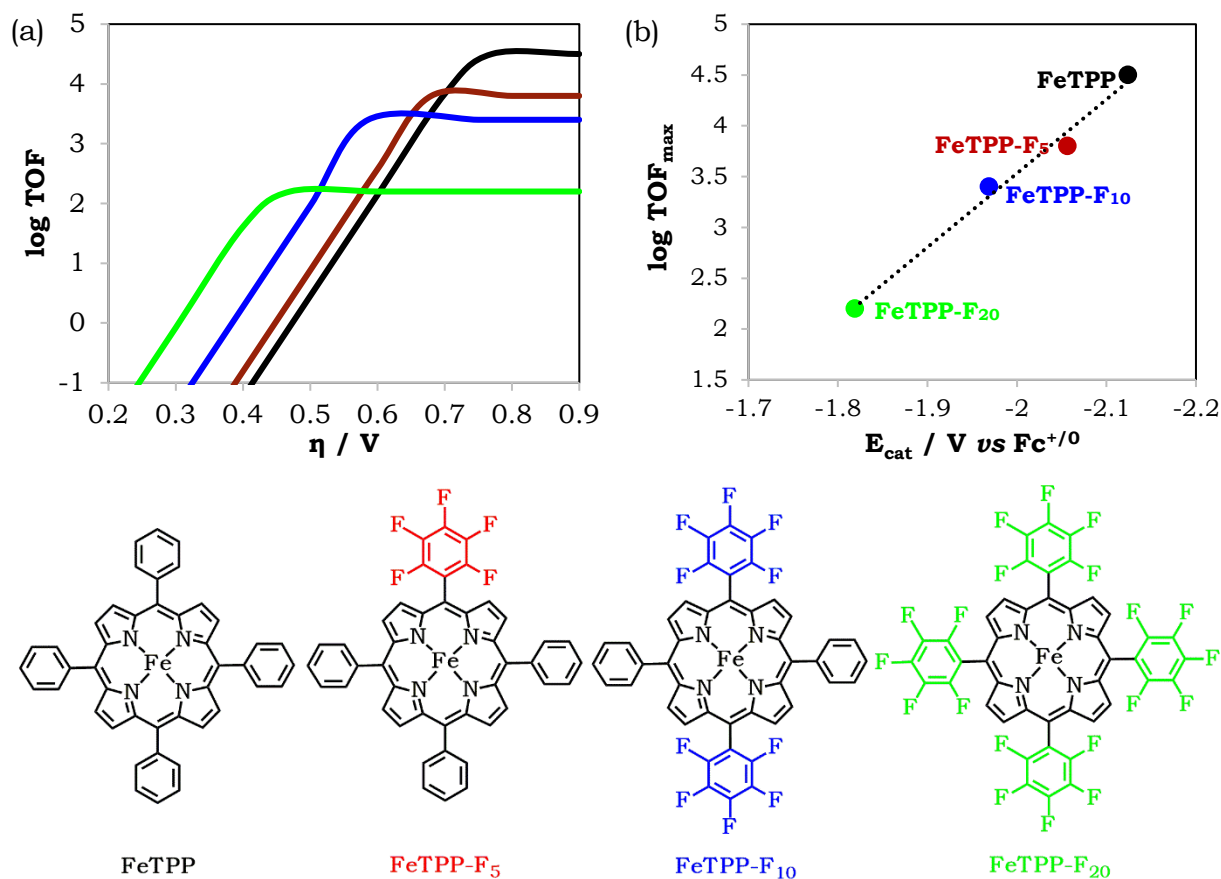


Figure 1-20. (a) Catalytic Tafel plots of modified analogues of iron porphyrin with the structures shown at the bottom. (b) Correlation of TOF_{max} with the catalytic potential showing through-structure substituent effects. Data from Ref. [83] in DMF with 3 M PhOH.

Similar linear scaling between the overpotential and TOF was observed for modifications in the Re-based catalyst, as shown in Figure 1-17. This suggests that in order to achieve a better catalytic performance, with higher catalytic rates at lower overpotential, strategies should go beyond the electronic through-structure effect. Substantial improvements were indeed observed when employing through-space substituent effects stabilizing or activating key reaction intermediates. This strategy has already been well-documented to be at work in the catalytic sites of enzymes known to perform at much higher efficiencies and stabilities. Employing such strategy in catalyst design would then require careful optimization of the second coordination sphere of the catalyst to incite such through-space interactions.

1.6.3. Catalysts Employing Second Coordination Sphere Effects

Second coordination sphere relates to the distal structure of the catalyst beyond the primary coordination sphere of the ligand structure with the metal center that may influence metal-bound intermediates and may or may not affect the electronic structure of the catalyst. Strategies relying on such effect have initially been extensively implemented in various synthetic catalysts for the reduction of oxygen and reduction of protons, mimicking features observed in natural systems. Recently, this has been applied to the development of CO₂ reduction catalysts and specific approaches can be generally categorized in the following: establishing local proton sources, tethering hydrogen bond relays, leveraging on cationic groups, and employing bimetallic structure.

Local proton source

The observation that addition of weak Brønsted acids^[75] enhanced the catalytic reduction of CO₂ already hinted the possibility of placing local acid proton sources in the periphery of the catalyst. This has been initially reported by the group of Savéant by placing pendant hydroxyl groups in FeTPP^[84] as shown in structure **20** in Figure 1-21. These pendant proton donors resulted in enhanced catalytic activity (log TOF_{max} of 3.8) and a decrease in overpotential (η of 0.66 V) in DMF with 2 M H₂O. Control experiments with methoxy (-OCH₃) groups instead of the -OH groups showed a poorer activity (log TOF_{max} of 2.5) at a much larger overpotential (η of 1.04 V). This highlights the crucial role of high local concentrations of phenolic protons in a push-pull (electron-proton) mechanism towards metal carboxylate intermediates.^[75] Nocera extended the investigation by establishing pendant acid sources (phenolic and sulfonic groups) in an iron hangman porphyrin configuration,^[85] shown in structures **21** and **22** in Figure 1-21. The pendant -OH groups caused a thermodynamically favored -5.0 kcal/mol stabilization of the CO₂ adduct. However, the introduction of sulfonic groups didn't improve the catalytic activity of the system because once deprotonated, they cannot be reprotonated by the weaker external PhOH donor (pK_a of SA is 3 vs pK_a of PhOH is 18 in DMF^[86]). The steric congestion and electrostatic repulsion from the negatively charged sulfonate resulted in a mismatch of orientation where the sulfonic groups are no longer pointed towards the bound CO₂ substrate. This highlights the importance of external acid sources in regenerating the pendant local proton sources to maintain the secondary sphere coordination effect.

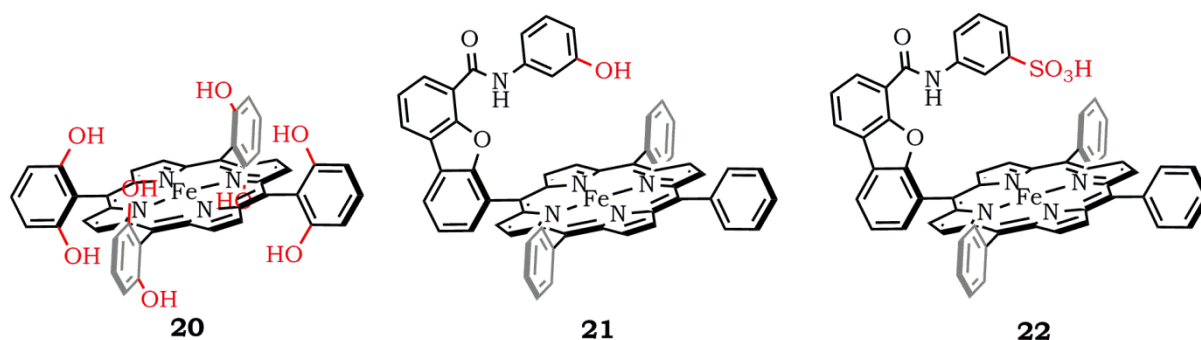


Figure 1-21. Introduction of local proton sources in iron porphyrin catalysts.^[84,85]

Local proton sources have also been investigated in Re- and Mn-based triscarbonyl bipyridyl complexes and Ni cyclams, as shown in Figure 1-22. The group of Manbeck has investigated the positional effects of phenolic sources in the Re-based catalyst by incorporation of OH groups at the 4,4' and 6,6' positions (structures **23** and **24**, respectively). Though both complexes show nearly identical electrochemical properties, only the 4,4' substitution was active for CO₂ reduction. The –OH bonds in the bipyridine ligand are cleaved by stepwise reduction, which was proposed to dearomatize the doubly-reduced bpy ligand. The slow CO release and decomposition of the intermediates at applied potentials limit the activity of the 6,6' substituted complex, highlighting the importance of proper positioning of these local proton sources. Asymmetric attachment of phenol moieties has been employed in Mn-based catalysts (**26** and **27** in Figure 1-22). This led to enhanced activity in comparison to the nonfunctionalized Mn catalyst,^[87,88] including the activity in the absence of proton source.^[87] Control experiments with methoxy groups showed insignificant catalytic activity, again highlighting the enhancement specifically made by the local phenolic protons. The competitive dimerization was, however, still apparent in both modified catalysts. Similar phenolic ligand structure was employed in a Re-based catalyst which prevented the dimerization usually observed for Mn-based catalysts, but upon photocatalysis, it showed higher selectivity towards formation of formate (TON_{HCCO⁻} of 86, selectivity of 75 %) rather than CO, indicating the mechanistic pathway deviation caused by such bpy modification. Carboxylic acids have been tethered in Re-based catalyst, shown in structure **25**^[53], but didn't improve the photocatalytic activity (TON_{CO} of 7.7) compared to the nonfunctionalized Re catalyst (TON_{CO} of 13). Such groups have also been asymmetrically positioned in a Ni cyclam catalyst (adsorbed in Hg-Au amalgam electrode) as shown in structure **28**^[89] which showed improved electro-catalytic

activity towards reduction of CO₂ to CO in water compared to the nonfunctionalized catalyst. The enhanced activity was attributed to its stability and selectivity for CO₂ reduction to CO even at pH 2, overcoming the competitive proton reduction.^[89]

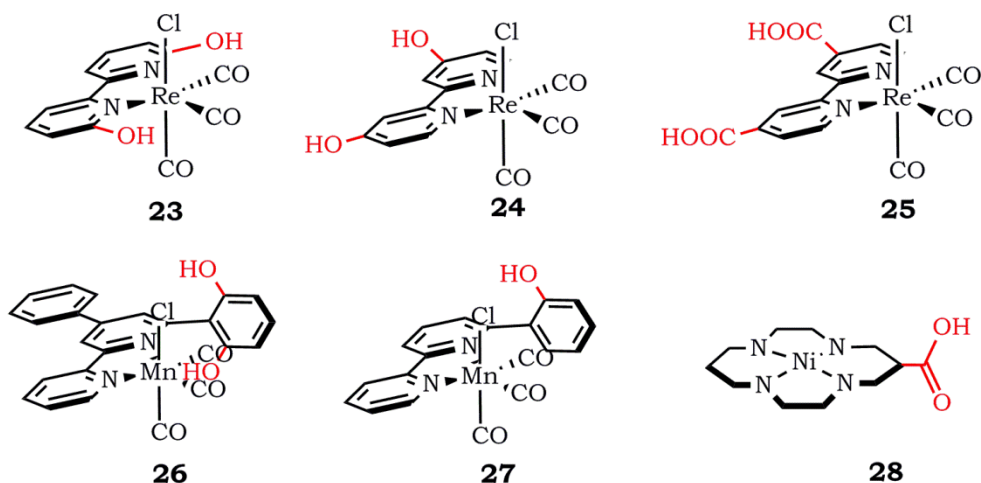


Figure 1-22. Establishment of local proton sources in Re- and Mn-based triscarbonyl bipyridyl complexes and Ni cyclams.^[53,87-90]

A bio-inspired approach was employed in Re-based catalysts by the group of Kubiak by incorporating peptide linkages of varying lengths containing tyrosine residues,^[91] as shown in structures **29** and **30** in Figure 1-23. Molecular dynamics simulation, 2D NMR experiments, and IR spectroelectrochemical experiments showed a stable configuration where the catalyst arm adopts a folded configuration that places the phenol moiety close to the bpy ligand, allowing interactions between the pendant proton and the metal-bound substrate. Catalyst **29** showed catalytic CO₂ reduction activity but catalyst **30** precipitated on the electrode under electrocatalytic conditions. This peptide-linkage approach is nevertheless interesting as the inorganic Re catalyst can be inserted at any desired point in the linkage during peptide synthesis, allowing more avenues of exploration and optimization.

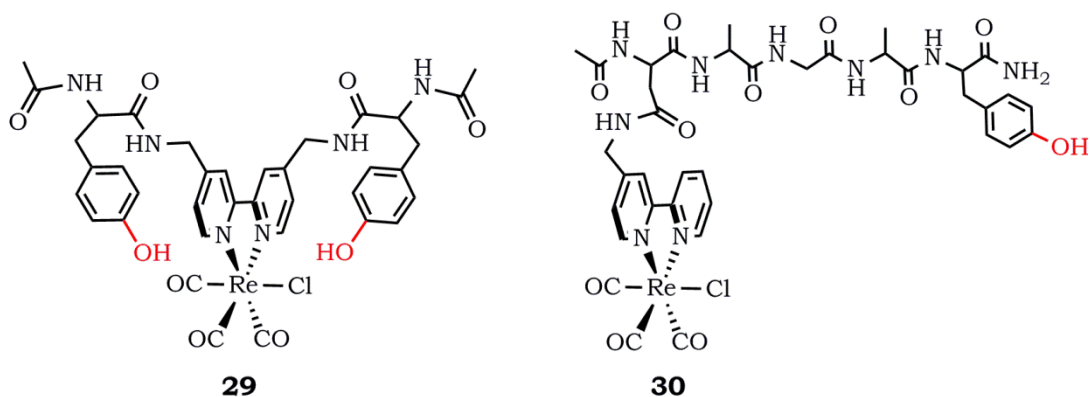


Figure 1-23. Incorporation of peptide linkages containing tyrosine residues in a Re-based triscarbonyl bipyridyl catalyst.^[91]

Hydrogen bond

Another approach for second coordination effects does not necessarily place local proton sources in the periphery of the catalyst, but places functional groups able to establish hydrogen bonding interactions either with the metal carboxylate adduct or with the external proton sources to synergistically stabilize CO₂ reduction intermediates. This has been observed in Ni-cyclam catalysts, one of the first known catalysts to electrochemically reduce CO₂ to CO in water.^[92–94] DFT studies by the group of Kubiak have shown that a *trans I* isomer of the catalyst as shown in structure **31** in Figure 1-24, one of the six possible isomers based on the orientation of the H atoms on the four metal-coordinated secondary amines in the macrocycle, is more favorable in stabilizing a CO₂ substrate by hydrogen bonding interactions.^[95] Further DFT studies by the group of Ye have shown that this isomer (four cofacial H-atoms) is greatly stabilizing the CO₂ adduct compared to the *trans III* isomer (two cofacial H-atoms) by approximately 3 kcal/mol.^[96] N-alkylated derivatives of [Ni(di-methylcyclam)]²⁺ and [Ni(tetra-methylcyclam)]²⁺ showed diminished electrocatalytic CO₂ reduction activities due to the absence of hydrogen-bond induced stabilization effects and increased steric congestion. This further highlight the importance of amine protons in promoting hydrogen bonding interactions.

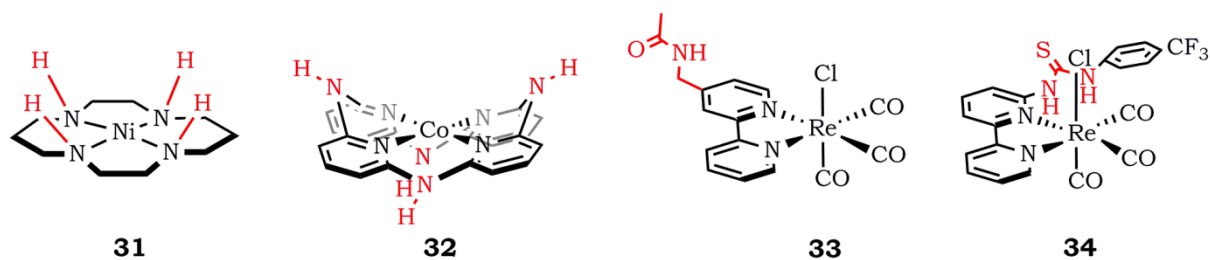


Figure 1-24. Establishment of hydrogen bond in the periphery of CO₂ reduction catalysts.

A systematic study was performed by the group of Marinescu on the effect of pendant secondary amines on a cobalt pyridine macrocycle (structure **32** in Figure 1-24) that showed a linear dependence of catalytic rate on the number of pendant hydrogen bond donors.^[97,98] Unlike the cyclams, the pendant amines lie completely outside the primary coordination sphere of the metal allowing isolated roles of the amines as hydrogen bond donors facilitating non-cooperative hydrogen bonds with the proton source in the solution. However, this improved catalytic activity comes with the cost of high overpotential (1080 mV). Kubiak reported a simple acetamidomethyl group in the 4 position of the bpy ligand (structure **33**) which shifted the potentials anodically (220 mV shift for the first reduction and 440 mV shift for the second reduction) compared to the nonfunctionalized catalyst.^[91] This positive shift in the potential was similarly observed if two acetamidomethyl groups were incorporated on the 4,4' positions of the bpy ligand.^[51] The enhancement was mainly attributed to the formation of hydrogen-bonded dimers which catalyze the reductive disproportionation of CO₂ to CO and CO₃²⁻ in a bimolecular mechanistic pathway. Thus, the H-bond donors in the amide moieties do not directly interact with the metal carboxylate intermediate. In a recent report, the group of Neumann has asymmetrically tethered thiourea functions in the periphery of the Re catalyst,^[99] as shown in structure **34** in Figure 1-24. ¹H NMR measurements showed that the proximal hydrogen atom of the thiourea moiety directly binds to the oxygen atom of the CO₂ substrate. In this way, the thiourea group can effectively bind CO₂ and stabilize the carboxylate intermediate and at the same time, act as a local proton donor.^[99] However, addition of any external proton source (i.e. water) inhibited the catalytic activity of the system, likely interfering with the hydrogen bonding interactions pre-established by the thiourea group on the CO₂ adduct.

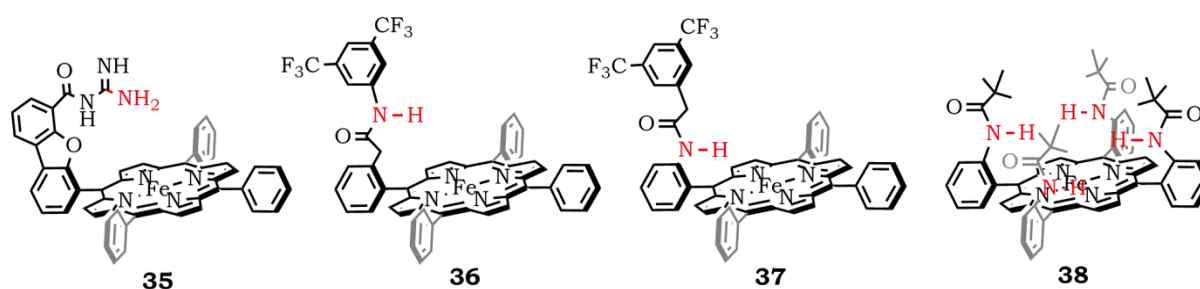


Figure 1-25. Incorporation of amino and amido donors in the periphery of iron porphyrin catalysts.^[85,100,101]

Hydrogen bonding donors have also been incorporated in iron porphyrin catalysts, as shown in Figure 1-25. Nocera has utilized a guanidinium group (structure **35**) in an iron hangman porphyrin and showed a thermodynamically favored -2.61 kcal/mol stabilization of the CO_2 adduct by DFT calculations. However, the effect was lower compared to the phenolic analogue (catalyst **21** in Figure 1-21), resulting in lower catalytic current. The group of Chang has systematically studied the effect of the position of amide moieties in similar iron hangman porphyrins. It was shown that *ortho* amides (log TOF_{max} of 4.35 – 6.74, η of 0.78 – 0.84 V) in the *meso*-phenyl of the porphyrin perform better than the corresponding *para* configuration (log TOF_{max} of 2.23 – 3.83, η of 0.81 – 0.82 V), and that a distal positioning (*ortho*-2-amide, structure **36**, log TOF_{max} of 6.74, η of 0.84 V) is better than a proximal one (*ortho*-1-amide, structure **37**, log TOF_{max} of 4.35, η of 0.78 V).^[100] This shows that proper positioning of the amide functions is critical in establishing suitable hydrogen bonding interactions with the metal carboxylate intermediate. They all improved the catalytic activity compared to nonfunctionalized FeTPP but the overpotentials were still not significantly improved. Recently, the group of Dey has synthesized a picket fence iron porphyrin that contains proximal amides, as shown in structure **38**. This resulted in an improvement of the catalytic activity in the presence of 3 M phenol (log TOF_{max} of 5.71, η of 0.62 V) compared to the single-point amides in structure **37**. This shows that aside from proper positioning, the number of such pendant amido groups can also affect the catalytic activity of the system.

Cationic Moieties

Substantial improvements were observed with the incorporation of cationic functionalities like trimethylammonium groups in iron porphyrin catalysts reported by the group of Savéant.^[83] The *ortho*-positioning (structure **39**, Figure 1-26) of the through-space electrostatic interactions between the positive charges of substituents and the negative charge developed in the metal carboxylate intermediate resulted in a significant decrease in overpotential (η of 0.25 V) while simultaneously increasing the TOF ($\log \text{TOF}_{\text{max}}$ of 6).^[102] This $\alpha\beta\alpha\beta$ atropisomer configuration of the substituents in the iron porphyrin was even better than the diffused electrostatic effects in the *para*-substituted alternative (structure **40**), highlighting the importance of suitable orientation of the electrostatic effect. On the other hand, the incorporation of negatively charged sulfonate substituents (structure **41**) resulted in a decrease in the TOF as a result of electrostatic repulsions with the negatively charged metal carboxylate intermediate. These effects are clearly observed in the deviations in the catalytic Tafel plots and linear scaling shown in Figure 1-26, with better catalysts appearing in the upward left part of the plot while the poor catalysts deviating towards the downward right part.

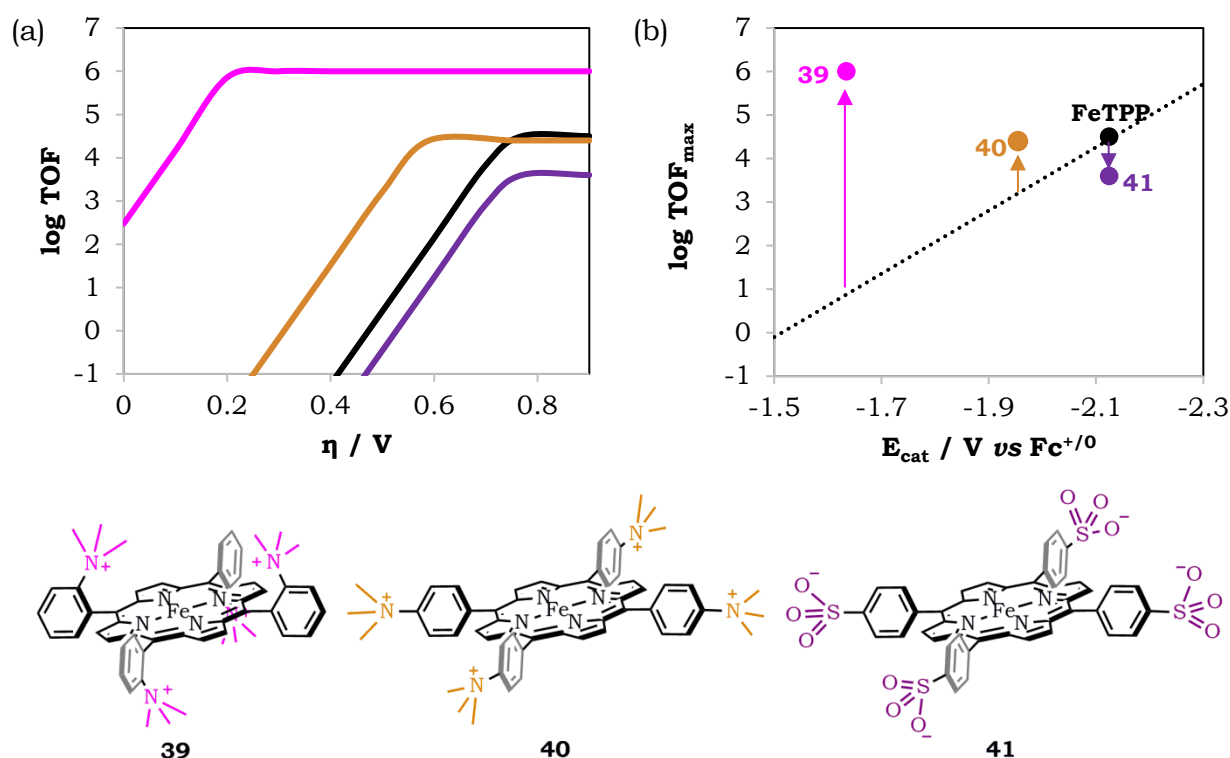


Figure 1-26. (a) Catalytic Tafel plots of modified analogues of iron porphyrin with the structures shown at the bottom. (b) Correlation of TOF_{max} with the catalytic potential showing through-space substituent effects. Data from Ref. ^[83] in DMF with 3 M PhOH.

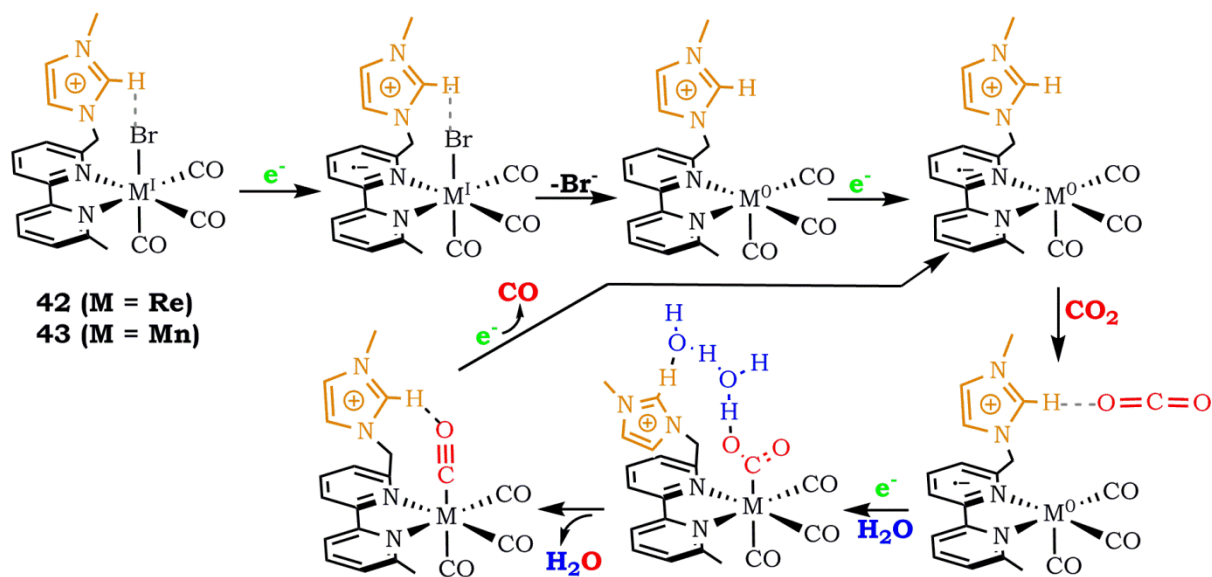


Figure 1-27. Incorporation of a cationic imidazolium moiety in the periphery of Re- and Mn-based catalysts with the proposed mechanism.^[103,104]

Recently, the group of Nippe even combined the synergistic effects of H-bond donors and electrostatic interactions by establishing imidazolium moieties in the periphery of the Re and Mn triscarbonyl bipyridine catalysts (structure **42** and **43** in Figure 1-27).^[103,104] Since this class of catalysts involves the loss of halide during the catalytic cycle, it was proposed that the C₂-H carbon of the imidazolium moiety interacts with the halide promoting its release upon first reduction. Addition of another electron forms the doubly reduced pentacoordinated active species, which in the presence of CO₂ forms a metal carboxylic acid intermediate. Subsequent addition of electrons and protons (from a water network) results to a tetra-carbonyl species, which upon reduction and CO dissociation regenerates the initial reactive species.^[104] This resulted in an improved catalytic activity (log TOF of catalyst **42** is 2.44 at a scan rate of 4 V/s in ACN with 2.8 M H₂O and η is 0.46 V; no data retrieved for catalyst **43**) compared to the nonfunctionalized catalyst. In a control experiment, when the imidazolium C₂-H was replaced with C₂-CH₃, the catalytic activity was lower indicating the critical role that C₂-H plays in the catalytic cycle.^[103] Though the overpotentials are lowered for these modified catalysts, the TOF and Faradaic efficiency for CO (77 % for catalyst **42** and 70 % for catalyst **43**) are still relatively low. Furthermore, addition of higher concentrations of water (beyond 2.8 M) significantly decreased the activity of the catalyst **42** which is usually not observed for the nonfunctionalized Re catalyst. This is indicative that such strategy inadvertently resulted in major alterations in the mechanistic pathways.

Bimetallic strategies

Another approach for secondary coordination effects is through the bimetallic approach, which has been similarly observed in the enzymes performing CO₂ reduction, as discussed previously. The bimetallic system works cooperatively to store charges and to activate the CO₂ substrate in a classical push-pull donor-acceptor configuration. An initial bio-inspired mimic was reported by the group of DuBois by synthesizing a bimetallic palladium phosphine complex (structure **44** in Figure 1-28). This was strategically done to overcome the low CO₂ binding of the monomeric counterpart, which was identified to be the rate determining step of the system. The complex showed low overpotential but suffered as well from low turnover number because of the formation of a Pd-Pd bond, which is considered an inactive form. Similar bimetallic strategy was employed by Naruta in modifying the well-known CO₂-reducing iron porphyrin catalysts in a cofacial configuration (structure **45**).^[105] Controlling the positioning of the porphyrin platforms in the phenyl linker made it possible to control the distance between the Fe metals. A higher catalytic activity (log TOF_{max} of 3.63, Faradaic efficiency of 95%, η of 0.7 V) was achieved compared to the monomeric catalyst with an *ortho* configuration of the dimer where the Fe-Fe distance is expected to be 3.2 – 4.0 Å, suitable for binding of the CO₂ substrate. The overpotential of the system was further optimized using electron-withdrawing substituents on the phenyl rings of the porphyrin achieving an overpotential of 0.4 V with a log TOF_{max} of 4.2.^[106]

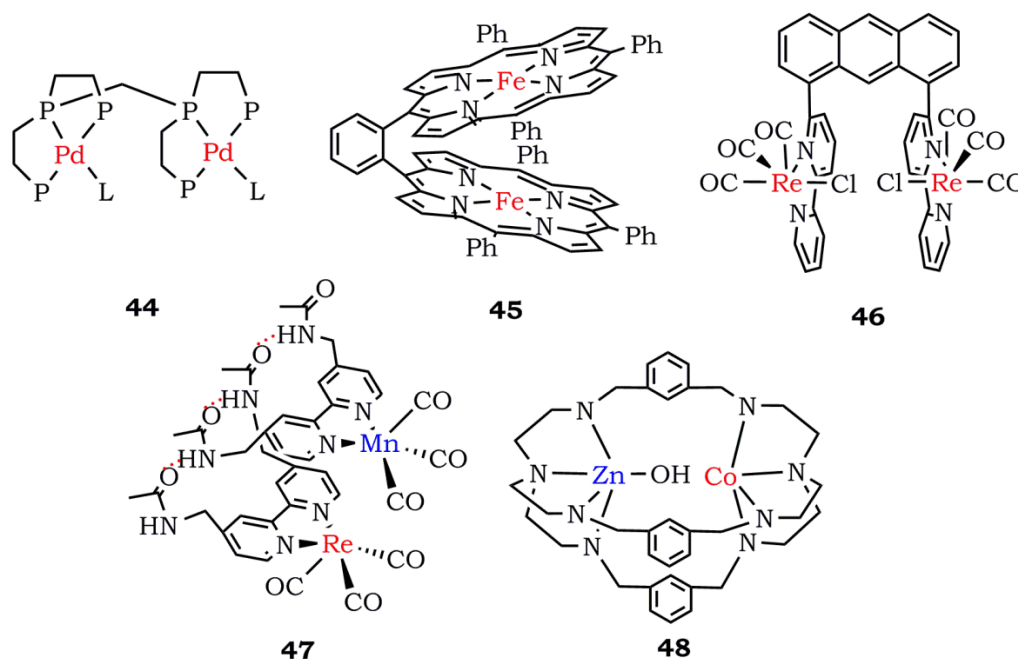


Figure 1-28. Bimetallic (homonuclear and heteronuclear) strategy for improving CO₂ reduction activity.

A rigid homobimetallic Re-based catalyst dimer was also reported by the group of Jurss using anthracene as a bridge to maintain proper distances between the metal centers.^[107] Electrochemical studies show distinct mechanisms for two isolated isomers of the dimers: the *cis* conformer (structure **46**) works via a cooperative bimetallic CO₂ activation and conversion while the *trans* conformer reduces CO₂ through well-established single-site and bimolecular pathways. Higher catalytic rates are observed for the *cis* conformer (log TOF of 1.55) relative to the *trans* conformer (log TOF 1.36), outperforming the monomeric Re catalyst (log TOF of 1.04).

It was previously discussed that a similar Re-based hydrogen-bonded supramolecular dimer was formed *in situ* when mixing acetoamidomethyl-modified bpy ligands.^[51] This dimer operated at 250 mV lower overpotential compared to the monomeric catalyst but still suffers from a low TOF and Faradaic efficiency as well. The group of Kubiak has further optimized the system by synthesizing a heterobimetallic Re-Mn dimer (structure **47**) just by mixing 1:1 equivalents of the Re- and Mn-centered acetoamidomethyl-modified ligands. Enhanced catalytic activity was observed and it was proposed that the Mn metal acts to activate the CO₂ substrate while the Re metal acts to transfer the electrons to the substrate. This similarly mimics the heterobimetallic activity observed in the [NiFe] CODH (Ni metal as redox active center while Fe metal as substrate-activating). Recently the group of Lu has synthesized a variety of cryptates holding Ni-Ni,^[108] Co-Co,^[109] and even a heterometallic Co-Zn^[110] catalyst (Complex **48**) which show improved photocatalytic activity compared to mononuclear counterparts. This catalyst resulted in a TON of 65000, TOF of 1.8 s⁻¹, and a 98% selectivity for CO when photosensitized by a Ru phenanthroline photosensitizer in the presence of triethanolamine as ED. Control experiments with Co-Co and Zn-Zn dimers showed the need for the synergistic effect of both metal centers where the Co metal acts as the redox active site while the Zn metal acts to activate the CO₂ substrate.^[110] These studies show great opportunities and promise for further optimizations and translations to other existing monomeric forms. Substantial mechanistic analysis is however needed to fully validate the proposed pathways by which these bimetallic catalysts operate.

1.7. Thesis Objectives and Scope

Considering the developments of catalyst design for CO₂ reduction presented above, there still seems a lot to be understood and optimized. The current performances of both photo- and electro-catalysts are still not at par to be operationally scaled, requiring optimum efficiency and stability. In response to this challenge, this thesis will focus on developing catalysts for CO₂ reduction by employing key insights obtained from natural systems known to sustainably utilize solar energy in transforming CO₂.

Chapter 2 will focus on the fundamental understanding of how the energy of a photon of light can be efficiently transformed to a reducing power able to reduce CO₂. This will entail validation and further investigation on a photocatalytic system composed of a ruthenium (II) trisbipyridine **[Ru(bpy)₃]²⁺** complex as photosensitizer and a rhenium (I) triscarbonyl bipyridyl **[Re(CO)₃(bpy)Br]** complex as catalyst.

Chapter 3 will focus on catalyst design that employs first coordination sphere modifications on a nickel (II) catalyst bearing a tetradentate N₂S₂ ligand towards photo-catalytic CO₂ reduction. Investigations will employ bio-inspired sulfur-rich pentadentate coordinating ligands on nickel catalysts that will be systematically studied using time-resolved spectroscopic techniques.

Chapter 4 will focus on employing second coordination sphere effects on CO₂ reduction catalysts similarly observed in the active site of CO dehydrogenase enzymes. This will involve the establishment of functional groups such as amino, urea, amido, and cationic imidazolium moieties in the periphery of rhenium triscarbonyl bipyridine and iron porphyrin catalysts. Systematic investigation will also deal with the specific pre-arrangement of these functional groups in the vicinity of the catalyst, critical for the activity.

Chapter 5 will focus on leveraging the carbon monoxide produced from these studied systems by mimicking the CO dehydrogenase/acetyl-CoA synthase partnership. This will involve a two-chamber system that immediately uses the photo-produced CO from one chamber for an amino-carbonylation reaction in the other chamber. This will indicate further opportunities and value for the catalytic reduction of CO₂.

Bibliography

- [1] D. P. Trans, D. R. Keeling, *BP Statistical Review of World Energy 2019*, Centre For Energy Economics Research And Policy, Heriot-Watt University, **2019**.
- [2] R. J. Detz, J. N. H. Reek, B. C. C. van der Zwaan, *Energy Environ. Sci.* **2018**, *11*, 1653–1669.
- [3] *Trends in Atmospheric Carbon Dioxide*, National Oceanic And Atmospheric Administration, Earth System Research Laboratory, **2019**.
- [4] R. K. Pachauri, L. A. Meyer, *Climate Change 2014: Synthesis Report*, Intergovernmental Panel On Climate Change, Geneva, Switzerland, **2014**.
- [5] N. J. L. Lenssen, G. A. Schmidt, J. E. Hansen, M. J. Menne, A. Persin, R. Ruedy, D. Zyss, *Journal of Geophysical Research: Atmospheres* **2019**, *0*, DOI 10.1029/2018JD029522.
- [6] *The Paris Agreement*, United Nations Climate Change, **2015**.
- [7] A. M. Appel, J. E. Bercaw, A. B. Bocarsly, H. Dobbek, D. L. DuBois, M. Dupuis, J. G. Ferry, E. Fujita, R. Hille, P. J. A. Kenis, et al., *Chem. Rev.* **2013**, *113*, 6621–6658.
- [8] A. J. V. Underwood, *Ind. Eng. Chem.* **1940**, *32*, 449–454.
- [9] J. Jones, *Platin. Met. Rev.* **2000**, *44*, 94–105.
- [10] L. Mond, C. Langer, F. Quincke, *J. Chem. Soc., Trans.* **1890**, *57*, 749–753.
- [11] W. Schneider, W. Diller, in *Ullmann's Encyclopedia of Industrial Chemistry*, American Cancer Society, **2000**.
- [12] O. S. Bushuyev, P. D. Luna, C. T. Dinh, L. Tao, G. Saur, J. van de Lagemaat, S. O. Kelley, E. H. Sargent, *Joule* **2018**, *2*, 825–832.
- [13] M. Aresta, A. Dibenedetto, A. Angelini, *Chem. Rev.* **2014**, *114*, 1709–1742.
- [14] K. Kalyanasundaram, M. Graetzel, *Current Opinion in Biotechnology* **2010**, *21*, 298–310.
- [15] D. Gust, T. A. Moore, A. L. Moore, *Acc. Chem. Res.* **2009**, *42*, 1890–1898.
- [16] J. A. Bassham, A. A. Benson, M. Calvin, *J. Biol. Chem.* **1950**, *185*, 781–787.
- [17] G. Fuchs, *Annu. Rev. Microbiol.* **2011**, *65*, 631–658.
- [18] M. Can, F. A. Armstrong, S. W. Ragsdale, *Chem. Rev.* **2014**, *114*, 4149–4174.
- [19] V. Svetlitchnyi, C. Peschel, G. Acker, O. Meyer, *Journal of Bacteriology* **2001**, *183*, 5134–5144.
- [20] J.-H. Jeoung, H. Dobbek, *Science* **2007**, *318*, 1461.
- [21] B. Zhang, C. F. Hemann, R. Hille, *J. Biol. Chem.* **2010**, *285*, 12571–12578.
- [22] H. Dobbek, L. Gremer, R. Kiefersauer, R. Huber, O. Meyer, *Proc Natl Acad Sci U S A* **2002**, *99*, 15971–15976.
- [23] T. Reda, C. M. Plugge, N. J. Abram, J. Hirst, *PNAS* **2008**, *105*, 10654–10658.
- [24] H. Dobbek, *Coordination Chemistry Reviews* **2011**, *255*, 1104–1116.
- [25] Y. Yamazaki, H. Takeda, O. Ishitani, *J. Photochem. Photobiol. C* **2015**, *25*, 106–137.
- [26] H. Takeda, C. Cometto, O. Ishitani, M. Robert, *ACS Catal.* **2017**, *7*, 70–88.
- [27] K. E. Dalle, J. Warnan, J. J. Leung, B. Reuillard, I. S. Karmel, E. Reisner, *Chem. Rev.* **2019**, DOI 10.1021/acs.chemrev.8b00392.
- [28] W. E. Jones, M. A. Fox, *J. Phys. Chem.* **1994**, *98*, 5095–5099.
- [29] K. Kalyanasundaram, *Coordination Chemistry Reviews* **1982**, *46*, 159–244.
- [30] C. Creutz, N. Sutin, *Inorg. Chem.* **1976**, *15*, 496–499.
- [31] Y. Tamaki, K. Watanabe, K. Koike, H. Inoue, T. Morimoto, O. Ishitani, *Faraday Discuss.* **2012**, *155*, 115–127.
- [32] A. Juris, V. Balzani, F. Barigelletti, S. Campagna, P. I. Belser, A. Von Zelewsky, *Coordination Chemistry Reviews* **1988**, *84*, 85–277.
- [33] L. Flamigni, A. Barbieri, C. Sabatini, B. Ventura, F. Barigelletti, in *Photochemistry and Photophysics of Coordination Compounds II*, Springer, Berlin, Heidelberg, **2007**, pp. 143–203.

- [34] F. O. Garces, K. A. King, R. J. Watts, *Inorg. Chem.* **1988**, *27*, 3464–3471.
- [35] H. Takeda, K. Ohashi, A. Sekine, O. Ishitani, *J. Am. Chem. Soc.* **2016**, *138*, 4354–4357.
- [36] Y. Du, R. M. Pearson, C.-H. Lim, S. M. Sartor, M. D. Ryan, H. Yang, N. H. Damrauer, G. M. Miyake, *Chemistry – A European Journal* **2017**, *23*, 10962–10968.
- [37] Y. Pellegrin, F. Odobel, *Comptes Rendus Chimie* **2017**, *20*, 283–295.
- [38] C. Creutz, *Inorg. Chem.* **1981**, *20*, 4449–4452.
- [39] E. Deponti, A. Luisa, M. Natali, E. Iengo, F. Scandola, *Dalton Trans.* **2014**, *43*, 16345–16353.
- [40] Y. Tamaki, T. Morimoto, K. Koike, O. Ishitani, *Proc Natl Acad Sci U S A* **2012**, *109*, 15673–15678.
- [41] X.-Q. Zhu, M.-T. Zhang, A. Yu, C.-H. Wang, J.-P. Cheng, *J. Am. Chem. Soc.* **2008**, *130*, 2501–2516.
- [42] J.-M. Savéant, *Chem. Rev.* **2008**, *108*, 2348–2378.
- [43] N. Elgrishi, M. B. Chambers, X. Wang, M. Fontecave, *Chem. Soc. Rev.* **2017**, *46*, 761–796.
- [44] J. Hawecker, J.-M. Lehn, R. Ziessel, *J. Chem. Soc., Chem. Commun.* **1983**, 536–538.
- [45] J. Hawecker, J.-M. Lehn, R. Ziessel, *Helv. Chim. Acta.* **1986**, *69*, 1990–2012.
- [46] B. P. Sullivan, C. M. Bolinger, D. Conrad, W. J. Vining, T. J. Meyer, *J. Chem. Soc., Chem. Commun.* **1985**, *0*, 1414–1416.
- [47] F. P. A. Johnson, M. W. George, F. Hartl, J. J. Turner, *Organometallics* **1996**, *15*, 3374–3387.
- [48] J. Agarwal, E. Fujita, H. F. Schaefer, J. T. Muckerman, *Journal of the American Chemical Society* **2012**, *134*, 5180–5186.
- [49] J. A. Keith, K. A. Grice, C. P. Kubiak, E. A. Carter, *J. Am. Chem. Soc.* **2013**, *135*, 15823–15829.
- [50] Y. Hayashi, S. Kita, B. S. Brunshwig, E. Fujita, *J. Am. Chem. Soc.* **2003**, *125*, 11976–11987.
- [51] C. W. Machan, S. A. Chabolla, J. Yin, M. K. Gilson, F. A. Tezcan, C. P. Kubiak, *J. Am. Chem. Soc.* **2014**, *136*, 14598–14607.
- [52] J. M. Smieja, E. E. Benson, B. Kumar, K. A. Grice, C. S. Seu, A. J. M. Miller, J. M. Mayer, C. P. Kubiak, *Proc. Natl. Acad. Sci. USA* **2012**, *109*, 15646–15650.
- [53] P. Kurz, B. Probst, B. Spingler, R. Alberto, *European Journal of Inorganic Chemistry* **2006**, *2006*, 2966–2974.
- [54] M. L. Clark, P. L. Cheung, M. Lessio, E. A. Carter, C. P. Kubiak, *ACS Catal.* **2018**, *8*, 2021–2029.
- [55] J. M. Smieja, C. P. Kubiak, *Inorg. Chem.* **2010**, *49*, 9283–9289.
- [56] M. L. Clark, B. Rudshiteyn, A. Ge, S. A. Chabolla, C. W. Machan, B. T. Psciuk, J. Song, G. Canzi, T. Lian, V. S. Batista, et al., *J. Phys. Chem. C* **2016**, *120*, 1657–1665.
- [57] H. Tsubaki, S. Tohyama, K. Koike, H. Saitoh, O. Ishitani, *Dalton Trans.* **2005**, *0*, 385–395.
- [58] H. Takeda, K. Koike, H. Inoue, O. Ishitani, *J. Am. Chem. Soc.* **2008**, *130*, 2023–2031.
- [59] P. Christensen, A. Hamnett, A. V. G. Muir, J. A. Timney, *Journal of the Chemical Society, Dalton Transactions* **1992**, *0*, 1455–1463.
- [60] H. Hori, F. P. A. Johnson, K. Koike, O. Ishitani, T. Ibusuki, *Journal of Photochemistry and Photobiology A: Chemistry* **1996**, *96*, 171–174.
- [61] J. M. Smieja, M. D. Sampson, K. A. Grice, E. E. Benson, J. D. Froehlich, C. P. Kubiak, *Inorg. Chem.* **2013**, *52*, 2484–2491.
- [62] M. Bourrez, F. Molton, S. Chardon-Noblat, A. Deronzier, *Angewandte Chemie International Edition* **2011**, *50*, 9903–9906.

- [63] M. Stanbury, J.-D. Compain, S. Chardon-Noblat, *Coordination Chemistry Reviews* **2018**, 361, 120–137.
- [64] C. Riplinger, M. D. Sampson, A. M. Ritzmann, C. P. Kubiak, E. A. Carter, *Journal of the American Chemical Society* **2014**, 136, 16285–16298.
- [65] S. E. Tignor, H.-Y. Kuo, T. S. Lee, G. D. Scholes, A. B. Bocarsly, *Organometallics* **2019**, 38, 1292–1299.
- [66] M. D. Sampson, A. D. Nguyen, K. A. Grice, C. E. Moore, A. L. Rheingold, C. P. Kubiak, *J. Am. Chem. Soc.* **2014**, 136, 5460–5471.
- [67] M. L. Clark, K. A. Grice, C. E. Moore, A. L. Rheingold, C. P. Kubiak, *Chem. Sci.* **2014**, 5, 1894–1900.
- [68] B. Gholamkhash, H. Mametsuka, K. Koike, T. Tanabe, M. Furue, O. Ishitani, *Inorg. Chem.* **2005**, 44, 2326–2336.
- [69] A. Nakada, K. Koike, T. Nakashima, T. Morimoto, O. Ishitani, *Inorg. Chem.* **2015**, 54, 1800–1807.
- [70] K. Koike, S. Naito, S. Sato, Y. Tamaki, O. Ishitani, *J. Photochem. Photobiol. A* **2009**, 207, 109–114.
- [71] E. Kato, H. Takeda, K. Koike, K. Ohkubo, O. Ishitani, *Chem. Sci.* **2015**, 6, 3003–3012.
- [72] Z.-Y. Bian, S.-M. Chi, L. Li, W. Fu, *Dalton Trans.* **2010**, 39, 7884.
- [73] Y. Tamaki, K. Koike, T. Morimoto, O. Ishitani, *J. Catal.* **2013**, 304, 22–28.
- [74] M. Hammouche, D. Lexa, J. M. Savéant, M. Momenteau, *Journal of Electroanalytical Chemistry and Interfacial Electrochemistry* **1988**, 249, 347–351.
- [75] C. Costentin, S. Drouet, G. Passard, M. Robert, J.-M. Savéant, *J. Am. Chem. Soc.* **2013**, 135, 9023–9031.
- [76] M. Hammouche, D. Lexa, M. Momenteau, J. M. Saveant, *J. Am. Chem. Soc.* **1991**, 113, 8455–8466.
- [77] C. Rö melt, J. Song, M. Tarrago, J. A. Rees, M. van Gastel, T. Weyhermüller, S. DeBeer, E. Bill, F. Neese, S. Ye, *Inorg. Chem.* **2017**, 56, 4745–4750.
- [78] B. Mondal, A. Rana, P. Sen, A. Dey, *J. Am. Chem. Soc.* **2015**, 137, 11214–11217.
- [79] C. Costentin, S. Drouet, M. Robert, J.-M. Savéant, *J. Am. Chem. Soc.* **2012**, 134, 11235–11242.
- [80] C. Costentin, G. Passard, J.-M. Savéant, *J. Am. Chem. Soc.* **2015**, 137, 5461–5467.
- [81] C. Costentin, J.-M. Savéant, *ChemElectroChem* **2014**, 1, 1226–1236.
- [82] I. Azcarate, C. Costentin, M. Robert, J.-M. Savéant, *J. Phys. Chem. C* **2016**, 120, 28951–28960.
- [83] I. Azcarate, C. Costentin, M. Robert, J.-M. Savéant, *J. Am. Chem. Soc.* **2016**, 138, 16639–16644.
- [84] C. Costentin, S. Drouet, M. Robert, J.-M. Savéant, *Science* **2012**, 338, 90–94.
- [85] C. G. Margarit, C. Schnedermann, N. G. Asimow, D. G. Nocera, *Organometallics* **2019**, 38, 1219–1223.
- [86] A. J. Libbey, J. T. Stock, *Anal. Chem.* **1970**, 42, 526–529.
- [87] F. Franco, C. Cometto, F. F. Vallana, F. Sordello, E. Priola, C. Minero, C. Nervi, R. Gobetto, *Chem. Commun.* **2014**, 50, 14670–14673.
- [88] J. Agarwal, T. W. Shaw, H. F. Schaefer, A. B. Bocarsly, *Inorg. Chem.* **2015**, 54, 5285–5294.
- [89] G. Neri, I. M. Aldous, J. J. Walsh, L. J. Hardwick, A. J. Cowan, *Chem. Sci.* **2016**, 7, 1521–1526.
- [90] G. F. Manbeck, J. T. Muckerman, D. J. Szalda, Y. Himeda, E. Fujita, *J. Phys. Chem. B* **2015**, 119, 7457–7466.

- [91] S. A. Chabolla, C. W. Machan, J. Yin, E. A. Dellamary, S. Sahu, N. C. Gianneschi, M. K. Gilson, F. A. Tezcan, C. P. Kubiak, *Faraday Discuss.* **2017**, *198*, 279–300.
- [92] M. Beley, J.-P. Collin, R. Ruppert, J.-P. Sauvage, *J. Chem. Soc., Chem. Commun.* **1984**, *0*, 1315–1316.
- [93] B. J. Fisher, R. Eisenberg, *J. Am. Chem. Soc.* **1980**, *102*, 7361–7363.
- [94] M. Beley, J. P. Collin, R. Ruppert, J. P. Sauvage, *J. Am. Chem. Soc.* **1986**, *108*, 7461–7467.
- [95] J. D. Froehlich, C. P. Kubiak, *Inorg. Chem.* **2012**, *51*, 3932–3934.
- [96] J. Song, E. L. Klein, F. Neese, S. Ye, *Inorg. Chem.* **2014**, *53*, 7500–7507.
- [97] A. Chapovetsky, M. Welborn, J. M. Luna, R. Haiges, T. F. Miller, S. C. Marinescu, *ACS Cent. Sci.* **2018**, *4*, 397–404.
- [98] A. Chapovetsky, T. H. Do, R. Haiges, M. K. Takase, S. C. Marinescu, *J. Am. Chem. Soc.* **2016**, *138*, 5765–5768.
- [99] E. Haviv, D. Azaiza-Dabbah, R. Carmieli, L. Avram, J. M. L. Martin, R. Neumann, *J. Am. Chem. Soc.* **2018**, *140*, 12451–12456.
- [100] E. M. Nichols, J. S. Derrick, S. K. Nistanaki, P. T. Smith, C. J. Chang, *Chem. Sci.* **2018**, *9*, 2952–2960.
- [101] P. Sen, B. Mondal, D. Saha, A. Rana, A. Dey, *Dalton Trans.* **2019**, *48*, 5965–5977.
- [102] C. Costentin, J.-M. Savéant, *Nature Reviews Chemistry* **2017**, *1*, 0087.
- [103] S. Sung, D. Kumar, M. Gil-Sepulcre, M. Nippe, *J. Am. Chem. Soc.* **2017**, *139*, 13993–13996.
- [104] S. Sung, X. Li, L. M. Wolf, J. R. Meeder, N. S. Bhuvanesh, K. A. Grice, J. A. Panetier, M. Nippe, *J. Am. Chem. Soc.* **2019**, *141*, 6569–6582.
- [105] E. A. Mohamed, Z. N. Zahran, Y. Naruta, *Chem. Commun.* **2015**, *51*, 16900–16903.
- [106] Z. N. Zahran, E. A. Mohamed, Y. Naruta, *Scientific Reports* **2016**, *6*, 24533.
- [107] W. Yang, S. Sinha Roy, W. C. Pitts, R. L. Nelson, F. R. Fronczek, J. W. Jurss, *Inorg. Chem.* **2018**, *57*, 9564–9575.
- [108] L.-M. Cao, H.-H. Huang, J.-W. Wang, D.-C. Zhong, T.-B. Lu, *Green Chem.* **2018**, *20*, 798–803.
- [109] T. Ouyang, H.-H. Huang, J.-W. Wang, D.-C. Zhong, T.-B. Lu, *Angew. Chem. Int. Ed.* **2017**, *56*, 738–743.
- [110] T. Ouyang, H.-J. Wang, H.-H. Huang, J.-W. Wang, S. Guo, W.-J. Liu, D.-C. Zhong, T.-B. Lu, *Angew. Chem. Int. Ed.* **2018**, *57*, 16480–16485.

Chapter 2

Understanding Photocatalysis:

How can visible light be used to reduce CO₂ to CO?

This Chapter includes work reported in: P. Gotico, A. Del Vecchio, D. Audisio, A. Quaranta, Z. Halime, W. Leibl, A. Aukauloo, *ChemPhotoChem* **2018**, 2, 715–719.

2.1. Introduction

The variability and nondispatchability of renewable low-carbon emission energy sources such as solar has limited their widespread and terawatt-scale adoption. To circumvent such limitations, research has been focused on transforming solar energy into stable chemical forms for storage and transport. Similar strategy is observed in natural photosynthesis where green plants use solar energy, water, and carbon dioxide (CO₂) to produce oxygen and carbon-based storage chemicals such as sugar. With the goal of harnessing solar energy and simultaneously addressing the problem of increasing concentrations of greenhouse gases such as CO₂ in the atmosphere, increasing interest and effort are currently deployed in the field of photocatalytic CO₂ reduction in an artificial photosynthetic scheme.

In order to advance research in this field, basic understanding of how visible light from the sun can be used to reduce CO₂ is necessary. CO₂ is a thermodynamically highly stable molecule. Thus, the addition of one electron to CO₂ requires a potential more negative than -1.9 V *vs* SHE, which correspond to a significant amount of energy. To circumvent such energetic cost, artificial photosynthesis aims to use solar energy to create a charge separate state in a photosensitizer, where the electron is used to activate a reduction catalyst and subsequently reduce CO₂, while the hole is used to activate an oxidation catalyst to oxidize water, as shown in the general scheme in Chapter 1.

There have been extensive developments in homogenous photocatalytic reduction of CO₂ in literature, as discussed in Chapter 1, focusing on improving the quantum efficiency, stability, and the selectivity of the photocatalytic system. Improvement, however, needs the mechanistic understanding and a basic visualization of how the energy of a photon is transformed to a reducing power able to activate catalysts for the reduction of CO₂. By identifying and monitoring the formation of intermediate species in such a mechanistic analysis, one can distinguish advantageous from deleterious pathways and learn how the electrons can be efficiently directed and used towards the reduction of CO₂. From such investigation, one can then identify important parameters to improve the photocatalytic activity of the system.

Focusing on the photocatalytic CO₂ reduction process requires an electron donor which replaces the water oxidation catalyst in an ideal complete system. The interaction between the photosensitizer (**PS**), electron donor (**ED**) and the reduction catalyst (**Cat**) depends on the nature of the emitting excited state of the photosensitizer and the quenching thermodynamics of the excited state. Once a photosensitizer absorbs light, an excited state is produced which then can be

quenched through an electron transfer either from the electron donor or the catalyst, as shown in Figure 2-1. A reductive quenching mechanism is observed when the excited photosensitizer (**PS***) is quenched by the electron donor, producing a reduced photosensitizer (**PS⁻**), which can then reduce the catalyst and generate back the ground state photosensitizer. On the other hand, an oxidative quenching mechanism is observed when the excited state of the photosensitizer is reducing enough to reduce the catalyst first, and the ground state photosensitizer is regenerated by electron transfer from the electron donor to the oxidized photosensitizer (**PS⁺**). The nature and the respective concentrations of the photosensitizer, electron donor, and catalyst have a direct impact on which mechanism will be favorable, and in consequence affect how the photocatalysis occurs. It is important then to observe the formation and decay of the intermediate species during the photo-induced events and comprehensively investigate (1) how efficiently the electrons are being transferred from the excited photosensitizer to the catalyst, (2) how the catalyst accumulates the electrons, and (3) how the catalyst uses these electrons to reduce CO₂.

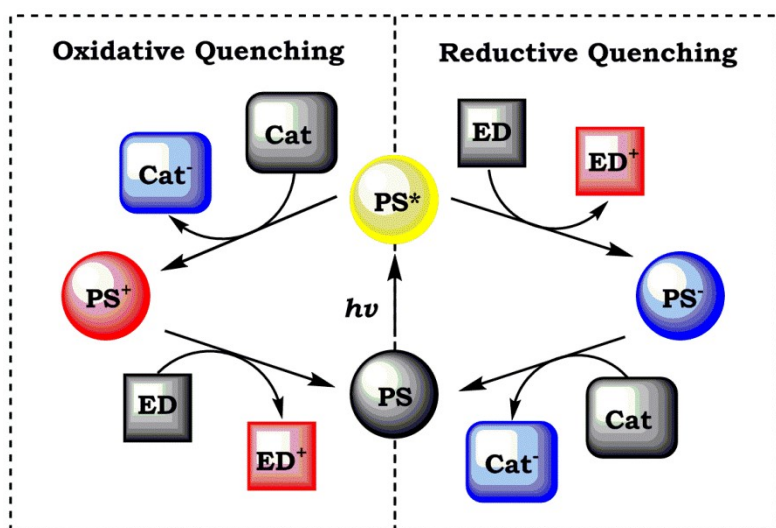


Figure 2-1. The two possible electron-transfer quenching mechanisms of an excited photosensitizer.

2.2. Objectives

This chapter will focus on tracking the journey of a visible-light photon and how it is transformed to a reducing power able to reduce CO₂. For this study, we chose a well-known photocatalyst system consisting of a rhenium tricarbonyl bipyridyl catalyst [**Re(CO)₃(bpy)Br**] and a ruthenium trisbipyridine photosensitizer [**Ru(bpy)₃]²⁺** using various electron donors (**ED**) such as 1-benzyl-1,4-dihydronicotinamide (**BNAH**), 1,3-dimethyl-2-phenylbenzimidazole (**BIH**), and

sodium ascorbate (**NaAsc**), with the structures shown in Figure 2-2. Specifically, this chapter aims:

- To combine literature knowledge and experimental results to paint a comprehensive picture of the first photo-induced electron transfer from the photosensitizer to the catalyst using nanosecond laser flash photolysis
- To optimize the photocatalytic activity of the system using various electron donors and solvent conditions and to rationalize their role in the catalysis
- To track two electron accumulation in the catalyst using a pump-pump-probe transient absorption technique and photo-accumulation studies

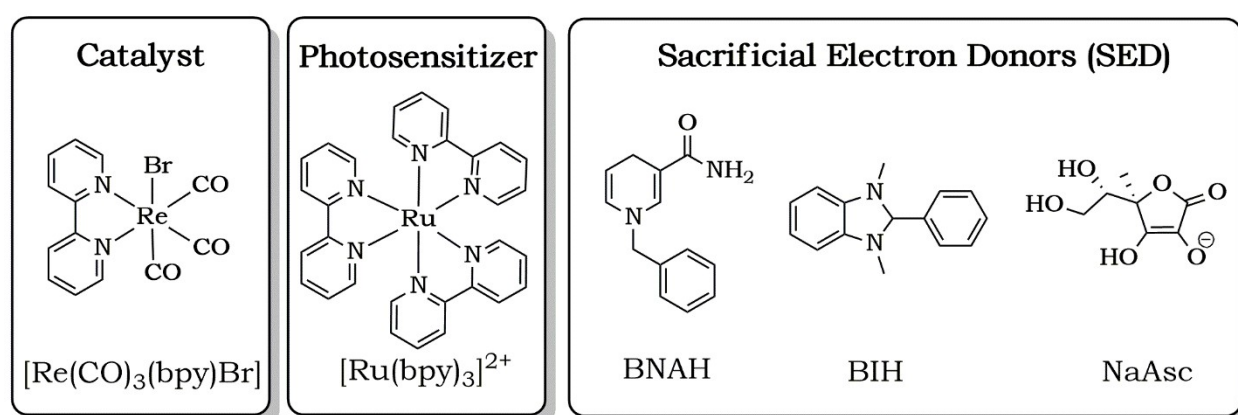


Figure 2-2. Different components used in the photocatalytic system for the reduction of CO₂ to CO.

2.3. Electrochemistry

Cyclic voltammetry (CV) of the **[Re(CO)₃(bpy)Br]** catalyst shows a reversible peak at -1.72 V (*vs* Fc^{+ / 0}) which has been reported to be a bipyridine-based reduction.^[1,2] The observation that (i) the solvent does not affect the peak potential and (ii) the peak potential is insensitive to the nature of the halide,^[1,2] confirms such attribution. The second reduction at -2.07 V (*vs* Fc^{+ / 0}) is irreversible and it is greatly affected by the solvent, as shown in Table 2-1 and Figure 2-3. This irreversible peak is attributed to a metal-based reduction that involves the loss of the halide.

The solvent effect (acetonitrile, ACN *vs* dimethylformamide, DMF) observed on this second peak potential might originate from the difference between the formed solvated species: **[Re(CO)₃(bpy)(ACN)]^{•-}** *vs* **[Re(CO)₃(bpy)(DMF)]^{•-}**, and it seems that the former is easier to reduce than the latter. This second reduction, eventually gives the catalytically active species, **[Re(CO)₃(bpy)]⁻** anion, which has a singlet ground state with a formal charge distribution of one electron in the bpy π*

orbital and the other electron in the Re dz^2 orbital, as determined by experimental spectroscopy (IR, XANES, EXAFS) and computational quantum chemistry (KS-DFT).^[3] This configuration has been shown to be more favorable to interact with a CO₂ substrate, because it offers a lower activation barrier for CO₂ binding compared to H⁺ binding, resulting in good selectivity for CO₂ reduction versus proton reduction.^[4,5]

Table 2-1. Half-wave potentials of the complexes studied in different solvents (ACN = acetonitrile, DMF = dimethylformamide) and their corresponding assignments.

Complex	$E_{1/2}$ / V vs $Fc^{+/0}$		Assignment
	ACN	DMF	
[Re(CO)₃(bpy)Br]	-1.72	-1.72	Bpy-based reduction
	-2.07 ^[a]	-2.21 ^[a]	Re-based reduction with Br ⁻ loss
[Ru(bpy)₃]²⁺	-1.74	-1.73	Bpy-based reduction
	-1.93	-1.91	Bpy-based reduction
	-2.17	-2.18	Bpy-based reduction

[a] Irreversible peaks and as such peak potential values are reported instead of $E_{1/2}$.

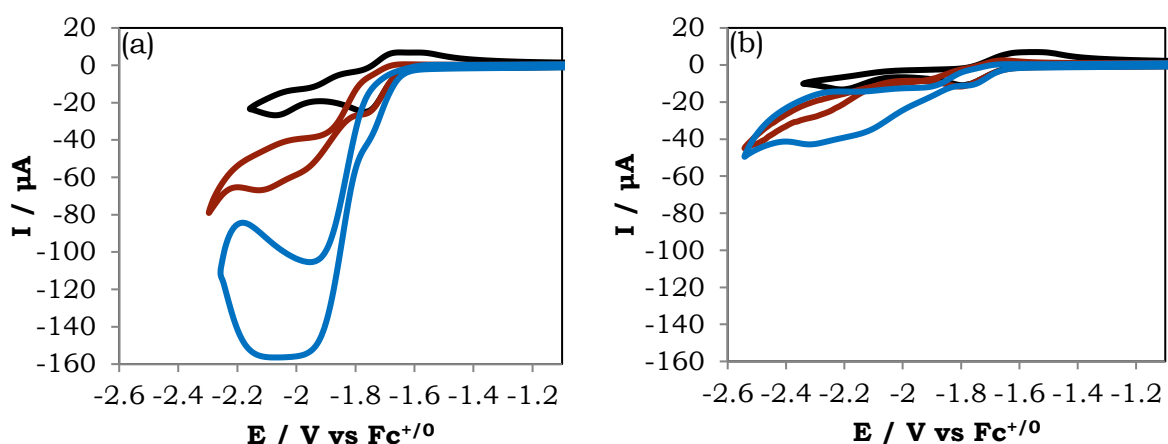


Figure 2-3. Cyclic voltammograms of 1 mM **[Re(CO)₃(bpy)Br]** in (a) ACN and (b) DMF under Ar (black), CO₂ (red), and CO₂ with 5.5 M H₂O (blue).

The CV of **[Re(CO)₃(bpy)Br]** catalyst shows a significant catalytic current upon purging with CO₂ in the presence of a proton source, ie. water, indicating a catalytic activity towards CO₂ reduction, with an onset just after the first reduction peak, as shown in Figure 2-3. A big difference in the catalytic current can be observed when using ACN or DMF as the solvent, indicating a certain role of the solvent in the electrocatalytic activity. Initial photocatalytic study by Lehn (1983) has been made in DMF, possibly because of better activity, and as such DMF was

also used initially for electrochemical studies until the group of Mayer (1985) used ACN as solvent,^[1] in which succeeding electrochemical studies have followed the same condition. The effect of solvent on the electrocatalytic activity of the Re catalyst has not been fully disclosed, but a recent study on similar solvent dependency (ACN *vs* DMF) on iron porphyrin electrocatalytic activity^[6] reasons out that the difference could originate on how the solvent affects the protonation step in the electrocatalytic reduction of CO₂. DMF is a stronger H-bond acceptor than ACN (based on Abraham's hydrogen-bond basicity metric), as such, it will sequester a greater population of the donating Brønsted acid. Additionally, since coordination of the solvent in the reduced species seems to affect the second reduction peak potential, this might further affect the catalytic current intensity.

On the other hand, the CV of **[Ru(bpy)₃]²⁺** shows, as expected, three reversible reductions at -1.74 V, -1.93, and -2.17 V (*vs* Fc⁺⁰), which are assigned to bipyridine-based reductions, as shown in Table 2-1. Comparing the first reduction potential of **[Ru(bpy)₃]²⁺** (-1.74 V) with that of **[Re(CO)₃(bpy)Br]** (-1.72 V), it can be deduced that once a reduced **[Ru(bpy)₂(bpy⁻)]⁺** is formed (photo-chemically), there is a small thermodynamic drive ($\Delta G \sim -20$ meV) to transfer an electron to the Re catalyst although it is not very large.

2.4. Mechanistic Analysis by IR Spectroelectrochemistry

To further understand what happens in the electrochemical reduction of the Re catalyst, infrared (IR) spectroelectrochemistry has been employed and the changes upon reduction in the carbonyl stretching frequencies were followed, as shown in Figure 2-4. Before any reduction, the **[Re(CO)₃(bpy)Br]** catalyst possesses three sharp C=O stretching peaks at 2023 cm⁻¹, 1919 cm⁻¹, and 1901 cm⁻¹. Upon a reduction, the original peaks disappear and form new ones with a general shifting of the peaks to lower wavenumbers (lower energy) indicative of increased Re→CO π back-bonding, that is, the added electrons are at least partly delocalized within the Re-bpy chelate ring, which in turn increases the electron density on the Re center.^[2]

As summarized in Table 2-2, four species have been identified upon reduction, with the identity of the species confirmed by comparison with known literature data. Upon first reduction, shown in Figure 2-5, immediate formation of a mixed species is observed and attributed to an anionic radical **[Re(CO)₃(bpy)Br]^{•-}** and simultaneous halide loss and solvent substitution resulting in the solvated radical **[Re(CO)₃(bpy)(ACN)][•]**. A clean separation between these reduced species was not accomplished in the conditions of the experiment (100 s electrolysis for each 50 mV potential step) which is indicative of the good lability of the bromide anion and the good coordination of ACN to the Re metal. Indeed, one-electron reduction of the

complex destabilizes the π^* LUMO of the bpy ligand and changes its nature from being a π acceptor to a strong σ donor, making the Re-halide bond more labile. Dimer $[\text{Re}(\text{CO})_3(\text{bpy})]_2$ formation (1950 and 1857 cm^{-1}),^[2] as has been proposed in some studies in THF^[2] once the halide is lost, is not observed in this system because the radical immediately interacts with ACN to form the solvated radical $[\text{Re}(\text{CO})_3(\text{bpy})(\text{ACN})]^\bullet$. This was similarly observed by the group of Johnson even in the presence of excess halide.^[7]

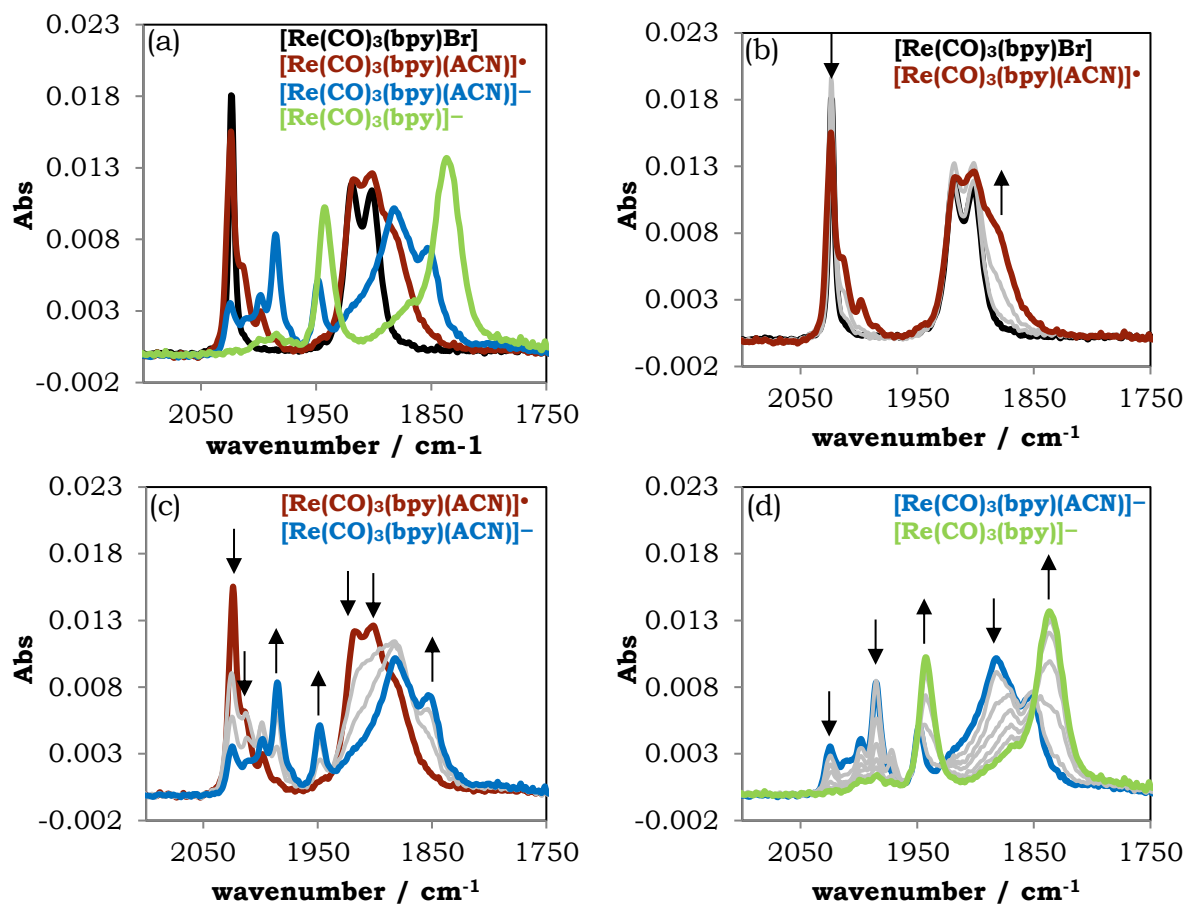


Figure 2-4. (a) Summary of identified reduced species during the IR spectro-electrochemistry of $\text{Re}(\text{CO})_3(\text{bpy})\text{Br}$ in ACN with 0.1 M TBAP under N_2 atmosphere with the evolution of the spectra shown in b-d. Colors are attributed to the species listed in Table 2-2. See Annex for details on experimental conditions.

Table 2-2. Experimental IR peaks determined by IR spectroelectrochemistry in ACN containing 0.1 M TBAP under N₂ atmosphere in comparison with literature values.

Species ^[a]	IR peaks, cm ⁻¹	
	Experimental Value (ACN)	Literature value (Solvent)
[Re(CO) ₃ (bpy)Br]	2023, 1919, 1901	2019, 1919, 1895 (THF) ^[2]
[Re(CO) ₃ (bpy)Br] ^{•-}	1998, 1882 br, 1860 br	1997, 1888, 1867 (THF) ^[2]
[Re(CO) ₃ (bpy)(ACN)] [•]	2012, 1882 br ^[b]	2011, 1895 (ACN) ^[7]
[Re(CO) ₃ (bpy)(ACN)] ⁻	1985, 1948, 1882 br, ^[b] 1852	1986, 1868, 1852 (ACN) ^[7]
[Re(CO) ₃ (bpy)] ⁻	1943, 1837	1948, 1846 (ACN) ^[7]

[a] Color of the species correspond to the same color scheme presented in Figure 2-4 and Figure 2-5.

[b] Broad peak at 1882 cm⁻¹ persisted making it difficult to conform with literature values

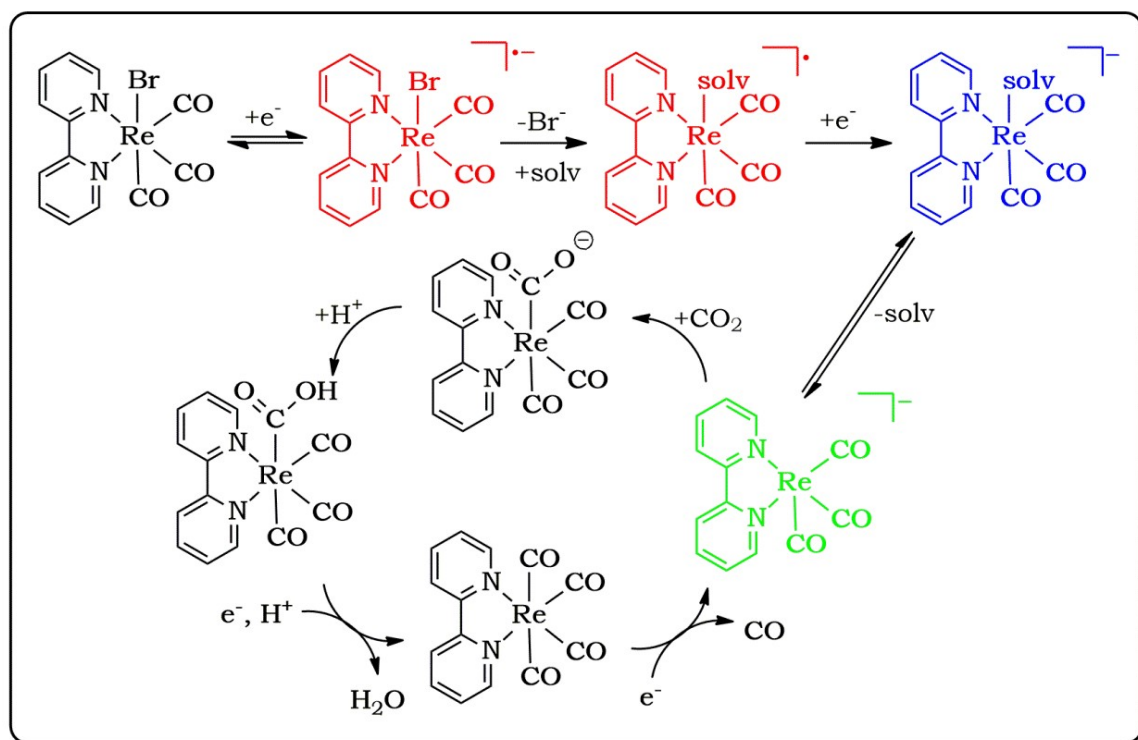


Figure 2-5. Proposed electrocatalytic cycle of **Re(CO)₃(bpy)Br** in ACN. Colored species correspond to spectroscopically identified species in Figure 2-4.

Once the **[Re(CO)₃(bpy)(ACN)][•]** radical has been formed, it can be easily reduced to give the solvated anion **[Re(CO)₃(bpy)(ACN)]⁻** given that it has a similar reduction potential as the starting Re complex.^[7] Further reduction eventually gives the penta-coordinated anion **[Re(CO)₃(bpy)]⁻**, which is shown to be the active species for CO₂ reduction based on stopped-flow kinetics and computational studies by the group of Kubiak.^[4] They reported that the dz² orbital of the Re catalyst can form a σ bond to the carbon atom of CO₂ and the interaction can be further

stabilized by a π interaction of the metal d_{xy} and d_{yz} orbitals with the p orbitals on the oxygen atoms of CO_2 , which is not present in the case of interaction of the Re catalyst with H^+ . Following the interaction of this active species with CO_2 using IR spectroelectrochemistry for mechanistic analysis seems difficult because of the immediate production of free carbonate species (1643 cm^{-1}) and free CO gas, and the lack of CO_2 -based intermediate species.^[7] The proposed catalytic cycle in Figure 2-5 was completed based on computational studies by the group of Carter and Kubiak.^[5] $[\text{Re}(\text{CO})_3(\text{bpy})]^-$ interacts more favorably with a CO_2 substrate than with a H^+ substrate, followed by a cascade of downhill reactions: a protonation step to give $[\text{Re}(\text{CO})_3(\text{bpy})(\text{COOH})]$ species, which undergoes a reduction and protonation step to give $[\text{Re}(\text{CO})_4(\text{bpy})]$, and further reduction gives back the active species $[\text{Re}(\text{CO})_3(\text{bpy})]^-$ with the release of CO. An important information from the computational study is that the intermediates on the CO_2 reduction pathway have sequentially more positive reduction potentials compared to the second reduction potential to form the active species $[\text{Re}(\text{CO})_3(\text{bpy})]^-$, indicating that the limiting step for the catalysis is the formation of the said active species.

2.5. Tracking the First Photo-Induced Electron Transfer

Key processes involved in the studied photocatalytic system involves: (1) photon absorption by a photosensitizer, (2) reductive quenching of the excited photosensitizer by an electron donor, (3) electron transfer from the reduced photosensitizer to the catalyst, and (4) charge accumulation on the catalytic moiety, and (5) CO_2 reduction by the catalyst. The last step has been addressed by the previous section, and in this section the first three steps leading to a photo-induced electron transfer to the catalyst will be probed using nanosecond transient absorption spectroscopy.

The ground state UV-visible spectrum of $[\text{Re}(\text{CO})_3(\text{bpy})\text{Br}]$ catalyst, denoted in this subsection as **[Re cat]**, shows a broad band at 372 nm assigned to a $\text{Re} \rightarrow \pi^*(\text{bpy})$ singlet metal-to-ligand charge transfer ($^1\text{MLCT}$) while the higher energy feature at $< 300\text{ nm}$ is associated with a bipyridine-based $\pi \rightarrow \pi^*$ transition, as shown in Figure 2-6. On the other hand, the $[\text{Ru}(\text{bpy})_3]^{2+}$ photosensitizer, denoted in this subsection as **[Ru PS]**, shows a strong absorption band in the visible region with a peak at 458 nm, which is attributed to $^1\text{MLCT}$ mainly from the d orbital of the Ru(II) center to the π^* orbital of bipyridine. Intense bands in the UV region ($< 300\text{ nm}$) are similarly assigned to the ligand-based $\pi \rightarrow \pi^*$ transition of the bipyridine units. In a 1:1 bimolecular mixture, it is expected that, based on the molar absorptivity coefficients of the molecules, the absorption spectrum will be dominated by the $^1\text{MLCT}$ band of **[Ru PS]**, which would be beneficial for

photocatalytic applications as it sensitizes the absorption in the visible region where solar irradiation is relatively high, as seen in Figure 2-6. Though the **[Re cat]** is expected to work as a photo-catalyst for reduction of CO₂ to CO based on the initial findings of the group of Lehn^[8,9], succeeding investigations have found it more efficient to isolate the role of the **[Re Cat]** as a catalyst, and coupling it with a visible-light photosensitizer.^[10-21]

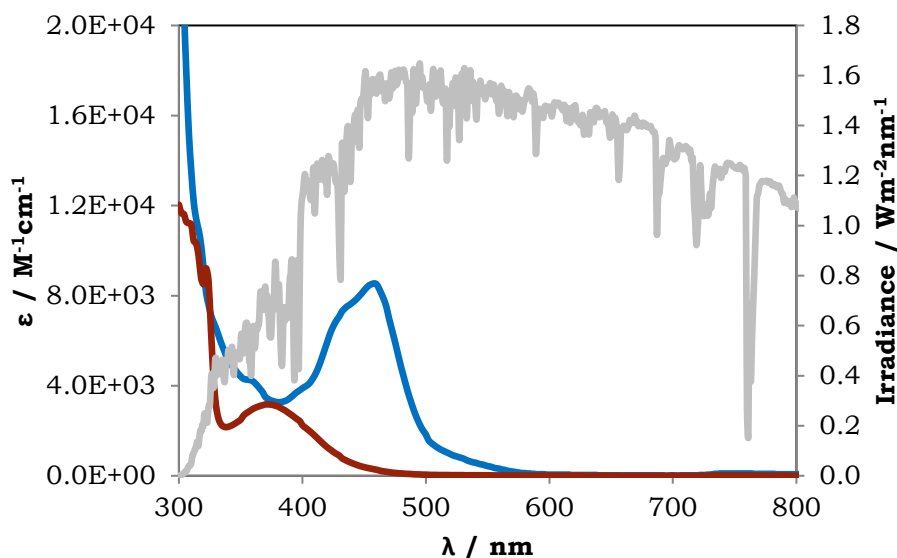


Figure 2-6. UV-visible spectra of the **[Ru(bpy)₃Cl₂]** photosensitizer (blue) and **[Re(CO)₃(bpy)Br]** catalyst (red) in 1:1 ACN:H₂O, in comparison with the solar irradiation spectrum (gray). Spectra of the complexes are not significantly affected by other solvent mixture (pure ACN, pure DMF, 1:1 DMF:H₂O).

When the **[Ru PS]** is excited in its ¹MLCT absorption band, rapid intersystem crossing (change of spin state) occurs which leads to the population of accessible triplet state (³MLCT) with a quantum efficiency of 1 made possible by strong spin-orbit coupling due to the presence of the Ru metal.^[22,23] This excited state (emission at 620 nm) is long-lived with a lifetime of ~900 ns in DMF because of the forbidden nature of ³MLCT to singlet ground state relaxation, and as such, it will allow enough time for diffusion-limited chemical reactions to occur. In the presence of an ED, efficient quenching of the emission of the **[Ru PS]*** was observed as a decrease of the emission lifetime (τ) as summarized in Table 2-3. The quenching rate constant (k_q), calculated from the Stern-Volmer plots, which relates emission lifetime with the concentration of ED (Figure 2-7), shows that the rate of quenching of the **[Ru PS]*** excited state is affected by the nature of the **ED**. The observed effect is mainly dominated by the thermodynamic drive between the **ED** and the **[Ru PS]***: **BNAH** < **BIH** < **NaAsc**, as observed in Table 2-3.

Table 2-3. Lifetime (τ) of emission kinetics at 620 nm of 13 μM $\text{Ru}(\text{bpy})_3\text{Cl}_2$ in DMF and associated rate constants (k_q) of different electron donors (**ED**). Similarly shown is the corresponding thermodynamic driving force (ΔG) of the process.

Entry	PS	ED	$E_{\text{ED}^{+/0}}$ [a] / V vs Fc	ΔG [b] / meV	τ [c] / ns	k_q / $\text{M}^{-1}\text{s}^{-1}$
1	$\text{Ru}(\text{bpy})_3\text{Cl}_2$	-	-	-	900	-
2	$\text{Ru}(\text{bpy})_3\text{Cl}_2$	BNAH	0.133	-137	450	2.90×10^8
3	$\text{Ru}(\text{bpy})_3\text{Cl}_2$	BIH	-0.146	-416	80	2.87×10^9
4	$\text{Ru}(\text{bpy})_3\text{Cl}_2$	NaAsc [d]	-0.369	-639	50	4.86×10^9

[a] determined by square wave voltammetry because of the irreversibility of the peaks; [b] ΔG estimated from the potential difference between $\text{ED}^{+/0}$ and $\text{Ru}^{\text{II}*/\text{I}}$; [c] lifetime at 3.74 mM **ED**, [d] in the presence of 10% water to dissolve NaAsc.

The three **EDs** were used for transient absorption measurements but because of the irreversible nature of the amine donors (**BNAH** and **BIH**), that is, accumulation of unwanted spectroscopically-overlapping species, only the use of **NaAsc**, a reversible electron donor, proved useful in probing the first photo-induced electron transfer between the photosensitizer and catalyst. A reductive quenching of $[\text{Ru PS}]^*$ by the **ED** was confirmed by the formation of the one-electron reduced (OER) species $[\text{Ru PS}]^{\bullet-}$ which has a characteristic absorption band at 510 nm (Figure 2-8a).

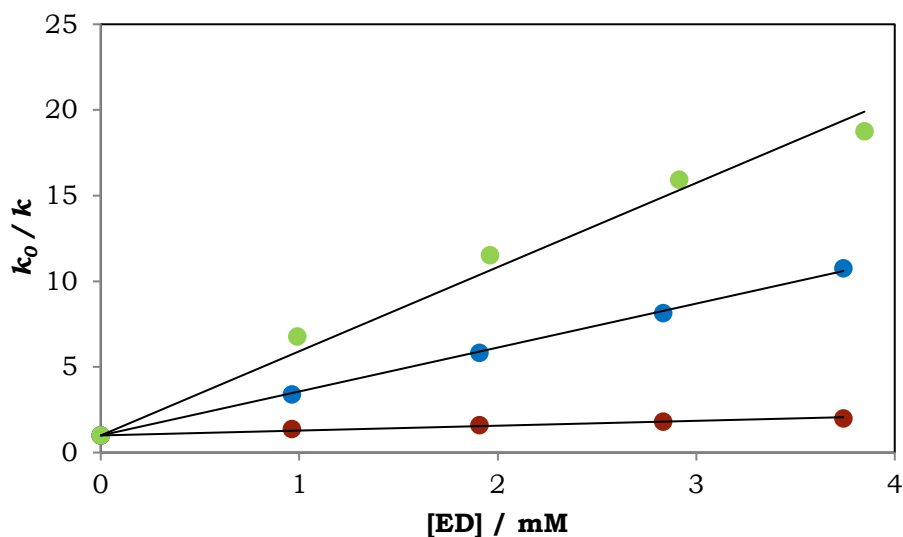


Figure 2-7. Stern-Volmer plots of the emission quenching (at 620 nm) of 13 μM $\text{Ru}(\text{bpy})_3\text{Cl}_2$ in DMF in the presence of different **EDs**: **BNAH** (red), **BIH** (blue), and **NaAsc** (green) with 10% H_2O . Laser energy = 6 mJ, Excitation at 460 nm, $\text{Abs}_{460} \sim 0.2$

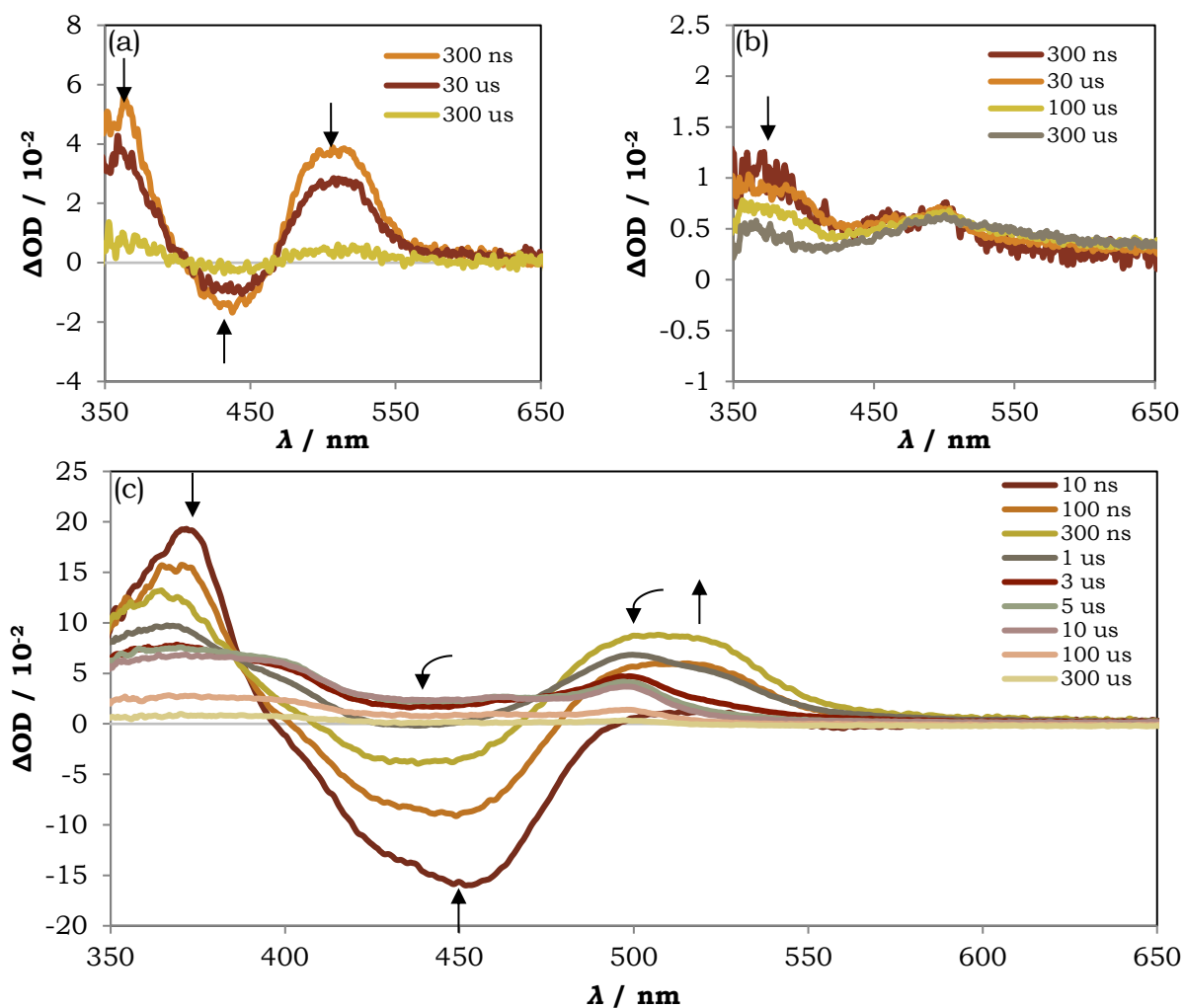


Figure 2-8. Transient absorption spectra of (a) $\text{Ru}(\text{bpy})_3\text{Cl}_2$ (b) $\text{Re}(\text{CO})_3(\text{bpy})\text{Br}$ and (c) 1:1 bimolecular mixture (60 μM) of both in 1:1 ACN:H₂O containing 30 mM of NaAsc as **ED** (Laser energy = 10 mJ, Excitation at 460 nm)

The formation of reduced $[\text{Re cat}]^{\bullet-}$ from the positive absorption at 445 nm, possess similar kinetics as the decay at 510 nm, as shown in Figure 2-9, and could be globally fitted. In addition, as the concentration of the catalyst is increased with constant concentration of the photosensitizer and electron donor, the decay at 510 nm and the growth at 445 nm become faster, with a linear relationship between the concentration and apparent rate constant, indicating a pseudo-first order. These observations confirm that electron transfer occurs from the $[\text{Ru PS}]^{\bullet-}$ to the $[\text{Re cat}]$, with a diffusion-limited bimolecular rate of $4.83 \times 10^9 \text{ M}^{-1}\text{s}^{-1}$. This result clearly indicates that even with little thermodynamic drive ($\Delta G \sim -20 \text{ meV}$) between $[\text{Ru PS}]^{\bullet-}$ and $[\text{Re cat}]^{\bullet-}$, a first photo-induced electron transfer is still observed.

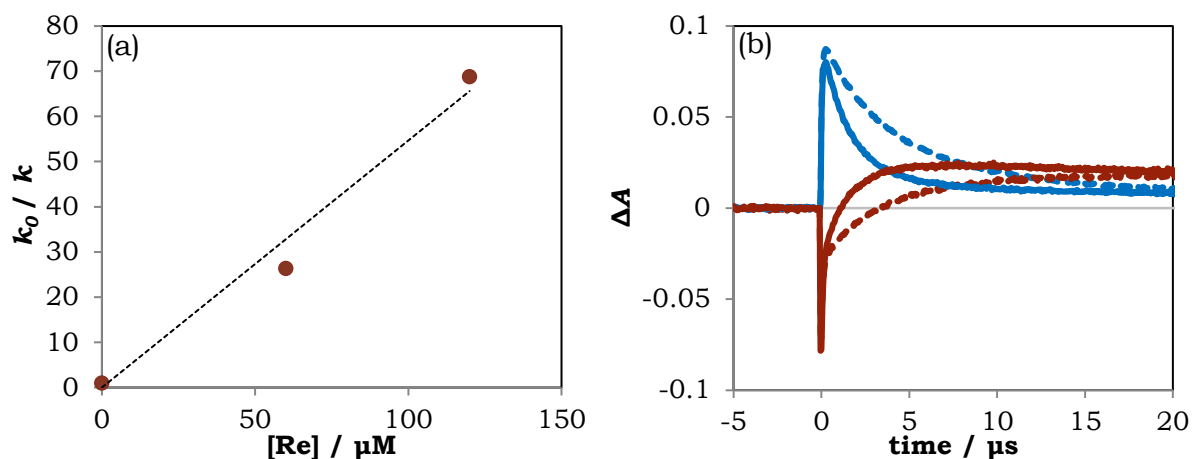


Figure 2-9. (a) Plot of normalized apparent rate constant as a function of concentration of $\text{Re}(\text{CO})_3(\text{bpy})\text{Br}$ catalyst giving a bimolecular rate constant of $4.83 \times 10^9 \text{ M}^{-1}\text{s}^{-1}$. Apparent rate constants calculated by (b) global fitting of absorption kinetics at 440 nm (red) and 525 nm (blue) of bimolecular mixture of 60 μM $\text{Ru}(\text{bpy})_3\text{Cl}_2$ photosensitizer and 60 μM (dotted line) and 120 μM (solid line) $\text{Re}(\text{CO})_3(\text{bpy})\text{Br}$ catalyst in 1:1 ACN:H₂O with 30 mM NaAsc as **ED** (Laser energy = 10 mJ, Excitation at 460 nm).

2.6. Optimization of Photocatalytic Performance

After confirming the possibility of a first photo-induced electron transfer from the photosensitizer to the catalyst, the bigger question is if the system can actually function in a photocatalytic condition, where light absorption is continuous and there is a need to accumulate electrons on the catalyst to perform the catalytic reduction of CO_2 , based on the proposed electrocatalytic mechanism in Figure 2-5. Continuous irradiation of a bimolecular mixture of **[Ru PS]** and **[Re Cat]** with a blue LED source (emission peak at 463 nm to selectively excite **[Ru PS]**) in the presence of CO_2 substrate and ED produced CO gas, confirming the photocatalytic activity of the system. As hinted by the equation of the two-electron two-proton reduction of CO_2 ,



optimizations of the photocatalytic performance were conducted by screening the electron donor and proton sources. Optimized conditions and results are summarized in Table 2-4.

Table 2-4. Optimizations for the photocatalytic reduction of CO₂ to CO.

Entry	Catalyst	Solvent	ED	n CO / μmol	TON ^[a]
1	Ru PS:Re Cat	DMF	BNAH	-	-
2	Ru PS:Re Cat	DMF:H ₂ O	Asc	-	-
3	Ru PS:Re Cat	DMF:H ₂ O	BNAH	1.2	8
4	Ru PS:Re Cat	DMF:H ₂ O	BIH	78.0	520
5	Ru PS:Re Cat	ACN:H ₂ O	BIH	0.8	5
6	Ru PS:Re Cat	DMF:TEOA	BIH	78.0	520
7	Ru PS:Re Cat	DMF:PhOH	BIH	32.6	217
8	Ru PS:Re Cat	DMF:PhOH:H ₂ O	BIH	79.7	537
9	Ru PS:Re Cat	DMF:TEOA:H ₂ O	BIH	117.6	784
10	Ru PS	DMF:H ₂ O	BIH	0.5	3
11	Re Cat	DMF:H ₂ O	BIH	5.6	37
12	-	DMF:H ₂ O	BIH	-	-

Reaction conditions: 0.15 μmol **[Ru(bpy)₃]²⁺** denoted as Ru PS, 0.15 μmol **[Re(CO)₃(bpy)Br]** denoted as Re Cat, 250 μmol **ED**, solution volume of 2.94 mL, headspace volume of 3.91 mL, light source: LED lamp with λ_{em} at 463 nm (FWHM 50 nm, 180 W/m²), 20 °C, 2 h irradiation. [a] TON calculated as moles of CO divided by moles of catalyst; No H₂ was detected by GC; bicarbonate and formate were detected by ¹³C NMR but were not quantified.

Irreversible donors such as 1-benzyl-1,4-dihydronicotinamide (**BNAH**) and 1,3-dimethyl-2-phenylbenzimidazoline (**BIH**) were much effective in photocatalytic conditions than the reversible electron donor (ie. **NaAsc**) used in transient absorption studies. This is due to the need for efficient accumulation of electrons in the catalyst to perform CO₂ reduction. Higher turnover number (TON), which is the amount of CO produced divided by the amount of catalyst used, were observed when **BNAH** was replaced by **BIH** as **ED**, as shown in Table 2-4 Entries 3 and 4 and Figure 2-10b. To explain this observation a difference in their electron donating ability could be evoked. It was already shown in Table 2-3 that there is a higher thermodynamic drive for the quenching of the excited photosensitizer by **BIH** ($\Delta G \sim -400$ meV) than **BNAH** ($\Delta G \sim -100$ meV) leading to a difference of one order of magnitude in the quenching rate.

More than this, the non-innocent nature of the accumulated oxidized species from the electron donor differentiates their donating ability. This difference was confirmed by monitoring the transient absorption kinetics at 510 nm, a wavelength where selectively formation of the reduced form of the **[Ru PS]** can be followed, as shown in Figure 2-10a. When **BNAH** was used as **ED**, **[Ru PS]^{•-}** was immediately formed upon laser flash excitation and decayed back due to back electron transfer, indicating reversibility of **BNAH** to a substantial extent on the time scale of the photophysical measurement. As such, **BNAH** acts as a single electron donor. It is reported in the literature that in a continuous light irradiation, aside from being a

one electron donor, BNAH also releases one proton upon oxidation, as shown in Figure 2-11. The resulting radical then dimerizes and accumulates in the solution.

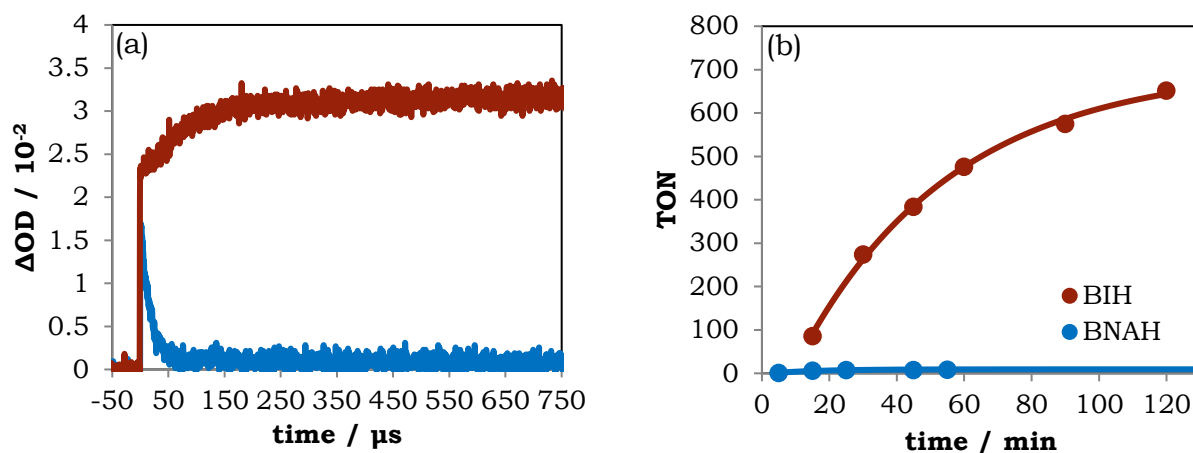


Figure 2-10. (a) Transient absorption kinetics of 13 μM $\text{Ru}(\text{bpy})_3\text{Cl}_2$ in DMF at 510 nm (indicating Ru^{I} species) in the presence of 3.74 mM **BNAH** (blue) and 3.74 mM **BIH** (red) as electron donors. (Laser energy = 6 mJ, Excitation at 460 nm, $\text{Abs}_{460} = 0.2$). (b) Effect of the nature of the **ED** (90 mM) on photocatalytic activity (50 μM $\text{Ru}(\text{bpy})_3\text{Cl}_2$, 50 μM $\text{Re}(\text{CO})_3(\text{bpy})\text{Br}$, 9:1 DMF:H₂O).

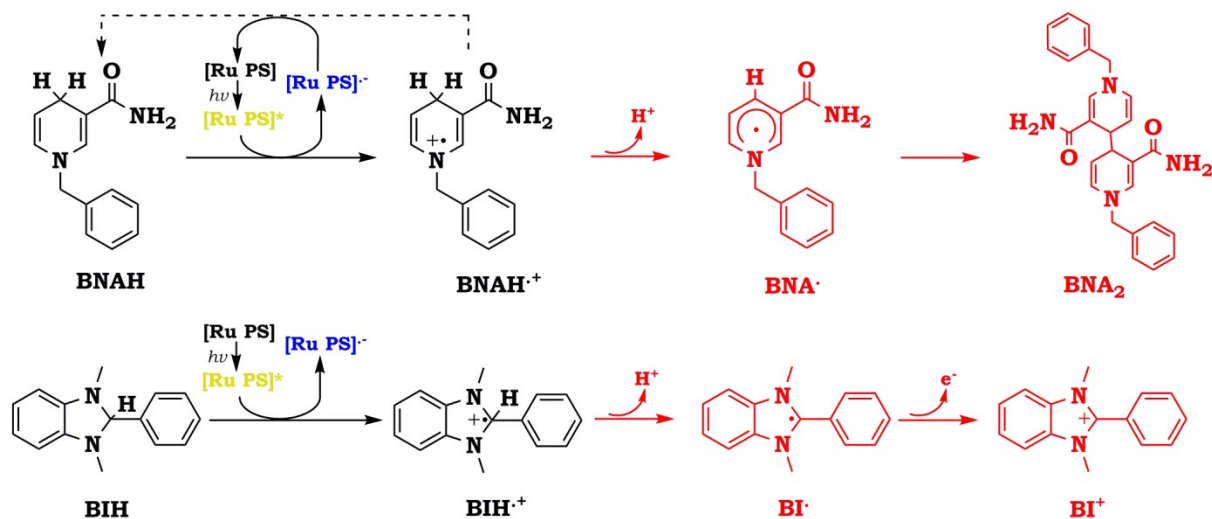


Figure 2-11. Fate of **BNAH**^[16] and **BIH**^[21] as electron donors upon interaction with excited photosensitizer.

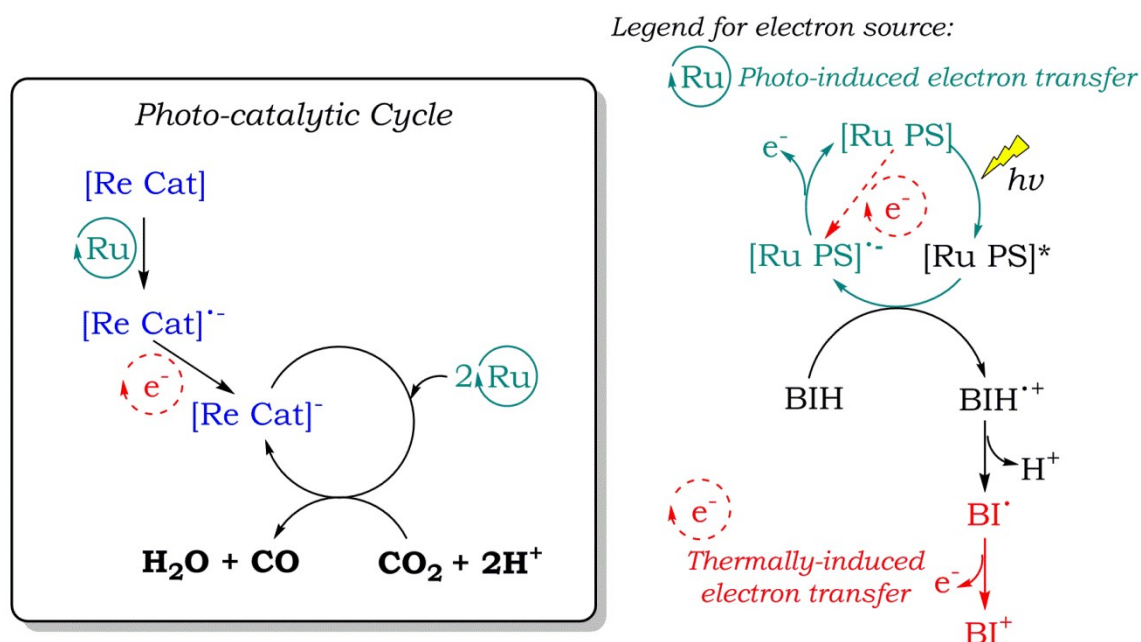


Figure 2-12. Proposed photocatalytic cycle involving **Re(CO)₃(bpy)Br** catalyst and **[Ru(bpy)₃]²⁺** photosensitizer and **BIH** as ED.

When **BIH** was used as a **ED**, however, a further increase in the concentration of **[Ru PS]•-** was observed after the end of the laser flash excitation, as shown in Figure 2-10a. This further increase at 510 nm is attributed to a thermal reduction of ground state **[Ru PS]** once the radical **BI•** is produced. As shown in Figure 2-11, **BIH** transfers one electron upon interacting with excited **[Ru PS]*** forming an oxidized species **BIH•+** which easily gives a proton, forming the radical **BI•**. This radical is highly reducing (-2.02 vs $\text{Fc}^{+/0}$)^[24] and, from a thermodynamic view point, can reduce **[Ru PS]**, as well as **[Re Cat]**. Overall, **BIH** acts as two-electron one-proton donor. However, it is important to stress, that such a reducing radical can only be accessed after an initial photo-activated electron transfer.

These results lead to the proposed photocatalytic cycle shown in Figure 2-12. **[Ru PS]•-** is produced both by the photochemical quenching of **[Ru PS]** by **BIH** and by the thermal electron transfer from **BI•** radical to **[Ru PS]**. The reducing power of **[Ru PS]•-** is sufficient to reduce **[Re Cat]** to **[Re Cat]•-** based on the thermodynamic potentials in Table 2-1 but the succeeding electron transfer steps are being provided by the reducing power of **BI•**. This rationalizes why turnover performances are much higher compared to other **EDs**. This advantage should be kept in mind because translating such photocatalytic results to photochemical devices as a final application (without sacrificial electron donors) necessitates a high reducing power in the photocathode for the catalyst to efficiently work.

Further optimization of the photocatalyst system showed that (i) DMF is a better solvent than ACN, (ii) water is a better Brønsted acid compared to phenol, and (iii) addition of a weak base like triethanolamine (TEOA) greatly improves the turnover performance of the system, as shown in Table 2-4 and Figure 2-13. Water and DMF have since been used by the group of Lehn for electro- and photo-catalytic activity of the Re catalyst^[9,25] while recent studies by the group of Ishitani showed that TEOA and TEOA-like ligands help stabilize CO₂ adduct in the Re catalyst.^[26,27]

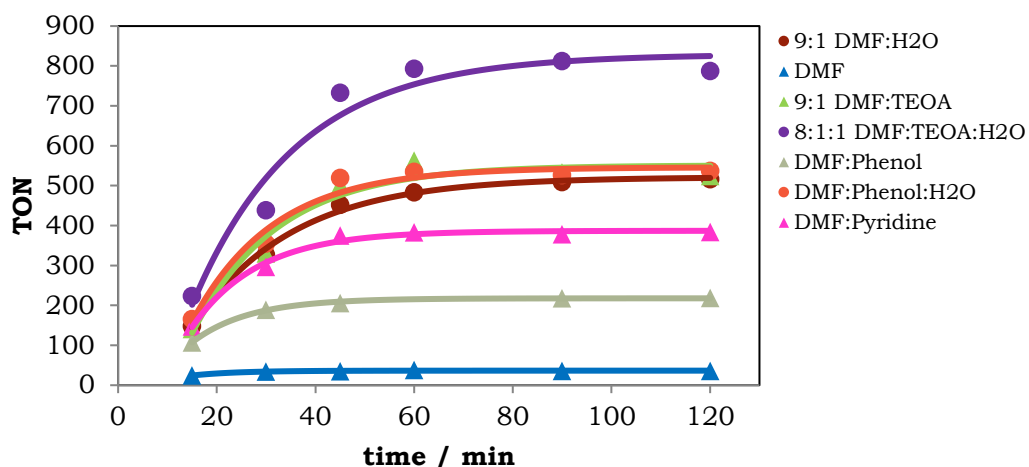


Figure 2-13. Effect of solvent conditions on the photocatalytic performance of 1:1 bimolecular mixture of 50 μM **Ru(bpy)₃Cl₂** and 50 μM **Re(CO)₃(bpy)Br** with 90 mM **BIH** as **ED**.

The activity of the photocatalyst system is, however, hindered by the stability of the photosensitizer. When the UV-visible spectrum was followed during continuous photo-irradiation, it was observed that the peak at 460 nm (corresponding to the ¹MLCT of the Ru photosensitizer) decreases, reaching to just 50% after 60 min, as shown in Figure 2-14a. This limitation due to photosensitizer degradation is confirmed by the observation that the photocatalytic activity was recovered once additional amount of photosensitizer was added to the system after the turnover number reaches a plateau, as shown in Figure 2-14b. Under the photocatalytic conditions of the study, it seems that the Ru photosensitizer is less stable than the Re catalyst, providing a clear point of improvement for future researches.

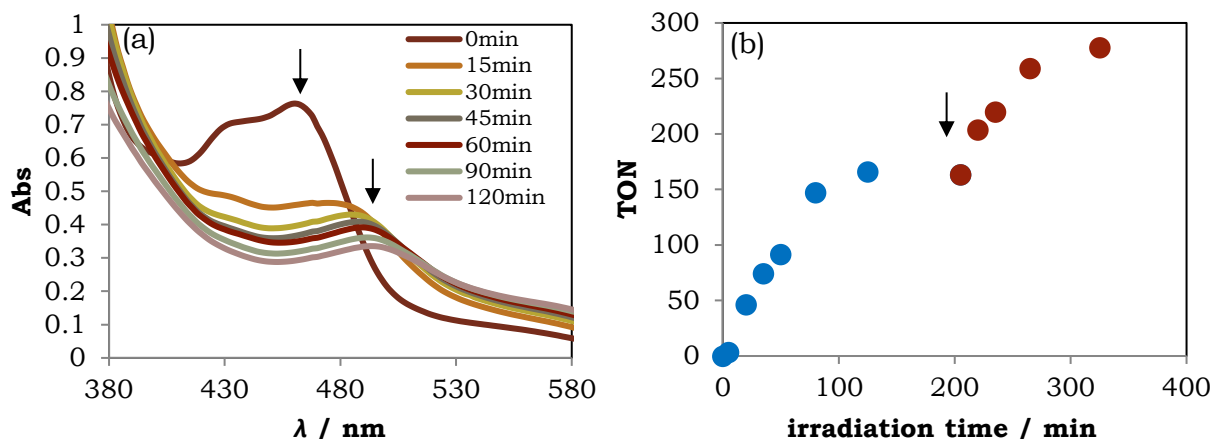


Figure 2-14. (a) UV-Vis spectra of the photocatalytic system ($\text{Ru}(\text{bpy})_3\text{Cl}_2 + \text{Re}(\text{CO})_3(\text{bpy})\text{Br} + \text{BIH}$ in 9:1 DMF:H₂O). (b) Recovery of the photocatalytic activity of the system when additional $\text{Ru}(\text{bpy})_3\text{Cl}_2$ was added after the catalytic plateau was reached.

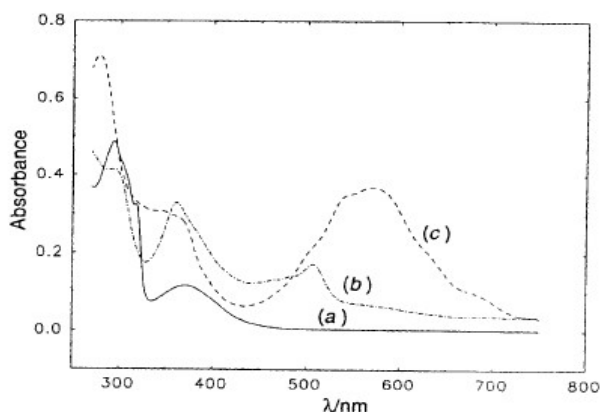
2.7. Tracking Electron Accumulation in the Re Catalyst

The results of the two previous sections (2.5 and 2.6) show that though tracking the first photo-induced electron transfer from the photosensitizer to the catalyst gives an initial assessment of the possibility of photocatalytic activity of the system, photocatalysis necessitates going beyond the first photo-induced event to identify points for performance improvement. From the mechanistic analysis in Figure 2-5 (section 2.4), the Re catalyst needs to accumulate two electrons to produce the active form able to reduce CO₂ to CO. As such, following the second reduced form of the Re catalyst would be beneficial as it would give hints to bottlenecks to its formation and interactions with a CO₂ substrate.

Based on the potentials reported in Table 2-1, once the Re catalyst is first reduced, transferring another electron from a $[\text{Ru}(\text{bpy})_2(\text{bpy}^{\bullet-})]^+$ to $[\text{Re}(\text{CO})_3(\text{bpy})\text{Br}]^{\bullet-}$ is thermodynamically uphill by ~330 meV. This initially gives a hint that though a photo-induced one-electron reduction of the Re catalyst is possible, a photo-induced two-electron accumulation is thermodynamically challenging. Justified by the successful photo-catalysis, it was attempted to further study the system by employing pump-pump-probe transient absorption spectroscopy to follow spectroscopic features of the doubly reduced species of **[Re cat]** using **NaAsc** as the reversible **ED** with **[Ru PS]**. The UV-vis spectral features of the doubly-reduced form of **[Re cat]** is distinct from the singly-reduced form based on reported spectroelectrochemical results by the group of Kirchoff,^[28] as shown in Figure 2-15 and summarized in Table 2-5, making it easier to distinguish and follow the different species.

Table 2-5. Reported UV-vis absorption peaks for the Re catalyst and its reduced forms as determined by spectroelectrochemistry in DMF.^[28]

Species	λ / nm (ϵ / M ⁻¹ cm ⁻¹)
[Re(CO)₃(bpy)Br]	294 (16100), 372 (3600)
[Re(CO)₃(bpy)Br]^{•-}	362 (11100), 509 (5700)
[Re(CO)₃(bpy)]⁻	277 (23700), 343 (17900), 570 (12100)

**Figure 2-15.** Reported absorption spectra of (a) **[Re Cat]** (solid line), (b) 1st reduced form **[Re Cat]^{•-}** (dotted line), and (c) 2nd reduced form **[Re Cat]⁻** (dashed line) in DMF, determined by UV-vis spectroelectrochemistry.^[28]

The pump-pump-probe transient absorption set-up in the Laboratory of Molecular Systems, Astrophysics, and Environment in Institut des Sciences Moléculaires d'Orsay (ISMO) was employed in collaboration with Thu Trang Than, Dr. Minh Huong Ha Thi, and Dr. Thomas Pino. Optimized concentrations of **Ru(bpy)₃Cl₂**, **Re(CO)₃(bpy)Br**, and **NaAsc** in 1:1 ACN:H₂O yielded a maximum efficiency of 26% for the production of **[Re(CO)₃(bpy)Br]^{•-}** upon single flash excitation. A second excitation is then given after 80 μ s, where the first photo-reduction event is completed. The recorded spectra were measured as shown in Figure 2-16a. Comparison of the single and double-flash measurements in Figure 2-16b show that there are no significant changes in the spectra, indicating that (i) the second excitation of **[Ru PS]** produced just another singly reduced species **[Re Cat]^{•-}** after electron transfer from **[Ru PS]^{•-}**, and (ii) there is no new species, i.e. doubly-reduced Re catalyst, formed, and as such, the two-electron accumulation in **[Re Cat]** cannot be photochemically-induced from **[Ru PS]**. This lack of formation of the doubly reduced species of the Re catalyst presumably comes from the thermodynamic barrier for a second photo-induced electron transfer as initially hypothesized. Other reasons might be the low efficiency of the first photo-reduction event, and/or competitive pathways due to possible excitation of the singly reduced Re species (since it has some absorption at the excitation wavelength). This result

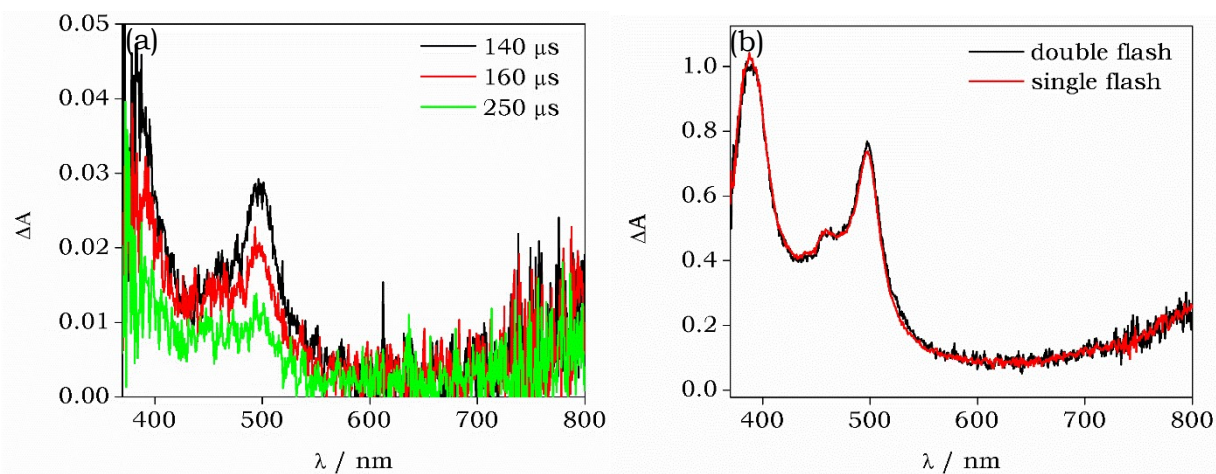


Figure 2-16. (a) Transient absorption spectra after second flash excitation (80 μs delay after the first excitation) at 460 nm of a solution containing 43 μM $\text{Ru}(\text{bpy})_3\text{Cl}_2$, 15 μM $\text{Re}(\text{CO})_3(\text{bpy})\text{Br}$, and 100 mM NaAsc . (b) Comparison of normalized transient absorption spectra taken 160 μs after each excitation.

confirms that the photocatalytic activity of the system would not efficiently occur with ascorbate as the electron donor because of the need for a species more reducing than the photo-induced $[\text{Ru PS}]^{\bullet-}$.

As proposed in the photocatalytic cycle in Figure 2-12, it seems that the drive for the second reduction of the Re catalyst comes not from the reduced photosensitizer but from the radical produced by the oxidized BIH. To confirm this proposal, steady-state photo-accumulation studies were performed to understand if the second reduced species is indeed observed, all in the absence of CO_2 and proton source to avoid any catalytic conditions. Initial investigation was done with a mixture of $[\text{Ru PS}]$ and $[\text{Re Cat}]$ with BIH as ED, but all attempts to track the spectral contributions due to the formation of the doubly-reduced Re catalyst were complicated because of the overlapping spectral signatures of both $[\text{Ru PS}]$ and $[\text{Re Cat}]$, and their respective reduced forms. As such, photo-accumulation studies were focused on just the $[\text{Re Cat}]$ with BIH as ED.

Continuous irradiation of the solution showed clear spectral signatures of initially-formed first-reduced species $[\text{Re Cat}]^{\bullet-}$, with characteristic peak at 505 nm and increased absorption at wavelengths <500 nm, followed by formation of a doubly-reduced species $[\text{Re Cat}]^-$, with characteristic absorption peak at 574 nm, as shown in Figure 2-17a. These spectral signatures clearly match those reported in Figure 2-15, and show that indeed BIH is driving the accumulation of the doubly reduced active form of the Re catalyst.

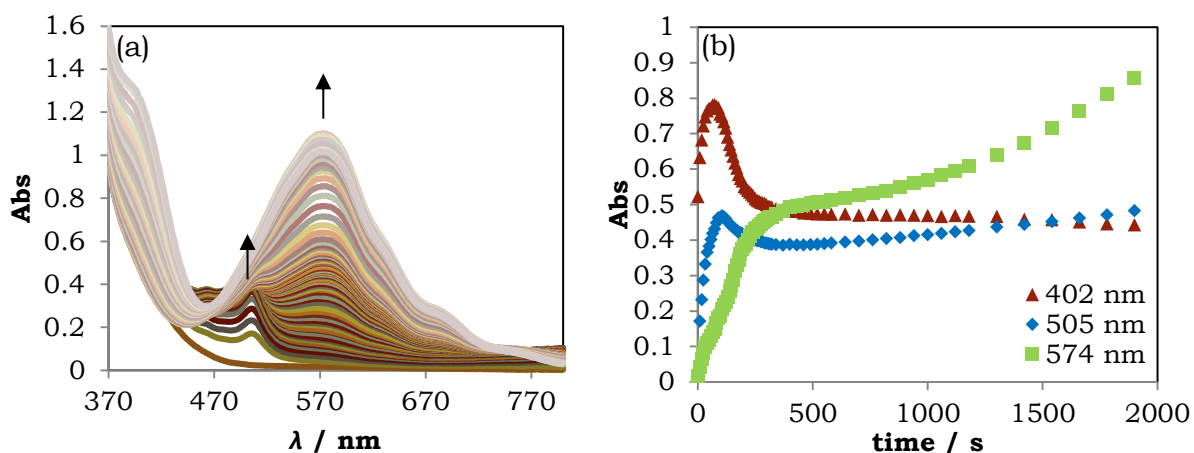


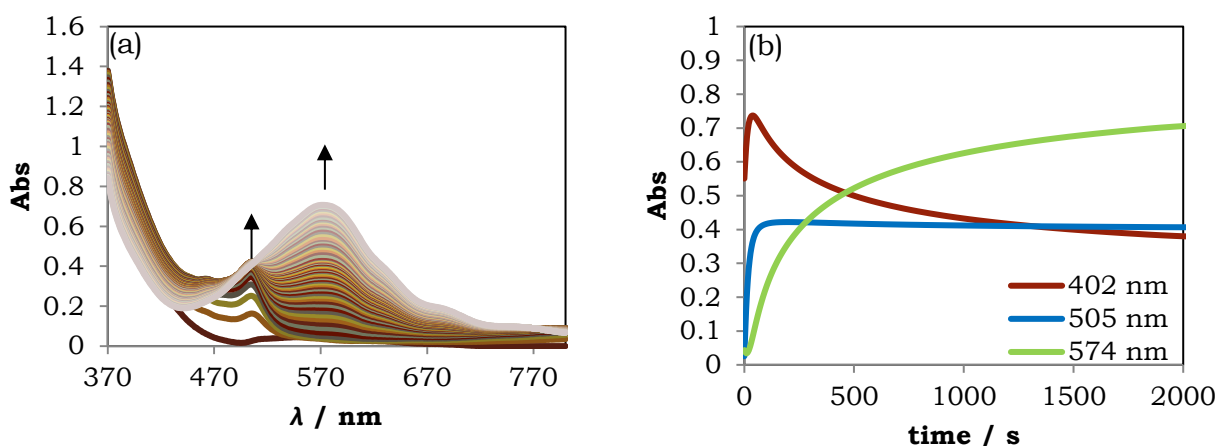
Figure 2-17. (a) Experimental absorption spectra and (b) kinetics at selected wavelengths during the photo-irradiation of 238 μM $\text{Re}(\text{CO})_3(\text{bpy})\text{Br}$ and 80 mM BIH in DMF with blue LED lamp (460 nm with FWHM of 50 nm).

The kinetics retrieved from such spectral measurements, as shown in Figure 2-17b, were then simulated with model-based fitting software, *Kintek Global Kinetic ExplorerTM*, to gain insights to the reactions steps involved in the photo-accumulation process. It is proposed in Table 2-6 that **[Re Cat]** is acting both as a photosensitizer and catalyst. Once excited, **[Re Cat]*** is effectively quenched by BIH forming the first reduced form **[Re Cat]•-** (entry 3). **BI•** radical is then responsible for a thermal electron transfer to a ground state **[Re Cat]** to accumulate the first-reduced species **[Re Cat]•-** (entry 4) which constitute a higher rate constant compared to the reductive quenching of **[Re Cat]***, possibly because of the high thermodynamic drive between the very reducing radical and the ground state **[Re Cat]**. The radical further reduces the first-reduced species **[Re Cat]•-** and results in the accumulation of the doubly-reduced species **[Re Cat]-** (entry 5), consistent with the previously described non-innocence of BIH as ED. Excitation of the first-reduced species **[Re Cat]•-** is possible in the system because of the significant absorption of the **[Re Cat]•-** species at 460 nm and it is reductively quenched to advantageously produce the doubly reduced species. This photo-induced second electron transfer step is however limited by the slow excitation step (entry 7), indicating that what dominantly drives the accumulation of the doubly reduced species **[Re Cat]-** is the thermal electron transfer from the **BI•** radical (entry 5). It is to be noted, however, that the reversible comproportionation-disproportionation step (entry 6) controls as well the accumulation of the singly and doubly reduced species.

Table 2-6. Reaction steps considered for the kinetics fitting of the results and their corresponding simulated rate constants.

Entry	Reaction	Process ^[a]	<i>k</i>
1	$[\text{Re Cat}] + h\nu \rightarrow [\text{Re Cat}]^*$	E	$3.93 \times 10^{-1} \text{ s}^{-1}$
2	$[\text{Re Cat}]^* \rightarrow [\text{Re Cat}]$	DGS	$1.05 \times 10^8 \text{ s}^{-1}$
3	$[\text{Re Cat}]^* + \text{BIH} \rightarrow [\text{Re Cat}]^{\bullet-} + \text{BI}^{\bullet} + \text{H}^+$	RQ	$0.082 \times 10^9 \text{ M}^{-1}\text{s}^{-1}$
4	$[\text{Re Cat}] + \text{BI}^{\bullet} \rightarrow [\text{Re Cat}]^{\bullet-} + \text{BI}^+$	T	$0.545 \times 10^9 \text{ M}^{-1}\text{s}^{-1}$
5	$[\text{Re Cat}]^{\bullet-} + \text{BI}^{\bullet} \rightarrow [\text{Re Cat}]^- + \text{BI}^+$	T	$0.011 \times 10^9 \text{ M}^{-1}\text{s}^{-1}$
6	$[\text{Re Cat}]^- + [\text{Re Cat}] \leftrightarrow 2 [\text{Re Cat}]^{\bullet-}$	C	$0.255 \times 10^9 \text{ M}^{-1}\text{s}^{-1}$ (k_{fwd})
		DP	$0.010 \times 10^9 \text{ M}^{-1}\text{s}^{-1}$ (k_{rev})
7	$[\text{Re Cat}]^{\bullet-} + h\nu \rightarrow [\text{Re Cat}]^{\bullet-*}$	E	$1.95 \times 10^0 \text{ s}^{-1}$
8	$[\text{Re Cat}]^{\bullet-*} \rightarrow [\text{Re Cat}]^{\bullet-}$	DGS	$6.88 \times 10^9 \text{ s}^{-1}$
9	$[\text{Re Cat}]^{\bullet-*} + \text{BIH} \rightarrow [\text{Re Cat}]^- + \text{BI}^{\bullet} + \text{H}^+$	RQ	$0.006 \times 10^9 \text{ M}^{-1}\text{s}^{-1}$

[a] Legend: E = excitation, DGS = decay to ground state, RQ = reductive quenching, T = thermal electron transfer, C = comproportionation, DP = disproportionation.

**Figure 2-18.** (a) Reconstructed absorption spectra of the photo-accumulation study as a result of the model-based fitting and (b) kinetics at selected wavelengths.

Fitting the experimental results with the reaction steps proposed in Table 2-6 indicated good agreement as shown in the similarity of the reconstructed spectra and kinetics shown in Figure 2-18. From the fitting parameters, the spectral signatures of the reaction intermediates involved in the process were reconstructed as shown in Figure 2-19, which agree very well with the spectral features of the reduced forms of the Re catalyst shown in Figure 2-15. This agreement confirms a good reliability of the proposed reaction steps in the model-based fitting. Similar reaction steps can be hypothesized with the Ru+Re photocatalyst system but with the **[Re Cat]** acting predominantly as a catalyst because most of the photons are initially absorbed by the photosensitizer **[Ru PS]**, indirectly confirming the proposed photocatalytic cycle in Figure 2-12.

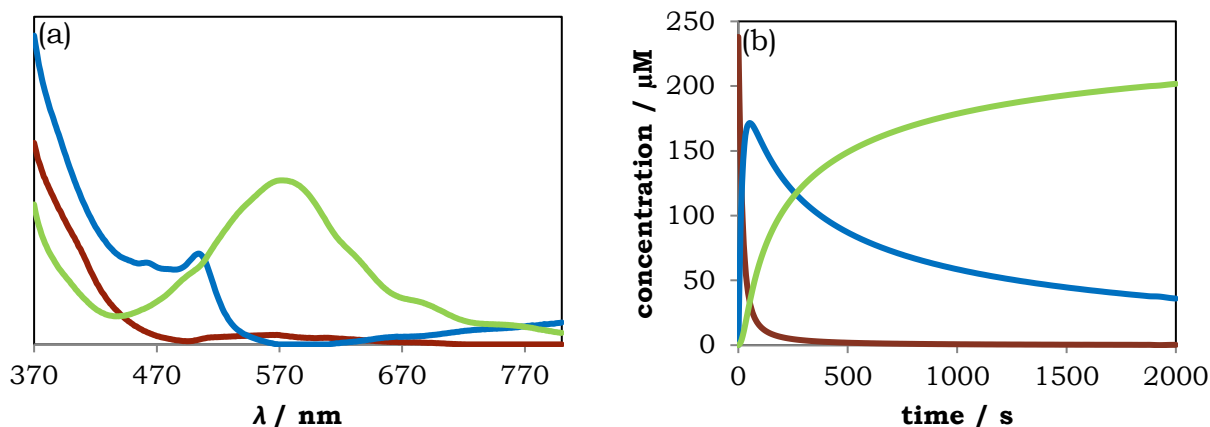


Figure 2-19. (a) Reconstructed absorption spectral signatures of **[Re Cat]** (red), 1st reduced form **[Re Cat]•-** (blue), and 2nd reduced form **[Re Cat]-** (green), and (b) their corresponding kinetics profile.

2.8. Conclusions

In conclusion, we have shown how visible light is used to reduce CO_2 to CO using a photocatalyst system comprising of a rhenium triscarbonyl bipyridyl catalyst **[Re(CO)₃(bpy)Br]** and a ruthenium trisbipyridine photosensitizer **[Ru(bpy)₃]²⁺**. Mechanistic investigation on the electrocatalytic cycle of the catalyst was validated by cyclic voltammetry and IR spectroelectrochemistry, and shows that two electrons are to be accumulated in the catalyst to form the active form that reduces CO_2 . Transient absorption spectroscopy was employed to track a first photo-induced electron transfer from the excited photosensitizer to the catalyst even though there is only a 20 meV thermodynamic drive and a close-to-diffusion-limited bimolecular electron transfer rate was determined. Optimized photocatalytic conditions are beyond the first photo-induced electron transfer event, however, as higher turnover numbers were achieved with 1,3-dimethyl-2-phenylbenzimidazole (**BIH**) as the most efficient electron donor because of (i) its high quenching efficiency of the excited state of the photosensitizer and (ii) the production of a non-innocent reducing **BI•** radical, that can provide the much needed two-electron accumulation in the catalyst by thermal electron transfer. This was confirmed by (i) the observation of accumulation of the doubly reduced species of the Re catalyst upon photo-accumulation studies with **BIH** as **ED** and (ii) the lack of photo-induced two-electron accumulation in the Re catalyst from the Ru photosensitizer using **NaAsc** as a reversible electron donor.

The results of this section give a precaution that the advantage of the two-electron donating ability of **BIH** should be critically handled as translation to photochemical devices, where sacrificial electron sources are absent and electrons

are ideally coming from an oxidation catalysis, would require a similar very reducing power like the **BI**[•] radical. In addition, the limitations of the Ru+Re photocatalyst system show that to improve the system, one must employ (i) a stable photosensitizer, and (ii) a stable and efficient catalyst where the thermodynamic potentials are matched to give the active form of the catalyst necessary for CO₂ reduction.

Bibliography

- [1] B. P. Sullivan, C. M. Bolinger, D. Conrad, W. J. Vining, T. J. Meyer, *J. Chem. Soc., Chem. Commun.* **1985**, 0, 1414–1416.
- [2] G. J. Stor, F. Hartl, J. W. M. van Outersterp, D. J. Stufkens, *Organometallics* **1995**, 14, 1115–1131.
- [3] E. E. Benson, M. D. Sampson, K. A. Grice, J. M. Smieja, J. D. Froehlich, D. Friebel, J. A. Keith, E. A. Carter, A. Nilsson, C. P. Kubiak, *Angew. Chem. Int. Ed* **2013**, 52, 4841–4844.
- [4] J. M. Smieja, E. E. Benson, B. Kumar, K. A. Grice, C. S. Seu, A. J. M. Miller, J. M. Mayer, C. P. Kubiak, *Proc. Natl. Acad. Sci. USA* **2012**, 109, 15646–15650.
- [5] J. A. Keith, K. A. Grice, C. P. Kubiak, E. A. Carter, *J. Am. Chem. Soc.* **2013**, 135, 15823–15829.
- [6] S. Sinha, J. J. Warren, *Inorg. Chem.* **2018**, 57, 12650–12656.
- [7] F. P. A. Johnson, M. W. George, F. Hartl, J. J. Turner, *Organometallics* **1996**, 15, 3374–3387.
- [8] J. Hawecker, J.-M. Lehn, R. Ziessel, *Helv. Chim. Acta.* **1986**, 69, 1990–2012.
- [9] J. Hawecker, J.-M. Lehn, R. Ziessel, *J. Chem. Soc., Chem. Commun.* **1983**, 536–538.
- [10] B. Gholamkhash, H. Mametsuka, K. Koike, T. Tanabe, M. Furue, O. Ishitani, *Inorg. Chem.* **2005**, 44, 2326–2336.
- [11] S. Sato, K. Koike, H. Inoue, O. Ishitani, *Photochem. Photobiol. Sci.* **2007**, 6, 454–461.
- [12] T. L. Easun, W. Z. Alsindi, M. Towrie, K. L. Ronayne, X.-Z. Sun, M. D. Ward, M. W. George, *Inorg. Chem.* **2008**, 47, 5071–5078.
- [13] Z.-Y. Bian, K. Sumi, M. Furue, S. Sato, K. Koike, O. Ishitani, *Dalton Trans.* **2009**, 983–993.
- [14] K. Koike, S. Naito, S. Sato, Y. Tamaki, O. Ishitani, *J. Photochem. Photobiol. A* **2009**, 207, 109–114.
- [15] Z.-Y. Bian, S.-M. Chi, L. Li, W. Fu, *Dalton Trans.* **2010**, 39, 7884.
- [16] Y. Tamaki, K. Watanabe, K. Koike, H. Inoue, T. Morimoto, O. Ishitani, *Faraday Discuss.* **2012**, 155, 115–127.
- [17] S. Meister, R. O. Reithmeier, A. Ogrodnik, B. Rieger, *ChemCatChem* **2015**, 7, 3562–3569.
- [18] A. Nakada, K. Koike, K. Maeda, O. Ishitani, *Green Chem.* **2015**, 18, 139–143.
- [19] Y. Yamazaki, H. Takeda, O. Ishitani, *J. Photochem. Photobiol. C* **2015**, 25, 106–137.
- [20] L. Frayne, N. Das, A. Paul, S. Amirjalayer, W. J. Buma, S. Woutersen, C. Long, J. G. Vos, M. T. Pryce, *ChemPhotoChem* **2018**, 2, 323–331.
- [21] Y. Tamaki, K. Koike, T. Morimoto, O. Ishitani, *J. Catal.* **2013**, 304, 22–28.
- [22] K. Kalyanasundaram, *Coordination Chemistry Reviews* **1982**, 46, 159–244.

- [23] A. Juris, V. Balzani, F. Barigelletti, S. Campagna, P. I. Belser, A. Von Zelewsky, *Coordination Chemistry Reviews* **1988**, *84*, 85–277.
- [24] X.-Q. Zhu, M.-T. Zhang, A. Yu, C.-H. Wang, J.-P. Cheng, *J. Am. Chem. Soc.* **2008**, *130*, 2501–2516.
- [25] J. Hawecker, J.-M. Lehn, R. Ziessel, *J. Chem. Soc., Chem. Commun.* **1984**, *0*, 328–330.
- [26] T. Morimoto, T. Nakajima, S. Sawa, R. Nakanishi, D. Imori, O. Ishitani, *J. Am. Chem. Soc.* **2013**, *135*, 16825–16828.
- [27] H. Koizumi, H. Chiba, A. Sugihara, M. Iwamura, K. Nozaki, O. Ishitani, *Chem. Sci.* **2019**, DOI 10.1039/C8SC04389B.
- [28] Y. F. Lee, J. R. Kirchhoff, R. M. Berger, D. Gosztola, *J. Chem. Soc., Dalton Trans.* **1995**, *0*, 3677–3682.

Chapter 3

Designing Catalysts:

First Coordination Sphere Modifications

3.1. Introduction

The urgent need to decarbonize the current energy mix because of global warming has accelerated research in the development of catalysts that can both utilize renewable solar energy and CO₂ and transform them into energy vectors that can be stored, transported, and used upon demand. Common forms would include the development of electrocatalysts and coupling them with photovoltaics harnessing solar energy, or the development of a direct photocatalytic system. Both forms still require the development of efficient and stable catalysts. A variety of catalyst design strategies have been reported for the homogenous reduction of CO₂ as discussed in Chapter 1 and an interesting approach is the development of bio-inspired catalysts.

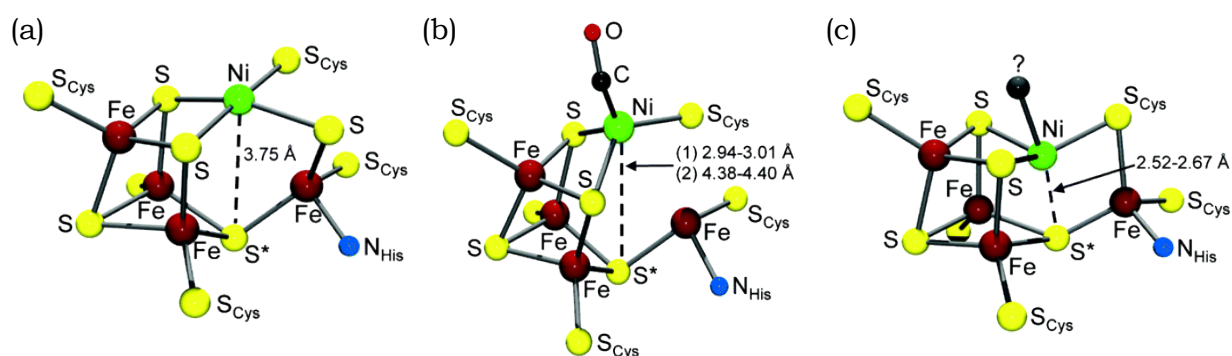


Figure 3-1. Crystallographic structures of the C-clusters in enzymes from three organisms: (a) dithionite-reduced *C. hydrogenoformans* CODH II at 1.1 Å, (b) CO-treated *M. thermoacetica* CODH at 1.9 Å, and (c) *R. rubrum* CODH at 2.8 Å. Figures taken from ref [1].

In nature, CO dehydrogenases (CODHs) are the only enzyme that catalyzes the reversible reduction of CO₂ to CO. The [NiFe] class of CODH derived from anaerobic bacteria and archaea exhibit turnover frequencies as high as 40000 s⁻¹ for the oxidation of CO and 45 s⁻¹ for CO₂ reduction.^[2] These enzymes operate near the thermodynamic potential of the CO₂/CO couple, indicating a significantly low overpotential compared to synthetic CO₂ reduction catalysts. Crystallographic studies show that the C-cluster active site of the enzyme generally consists of Ni and Fe metal centers bridged by a [Fe₃S₄] cluster that fix the positions of these two metal centers in close proximity, as shown in Figure 3-1. Various organisms possess enzymes which display different coordination around the nickel atom with a planar NiS₄ coordination in *Carboxydotherrmus hydrogenoformans* CODH II (Figure 3-1a) or a distorted tetrahedral one in *Moorella thermoacetica* CODH (Figure 3-1b)

and *Rhodospirillum rubrum* CODH (Figure 3-1c)^[3] with varying distances between the Ni atom and the axially-positioned S* atom from the cubanoid [Fe₃S₄] cluster.^[1]

Though several of these structures display partial atom occupancies and disordered positions, the described core structural features are still maintained. The most accurate definition of the biologically-active structure was reported in 2007 by the group of Dobbek as shown in Figure 3-2a where the coordinatively unsaturated Ni^{II} species binds three S ligands in an apparent T-shaped environment.^[4] Upon addition of CO₂ to this reduced state, CO₂ binds to the redox active Ni^{II} acting as a η^1 OCO ligand and completes the square planar coordination geometry found for Ni ions, as shown in Figure 3-2b. The change from the distorted T-shaped to the square planar coordination at the Ni ion only induces minor changes in the geometry of the cluster as observed in the superposition of the structures in Figure 3-2c. In the CO₂ adduct, Ni acts as Lewis base while the nearby Fe1 acts as Lewis acid that stabilizes the negative partial charge on O1 of CO₂.^[5] The [Fe₃S₄] cubanoid cluster provides a metal-sulfur frame in which Ni and Fe1 are held in place and serves as an electronic buffer to compensate for the electronic changes during the catalytic cycle. The low reorganization energy arising from the small structural changes of the active site during the catalytic cycle ensures the high efficiency and stability of the enzyme.

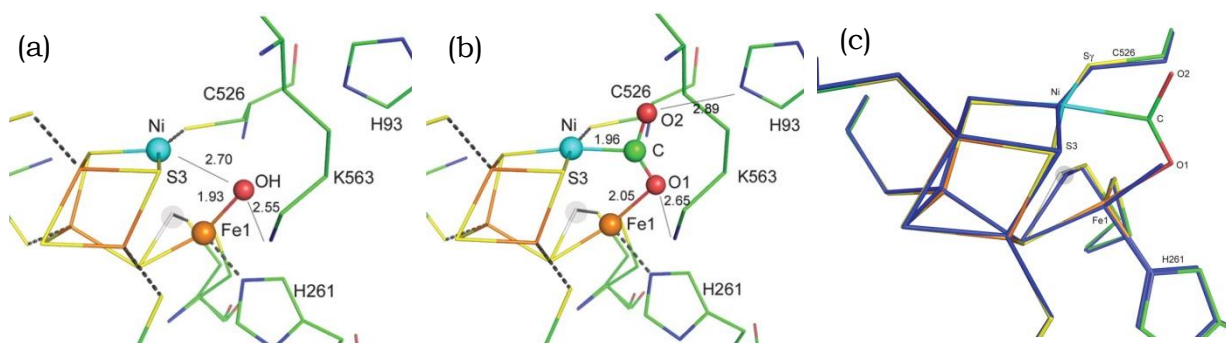


Figure 3-2. Crystallographic data on the reduced state (-600 mV *vs* SHE) of the active site of *C. hydrogenoformans* CODH II in the (a) absence and (b) presence of CO₂, and (c) the corresponding superposition of the structures. Figures taken from ref [4].

Closest synthetic models of the CODH C-cluster have been extensively investigated by the group of Holm even before the advent of the protein structures. They successfully synthesized the first [NiFe₃S₄] cubane model,^[6] complex 1 in Figure 3-3. Other [NiFe₃S₄] complexes consist of the closely-resembling square

planar Ni^{II} species as shown by the Ni-S₂P₂ type^[1,7] in complex 2 and Ni-S₄ type^[8] in Complex 3. However, no activity of these complexes for CO₂ reduction was reported.

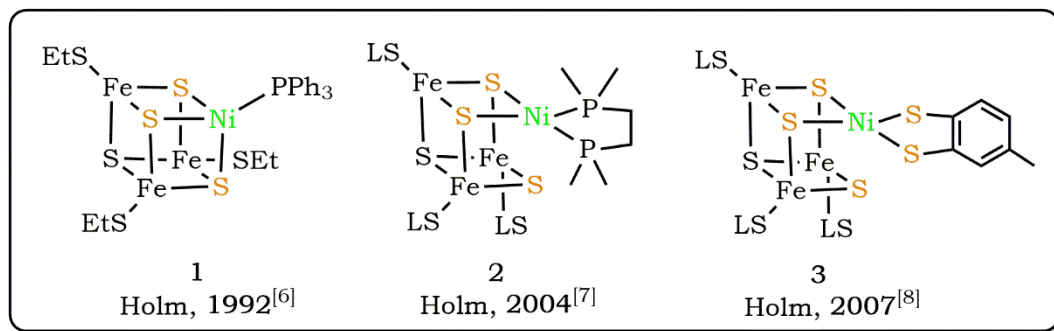


Figure 3-3. Structural mimics of the Ni-centered C cluster site of CODH.

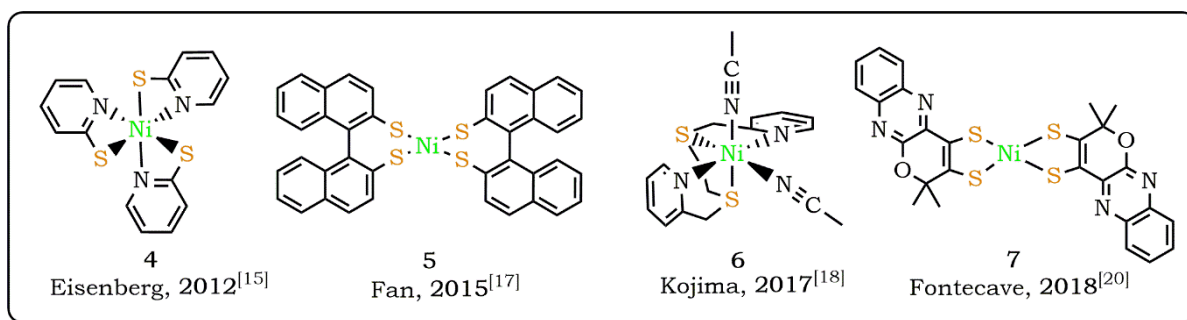


Figure 3-4. Some notable functional models of sulfur-rich Ni-centered catalysts able to perform proton reduction to dihydrogen (complexes 4-5), CO₂ reduction to CO (complex 6), and CO₂ reduction to HCOOH (complex 7).

Functional models mimicking the sulfur-rich environment around the metal centers are rare for CO₂ reduction but were extensively investigated for hydrogenase mimics for proton reduction.^[9] Functional models of metal-sulfur enzymes have been pioneered by the group of Sellmann^[10] leveraging the unique electronic flexibility of sulfur ligands (such as sulfides, thiolates, and thioethers) which can accommodate both hard and soft ancillary ligands. Synthetic analogues of the [NiFe] hydrogenase have been well-reviewed by Pickett^[11] and Bouwman^[12] showing various macrocyclic and acyclic nickel complexes with sulfur ligands, as well as mixed-donor ligand structures containing oxygen, phosphorus, and nitrogen donor atoms. In 2011, the group of Eisenberg and Holland has reported the photocatalytic activity of a Ni-N₂P₂ type Dubois' electrocatalyst^[13] when coupled with a Ru or eosin Y photosensitizer (PS) and using ascorbate as electron donor (ED).^[14] A Ni-N₃S₃ type nickel pyridinethiolate catalyst, shown as complex 4 in Figure 3-4, was also

reported by the same group for the photocatalytic H₂ evolution in the presence of fluorescein as the PS and triethylamine as the ED. One of the coordinating N atoms was proposed to be hemilabile and to play the role of proton relay during the formation of the H-H bond.^[15,16] This role was attributed to an S atom in the photocatalytically active nickel complexes with bidentate dithiolenes (Ni-S₄ type shown in complex 5) reported by the group of Fan^[17] Only recently, the group of Kojima published a Ni complex bearing thioethers in the form of tetradentate N₂S₂ ligands (complex 6) that showed photo-catalytic activity towards CO₂ reduction to CO with a Ru PS and 1,3-dimethyl-benzoimidazole (BIH) as ED.^[18] A later study then showed that the same catalyst is active towards photocatalytic proton reduction when done in an ascorbate-containing acetonitrile solution.^[19] The group of Fontecave has similarly investigated sulfur-rich ligands by synthesizing Ni(bisdithiolene) catalysts with the Ni-S₄ type of coordination (complex 7) which are capable of electrocatalytically reducing CO₂ to formate with an Hg/Au working electrode.^[20,21] These dithiolene ligands mimic the natural molybdopterin cofactor present in the active site of formate dehydrogenase. The same group has also reported a molybdenum complex consisting of similar dithiolene ligands which showed a photocatalytic activity for the reduction of CO₂ to formate when coupled to a Ru PS and using BIH as ED.^[22] These few reports on Ni-centered CO₂ reduction catalysts containing a sulfur-rich environment seem promising for investigation of bio-inspired catalyst design.

3.2. Objectives

Inspired by the sulfur-rich environment found in the Ni-centered active site of CO dehydrogenase, we employed a comparative study on the catalytic activities of Ni (II) complexes by modifying the primary coordination sphere of the reported **Ni-N₂S₂** catalyst, with the structures shown in Figure 3-5. Specifically, this chapter aims at:

- investigating how (i) the extra thioether donor in a pentadentate **Ni-N₂S₃** catalyst compared to the tetradentate **Ni-N₂S₂**, and (ii) replacement of the pyridine donors in **Ni-N₂S₃** with phosphine donors in **Ni-P₂S₃**, affect the electrocatalytic reduction activity

- investigating the differences in the photocatalytic CO₂ and proton reduction activities of **Ni-N₂S₂** and **Ni-N₂S₃** and mechanistically follow the intermediate species by time-resolved UV-Vis and X-ray absorption spectroscopy.

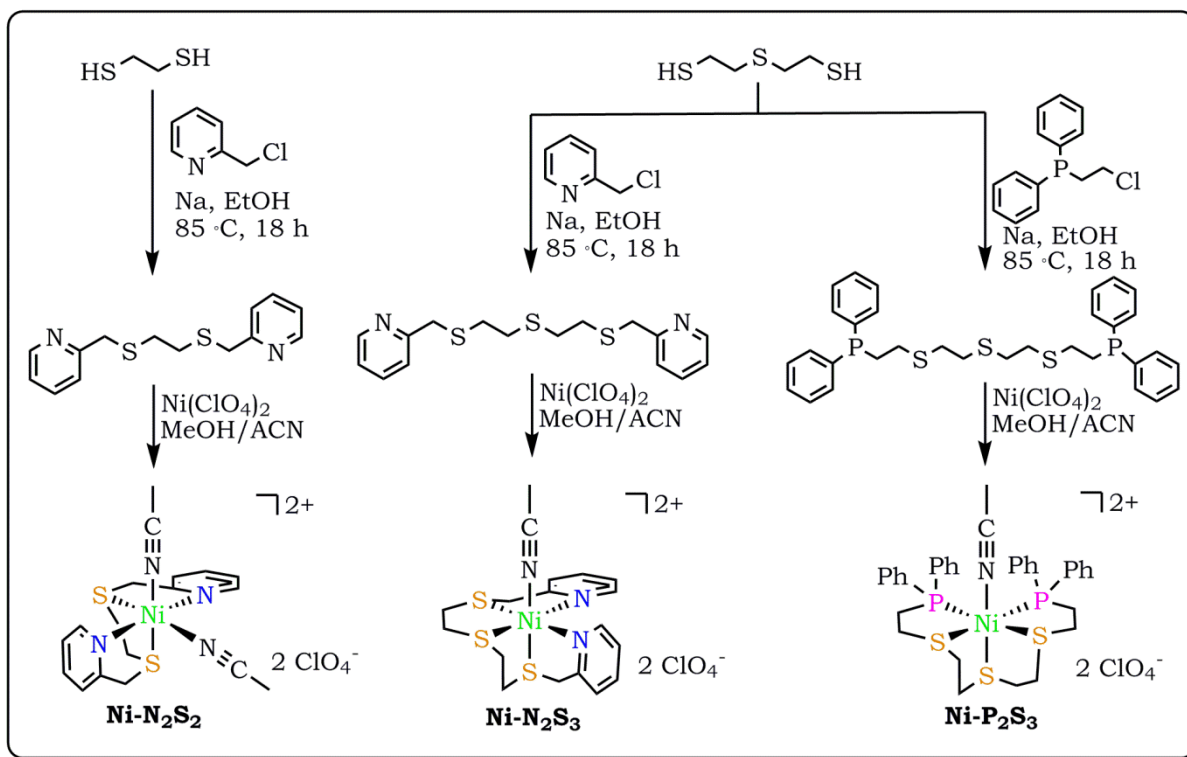


Figure 3-5. Synthesis of the catalysts **Ni-N₂S₂**, **Ni-N₂S₃**, and **Ni-P₂S₃**.

3.3. Syntheses and Structural Characterization

The pentadentate ligands **N₂S₃** and **P₂S₃**, as well as the tetradentate **N₂S₂** ligand were synthesized following some modifications of reported methods.^[23,24] As shown in Figure 3-5, reaction of 2-picolyl chloride with 1,2-ethanedithiol yields the **N₂S₂** ligand, while reaction of 2-picolyl chloride or 2-chloroethyl diphenylphosphine with 2,2'-thiodiethanethiol yields the **N₂S₃** and **P₂S₃** ligands, respectively. These ligands were characterized by proton NMR and mass spectrometry measurements as shown in the supplementary information in Annex. Nickel (II) complexes were then obtained by complexation of the ligands with a Ni perchlorate salt in methanol/acetonitrile solution resulting respectively in **Ni-N₂S₂**, **Ni-N₂S₃**, and **Ni-P₂S₃**, as confirmed by mass spectrometry measurements.

Single crystals suitable for X-ray diffraction analysis were obtained by slow diffusion of ethyl acetate in an acetonitrile (ACN) solution of the complexes. As

shown in Figure 3-6, X-ray structures of the **Ni-N₂S₂** and **Ni-N₂S₃** complexes show a hexacoordinated Ni in a slightly distorted octahedral geometry. In both cases, the central metal is coordinated by two aromatic nitrogens from the pyridines and three or two sulfur atoms from the thioethers. The first coordination sphere is completed by one (for **Ni-N₂S₃**), or two (for **Ni-N₂S₂**) nitrogens from acetonitrile solvent. As shown in Table 3-1, the bond angles in **Ni-N₂S₃** are more deviated from the ideal 90° compared to **Ni-N₂S₂**, indicating a greater distortion of the coordination sphere in **Ni-N₂S₃**. The bond with coordinated axial S1 atom from thioether is more elongated in **Ni-N₂S₃** than in **Ni-N₂S₂** and is even longer than the bond length of coordinated ACN solvent, indicating a weak coordination bond for the S1 atom. This is an indication that S1 may be relatively labile in solution for **Ni-N₂S₃**.

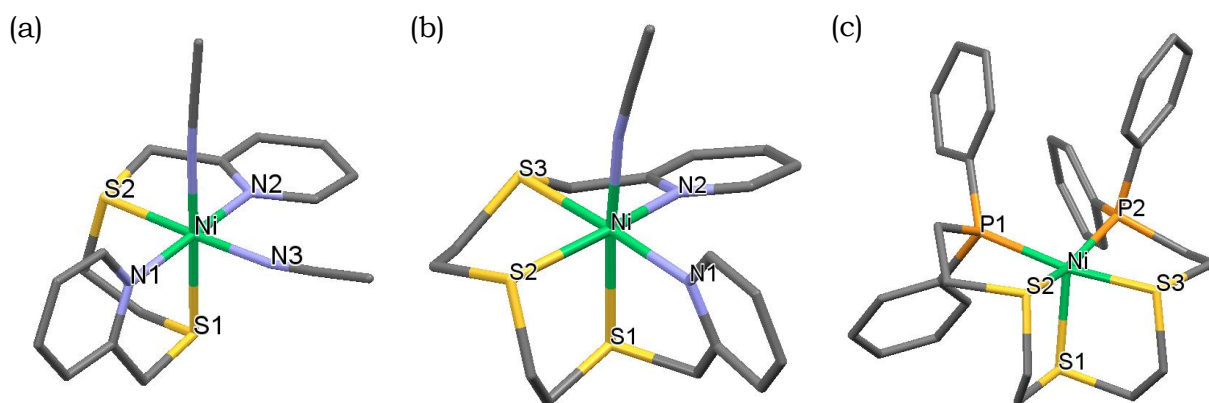


Figure 3-6. Capped sticks representation of the X-ray crystal structures of (a) **Ni-N₂S₂**, (b) **Ni-N₂S₃**, and (c) **Ni-P₂S₃**. Counter anions and hydrogen atoms are omitted for clarity.

Unlike these two complexes, **Ni-P₂S₃** maintains a slightly distorted square pyramidal geometry. The absence of any coordinated solvent in **Ni-P₂S₃** may come from the bulkiness of the nearby phenyl rings and might indicate a possible limited access as well for any substrate. The distance between the nickel atom and phosphorous atom from the phosphines in **Ni-P₂S₃** are much longer compared to the distance between the nickel atom and nitrogen atom of the pyridines in **Ni-N₂S₂** and **Ni-N₂S₃**. Metal-phosphine complexes are known to display π backbonding as the phosphine ligands can accept the electron density from the metal. These electrons then populate the Ni-P σ^* antibonding orbital lengthening the Ni-P distance. This observation could be an initial indication that compared to the

pyridine-based **Ni-N₂S₂** and **Ni-N₂S₃**, phosphine-based **Ni-P₂S₃** can greatly stabilize lower oxidation states of the Ni metal.

Table 3-1. Selected bond lengths and angles of the crystal structures of the complexes shown in Figure 3-6.

Parameter	Ni-N₂S₂	Ni-N₂S₃	Ni-P₂S₃
Ni-S1, Å	2.4073(3)	2.4419(4)	2.4220(7)
Ni-S2, Å	2.4108(5)	2.4157(3)	2.2643(7)
Ni-S3, Å	-	2.3860(4)	2.2854(6)
Ni-N1 / Ni-P1, Å	2.080(1)	2.099(1)	2.2146(7)
Ni-N2 / Ni-P2, Å	2.102(2)	2.0659(9)	2.2001(7)
Ni-N(ACN)	2.061(1)	2.065(1)	-
	2.052(1)		
∠S1-Ni-S2, °	89.40(1)	85.58(1)	90.14(2)
∠N1/P1-Ni-S2, °	89.59(4)	94.03(3)	86.92(2)

3.4. Electrochemical Characterization

The redox behavior of the modified catalysts was characterized by cyclic voltammetry (CV) as shown in Figure 3-7. It can be observed that the first reduction peak, attributed to the reduction of Ni^{II} to Ni^I, shifts anodically going from **Ni-N₂S₂** to **Ni-N₂S₃** and to **Ni-P₂S₃**, as seen in Table 3-2. The addition of the extra thioether in **Ni-N₂S₃** resulted in a potential shift of 180 mV compared to **Ni-N₂S₂**. This was similarly observed in an earlier systematic study by the group of Adhikary on Ni complexes bearing N₂S_x ligands (where x represents increasing number of sulfur donors).^[23] Thioethers are considered as soft ligands, indicating high polarizability of the electron density of the ligand. Its availability in a mixed coordination environment (with hard ligands like pyridine) stabilizes the Ni^I state.^[25] A much greater stabilization was achieved when the pyridines are replaced with the softer phosphine ligands, achieving an anodic shift of 240 mV when comparing **Ni-N₂S₃** and **Ni-P₂S₃**. This even resulted in the reversibility of the reduction peaks in **Ni-P₂S₃**.

A second irreversible reduction is observed at -1.47 V (*vs* Fc⁺⁰) for **Ni-N₂S₂** and -1.56 V for **Ni-N₂S₃**. Contrary to the anodic shift observed for the first reduction

of **Ni-N₂S₃** compared to **Ni-N₂S₂**, a 90 mV cathodic shift is observed for this second wave. This irreversible reduction wave was attributed by the group of Kojima to the Ni^{I/0} couple which involves a large structural change from an octahedral Ni^I complex having a d⁹ electronic configuration to a tetrahedral Ni⁰ complex with a d¹⁰ configuration. As such, the change from a tetradentate ligand structure in **Ni-N₂S₂** to the sterically hindered pentadentate ligand structure in **Ni-N₂S₃** can explain the cathodic shift in the second reduction process. However, the reversibility is gained, and an anodic shift of 70 mV is observed when the pyridines are replaced by phosphines in **Ni-P₂S₃**. This is indicative of the fact that even though **Ni-N₂S₃** and **Ni-P₂S₃** share the same pentadentate configuration, the high polarizability of the phosphine ligands in tandem with the thioether donors can stabilize the Ni⁰ state. The observed shifts for the second reduction peak are not as significant however, as the shifts in the first reduction peak.

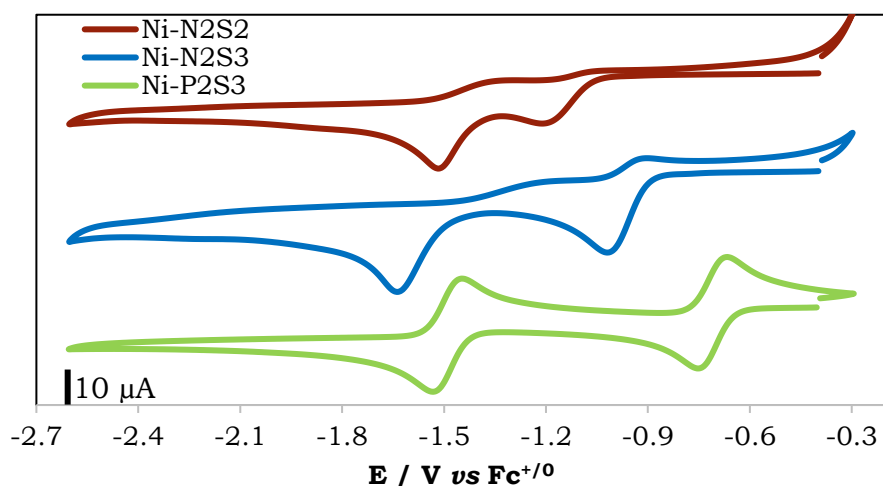


Figure 3-7. Cyclic voltammograms of 1 mM of catalyst **Ni-N₂S₂** (red), **Ni-N₂S₃** (blue), and **Ni-P₂S₃** (green) in Ar-degassed ACN containing 0.1 M TBAP.

Table 3-2. Reduction potentials of the catalysts **Ni-N₂S₂**, **Ni-N₂S₃**, and **Ni-P₂S₃** in ACN determined from the CVs in Figure 3-7.

Complex	E / V vs Fc ^{+/0}	
	1 st reduction	2 nd reduction
Ni-N₂S₂	-1.133	-1.465*
Ni-N₂S₃	-0.952	-1.556*
Ni-P₂S₃	-0.710	-1.484

*For irreversible peaks, potentials are reported from the half wave point.

The CVs of the modified catalysts under a CO₂-saturated solution in the presence of water as a proton source was recorded to determine their electrocatalytic activity towards CO₂ reduction. As shown in Figure 3-8, there are no significant current enhancements observed for all catalysts. For the reported **Ni-N₂S₂**, a small current enhancement is observed just before the second reduction peak, while it is observed only after the second reduction in **Ni-N₂S₃** and **Ni-P₂S₃**. Kojima has proposed that such Ni catalysts need to be reduced to their Ni⁰ state to be active for CO₂ reduction.^[18] Comparing the CVs of these catalysts in Figure 3-8d, it shows that an earlier onset in current enhancement is observed for **Ni-N₂S₂**, though a greater intensity is observed at more negative potentials for the **Ni-N₂S₃**. Even though much greater stabilization of lower oxidation states was achieved by **Ni-P₂S₃**, it doesn't seem to show any improved CO₂ reduction activity.

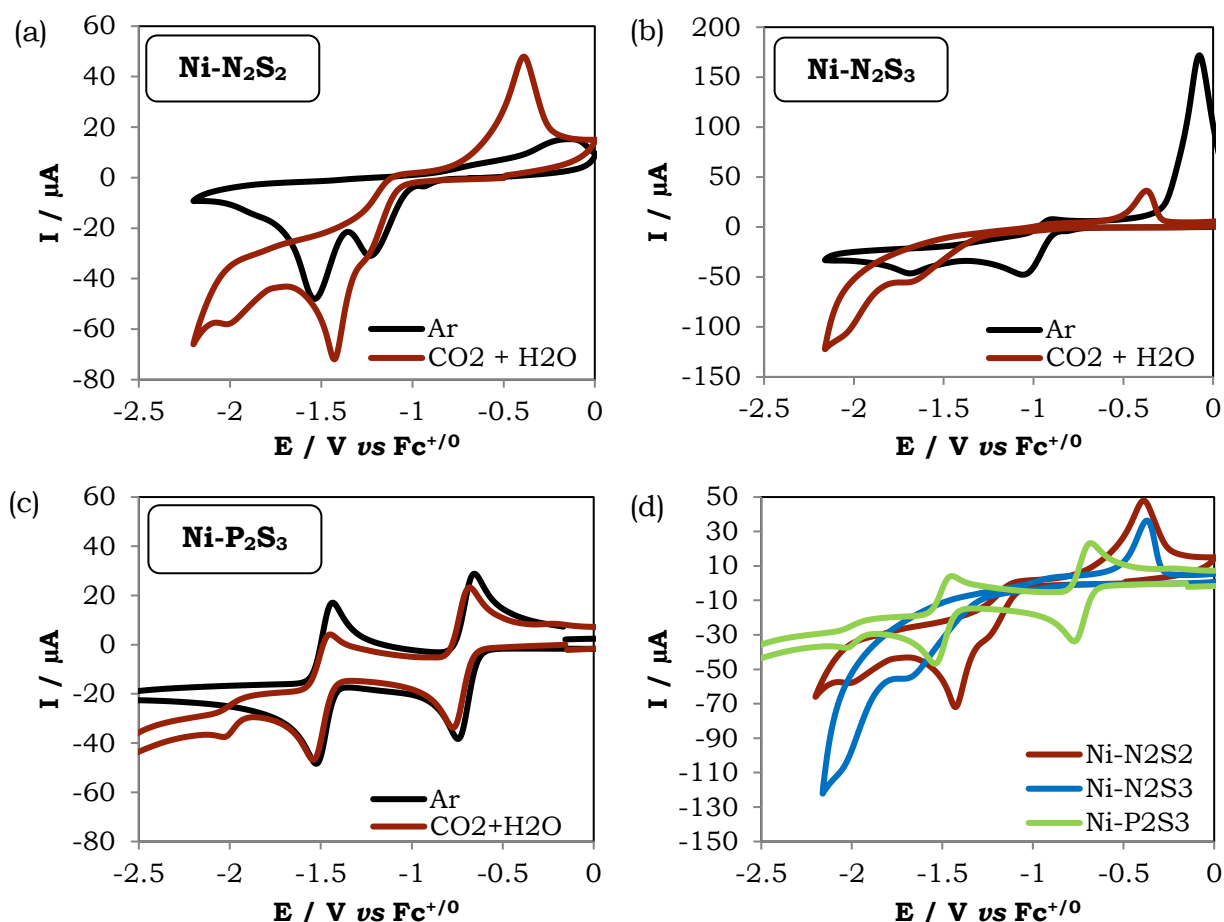


Figure 3-8. Cyclic voltammograms of 1 mM of catalyst (a) **Ni-N₂S₂**, (b) **Ni-N₂S₃**, and (c) **Ni-P₂S₃** in the absence (black) and presence of CO₂ with 5.5 M H₂O (red) in ACN containing 0.1 M TBAP. (d) Comparison of the CVs of the catalysts under catalytic conditions (CO₂ + 5.5 M H₂O).

It was observed though that the modified catalysts, in the presence of acidic proton sources but absence of any CO_2 substrate, showed some proton reduction activity. This was similarly reported by the group of Kojima when they later published the proton reduction activity of the **Ni-N₂S₂** catalyst.^[19] As shown in Figure 3-9, the CVs of the modified catalysts in the presence of acetic acid showed catalytic current enhancement after the second reduction peak.

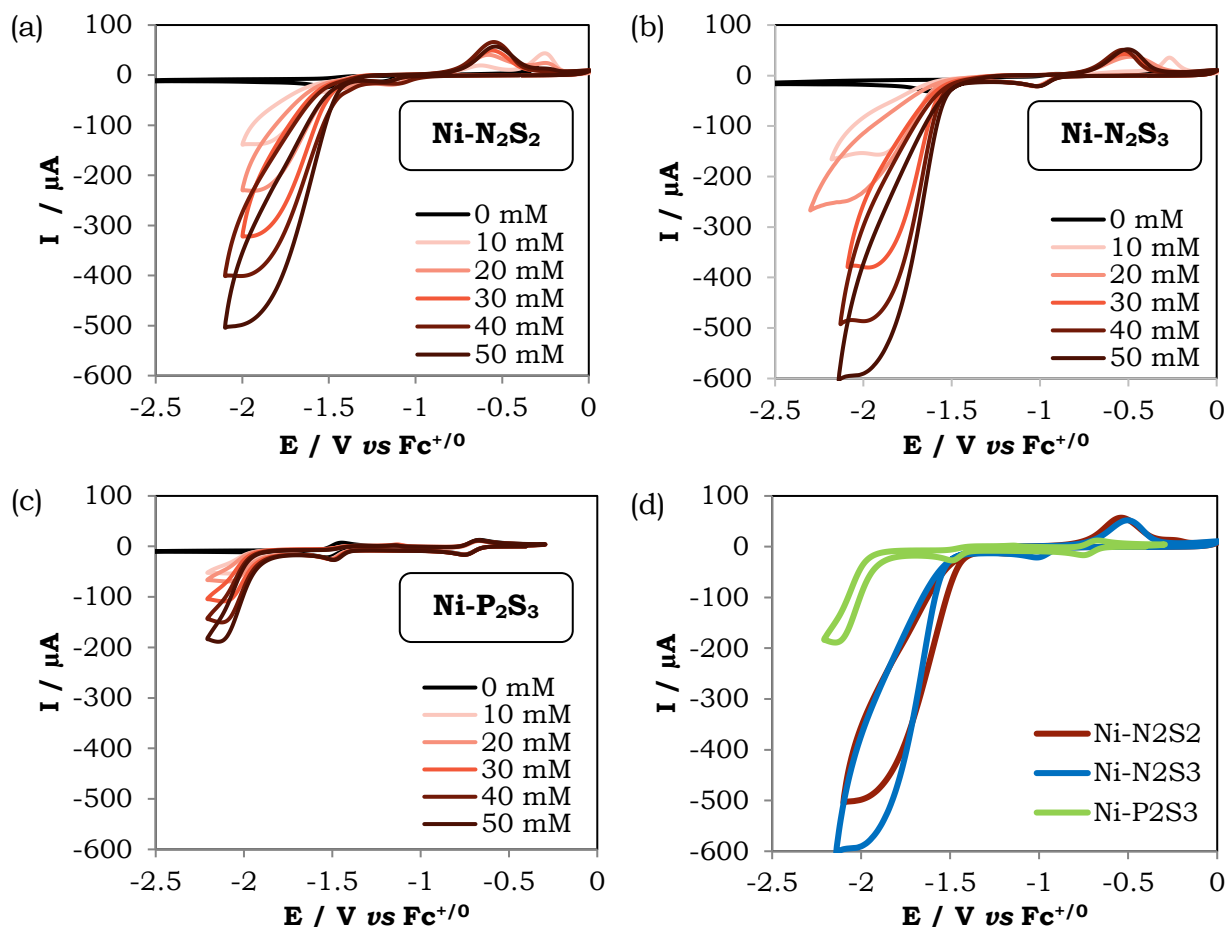


Figure 3-9. Cyclic voltammograms of 1 mM of catalyst (a) **Ni-N₂S₂**, (b) **Ni-N₂S₃**, and (c) **Ni-P₂S₃** in the absence (black) and presence of increasing concentrations of acetic acid in ACN containing 0.1 M TBAP. (d) Comparison of the CVs of the catalysts under catalytic conditions (50 mM acetic acid).

Increasing the concentration of acetic acid does not shift the first reduction potential indicating that the reduction process corresponding to the $\text{Ni}^{\text{II/I}}$ couple is not proton-coupled. However, in addition to the increase in the catalytic current, an anodic shift of the onset potential is observed for the second reduction wave indicating a proton-coupled electron transfer process involved in the catalytic H_2

evolution. In the presence of 50 mM of acetic acid, **Ni-N₂S₃** has an onset catalytic potential of -1.52 V (*vs* Fc^{+ / 0}) and **Ni-N₂S₂** of -1.44 V, all in accordance with the relative positioning of the second reduction peak. The catalytic current plateau is attained at -2 V (*vs* Fc^{+ / 0}) in both cases, with **Ni-N₂S₃** possessing higher catalytic current than **Ni-N₂S₂**. Although **Ni-P₂S₃** has a more anodic second reduction potential compared to **Ni-N₂S₂** and **Ni-N₂S₃**, catalytic proton reduction only occurred at -1.80 V, located 320 mV more cathodic than its second reduction peak. This can be attributed to a formation of a possible hydride intermediate that needs a more negative potential to be reduced, as similarly shown by the group of Artero for nickel dithiolate complexes.^[26] The intensity of the current enhancement for **Ni-P₂S₃** though is not at par with that of **Ni-N₂S₂** and **Ni-N₂S₃**, indicating again that the extra stabilization gained by such complex does not improve its catalytic activity. The case of **Ni-N₂S₃** is interesting however as both electronic and structural changes induced an anodic shift of the first reduction potential but a cathodic shift of the second reduction potential, which resulted to higher current enhancements for both proton and CO₂ catalytic reduction activities.

Though the differences observed in these complexes are interesting to be further probed by electrochemistry-based techniques (e.g. spectroelectrochemistry), a weakly-bound film is always adsorbed at the glassy carbon working electrode after each CV measurement, preventing any accurate succeeding measurements. As such, this required careful rinsing and polishing of the electrode after each measurement. Roberts^[27] and Dempsey^[28,29] have attributed similar observation to the vulnerability of Ni-S bonds which leads to the electrochemical degradation of the catalyst in acidic media. The homogenous catalysts then become a precursor for a heterogeneous catalyst that is more active towards proton reduction. This observation precluded any accurate comparative studies using electrolysis, as it would be difficult to distinguish the homogenous nature of the catalysis from the heterogeneous activity of the adsorbed film. The photocatalytic activity of the catalysts was instead investigated as described in the next section.

3.5. Photocatalytic Activity

The photocatalytic activity of the catalysts was investigated because it allows tracking spectral changes of the catalyst in the solution. Though this method of catalyst activation may result in a different mechanistic pathway as it involves other

players (photosensitizer and electron donor) than electrocatalysis, the reduction potentials determined from electrochemistry are still relevant and useful for determining the thermodynamic driving forces of the photocatalytic system.

The photo-induced CO₂ reduction activity of the modified catalysts was investigated in a typical catalyst/photosensitizer bimolecular system using ruthenium trisbipyridine [Ru(bpy)₃]²⁺ as the photosensitizer and 1,3-dimethylbenzimidazole (BIH) as electron donor in a CO₂-saturated dimethylacetamide solution containing 5.5 M water as the proton source. These conditions were chosen to match those reported in literature^[18] for easier comparison. As shown in Figure 3-10, **Ni-N₂S₂** largely outperforms **Ni-N₂S₃** and **Ni-P₂S₃** for the photocatalytic reduction of CO₂ to CO with a TOF of 445 h⁻¹ and TON of 1130 after 19 h. As shown in the inset of Figure 3-10, the pyridine-based **Ni-N₂S₃** shows a better photocatalytic activity with a TOF of 48.6 h⁻¹ and TON of 70 compared to the phosphine-based catalyst **Ni-P₂S₃** (TOF 24.6 h⁻¹, TON 40).

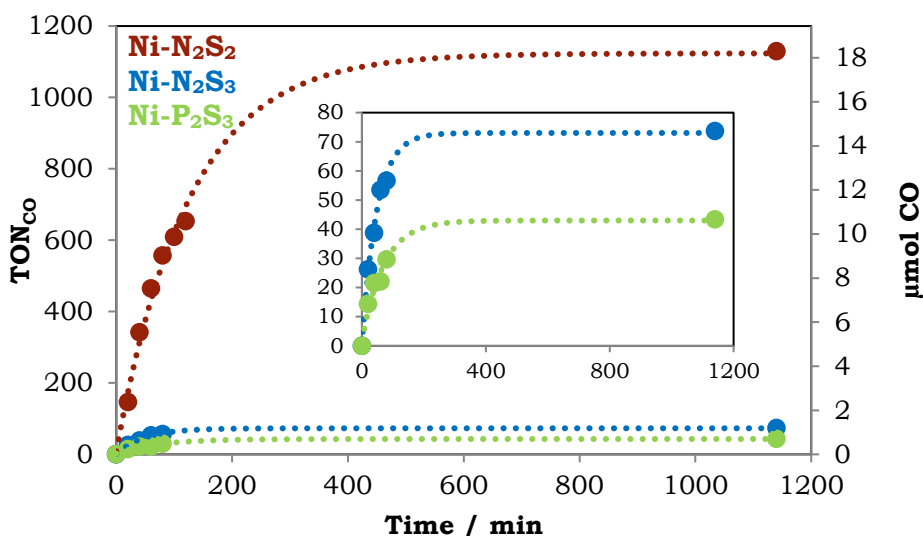


Figure 3-10. Photocatalytic production of CO using 5 μM of catalyst (**Ni-N₂S₂** in red, **Ni-N₂S₃** in blue, and **Ni-P₂S₃** in green), 50 μM [Ru(bpy)₃]²⁺, 100 mM BIH and 5.5 M H₂O in CO₂-saturated dimethylacetamide. Inset shows a magnified view comparing the activities of **Ni-N₂S₃** and **Ni-P₂S₃**. Irradiation source: blue LED lamp centered at 463 nm.

All the catalysts selectively produced CO with no H₂ detected, possibly because the proton source in these conditions (H₂O/HCO₃⁻ equilibrium), is not acidic enough. As the **Ni-N₂S₃** and **Ni-N₂S₂** catalysts were earlier noted to perform better in the electrocatalytic reduction of protons than of CO₂, the photocatalytic

proton reduction activity was investigated with the optimized condition of using $\text{Ru}(\text{bpy})_3]^{2+}$ as the photosensitizer but with an aqueous ascorbate buffer of pH 4 (1:1 v/v buffer:ACN) as both proton source and electron donor. Though both $\text{Ni-N}_2\text{S}_3$ and $\text{Ni-N}_2\text{S}_2$ have sluggish catalytic activity compared to other Ni catalysts reported in the literature,^[14,15,30,31] a better photocatalytic proton reduction activity is observed for the pentadentate-coordinated $\text{Ni-N}_2\text{S}_3$ with a TOF of 3.8 h^{-1} compared to the tetradentate-coordinated $\text{Ni-N}_2\text{S}_2$ (TOF 2.2 h^{-1}). These photocatalytic activities are too different compared to the electrocatalytic activities for both proton and CO_2 reduction, indicating differing mechanisms at play. On the other hand, the $\text{Ni-P}_2\text{S}_3$ catalyst didn't produce any detectable amount of H_2 gas possibly owing to the large overpotential observed for the catalytic proton reduction to occur.

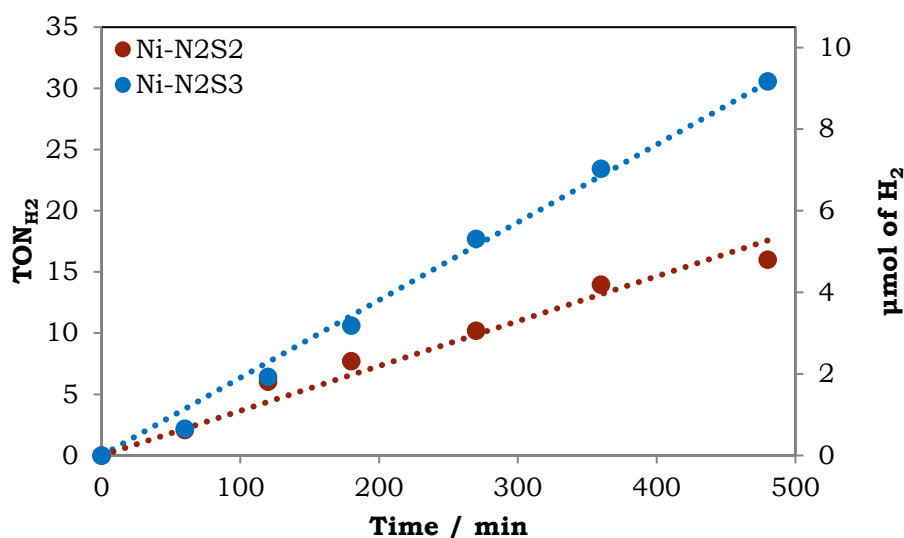


Figure 3-11. Photocatalytic production of H_2 using $100 \mu\text{M}$ of catalyst ($\text{Ni-N}_2\text{S}_2$ in red and $\text{Ni-N}_2\text{S}_3$ in blue) and $250 \mu\text{M}$ $[\text{Ru}(\text{bpy})_3]^{2+}$ in Ar-saturated 1:1 dimethylacetamide : ascorbate buffer (pH 4, 100 mM).

3.6. Tracking the First Photo-Induced Electron Transfer

To rationalize the observed differences in performance between the catalysts $\text{Ni-N}_2\text{S}_3$ and $\text{Ni-N}_2\text{S}_2$, time-resolved UV-visible spectroscopy was employed to determine eventual differences in the photo-induced electron transfer dynamics. The investigations were focused on these two catalysts as they show differing photocatalytic activities which could be related to changes in the primary coordination sphere. The initial photo-induced electron transfer was investigated using similar conditions as for preparative photocatalytic reactions: $[\text{Ru}(\text{bpy})_3]^{2+}$

(denoted as **Ru^{II}**) as photosensitizer, and ascorbate buffer (pH 4) as the reversible electron donor (denoted as **ED**) in aqueous acetonitrile solution (1:1 v/v). The thermodynamic potentials of each of these components were determined electrochemically and the energy diagram is mapped in Figure 3-12.

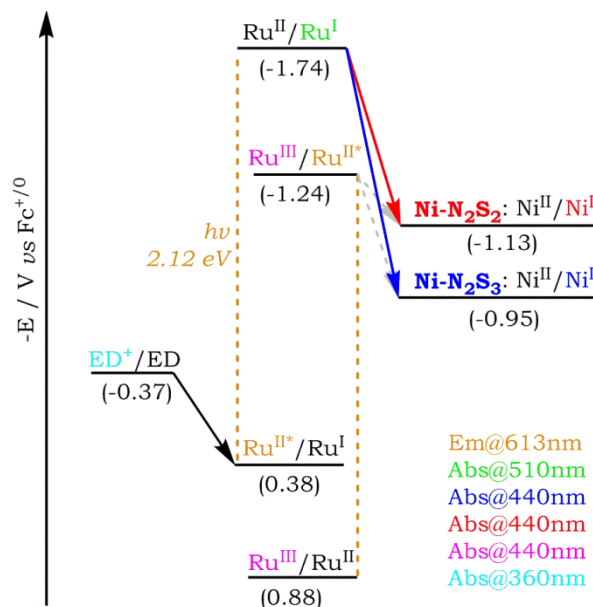


Figure 3-12. Thermodynamic diagram associated with the photocatalytic cycle involving the catalysts **Ni-N₂S₃** (blue) or **Ni-N₂S₂** (red), **Ru^{II}** as photosensitizer and ascorbate as electron donor (**ED**). Colored text indicates the spectral signatures followed for the time-resolved absorption measurements.

Once the **Ru^{II}** is excited at 460 nm, a characteristic emission at 613 nm from the triplet excited state **Ru^{II*}** is typically observed. This excited state is efficiently quenched by the ascorbate compared to the sluggish quenching by the catalyst, as shown in Figure 3-13. This indicates that even though the excited **Ru^{II*}** is sufficiently reducing to transfer an electron to the Ni catalysts, shown by the gray dashed arrow in Figure 3-12, the catalyst does not efficiently quench the excited state compared to the **ED** at the same concentrations. This is mainly attributed to the higher thermodynamic drive for the quenching of **Ru^{II*}** by the **ED** ($\Delta G = -750$ meV) compared to that by the catalyst ($\Delta G = -110$ to -290 meV). The emission quenching by the **ED** is accompanied by a growth at 510 nm in the transient absorption spectra, indicating the formation of the one-electron reduced (OER) species of the photosensitizer, denoted as formal **Ru^I**. This is indicative of a reductive quenching mechanism. A bimolecular rate constant of $2.3 \times 10^8 \text{ M}^{-1}\text{s}^{-1}$ was determined from the Stern-Volmer plot for the electron transfer from **ED** to **Ru^{II*}** forming **ED⁺** and **Ru^I**.

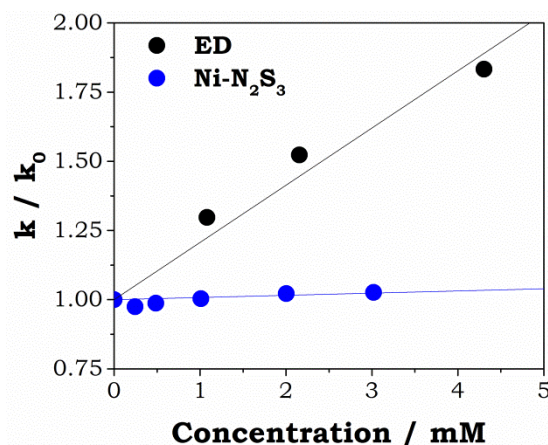


Figure 3-13. Stern-Volmer plot of the emission quenching of **Ru^{II*}** monitored at 613 nm in Ar-purged ACN:ascorbate buffer (pH 4, 1:1 v/v) at various concentrations of either ascorbate buffer (black) or **Ni-N₂S₃** (blue).

In the presence of both **ED** and the **Ni-N₂S₃** catalyst, the transient absorption spectra shown in Figure 3-14, show the expected formation of **Ru^I** observed at 510 nm. This species decays to give a new species with a characteristic positive absorption from 440 nm to 550 nm, which is assigned to the OER of **Ni-N₂S₃**, denoted as **Ni^I** and an absorption at 360 nm due to oxidized ascorbate. Following the kinetics at both 510 nm and 440 nm gives a clear picture that the decay of **Ru^I** is concomitant with the growth of **Ni^I**, as shown in Figure 3-15. Increasing the concentration of **Ni-N₂S₃**, accelerates the decay of **Ru^I** and increases the amount of reduced **Ni^I** formed. By implementing a global fit of these kinetic data, a close-to-diffusion-limited bimolecular rate constant of $1.11 \times 10^8 \text{ M}^{-1}\text{s}^{-1}$ was determined for the electron transfer from **Ru^I** to **Ni^{II}** (**Ni-N₂S₃**) forming **Ru^{II}** and **Ni^I**.

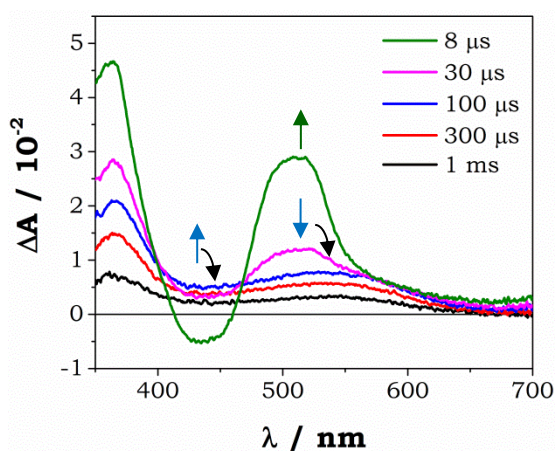


Figure 3-14. Transient absorption spectra of 24 μM **[Ru(bpy)₃]²⁺**, 660 μM **Ni-N₂S₃**, in Ar-purged ACN:asc buffer (100 mM buffer at pH 4; 1:1 v/v). Laser energy = 8 mJ, λ_{exc} at 460 nm. Green solid arrow shows initial growth of **Ru^I**, blue arrows show decay of **Ru^I** with concomitant growth of **Ni^I**, and black arrows show decay of **Ni^I**.

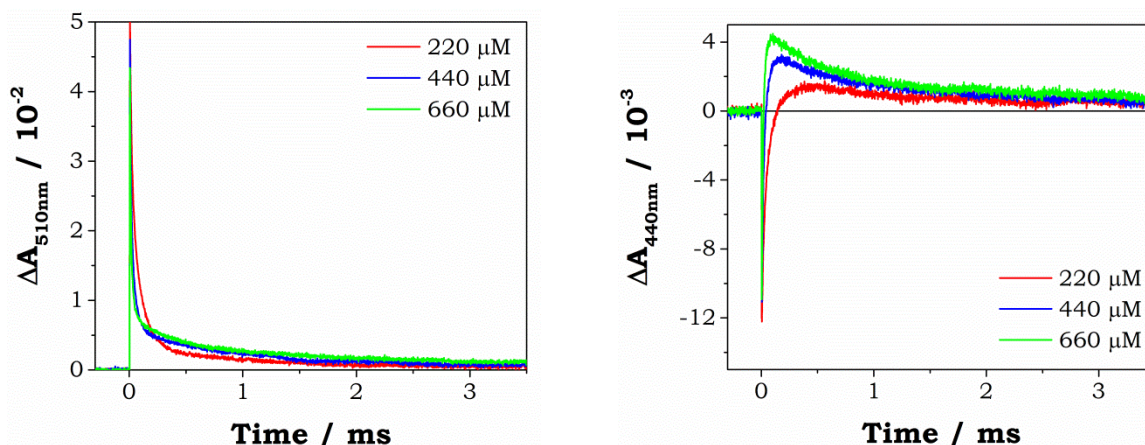


Figure 3-15. Transient absorption kinetics at 510 nm (left) due to the formation and decay of Ru^{I} and 440 nm (right) due to the growth and decay of Ni^{I} ($\text{Ni-N}_2\text{S}_3$) as a function of catalyst concentration in Ar-purged ACN/asc buffer (pH 4, 1:1 v/v).

Concentration-dependent transient absorption kinetics were also obtained for $\text{Ni-N}_2\text{S}_2$ as shown in Figure 3-16. Global fitting of the kinetic data, however, showed a rate constant of $2.16 \times 10^7 \text{ M}^{-1}\text{s}^{-1}$ for the first photo-induced electron transfer from Ru^{I} to Ni^{II} ($\text{Ni-N}_2\text{S}_2$) forming Ru^{II} and Ni^{I} . This is five times slower compared to $\text{Ni-N}_2\text{S}_3$, as shown in the comparison in Figure 3-17. This might plausibly originate from the difference in the thermodynamic drive for the first electron transfer, as shown in Figure 3-12. $\text{Ni-N}_2\text{S}_3$ has more positive first reduction potential ($E = -0.95 \text{ V vs Fc}^{+/0}$) compared to $\text{Ni-N}_2\text{S}_2$ ($E = -1.13 \text{ V vs Fc}^{+/0}$), indicating that there is a higher thermodynamic drive for the first electron transfer from Ru^{I} to $\text{Ni-N}_2\text{S}_3$ ($\Delta G = -790 \text{ meV}$) than to $\text{Ni-N}_2\text{S}_2$ ($\Delta G = -610 \text{ meV}$).

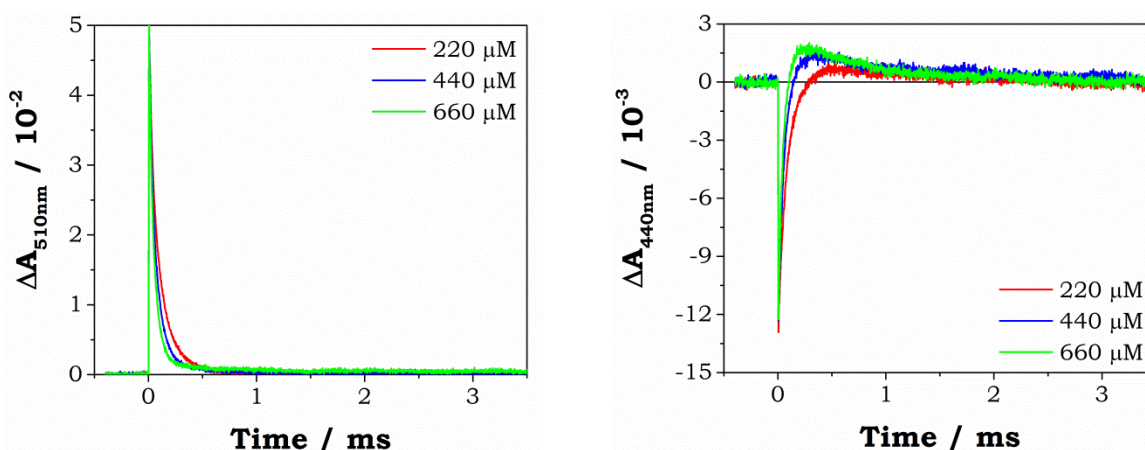


Figure 3-16. Transient absorption kinetics at 510 nm (left) due to the formation and decay of Ru^{I} and at 440 nm (right) due to the growth and decay of Ni^{I} ($\text{Ni-N}_2\text{S}_2$) as a function of catalyst concentration in Ar-purged ACN/asc buffer (pH 4, 1:1 v/v).

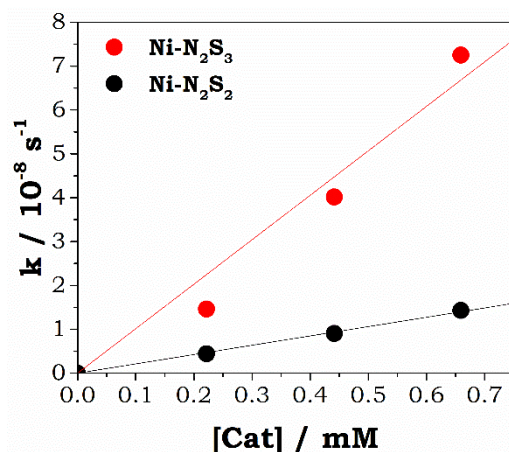


Figure 3-17. Comparison of the plots of globally fitted k against concentration of **Ni-N₂S₃** (red) and **Ni-N₂S₂** (black) giving electron transfer rate constants of $1.11 \times 10^8 \text{ M}^{-1}\text{s}^{-1}$ and $2.16 \times 10^7 \text{ M}^{-1}\text{s}^{-1}$, respectively.

A global fitting procedure was employed for the transient absorption kinetics at each wavelength and resulted in two time constants, as shown in Figure 3-18. The first time constant (τ_1) was attributed to the concentration-dependent electron transfer from **Ru^I** to **Ni^{II}**. The figure showed that there is a faster time constant ($\tau_1 = 16 \mu\text{s}$) for **Ni-N₂S₃** compared to **Ni-N₂S₂** ($\tau_1 = 39 \mu\text{s}$), indicating that there is a faster electron transfer observed for the former than the latter. This observed difference has been previously attributed to the difference for the thermodynamic drive between **Ru^I** and the Ni catalyst. On the other hand, the slower time constant (τ_2) was attributed to the charge recombination between **Ni^I** and **Asc⁺**. This time, the charge recombination was faster for **Ni-N₂S₂** ($667 \mu\text{s}$) compared to **Ni-N₂S₃** ($925 \mu\text{s}$). This difference is similarly attributed to the higher thermodynamic drive for the charge recombination between **Ni^I** and **Asc⁺** for **Ni-N₂S₂** ($\Delta G = -760 \text{ meV}$) compared to **Ni-N₂S₃** ($\Delta G = -580 \text{ meV}$). The decay associated spectra indicate that the **Ni^I** species for this class of catalysts shows positive absorption from 440 nm to 550 nm. These are in agreement with the DFT-calculated **Ni^I** spectrum of **Ni-N₂S₃** as shown in Figure 3-19, and the chemically reduced **Ni^I** spectrum of **Ni-N₂S₂**.^[19]

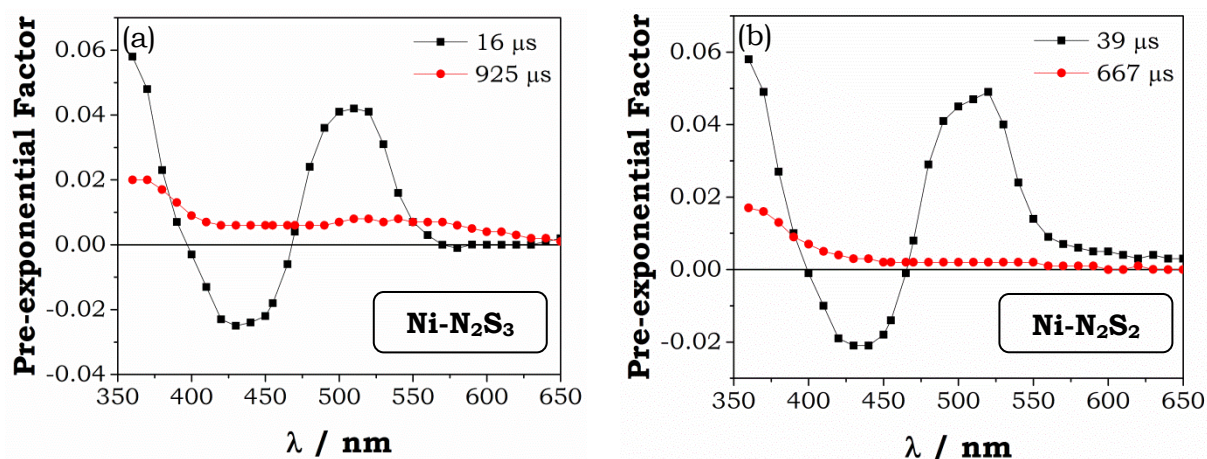


Figure 3-18. Decay associated spectra (DAS) of the transient absorption kinetics of (a) $\text{Ni-N}_2\text{S}_3$ and (b) $\text{Ni-N}_2\text{S}_2$ catalysts taken at 1 ms delay at various wavelengths with similar conditions as described in Figure 3-14. Black lines correspond to $[(\text{Ru}^{\text{I}} + \text{Asc}^+) - (\text{Ru}^{\text{II}} + \text{Asc})]$ while the red lines correspond to $[(\text{Ni}^{\text{I}} + \text{Asc}^+) - (\text{Ni}^{\text{II}} + \text{Asc})]$, with their respective lifetimes.

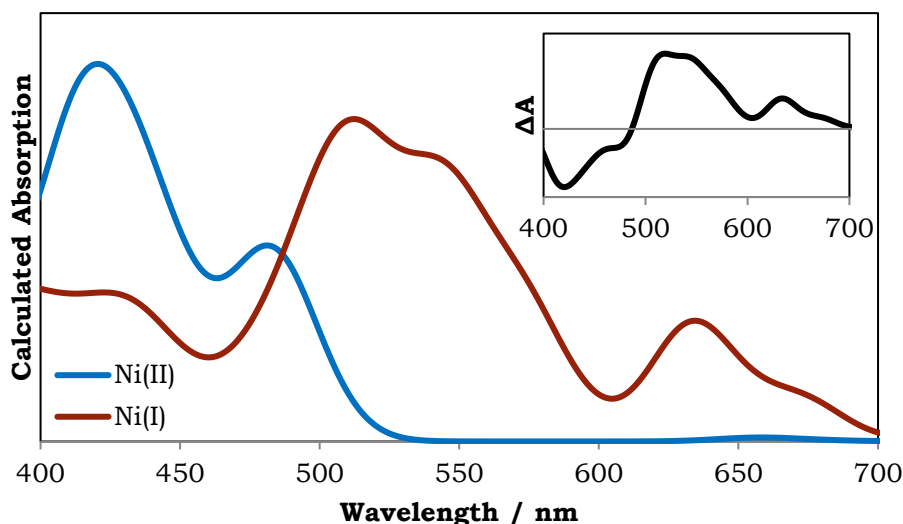


Figure 3-19. DFT-optimized UV-visible absorption spectra for the proposed Ni^{II} and Ni^{I} geometries of the $\text{Ni-N}_2\text{S}_3$ catalyst. Inset shows the difference spectra between Ni^{II} and Ni^{I} . See Appendix for calculation details.

The observed differences in the first electron transfer kinetics between the catalysts are consistent with the trend in the photocatalytic proton reduction activities shown in Figure 3-11. However, this first photo-induced electron transfer may not be the rate-determining step as hinted by the redox behaviors in Figure 3-8 and Figure 3-9, where the formation of the doubly-reduced Ni species is needed to achieve catalytic reduction of both carbon dioxide and protons. Though tracking the first photo-induced electron transfer showed interesting differences between the

catalysts, there is a need to track the two-electron accumulation in the catalysts. This is still being pursued in our laboratory. The main difficulty is the need to optimize the yield of the first photo-induced event as a prerequisite to identify the spectral features of the doubly reduced Ni catalyst in a second photo-induced event. This is critical since the Ni catalysts have intrinsically low absorption coefficients.

3.7. X-ray Absorption Spectroscopy Measurements

The photocatalytic investigations were then coupled with static and time-resolved X-ray absorption spectroscopy (tr-XAS) techniques to determine the changes in the coordination environment and oxidation states of the Ni metal of the **Ni-N₂S₃** and **Ni-N₂S₂** catalyst during photocatalysis. This was done in collaboration with Dr. Dooshaye Moonshiram from IMDEA Nanociencia in Madrid. The X-ray absorption near structure (XANES) of **Ni-N₂S₃** and **Ni-N₂S₂** was first investigated in a mixture of acetonitrile and water, as shown in Figure 3-20. Although the metal centers in both catalysts have the same oxidation states, the local coordination spheres and geometries of both complexes are clearly different explaining the shift in energy and changes in the $1s \rightarrow 4p$ main transitions along the rising edge. The energy shift is well reproduced by spectra simulated by time-dependent Density Functional Theory (td-DFT) methods (Figure 3-20 inset) showing that geometry optimizations and ab-initio XANES simulations used for both catalysts reproduce the experimental data well.

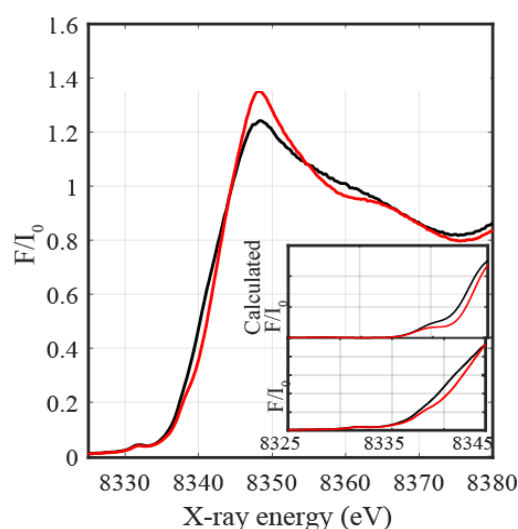


Figure 3-20. Normalized experimental Ni K-edge XANES of **Ni-N₂S₃** (black) and **Ni-N₂S₂** (red) in 1:1 (v/v) ACN:H₂O. Inset shows the details of the pre-edge and rising edge regions in comparisons to the calculated XANES spectra of **Ni-N₂S₃** and **Ni-N₂S₂** using DFT-optimized coordinates (see Appendix).

The extended X-ray absorption fine structure (EXAFS) spectra of **Ni-N₂S₃** and **Ni-N₂S₂** are shown in Figure 3-21a. Two prominent peaks are observed in both spectra corresponding to the distinct Ni-N and Ni-S bond distances. Analysis of the first peak in **Ni-N₂S₃** clearly resolves 3 Ni-S distances at 2.41 Å, and 3 Ni-N distances at 2.05 Å, and. Similarly, fitting of **Ni-N₂S₂** shows 4 Ni-N and 2 Ni-S distances at 2.06 Å and 2.40 Å, respectively. The increased Ni-N and decreased Ni-S coordination numbers in **Ni-N₂S₂** are clearly demonstrated by the increased amplitude of the first peak and decrease in the second peak's intensity in comparison to **Ni-N₂S₃**. The fitted Ni-N and Ni-S bond distances agree with the reported XRD structures and relaxed structures from DFT geometry optimizations. Further changes detected in experimental EXAFS for **Ni-N₂S₃** and **Ni-N₂S₃** correlate well with the data trends from XRD analysis and FEFF simulations of DFT-optimized coordinates as shown by Figure 3-21b, confirming that these methods can be reliably used for the analysis of the unknown transient species involved in the photo-catalytic cycle.

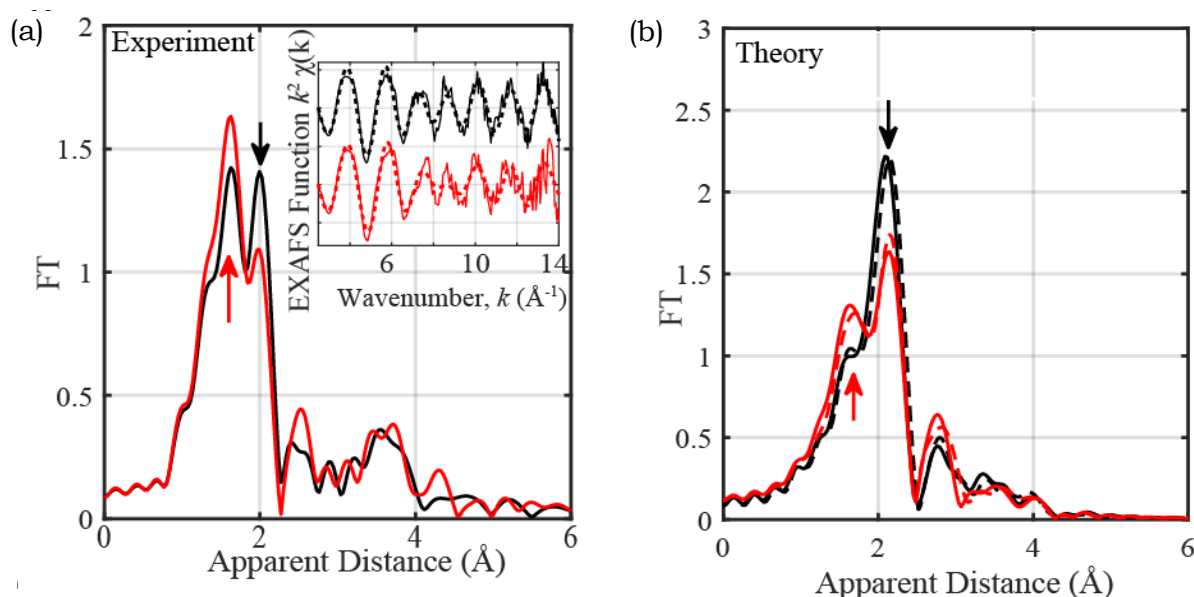


Figure 3-21. (a) Fourier transforms of k^2 -weighted Ni EXAFS of **Ni-N₂S₃** (black) and **Ni-N₂S₂** (red) in 1:1 (v/v) ACN:H₂O. Inset shows the back Fourier transforms of the experimental results (solid lines) and fitting of $k^2\chi(k)$ (dashed lines). (b) Simulated EXAFS spectra (solid lines); atomic coordinates were obtained from single crystal X-ray diffraction structures of the catalysts and from DFT simulations (dashed lines).

Time-resolved XAS in the ns- μ s time range was used to monitor the kinetics and structural dynamics of the photo-induced **Ni^I** species in an ACN:H₂O mixture consisting of the **Ni-N₂S₃** catalyst with the **[Ru(bpy)₃]²⁺** as the photosensitizer in

1:10 ratio, and an equimolar mixture of sodium ascorbate and ascorbic acid as the electron donor and proton source. The complete photocatalytic system was optically pumped at 400 nm with a 10 KHz repetition-rate laser and probed with x-ray pulses at several time delays from 100 ps to 25 μs . Features in the time-resolved spectra, obtained by subtracting the laser-on and laser-off (dark) spectra, provided information about the transient states involved in the photo-catalytic cycle. Figure 3-22a shows the tr-XAS spectra at an averaged delay of $\sim 12 \mu\text{s}$. A prominent peak at 8340 eV together with a broad dip at 8350 eV relates to the formation of the reduced Ni^{I} species and the bleaching of the Ni^{II} ground state, respectively (Figure 3-22c). These energy transitions in turn show that the K-edge of the Ni center shifts to lower energy, indicating the reduction of Ni^{II} and confirming formation of Ni^{I} from electron transfer from the reduced Ru^{I} .

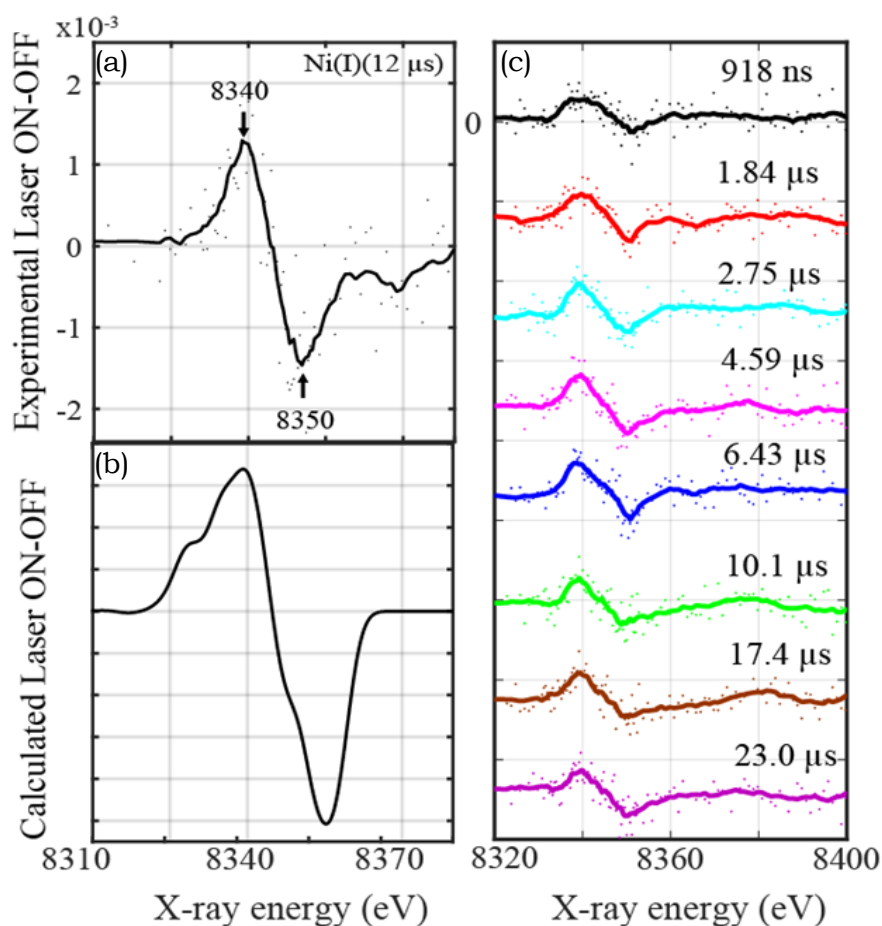


Figure 3-22. (a) Experimental difference spectra corresponding to the Ni^{I} transient signal for $\text{Ni-N}_2\text{S}_3$ at $\sim 12 \mu\text{s}$. (b) Theoretical XANES simulations corresponding to the difference between Ni^{II} with a bound acetonitrile molecule and Ni^{I} with unbound solvent molecule. (c) Stacked spectra corresponding to a series of time-delays between laser and X-ray pulses. These measurements were carried out for a range of averaged time delays from 0-23 μs for a complete photocatalytic system when bubbled in N_2 gas.

Various geometries with different coordinated ligands for a Ni^{I} species were considered, namely a square bipyramidal and octahedral geometries with a bound acetonitrile and water molecule, as shown in Figure 3-23a. The solvent molecule is in this case loosely bound to the Ni^{I} metal center with a Ni-N/O distance of ~ 2.91 - 4.30 Å. Additionally, one of the Ni-S is loosely coordinated with a Ni-S bond distance of 2.56 - 2.77 Å. Comparison of the DFT-optimized optical absorption spectra (Figure 3-23b) with the decay associated spectra of Ni^{I} of $\text{Ni-N}_2\text{S}_3$ in Figure 3-18a, as well as the comparison of theoretical (Figure 3-23c) and experimental XANES (Figure 3-22) reveal that a distorted square bipyramidal Ni^{I} complex with an unbound solvent molecule is the most-likely configuration of the photo-produced Ni^{I} species.

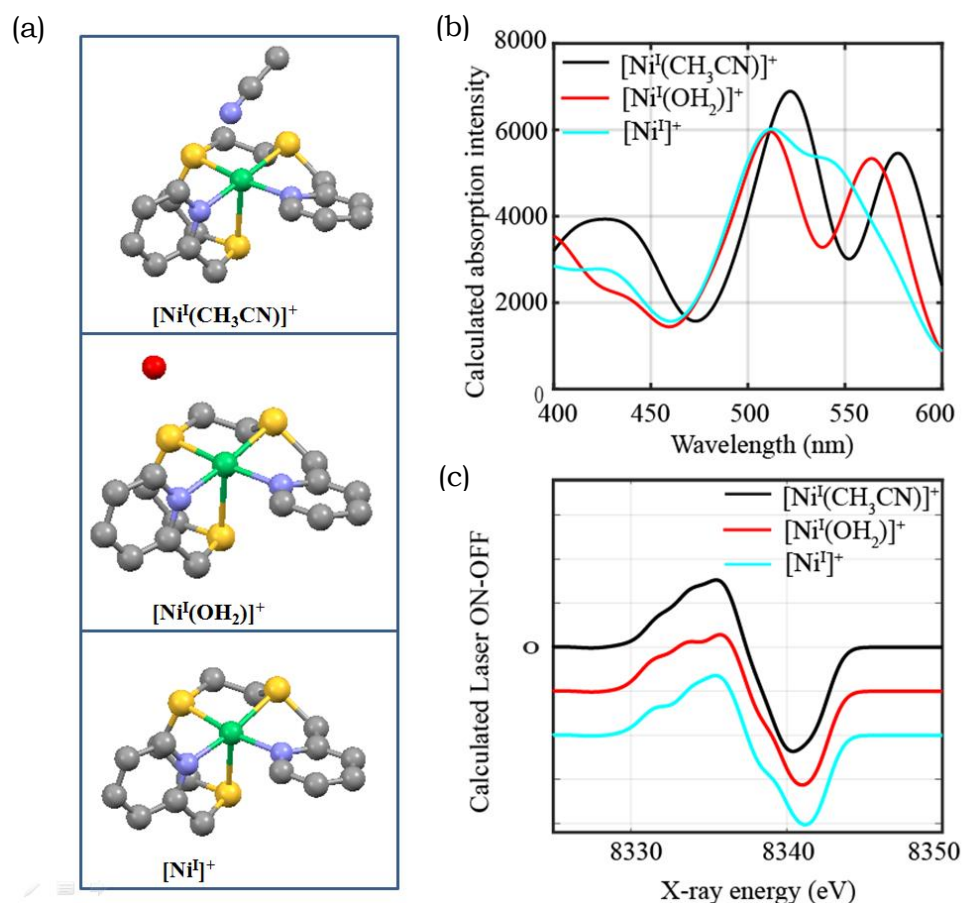


Figure 3-23. (a) Calculated Ni^{I} geometries with different coordinated ligands. (b) Calculated optical absorption spectra corresponding to the optical signatures of Ni^{I} with a bound acetonitrile molecule (black), Ni^{I} with a bound water molecule (red) and Ni^{I} with no solvent molecule (cyan). (c) Theoretical XANES simulations corresponding to the difference between Ni^{II} with a bound acetonitrile molecule and Ni^{I} with a bound acetonitrile molecule (black), Ni^{I} with a bound water molecule (red) and Ni^{I} with no solvent molecule (cyan).

The elucidation of the electronic and structural configuration of the reduced Ni^{I} species through time-resolved XAS and DFT calculations, complemented the kinetics and spectral information attained by time-resolved visible absorption measurements. This information point to some interesting initial events, as proposed in Figure 3-24. An acetonitrile-coordinated $\text{Ni}^{\text{II}}\text{-N}_2\text{S}_3$, is initially observed when dissolved in the aqueous acetonitrile solution. In the presence of light, an excited $\text{Ru}^{\text{II}*}$ is formed which is efficiently quenched by the ascorbate electron donor producing the reduced Ru^{I} . This species then transfers an electron to the catalyst with a close-to-diffusion-limited bimolecular rate constant of $1.11 \times 10^8 \text{ M}^{-1}\text{s}^{-1}$. The reduced catalyst is described by having a metal-centered reduction giving a Ni^{I} species with a square bipyramidal geometry, where the solvent is no longer coordinated. After this intermediate, proceeding steps are proposed based on initial observations from cyclic voltammetry measurements that a second electron transfer is needed to form the active form of the catalyst. This second electron transfer is expected to be coupled to a proton transfer for proton reduction activity, but this might not be the case for CO_2 reduction activity^[15,18,19]. The reaction sequence in this proposed mechanism need to be confirmed by further experimental and theoretical investigations.

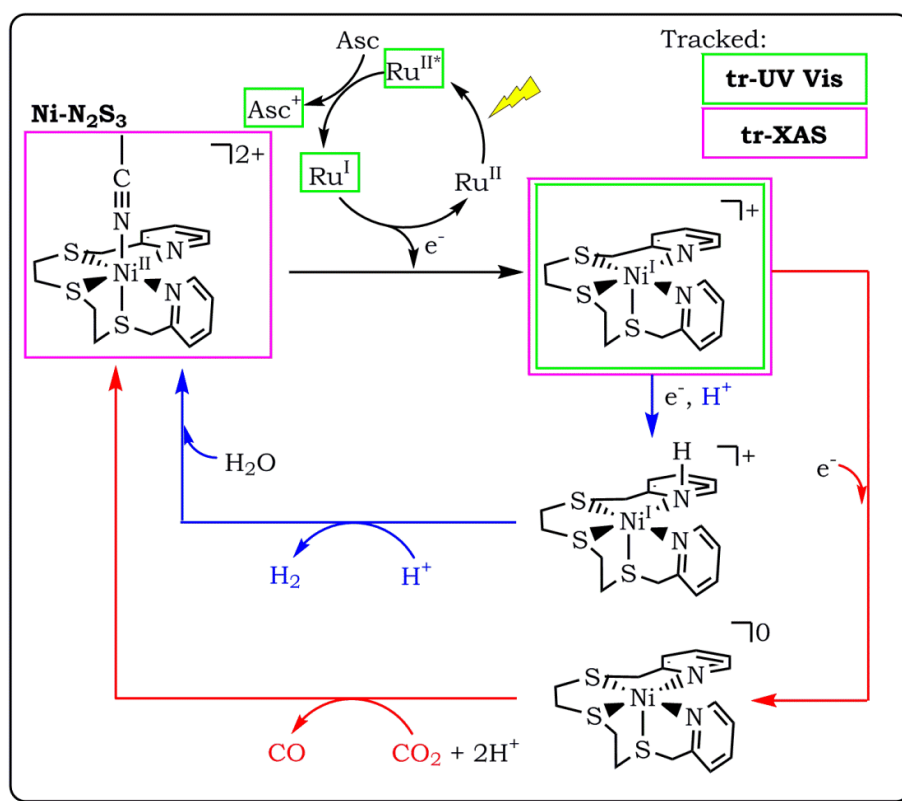


Figure 3-24. Proposed catalytic cycle for the photocatalytic reduction of either protons (blue) or CO_2 (red) by $\text{Ni-N}_2\text{S}_3$ with the colored boxes indicating the spectroscopic tracking of the intermediates performed in this work.

3.8. Conclusions

In conclusion, we have described a strategy of modifying the first coordination sphere of a known nickel catalyst bearing an N_2S_2 ligand structure, inspired from the sulfur-rich uncoordinated environment found in the Ni-centered C cluster site of CO dehydrogenase (CODH) enzymes. The introduction of more thioether donors in the **Ni-N₂S₃** catalyst resulting in a pentadentate coordination or even replacing the pyridine donors with softer phosphine ligands in the pentadentate **Ni-P₂S₃** catalyst did indeed stabilize low oxidation states of Ni^I as observed in the anodic shift of the Ni^{III/I} redox couple. However, this extra stabilization didn't translate to an enhanced electro- and photo-catalytic reduction of CO₂ to CO. Unexpectedly, the **Ni-N₂S₃** catalyst exhibited improved electro- and photo-catalytic reduction of protons to hydrogen gas compared to **Ni-N₂S₂**. Time-resolved UV-vis and X-ray absorption spectroscopic techniques were able to track down and identify the nature and environment of the intermediates leading to the formation of a photo-induced **Ni^I** complex. Rationalizing the differences observed in the catalytic activities requires however further investigation of the subsequent steps.

Though a strategy of modifying the primary coordination sphere of the nickel catalyst can in most cases shed light on the structural features of the active site of the CODH enzyme, it seems that systematic changes in such primary coordination positions does not necessarily translate to expected systematic improvements in the catalytic activity. This is in part due to the interplay of electronic and structural changes that might critically affect the reaction pathways of the catalyst. Furthermore, the similarity of the sulfur-rich environment with the active site of hydrogenase enzymes makes such strategy limited in controlling and preventing the competitive proton reduction activity.

Bibliography

- [1] R. Panda, C. P. Berlinguette, Y. Zhang, R. H. Holm, *J. Am. Chem. Soc.* **2005**, *127*, 11092–11101.
- [2] A. M. Appel, J. E. Bercaw, A. B. Bocarsly, H. Dobbek, D. L. DuBois, M. Dupuis, J. G. Ferry, E. Fujita, R. Hille, P. J. A. Kenis, et al., *Chem. Rev.* **2013**, *113*, 6621–6658.
- [3] H. Dobbek, V. Svetlitchnyi, J. Liss, O. Meyer, *J. Am. Chem. Soc.* **2004**, *126*, 5382–5387.
- [4] J.-H. Jeoung, H. Dobbek, *Science* **2007**, *318*, 1461.

- [5] J. Fessler, J.-H. Jeoung, H. Dobbek, *Angew. Chem. Int. Ed.* **2015**, *54*, 8560–8564.
- [6] S. Ciurli, P. K. Ross, M. J. Scott, S. B. Yu, R. H. Holm, *J. Am. Chem. Soc.* **1992**, *114*, 5415–5423.
- [7] R. Panda, Y. Zhang, C. C. McLauchlan, P. Venkateswara Rao, F. A. Tiago de Oliveira, E. Münck, R. H. Holm, *J. Am. Chem. Soc.* **2004**, *126*, 6448–6459.
- [8] J. Sun, C. Tessier, R. H. Holm, *Inorg. Chem.* **2007**, *46*, 2691–2699.
- [9] V. Artero, M. Fontecave, *Coordination Chemistry Reviews* **2005**, *249*, 1518–1535.
- [10] D. Sellmann, J. Sutter, *Acc. Chem. Res.* **1997**, *30*, 460–469.
- [11] C. Tard, C. J. Pickett, *Chem. Rev.* **2009**, *109*, 2245–2274.
- [12] E. Bouwman, J. Reedijk, *Coordination Chemistry Reviews* **2005**, *249*, 1555–1581.
- [13] M. L. Helm, M. P. Stewart, R. M. Bullock, M. R. DuBois, D. L. DuBois, *Science* **2011**, *333*, 863–866.
- [14] M. P. McLaughlin, T. M. McCormick, R. Eisenberg, P. L. Holland, *Chem. Commun.* **2011**, *47*, 7989–7991.
- [15] Z. Han, W. R. McNamara, M.-S. Eum, P. L. Holland, R. Eisenberg, *Angewandte Chemie International Edition* **2012**, *51*, 1667–1670.
- [16] Z. Han, L. Shen, W. W. Brennessel, P. L. Holland, R. Eisenberg, *J. Am. Chem. Soc.* **2013**, *135*, 14659–14669.
- [17] H. Rao, Z.-Y. Wang, H.-Q. Zheng, X.-B. Wang, C.-M. Pan, Y.-T. Fan, H.-W. Hou, *Catal. Sci. Technol.* **2015**, *5*, 2332–2339.
- [18] D. Hong, Y. Tsukakoshi, H. Kotani, T. Ishizuka, T. Kojima, *J. Am. Chem. Soc.* **2017**, *139*, 6538–6541.
- [19] D. Hong, Y. Tsukakoshi, H. Kotani, T. Ishizuka, K. Ohkubo, Y. Shiota, K. Yoshizawa, S. Fukuzumi, T. Kojima, *Inorg. Chem.* **2018**, *57*, 7180–7190.
- [20] T. Fogeron, T. K. Todorova, J.-P. Porcher, M. Gomez-Mingot, L.-M. Chamoreau, C. Mellot-Draznieks, Y. Li, M. Fontecave, *ACS Catal.* **2018**, *8*, 2030–2038.
- [21] T. Fogeron, P. Retailleau, M. Gomez-Mingot, Y. Li, M. Fontecave, *Organometallics* **2018**, *38*, 1344–1350.
- [22] T. Fogeron, P. Retailleau, L.-M. Chamoreau, Y. Li, M. Fontecave, *Angewandte Chemie International Edition* **2018**, *57*, 17033–17037.
- [23] B. Adhikary, S. Liu, C. R. Lucas, *Inorg. Chem.* **1993**, *32*, 5957–5962.
- [24] S. Liu, C. R. Lucas, R. C. Hynes, J.-P. Charland, *Can. J. Chem.* **1992**, *70*, 1773–1783.
- [25] A. McAuley, S. Subramanian, *Inorg. Chem.* **1990**, *29*, 2830–2837.
- [26] A. Zarkadoulas, M. J. Field, V. Artero, C. A. Mitsopoulou, *ChemCatChem* **2017**, *9*, 2308–2317.
- [27] M. Fang, M. H. Engelhard, Z. Zhu, M. L. Helm, J. A. S. Roberts, *ACS Catal.* **2014**, *4*, 90–98.
- [28] B. D. McCarthy, C. L. Donley, J. L. Dempsey, *Chem. Sci.* **2015**, *6*, 2827–2834.
- [29] D. J. Martin, B. D. McCarthy, C. L. Donley, J. L. Dempsey, *Chemical Communications* **2015**, *51*, 5290–5293.
- [30] H. Rao, W.-Q. Yu, H.-Q. Zheng, J. Bonin, Y.-T. Fan, H.-W. Hou, *Journal of Power Sources* **2016**, *324*, 253–260.
- [31] H. Cui, J. Wang, M. Hu, C. Ma, H. Wen, X. Song, C. Chen, *Dalton Trans.* **2013**, *42*, 8684–8691.

Chapter 4

Designing Catalysts:

Second Coordination Sphere Effect

This Chapter includes work reported in:

- P. Gotico, B. Boitrel, R. Guillot, M. Sircoglou, A. Quaranta, Z. Halime, W. Leibl, A. Aukauloo, *Angew. Chem. Int. Ed.* **2019**, 58, 4504–4509.
- A. Khadhraoui, P. Gotico, B. Boitrel, W. Leibl, Z. Halime, A. Aukauloo, *Chem. Commun.* **2018**, 54, 11630–11633.

4.1. Introduction

The criticality of global warming effects due to increasing emission of carbon dioxide (CO₂) is challenging scientists to advance research in the development of catalysts that can help capture, activate, and reduce CO₂. An emphasis is currently being put on the discovery of new cost-efficient molecular catalysts to drive the electrocatalysis of CO₂ reduction and ultimately to use solar energy to drive these energetically uphill chemical transformations.^[1-10] Still, the route towards industrial upscale applications requires much improvement in the efficiency of these catalysts while maintaining their stability and selectivity.

Rational strategies for catalyst design and improvement hinge on what we continually learn from natural systems, as they exhibit exceptional stabilities and performance. Carbon monoxide dehydrogenase (CODH) stands as the typical inspiration for scientists working on the field as it is known to catalyze the reversible reduction of CO₂ to CO. Lessons from the structure and function of this enzyme point out to some important features that can be artificially mimicked by catalyst design: (1) a bifunctional activation of CO₂ substrate by two metal centers, (2) an iron-sulfur cluster acting as an electronic relay and buffer to the catalytic unit and (3) precisely positioned amino acid residues to form a hydrogen-bond stabilization network with the CO₂ substrate.^[11-13]

Inorganic structural mimics of CODH active site were pioneered by the group of Holm synthesizing a closely-resembling [NiFe₃S₄] cubane model^[14] (Complex **1** in Figure 4-1) and even maintaining a square planar configuration for the redox-active Ni atom (Complex **2**).^[15] The biomimicry was even extended by synthesizing a heterobimetallic analogue in the form of Complex **3**^[16] resembling the [NiFe] bimetallic center in the CODH active site. Though these models achieve a substantial structural similarity with the active site of the enzyme, they were not reported to catalyze the reversible reduction of CO₂ to CO. A similar barrier was faced when scientists tried to structurally mimic the active sites of hydrogenases to develop synthetic catalysts towards reversible reduction of protons to hydrogen.^[17] As such, there is a growing consensus in the community of bio-inspired synthetic chemistry that for the development of efficient catalysts, key principles observed in biologically active sites including the nearby biomolecular environment should be applied to systems possessing different ligands and metal centers, as shown in Figure 4-1.

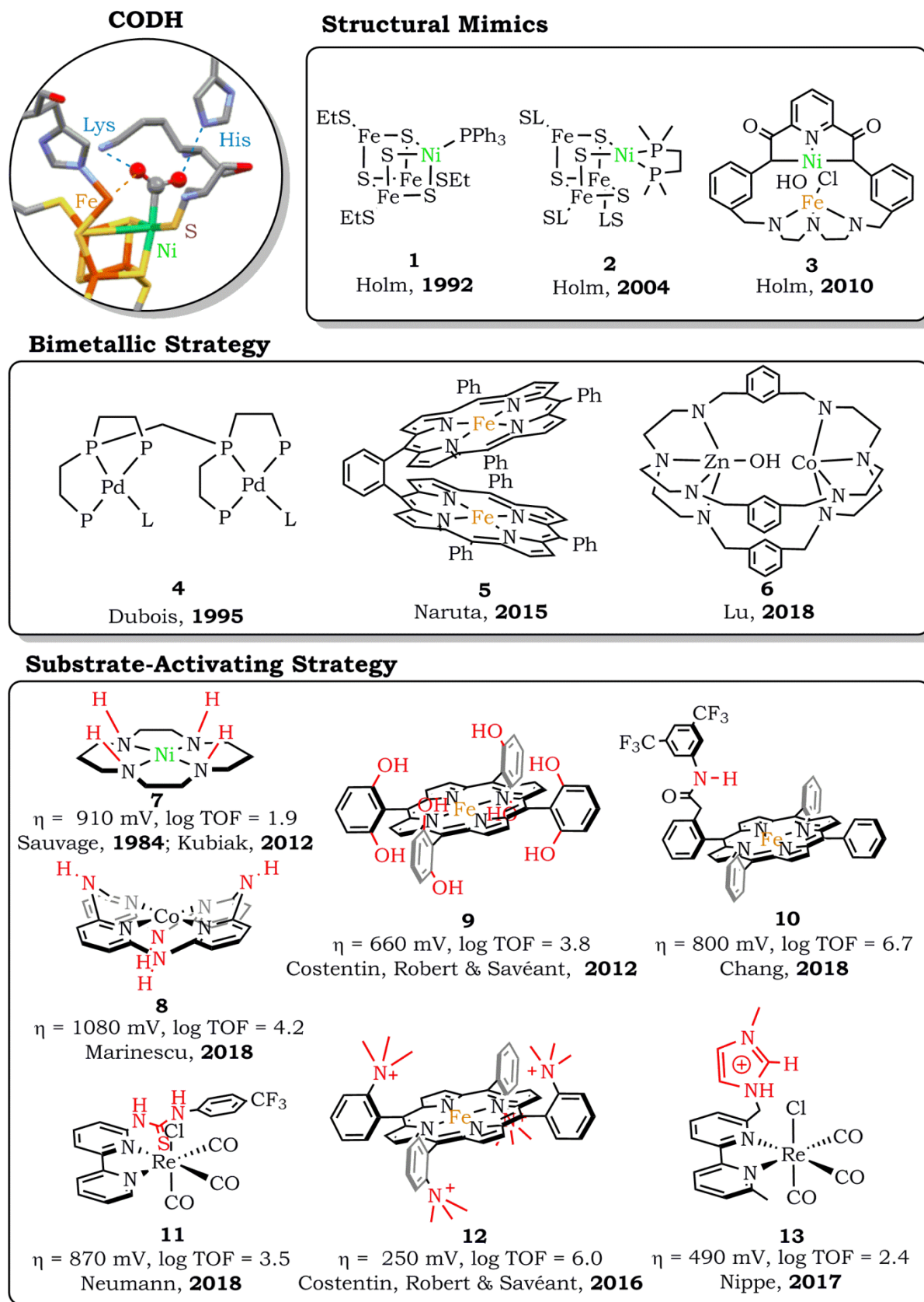


Figure 4-1. Active site of CO dehydrogenase (CODH) and some notable synthetic analogues showing bio-mimetic (structural) and bio-inspired (bimetallic and substrate-activating) strategies.

Two kinds of bio-inspired strategies were elucidated from key insights from CODH: (1) implementation of a bimetallic feature for CO₂ reduction resembling the Ni and Fe metals or (2) modifications of the secondary coordination sphere of catalysts to bring a substrate activating environment like the one created by nearby amino acid residues in the biological system. Palladium phosphine complexes, pioneered by the group of DuBois, have been shown to be highly active catalysts for CO₂ reduction to CO at low overpotentials^[18] but suffer from low CO₂ binding, which is considered as the rate determining step in the system. A bimetallic Pd catalyst was synthesized (Complex **4**)^[19] to increase the affinity for CO₂, mimicking the same activation in the metal centers in CODH. This strategy helped improve the electrocatalytic rate of the system but suffered from low turnover because of catalyst deactivation due to the formation of Pd-Pd bond. A similar bimetallic strategy was employed by Naruta in modifying the well-known CO₂-reducing iron porphyrin catalysts in a cofacial configuration shown in Complex **5**.^[20] Controlling the relative position of the porphyrin platforms by using a phenyl linker made it possible to control the distance between the Fe metals and an optimized catalytic rate was attained with an ortho configuration of the dimer. In this case also, no improvement of the overpotential was observed going from the monomer to the dimer. Recently the group of Lu has synthesized a variety of cryptates holding Ni-Ni,^[21] Co-Co,^[9] and even a heterometallic Co-Zn^[10] catalyst (Complex **6**) which all show improved photocatalytic activity compared to mononuclear counterparts. The Co-Zn system is one of the few dinuclear heterometallic catalysts closely reproducing the roles proposed for the bifunctional activation in CODH (Ni metal as redox active center while Fe metal as substrate-activating). Though recent progress in bimetallic strategy for CO₂ reduction catalysts is promising, the synthesis of bimetallic catalysts remains complicated and the formation of the M-M inactive species seems to be unavoidable in some cases.

The latter strategy consisting of introducing a second coordination sphere on the structure of the catalyst offers more versatility as evidenced by the rich literature on catalysts for the activation of small molecules like H⁺/H₂ ^[17,22,23] and O₂/H₂O^[24–26]. Such strategy is just gaining momentum for improving CO₂ reducing catalysts but has already shown some promising results, as discussed in Chapter 1. DFT studies on the Ni cyclam catalyst^[27] show that a *trans* I isomer of the catalyst (shown in Complex **7**) is more favorable in stabilizing a CO₂ substrate by hydrogen bonding to the NH protons of the ligand. A systematic study was performed by the

group of Marinescu on the effect of pendant secondary amines as proton relays on a cobalt pyridine macrocycle and showed a linear dependence on the number of pendant amines in the second coordination sphere.^[28,29] Unlike the metal cyclams, the pendant amines lie completely outside the primary coordination sphere of the metal allowing different roles of the amines as proton relays facilitating noncooperative hydrogen bonds with the acids in the solution. However, this improved catalytic activity comes at the cost of high overpotential (1080 mV). Other H-bond donors are reported in the form of guanidines in an iron hangman porphyrin by the group of Nocera,^[30] positional amides in similar iron hangman porphyrins by the group of Chang,^[31] and recently, thioureas in a Re catalyst by the group of Neumann.^[32] The relative position with respect to the metal center of such H-bond donors is critical for the resulting catalytic activity as observed in a systematic study by Chang where ortho amides are better than the corresponding para configuration and a distal positioning (ortho-2-amide, Complex **10**) is better than a proximal one (ortho-1-amide).^[31] Careful design must be put in place as the position can affect the mechanistic CO₂ reduction pathway as shown by the loss of performance of the thiourea-tethered Re catalyst (Complex **11**) in the presence of external proton source (i.e. water).^[32] Though these pendant H-bond donors improve the catalytic rates compared to the catalyst, they still don't significantly improve the overpotential of the system.

Local proton sources on the periphery of the catalysts were also implemented in the form of phenols in iron porphyrins (Complex **9**) by the group of Costentin, Robert and Savéant,^[33-35] phenols in Mn catalyst by the group of Nervi^[36] and Bocarsly,^[37] tyrosine residues in Re catalyst by the group of Kubiak,^[38] and carboxylic acids in water-soluble Ni cyclam^[39] and Mn bipyridine^[40] catalysts by the group of Cowan. Though such functionalities have been shown to stabilize the CO₂ adduct, the modified catalysts didn't display significant improvements in overpotential and turnover frequency (TOF). Substantial improvements of both catalytic rates and overpotential were observed when cationic groups such as trimethylammonium were introduced in iron porphyrins (Complex **12**) reported by Costentin, Robert, and Savéant.^[41] The specific positioning in the *ortho* position of the aryls promotes through-space electrostatic interactions between the positive charges of substituents and the negative charge of an Fe-CO₂ adduct resulted in a significant decrease in overpotential while simultaneously increasing the TOF.^[5] The same class of catalyst was also reported to photo-catalytically reduce CO₂ to CH₄

when coupled to an Ir-based photosensitizer.^[42–44] Recently, the group of Nippe combined the synergistic effects of H-bond donors and electrostatic interactions by introducing imidazolium moieties in the periphery of the Re (Complex **13**) and Mn bipyridine catalysts.^[45,46] Though the overpotentials are lowered for these modified catalysts, the TOFs are still relatively low.

4.2 Objectives

Inspired by the exceptional efficiency and stability of CODH enzymes in reversibly reducing CO₂ to CO, we envisioned a strategy of introducing substrate-activating and intermediate-stabilizing functions in the second coordination sphere of CO₂ reduction catalysts, as shown in Figure 4-2, to obtain insights and understandings to guide the use of the growing synthetic tools for improving catalyst performance. Specifically, this chapter aims:

- To investigate the effects of the number of distal amines placed on the ortho position of bipyridyl ligands (6,6' sites) of rhenium tricarbonyl bipyridine catalysts
- To investigate the effects of urea and amide groups as functional clefts ($\alpha\beta\alpha\beta$ configuration) in an iron porphyrin catalyst
- To investigate the effects of introducing cationic imidazolium moieties in a picket-fence ($\alpha\alpha\alpha\alpha$ configuration) iron porphyrin catalyst

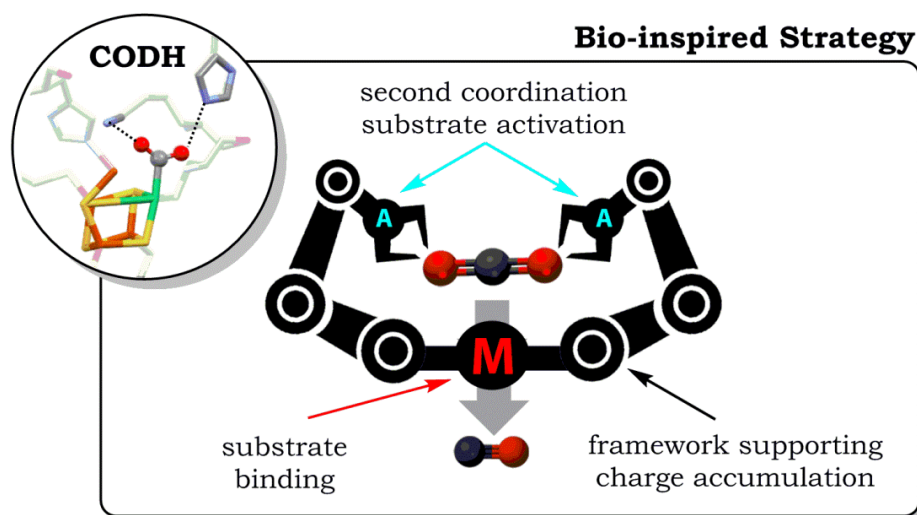


Figure 4-2. General bio-inspired strategy focusing on second coordination substrate activation in improving CO₂ reduction catalysts.

4.3. Implications of Proximal Amines

From the key observation of the presence of amino acid residues in the vicinity of the Ni active site in CODH, we initially investigated the effect of similar amino groups in the vicinity of the metal of CO₂ reduction catalysts. Bio-inspired modifications of the well-known Re catalyst include the introduction of a functional group, such as phenol^[38,47], amide,^[38] thiourea^[32], and imidazolium,^[45] all designed to provide single-point hydrogen bonding interactions with the CO₂ substrate. Di-substituted bipyridyl ligands on the 4,4' positions have been reported for biomimetic groups such as carboxylic acids,^[48] hydroxymethyl groups,^[49] peptide-length tyrosine residues^[38], as well as other non-biomimetic functions.^[50] Substitutions on the 6,6' positions are rare^[51] and recent bio-inspired reports^[32,45,46] only show mono-substitutions. With the goal of further improving the efficiency of the Re catalyst by bio-inspired modifications, the synthesis of 6-amino-substituted bipyridyl ligand for **ReAm1** and a 6,6'-diamino substituted bipyridyl ligand for **ReAm2** was performed, as shown in Figure 4-3, to mimic the multi-point stabilization roles of the lysine and histidine residues found within the active site of CODH. The choice of the substitutions was motivated by the ease of synthesis starting from commercially available ligands. Systematic study of these catalysts would provide an understanding of the effects of proximal modifications on 6,6' positions of the bipyridyl ligand, as well as the effect of number of available H-bond donors, on the performance of the catalyst.

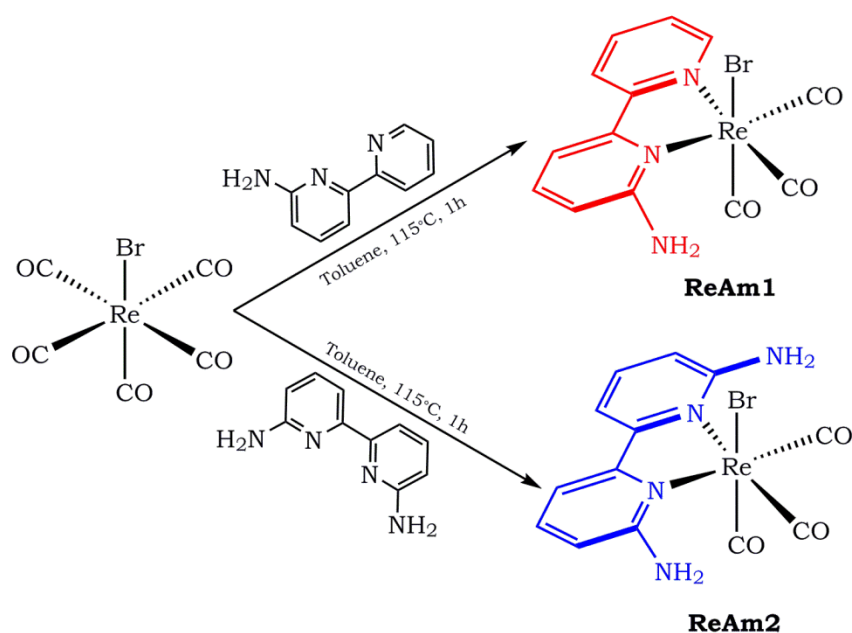
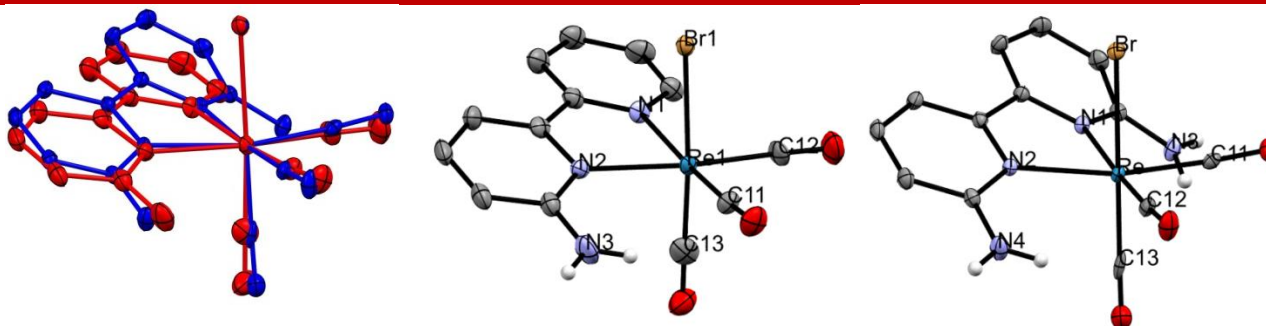


Figure 4-3. Synthesis of rhenium triscarbonyl mono-amino (**ReAm1**) and di-amino (**ReAm2**) substituted bipyridyl catalysts.

Table 4-1. X-ray crystal structures (ORTEP thermal ellipsoids set at 50% probability) and selected bond lengths and angles of **ReAm1** and **ReAm2**. Superposition of the crystal structures (red – **ReAm1**, blue – **ReAm2**) is also shown on the top left. Hydrogen atoms are omitted for clarity except the ones from amines.



	ReAm1	ReAm2
Re-Br, Å	2.6314(7)	2.6381(4)
Re-N1, Å	2.175(6)	2.181(2)
Re-N2, Å	2.194(6)	2.183(2)
\angle Br-Re-N1, °	83.6(2)	83.68(5)
\angle Br-Re-N2, °	85.5(2)	83.40(5)
\angle C13-Re-N1, °	94.6(3)	98.26(8)
\angle C13-Re-N2, °	91.1(3)	96.55(8)

X-ray structures obtained from single crystals of **ReAm1** and **ReAm2** show the typical octahedral ligand arrangement with facial triscarbonyl moiety, even maintaining similar bond lengths, as reported in Table 4-1. A distinguishing feature is observed however on the deviation of the bipyridyl ligand from the horizontal plane of the octahedron, clearly seen on the superposed structures. The presence of one amino group in the 6 position of the bipyridine in **ReAm1** deviates the \angle C13-Re-N1 angle to 94.6° and adding a second amino group in the 6,6' positions in **ReAm2** induces even greater deviation (98.26°). This significant deviation is not observed in the nonfunctionalized Re catalyst or other reported mono-substituted^[38,45,47] or di-substituted bipyridyl ligands.^[48] These deviations don't affect the Re-Br bond length in the initial state of the catalyst, though they may play a role once the Br is lost in the doubly-reduced active form, and as such they might affect the resulting activity of the system.

The electrochemical features of the modified **ReAm1** and **ReAm2** catalysts were compared with those of nonfunctionalized **Re** catalyst, as shown in the Cyclic Voltammograms (CVs) in Figure 4-4. As the number of amines is increased, the first

reduction potential is shifted towards more negative potential. The bpy-based first reduction potential decreases by about 100 mV for every amino group introduced on the 6,6' position. This shift can be mainly attributed to the strong electron donating nature of the amines via resonance effects with the bipyridine ligand. A loss of reversibility in the first reduction peak was also observed when the number of amine ligands increase, indicating a more labile halide once a first electron is transferred to the bipyridine ligand. The second reduction, which is reported to be a metal-centered reduction, is similarly shifted towards more negative potentials with greater cathodic shift for **ReAm2** (330 mV) compared to **ReAm1** (60 mV).

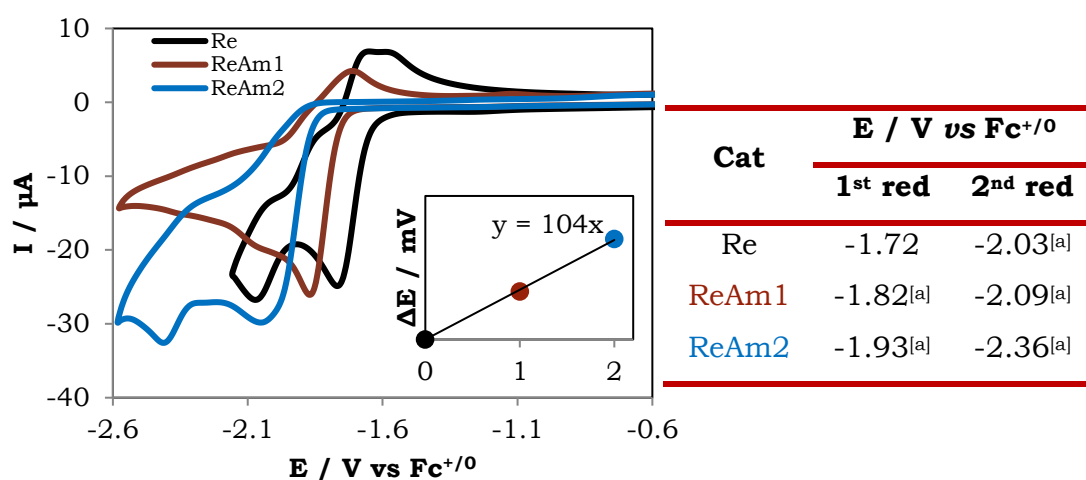


Figure 4-4. Cyclic voltammograms of 1 mM **ReAm1** (red) and **ReAm2** (blue) in comparison with the nonfunctionalized **Re** catalyst (black) in Ar-purged ACN with 0.1 M TBAP at a scan rate of 100 mV/s. Inset shows the effect on the first reduction potential peak of each addition of amine (slope = mV / amine).

^[a] For irreversible peaks, potentials at half-wave point are reported.

To rationalize the observed electrochemical differences between the two modified Re catalysts, infrared spectroelectrochemistry was employed to further understand the transformation induced by reduction process. In the unreduced forms, both **ReAm1** and **ReAm2** show the typical three sharp C=O stretching peaks at 2022 cm⁻¹, 1915 cm⁻¹ and 1899 cm⁻¹ for **ReAm1**, and 2023 cm⁻¹, 1916 cm⁻¹ and 1896 cm⁻¹ for **ReAm2** (Figure 4-5 and Table 4-2). These IR peaks compare well to those of the nonfunctionalized **Re** catalyst, as shown in Figure 4-7a. Though structural differences are observed in the crystal structures of these catalysts, it seems that the deviation of the bipyridyl ligand from the horizontal plane does not have a significant effect on the stretching modes of the surrounding carbonyl ligands in the unreduced form of the catalysts.

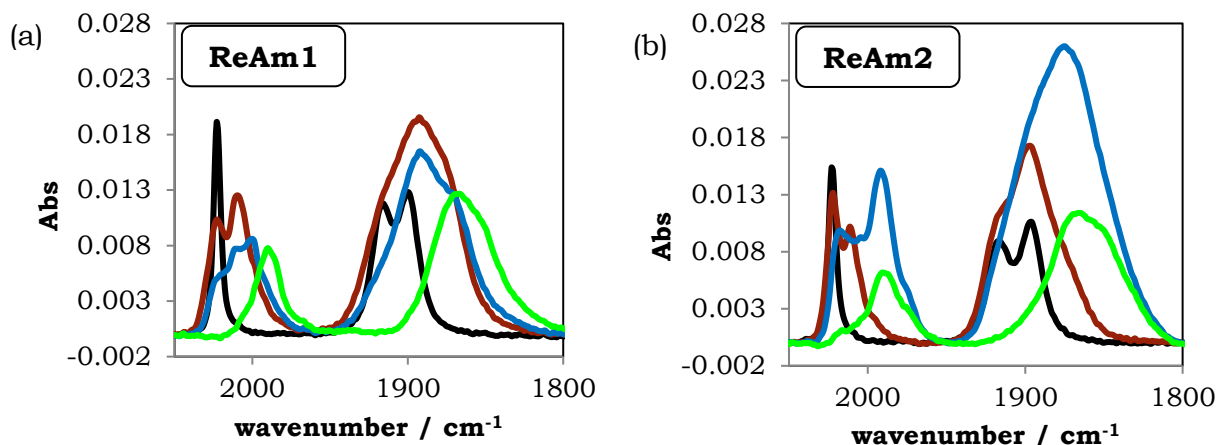


Figure 4-5. Spectra of observed species during IR spectroelectrochemistry of (a) **ReAm1** and (b) **ReAm2** in ACN with 0.1 M TBAP under N_2 atmosphere. (Colors correspond to cycle proposed in Figure 4-6: black – unreduced species, red – singly-reduced species, blue – solvated doubly-reduced species, and green – unsolvated doubly-reduced species). Condition consisted of 100 s electrolysis per 50 mV stepwise reduction and as such, contributed to persistence of some peaks in the proceeding potential steps; intermediates attained at the following V vs $Fc^{+/0}$, **ReAm1**: -1.79, -1.89, -2.29; **ReAm2**: -1.84, -2.24, -2.54;

Table 4-2. Values of IR peaks observed for reduced species of **ReAm1** and **ReAm2** identified during IR spectroelectrochemistry in ACN containing 0.1 M TBAP under N_2 atmosphere.

Species	IR peaks, cm^{-1}	
	ReAm1 (R = NH_2 , R' = H)	ReAm2 (R = R' = NH_2)
$[Re(CO)_3(bpy-R,R')Br]$	2022, 1915, 1899	2023, 1916, 1896
$[Re(CO)_3(bpy-R,R')(ACN)]\cdot$	2009, 1892 br	2010, 1896
$[Re(CO)_3(bpy-R,R')(ACN)]^-$	1999, 1892, 1870	1992, 1876 br
$[Re(CO)_3(bpy-R,R')]^-$	1989, 1868 br	1988, 1866 br

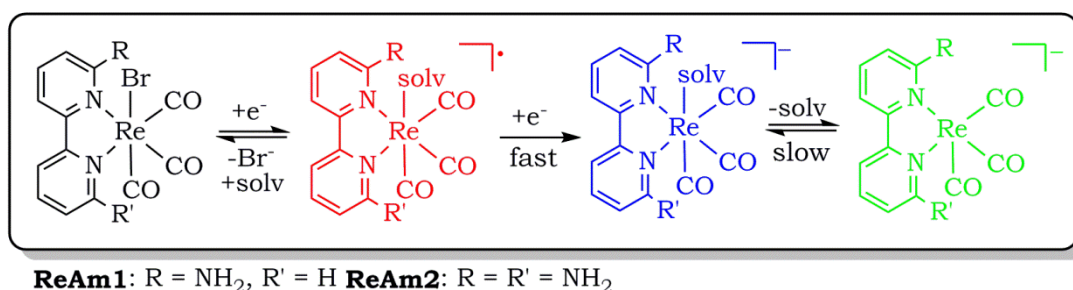


Figure 4-6. Proposed catalytic cycle for the modified catalysts **ReAm1** and **ReAm2**.

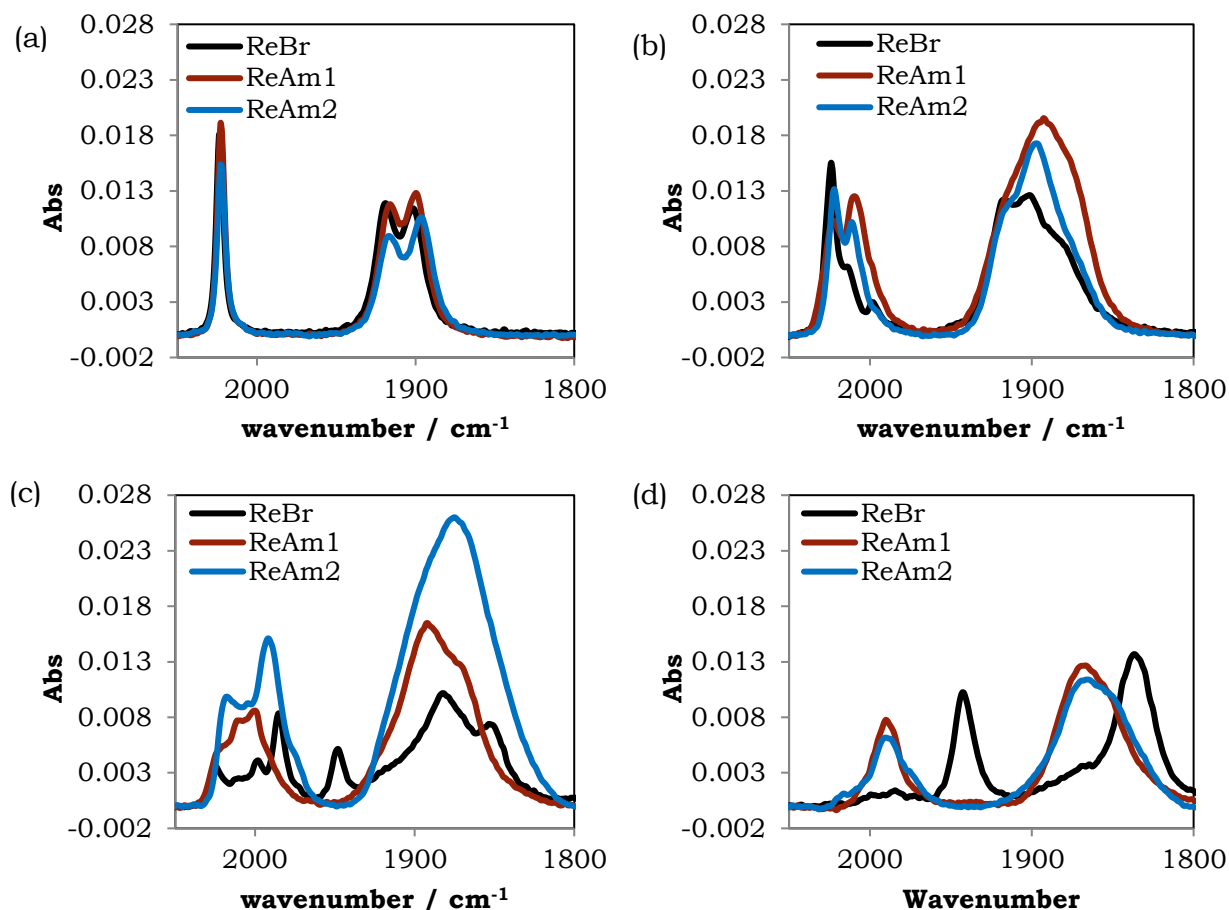


Figure 4-7. Comparison of the IR spectral signatures of the redox species of Re (black), **ReAm1** (blue), and **ReAm2** (red): (a) unreduced species, (b) singly reduced species, (c) solvated doubly reduced species, and (d) unsolvated doubly reduced species.

The one-electron reduced species show IR peaks at 2009 cm^{-1} and 1892 cm^{-1} for **ReAm1** and similar peaks for **ReAm2** (2010 cm^{-1} and 1896 cm^{-1}). The absence for both catalysts of a peak at 1998 cm^{-1} ,^[52] attributed to the presence of the halide in the nonfunctionalized Re catalyst, indicate that the first electron reduction induces the loss of the halide and it is possibly replaced by ACN solvent, $[\text{Re}(\text{CO})_3(\text{bpy-}\mathbf{R},\mathbf{R}')](\text{ACN})^+$. This indicates that the halide is more labile in these modified catalysts. The loss of reversibility of the first reduction peak observed in the cyclic voltammetry measurements is in accordance with this halide loss. It should be noted that no significant changes in the carbonyl stretching values were observed between the nonfunctionalized and the substituted catalysts.

When a potential corresponding to the second reduction is gradually applied to the catalysts, the C=O stretching observed at 2009 cm^{-1} , attributed to the axial carbonyl ligand, is shifted towards lower wavenumbers in **ReAm1** (1999 cm^{-1}) and

ReAm2 (1992 cm^{-1}) with a broadening of the stretching of the other carbonyls (1870 cm^{-1} for **ReAm1** and 1876 cm^{-1} for **ReAm2**) is observed. The decrease of the wavenumber corresponds to better stabilization of the carbonyl ligands due to the increased π back-bonding from the reduced metal to the CO ligand. This reduced species can be formulated as $[\text{Re}(\text{CO})_3(\text{bpy-R,R}')(\text{ACN})]^-$, with an ACN molecule in the coordination sphere, based on comparison of the IR peaks with literature reports on nonfunctionalized **Re** catalyst. Further electrolysis eventually removes this coordinated solvent, giving the penta-coordinated doubly reduced form, $[\text{Re}(\text{CO})_3(\text{bpy-R,R}')]$. This form is characterized by IR absorption bands at 1989 cm^{-1} and 1868 cm^{-1} for **ReAm1** and very similarly observed in **ReAm2** (1988 cm^{-1} and 1866 cm^{-1}). The IR peaks of this final active form are shifted to higher wavenumbers (higher vibrational energy) compared to the IR peaks observed in the nonfunctionalized **Re** catalyst shown in Figure 4-7d. This is indicative of the destabilization of the C=O ligands either due to the presence of the amino groups in the proximal position of the bipyridyl ligand (6,6' position) or the relocation of electron density away from the carbonyl ligands once a pentadentate doubly reduced form is attained. This destabilization does not depend however on the number of amines (no difference in wavenumbers between **ReAm1** and **ReAm2**), indicating that already one amine placed in the 6/6' position of the bipyridyl ligand causes such higher energy stretching of the carbonyl ligands of the doubly-reduced form. This effect of amino substitution observed by IR spectroscopy could indicate differences in the activity of the modified catalysts compared to the nonfunctionalized one. How it translates to catalytic activity is another aspect that needs to be further investigated because IR spectral changes from this active form are not easily tracked under catalytic conditions.

The electrocatalytic activity of the modified catalysts was then investigated by performing CVs in the presence of CO_2 substrate and proton source (Figure 4-8). In the presence of CO_2 , some enhancement of the cathodic current is observed on the second reduction wave. More significant enhancements can be observed in the presence of weak Brønsted acids like water or trifluoroethanol (TFE). Similar behavior was observed when the nonfunctionalized **Re** catalyst was first reported by the group of Lehn^[53] and in a systematic study by the group of Wong on the effect of Brønsted acids on such catalysts. The catalytic enhancement is also strongly dependent on the $\text{p}K_a$ of the acid added as evidenced by the difference in the

intensity of catalytic current when water (pK_a in ACN = 38-41)^[54] was replaced by the stronger acid TFE (pK_a in ACN = 35.4).^[55]

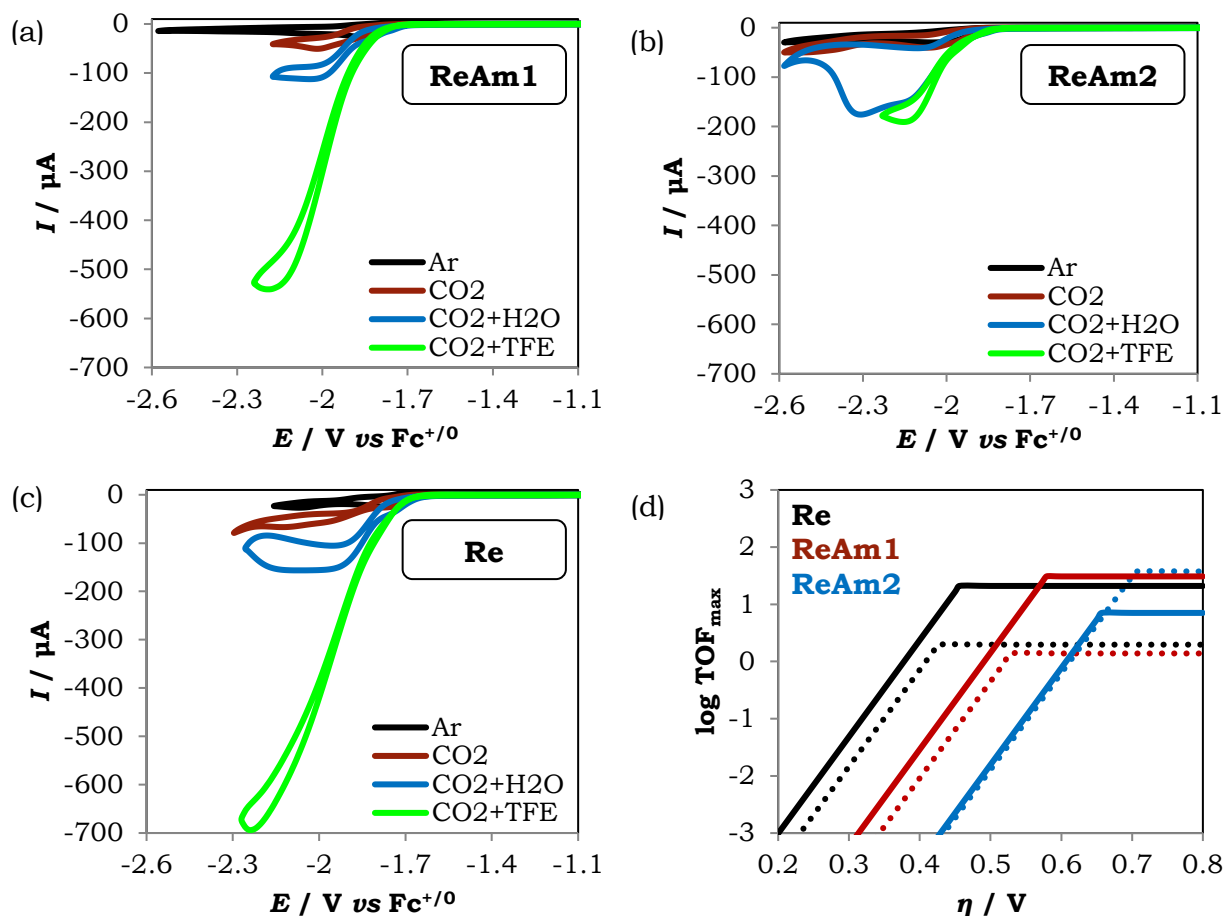


Figure 4-8. Cyclic voltammograms of 1 mM of catalysts: (a) **ReAm1** (b) **ReAm2**, and (c) **Re**, in the presence of Ar (black), CO₂ (red), CO₂ + 5.5 M H₂O (blue), and CO₂ + 700 mM TFE (green) in ACN containing 0.1 M TBAP at a scan rate of 100 mV/s. (d) Comparison of catalytic Tafel plots (**Re** – black, **ReAm1** – red, **ReAm2** – blue; with water (dotted line) or TFE (solid line) as proton source water; see Annex for calculation details).

For more thorough comparison of the performance of the modified catalysts with that of the nonfunctionalized **Re** catalyst, we used foot-of-the-wave (FOW) analysis method developed by the group of Costentin, Robert, and Savéant.^[56] In this analysis, the kinetics of the catalytic reaction represented by turnover frequency (TOF) is associated with the overpotential (η) at which the catalyst operate (see Annex for calculation details). A catalytic Tafel plot can be extracted from this analysis with a plot of \log of TOF versus overpotential. Good catalysts can easily be identified as having low overpotentials while having high TOF, which would translate to an upper left deviation of the plot.

From the catalytic Tafel plots in Figure 4-8d, it can be observed that the plots of **ReAm1** and **ReAm2** are shifted to the right because of the higher overpotentials needed for the modified catalysts as initially hinted by electron donating effect of the amines. The higher the number of amines introduced in the 6,6' positions of the bipyridine, the greater is the catalytic overpotential. The plot shown in Figure 4-9 also displays that values for TOF are affected by the nature of the proton source. When water (pK_a in ACN = 38-41)^[54] is used as a proton source, the TOF_{max} of **ReAm1** is not too different from the nonfunctionalized **Re** catalyst but is significantly enhanced in the case of **ReAm2**. When a more acidic source of proton is used like TFE (pK_a in ACN = 35.4),^[55] there is some improvement in the TOF_{max} of **ReAm1** but the TOF_{max} of **ReAm2** is significantly lower than that of the nonfunctionalized **Re** catalyst. This trend of activities obviously goes beyond the electronic effects of increasing number of proximal amines in the bipyridyl ligand, as the typical electronic scaling would suggest a higher TOF_{max} for higher overpotentials, as observed in iron porphyrin catalysts.^[5] This could be due to (i) the interplay of the effects of the amines on both the first and second coordination sphere, (ii) the unsuitable positioning of the amines relative to the CO_2 adduct, and/or (iii) some unexpected mechanistic deviations during catalytic conditions. From these investigations, key learnings for catalyst design would then include (i) the need for isolation of the second coordination sphere from the first coordination sphere and (ii) the need for carefully designed ligand geometries to provide the necessary activation of the CO_2 adduct.

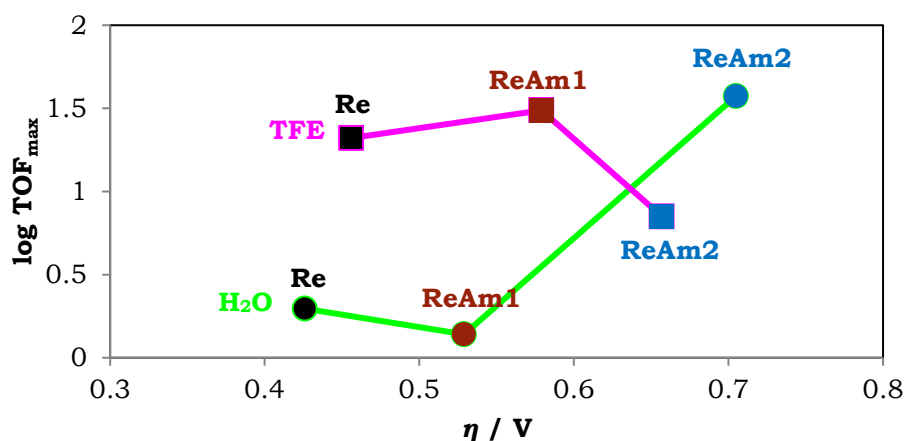


Figure 4-9. Comparison of the TOF_{max} and catalytic overpotentials of **ReAm1** (red) and **ReAm2** (blue) with the nonfunctionalized **Re** catalyst (black). Effect of proton source is shown with water (green line, circular markers) and TFE (pink line, square markers).

4.4. Urea and Amide Moieties as Hydrogen-Bond Relays

Reports have shown promise for amide and urea as potential bio-inspired functions for activating the CO₂ substrate. As previously discussed, a single amido group had been placed on the bipyridyl ligand of a rhenium catalyst by the group of Kubiak^[38] and positional effects of second-sphere amide functions have been systematically investigated by the group of Chang in an iron hangman porphyrin.^[31] Recently, the group of Das has reported a crystallographic structure of a neutral urea scaffold that fixes atmospheric CO₂ as carbonate clusters held together by an extended H-bonding network.^[57] The group of Chang have also leveraged this multipoint hydrogen bond donation of urea as an external additive to improve the electrocatalytic activity of nickel cyclam at the same overpotential.^[58] Neumann and coworkers have even tethered a thiourea function on the second coordination sphere of a rhenium catalyst that improved the electrocatalytic activity in the absence of external proton source.^[32] However, the presence of weak acids, such as water, inhibits the activity of the latter system which will be problematic when aligning with the sustainable goal of using water as a free source of electrons and protons.

In the quest of improving catalytic activities by a bio-inspired strategy mimicking the multipoint hydrogen bonding scheme of histidine and lysine residues in stabilizing the CO₂ adduct in CODH, two super-structured iron porphyrins holding in one case four urea functions (**FeTPPUR**) and in another four amido groups (**FeTPPAm**) were synthesized as shown in Figure 4-10. Both functions carried a phenyl ring bearing two -CF₃ motifs as electron withdrawing groups to enhance hydrogen bonding aptitude of the NH fragments. Unlike studies utilizing hangman,^[31,59] and picket fence^[33,60] structures of porphyrins for CO₂ reduction, an $\alpha\beta\alpha\beta$ atropoisomer was chosen with the target to provide two sets of hydrogen bonding network in a *trans* fashion towards a metal bound CO₂ molecule and at the same time to confer two identical chemical faces on each side of the porphyrin molecular platform. As shown in Figure 4-10, the addition of four equivalents of 3,5-bis(trifluoromethyl)phenyl isocyanate or 3,5-bis(trifluoromethyl)benzoyl chloride to 5,10,15,20-*tetrakis*(2-aminophenyl)porphyrin with an $\alpha\beta\alpha\beta$ configuration (TAPP $\alpha\beta\alpha\beta$)^[61,62] leads respectively to porphyrin ligands bearing four urea (**TPPUR**) or four amido (**TPPAm**) groups. Iron insertion was then performed using ferrous bromide and 2,6-lutidine to attain the catalysts **FeTPPUR** and **FeTPPAm**.

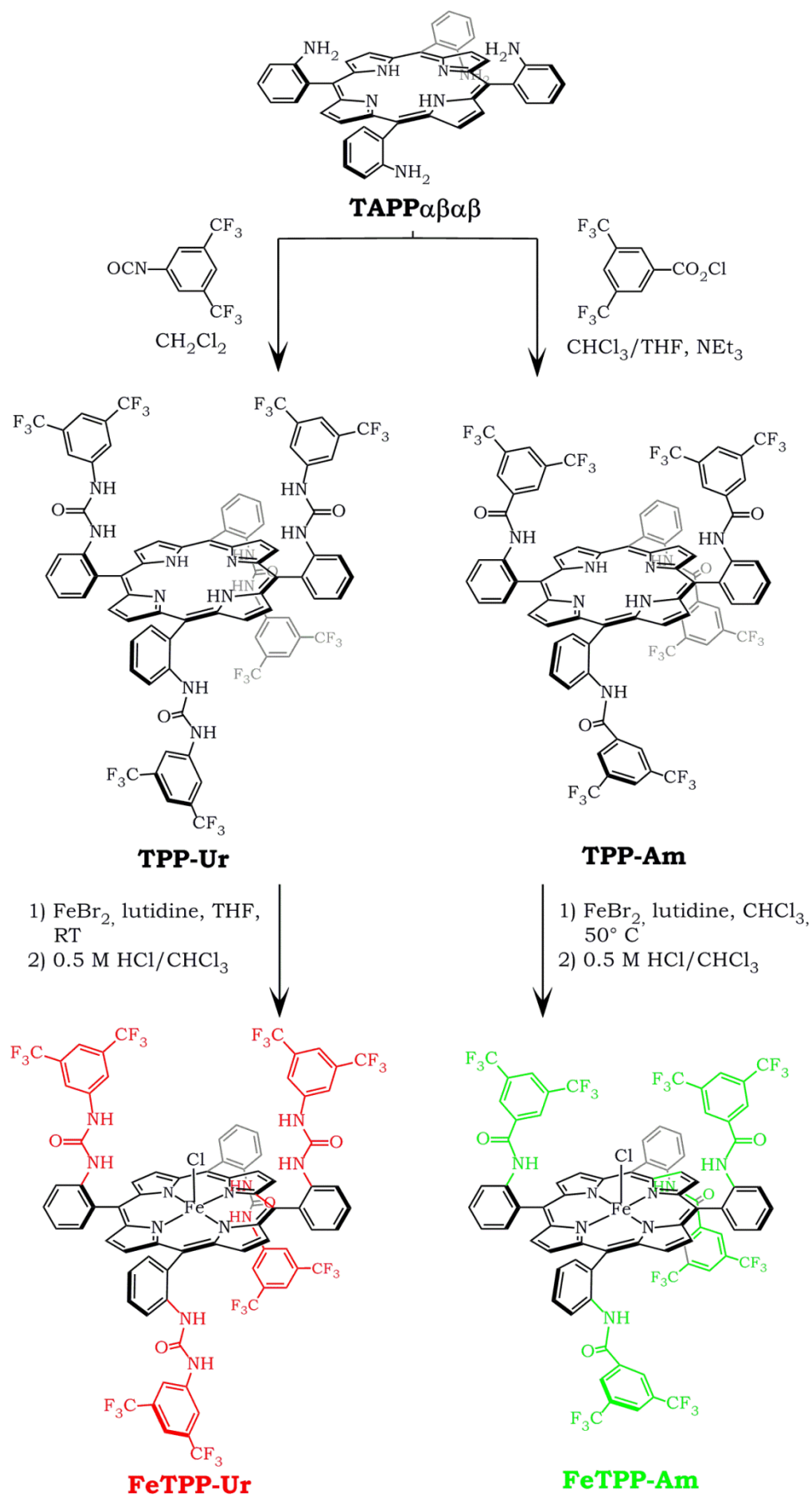


Figure 4-10. Synthetic scheme for the preparation of **FeTPP-Ur** and **FeTPP-Am**.

X-ray diffraction analyses were performed for both catalysts **FeTPPUr** and **FeTPPA_m**, as shown in Figure 4-11. The preservation of the $\alpha\beta\alpha\beta$ configuration was confirmed by the disposition of the tethered Ur and Am arms on the periphery of the porphyrin skeleton. For both complexes, the metric distances around the iron (III) center best fit with a high spin configuration with an axial methoxide ligand. Of note, the hydrogen atoms of the amido and the urea groups are oriented towards the iron catalytic center, with $\text{Fe}\cdots\text{H}$ distances of 4.840 Å for the amido groups and from 4.796 Å to 5.970 Å for the two hydrogen atoms of the urea groups, presaging potential hydrogen bond interactions with CO_2 adduct coordinated to the metal center.

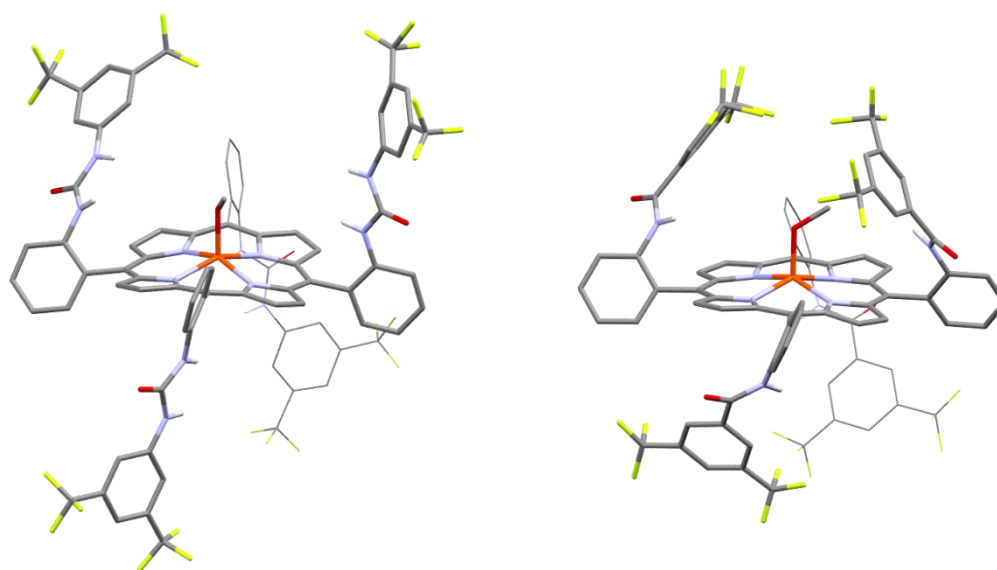


Figure 4-11. Wireframe and capped sticks representation of the X-ray structures of **FeTPPUr** (left) and **FeTPPA_m** (right) having methoxide anion as an axial ligand. Only urea and amide protons are explicitly shown, and solvent molecules are omitted for clarity.

The electrochemical properties of **FeTPPUr** and **FeTPPA_m** were studied using cyclic voltammetry in Ar-degassed DMF solution. In this study, we used as reference catalysts those of the nonfunctionalized iron porphyrin **FeTPP**, as well as its fluorinated analogues **FeTPPF₈** (containing 8 fluorine atoms) and **FeTPPF₂₀** (containing 20 fluorine atoms), as shown in Figure 4-12. Following a classic approach to lower the overpotential of iron porphyrins, the fluorine atoms were introduced at the periphery of iron porphyrins as electron withdrawing groups.

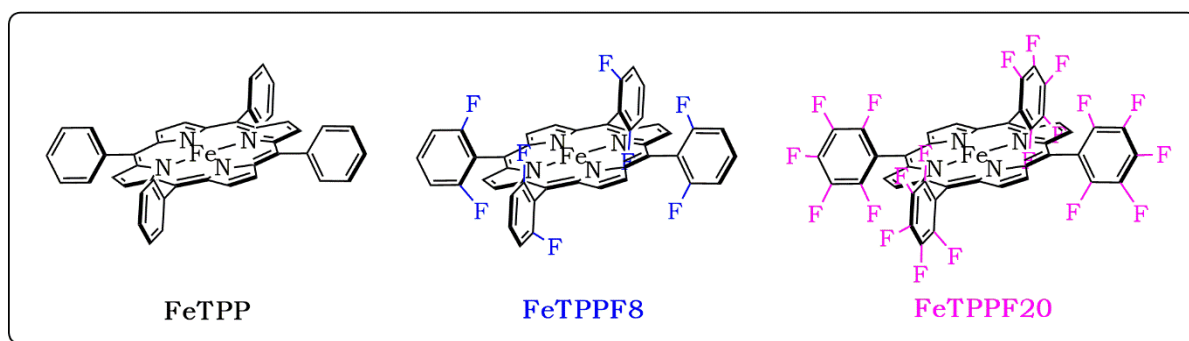


Figure 4-12. Reference complexes, including the nonfunctionalized **FeTPP**, and its fluorinated analogues **FeTPPF8** and **FeTPPF20** used for comparison.

The CV of **FeTPPUr** showed three reversible redox waves at -0.468 V, -1.326 V, and -1.812 V *vs* $\text{Fc}^{+/0}$, corresponding respectively to the formal $\text{Fe}^{\text{III}/\text{II}}$, $\text{Fe}^{\text{II}/\text{I}}$, $\text{Fe}^{\text{I}/0}$ couples (Figure 4-13). All three waves show an anodic shift when compared to those of **FeTPP** under similar experimental conditions. However, the third redox wave is markedly shifted by over 300 mV to more positive potential, a shift similar to that of **FeTPPF20**. This substantial shift cannot be attributed only to the withdrawing inductive effect of the two $-\text{CF}_3$ groups on the aryl ring at the other end of each urea groups. In the case of **FeTPPAm** holding the same fluorinated substituted aryl groups, only a small anodic shift was noted. Instead, the observation can be attributed also to the strong electron delocalization on the urea groups helping to contain the addition of electron on the catalytic unit.

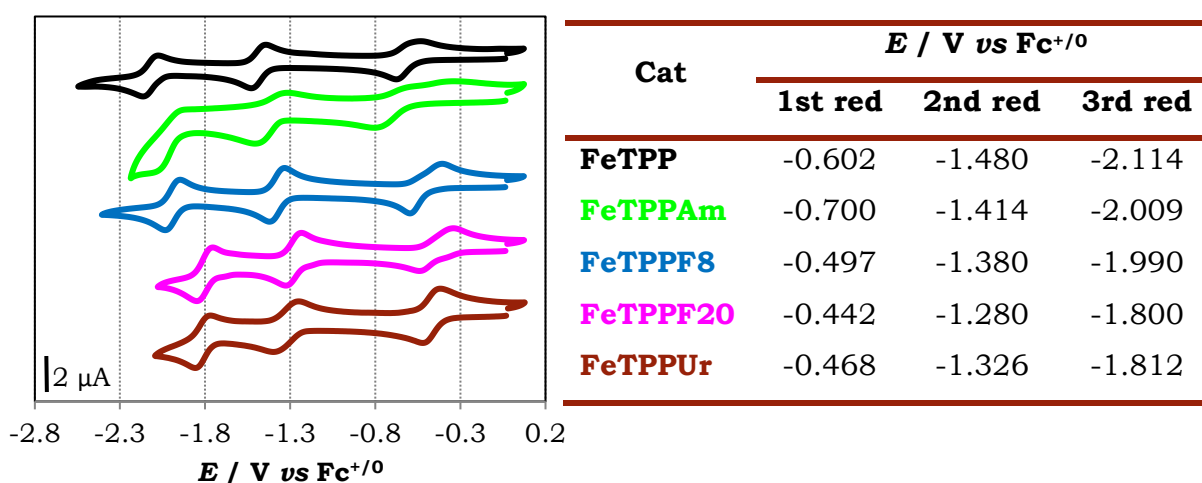


Figure 4-13. CVs of 1 mM **FeTPP** (black) and its modified analogues (green = **FeTPPAm**, blue = **FeTPPF8**, pink = **FeTPPF20**, red = **FeTPPUr**) in Ar-saturated DMF containing 0.1 M TBAP at a scan rate of 100 mV/s.

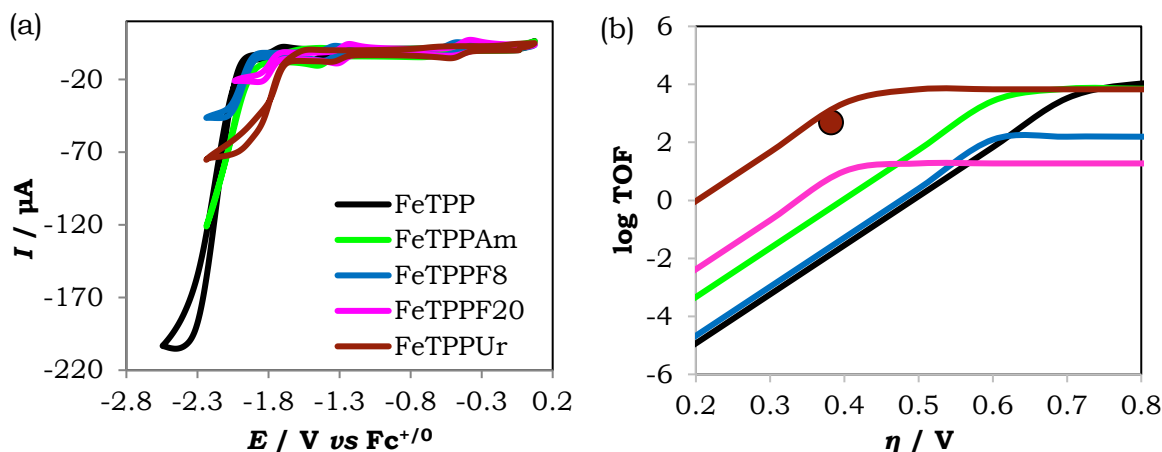


Figure 4-14. (a) CVs of 1 mM **FeTPP** (black) and its modified analogues (green = **FeTPPAm**, blue = **FeTPPF8**, pink = **FeTPPF20**, red = **FeTPPUr**) in CO₂-saturated DMF containing 0.1 M TBAP and 5.5 M H₂O at a scan rate of 100 mV/s. (b) Catalytic Tafel plot comparisons of the catalysts with the red dot corresponding to bulk electrolysis result of **FeTPPUr** (see Annex for calculation details).

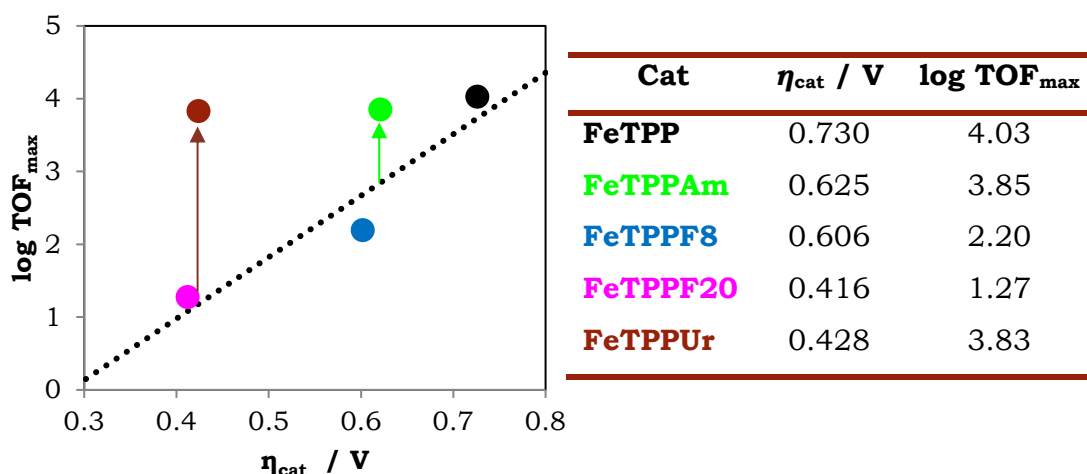


Figure 4-15. Comparison of the TOF_{max} and catalytic overpotentials of **FeTPPUr** and **FeTPPAm** with the expected electronic scaling effect observed in **FeTPP**, **FeTPPF8**, and **FeTPPF20**.

The CVs of reference complexes **FeTPP** and the fluorinated analogues **FeTPPF8** and **FeTPPF20** in CO₂-saturated solution show a catalytic current on the third reduction wave corresponding to the catalytic 2-electron reduction of CO₂ to CO (Figure 4-14a). As discussed previously by the group of Costentin, Robert, and Savéant, the counterpart of lowering the overpotential through classic incorporation of electron withdrawing groups, leads to a decrease in the TOF of the catalysts.^[5] This can be observed by the downward left shift of the catalytic Tafel plot in Figure 4-14b and the linear scaling relationship, called iron law (Figure 4-15), going from **FeTPP** to **FeTPPF8** and **FeTPPF20**. An escape from this iron law was exemplified

with catalysts having a local proton source or favorable second sphere interactions.^[33,41] In the case of **FeTPPAm**, where hydrogen bond interaction with amide groups can be expected, only a small upward left deviation is observed. This positive deviation is much more pronounced in the case of **FeTPPUr** catalyst which has comparable TOF to that of **FeTPP** but with ~300 mV less overpotential. These comparative studies indicate that the significant enhancement in **FeTPPUr** can be assigned to the multi-point hydrogen bonding induced by the urea groups compared to the single-point hydrogen bonding in **FeTPPAm**.

In a control experiment, the addition of an excess of urea as an external additive during the catalytic reduction of CO₂ by **FeTPP** did not bring any improvement to either the catalytic current or the catalytic potential (Figure 4-16). This result underlines the important aspect of the 3D pre-organization of the **FeTPPUr** catalyst which places the two urea groups on one side of the porphyrin platform in a position where all four hydrogen atoms of the urea groups can establish hydrogen bonding interactions with a CO₂ substrate on the metal-center from two opposite meso-positions of the porphyrin macrocycle. This result is a clear demonstration on the importance of positioning the hydrogen bonding patterns for optimizing the electrocatalytic properties of the bio-inspired catalyst **FeTPPUr**. It is not the sum of the additional NH interactions as compared to **FeTPPAm** derivative but should rather be considered as a close mimic of the lysine and histidine residues of CODH active site. Indeed, based on the structure-function proposal for the enzyme, this pair of amino acids conspires to stabilize a carboxylate intermediate (M-CO₂) through multi-point hydrogen bonding.^[11]

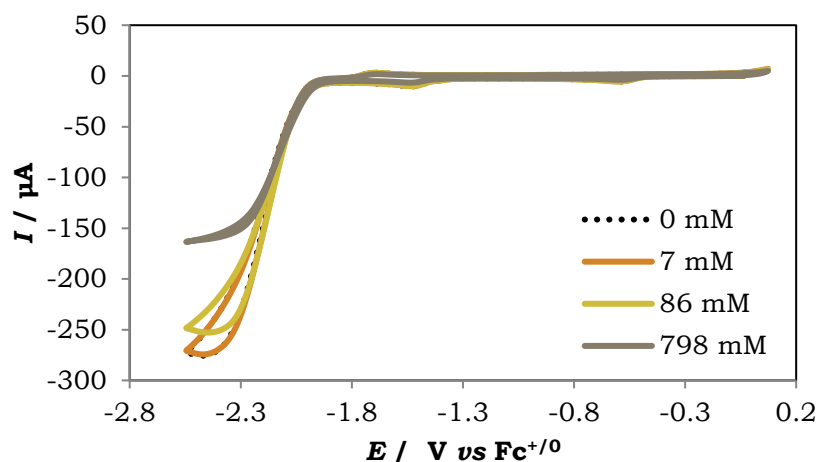


Figure 4-16. CVs of 1 mM **FeTPP** in the absence (dotted line) and presence of increasing amounts of external urea additive (solid line: 7 mM, 86 mM, 798 mM) in CO₂-saturated DMF containing 5.5 M H₂O.

The choice of introducing urea groups in the second coordination sphere of an iron porphyrin catalyst was motivated by their ability to bind oxygen atoms of carbonyl groups as well as carbonates.^[63–65] In some cases, urea groups can even capture atmospheric CO₂ as carbonates/bicarbonate.^[57] X-ray structures resolved from single crystals obtained by slow evaporation of H₂O/acetone-saturated solution of **TPPUr** porphyrin, revealed the presence of four acetone molecules bound to the four urea groups through N-H···O=C hydrogen bonding interactions (Figure 4-17), confirming the stabilization of the carbonyls by urea moieties.

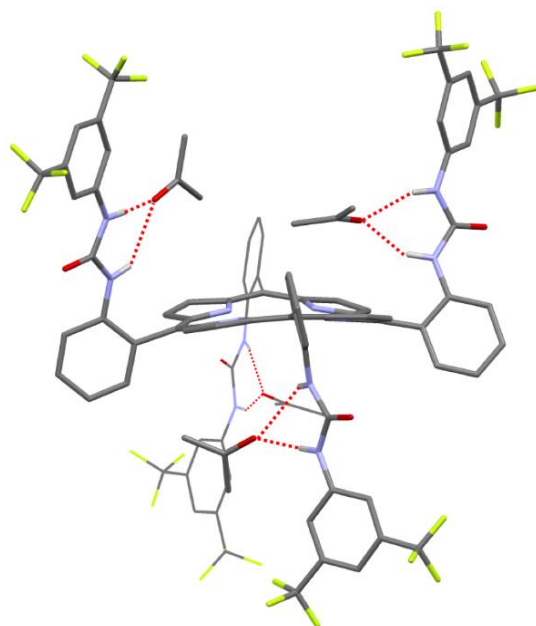


Figure 4-17. Wireframe and capped sticks representation of the X-ray structure of **TPPUr** showing H-bonding interactions between the hydrogen atoms of urea and the carbonyl of acetone molecules.

In order to assess the contribution of the urea arms to the binding affinity of CO₂, the CV of **FeTPPUr** was performed under CO₂ but in the absence of a proton source. In these conditions, where the catalytic 2-electron and 2-proton reduction of CO₂ cannot proceed, both a loss of reversibility and an anodic shift of the third reduction wave was observed (Figure 4-18c). These characteristics are unprecedented for **FeTPP** catalyst (Figure 4-18a) but were reported as indicative of a good CO₂ binding for other macrocyclic catalysts.^[66,67] For a thorough comparison, the CO₂ binding rate constants was estimated using the reported method by Savéant based on irreversible kinetics upon CO₂ binding (see Annex for calculation details). It was found that the CO₂ binding rate constant of **FeTPPUr** to be an order of magnitude higher than that of reference compounds such as **FeTPP** or even **FeTPPAm** (Table inset in Figure 4-18).

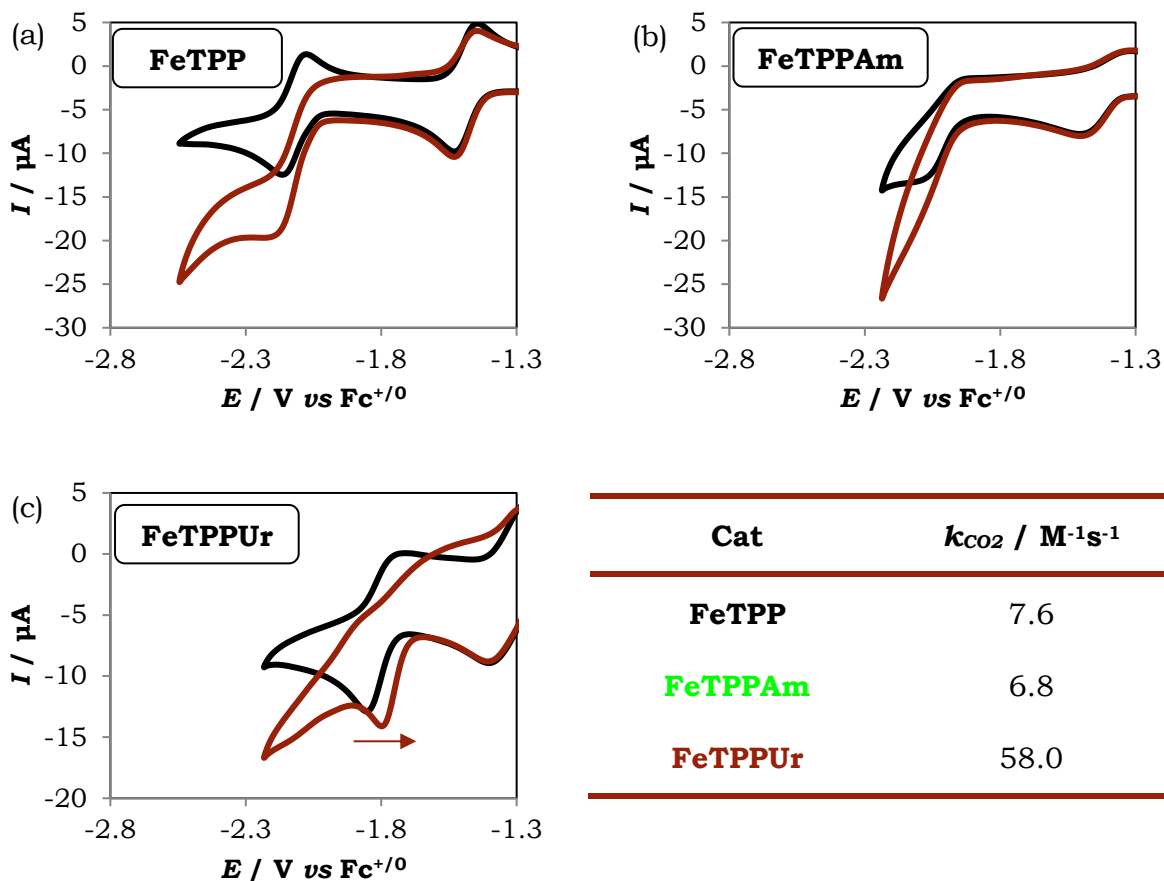


Figure 4-18. CV of 1 mM catalyst: (a) **FeTPP**, (b) **FeTPPAm**, and (c) **FeTPPUr** in the absence (black) and presence of CO_2 (red) in dry DMF at a scan rate of 100 mV/s. The table displays the estimated CO_2 binding rate constant based on reported method^[68] considering irreversible kinetics upon CO_2 binding (see Annex for calculation details).

However, this increased CO_2 binding affinity may not be the only parameter to account for the high catalytic performance of **FeTPPUr**. As discussed, a stabilization of reactive intermediates such as Fe- CO_2 species through hydrogen bonding interactions with the NH of urea groups may also contribute. To back up this hypothesis, density functional theory (DFT) calculations were performed on model compounds to investigate on the possible geometry of the CO_2 adducts of the triply reduced iron porphyrins. In the case of **FeTPPAm**, only two weak hydrogen bonding interactions between the amide arms and the coordinated CO_2 substrate were found, as shown in Figure 4-19, with $\text{H}\cdots\text{O}$ donor-acceptor distances of 2.007 Å and 2.345 Å, with average $\text{N}\cdots(\text{H})\cdots\text{O}$ distance of 3.187 Å. In marked contrast, two strong hydrogen bonds were engaged by each urea arms of **FeTPPUr** yielding four short $\text{H}\cdots\text{O}$ distances of 1.756 Å, 1.759 Å, 1.880 Å, and 1.888 Å, with an average

$\text{N}\cdots(\text{H})\cdots\text{O}$ distance of 2.802 Å comparable to those evidenced in the active site of the CODH (2.637 and 2.884 Å with Lys and His residues, respectively). This multipoint anchoring of CO_2 is responsible of a free enthalpy of stabilization of 29 kcal mol⁻¹.

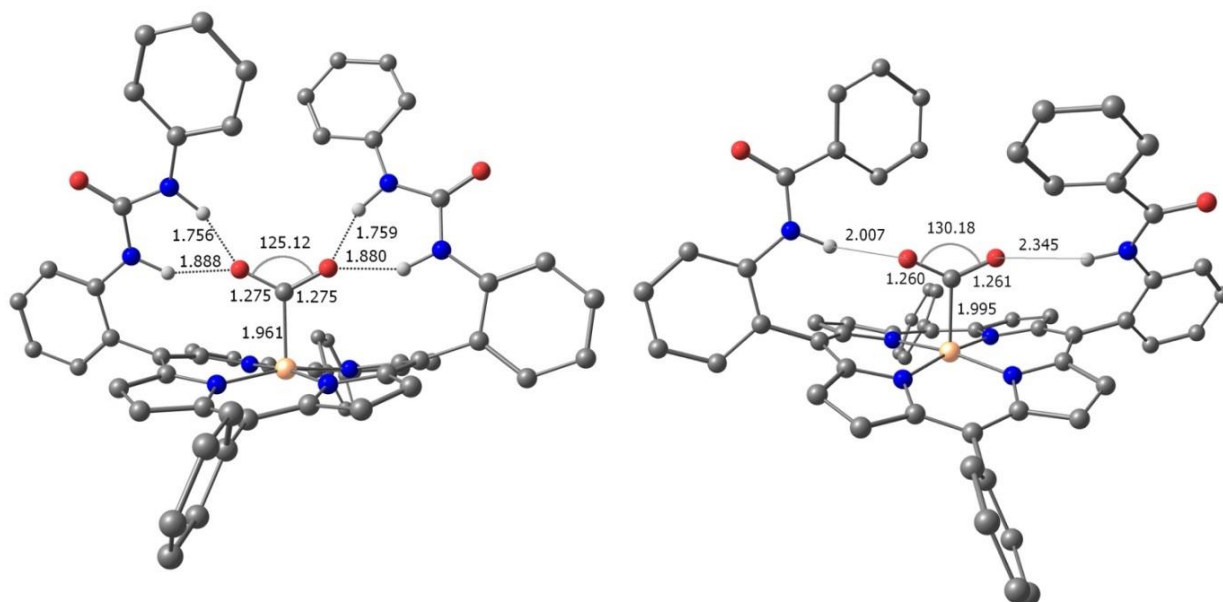


Figure 4-19. Optimized geometries of model compound $[\text{FeTPPUR-CO}_2]^{2-}$ (left) and $[\text{FeTPPAm-CO}_2]^{2-}$ (right) showing main structural parameters.

The proton source, a pre-requisite for the reduction of CO_2 , was further interrogated. A 5.77 normal kinetic isotope effect (KIE) was measured for the electrocatalytic reduction of CO_2 by **FeTPPUR** with $\text{H}_2\text{O}/\text{D}_2\text{O}$ as a proton source indicating that proton transfer is involved in the rate-determining step (Figure 4-20a). The investigation was extended to other sources of proton currently used in this field, i.e. trifluoroethanol (TFE) and phenol (PhOH), by comparing the catalytic rates estimated from the FOW analysis. Although H_2O is less acidic ($\text{p}K_{\text{a}}$ in DMF = 31.5) than TFE ($\text{p}K_{\text{a}}$ in DMF = 24.0) or PhOH ($\text{p}K_{\text{a}}$ in DMF = 18.8),^[69] surprisingly, it has by far the most marked effect on improving the catalytic rate compared to PhOH or TFE (Figure 4-20b). This result is in sharp contrast with a recent study by the group of Neumann for a thiourea-tethered rhenium catalyst, where the authors observed a severe drop in the catalytic rate upon addition of H_2O or PhOH.^[32] They suggested, based on DFT calculations, that external protons may disrupt the pre-established hydrogen-bond stabilization of the thiourea moiety with the CO_2 adduct.

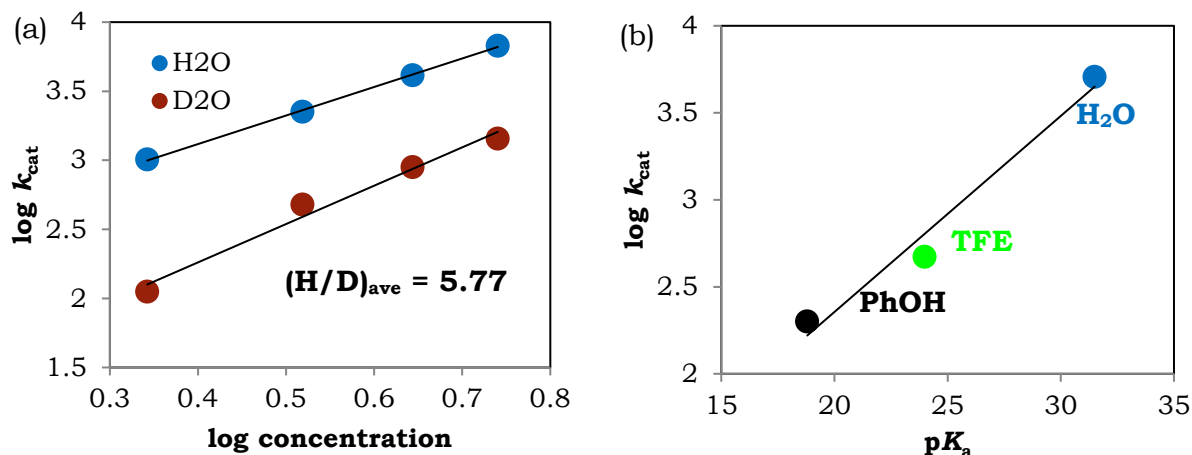


Figure 4-20. (a) Plot of calculated k_{cat} (calculated from FOW analysis) of 1 mM **FeTPPur** in CO₂-saturated DMF as a function of concentration of added H₂O (blue) or D₂O (red). (b) plot of $\log k_{\text{cat}}$ as a function of $\text{p}K_{\text{a}}$ of the acid (PhOH – black, TFE – green) at 5 M concentration.

In the case of **FeTPPur**, water seems to work in synergy with the urea arms to manage the proton supply. Hints for this proposal come from the network of water molecules observed in the X-ray structure of **FeTPPur**, as shown in Figure 4-21a, suggesting that such a network may also be in play during the catalytic reduction of CO₂. A similar water network in the vicinity of the active site of CODH revealed by high resolution X-ray structure (Figure 4-21b) was proposed to have a major role in the enzyme reactivity.^[11,13] The geometry of a model structure where a water molecule was inserted in between a urea arm of **FeTPPur** and CO₂ could be optimized by DFT calculation as a local minimum, as shown in Figure 4-22. This configuration is similar to one of the water molecules in the X-ray structure of **FeTPPur** (O4 in Figure 4-21a). In contrast with the previously mentioned thiourea-tethered Re catalyst, the CO₂ is in this case maintained in a quasi-unchanged topology while being put in contact with a water molecule held by the second urea arm. The less important effect of PhOH and TFE can be due to i) their higher acidity which can prevent the formation of pre-established intramolecular hydrogen bonds between urea groups and CO₂ adduct, and/or ii) their steric hindrance which can limit their access to the catalytic center in between the two urea arms. Further calculations are needed to probe the reaction pathway involving such catalyst to rationalize the interesting effect of proton source.

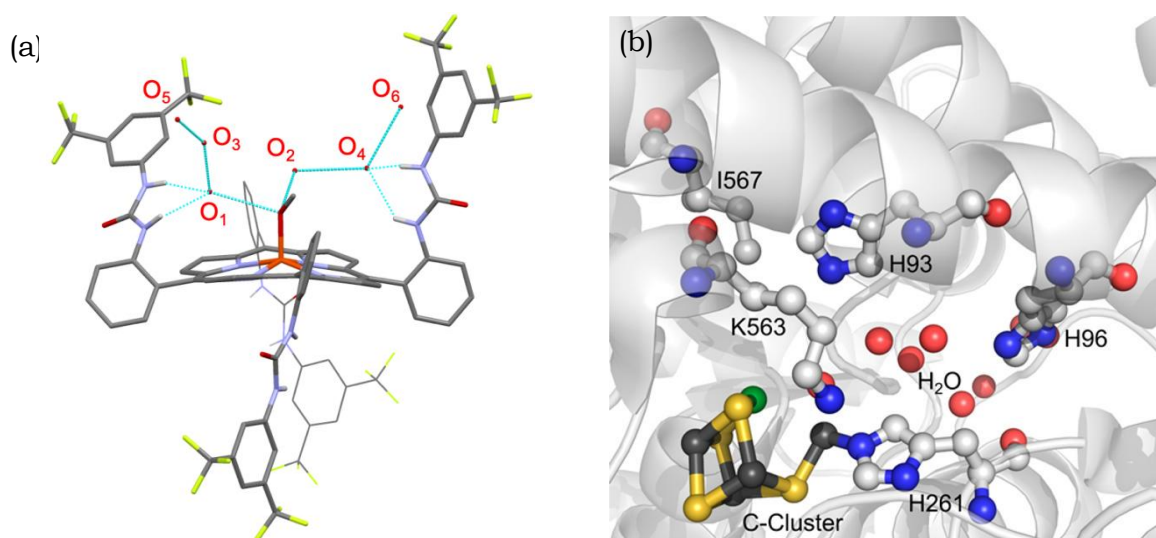


Figure 4-21. (a) Wireframe and capped sticks representation of **FeTPP-Ur** x-ray structure showing water molecules network in the vicinity of the active site. Only urea protons are explicitly shown for clarity; O₁, O₂, O₃ and O₄ are water molecules; O₅ and O₆ are oxygen atoms from neighboring urea groups. (b) Network of H₂O molecules (red) observed in the C-cluster of CODH enzyme (taken from Ref [13]).

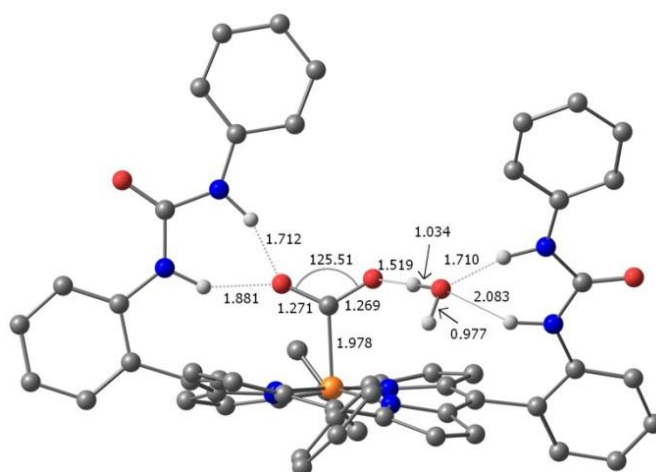


Figure 4-22. Optimized geometries of model compound of **[FeTPP-Ur-CO₂]²⁻** where a water molecule was inserted showing main structural parameters.

Bulk electrolysis experiment was performed on **FeTPPUr** at $-1.77\text{ V vs Fc}^{+/0}$ to measure the efficiency at which CO is produced and to evaluate the stability of the catalyst. Gas chromatography analysis of the reaction headspace during bulk electrolysis showed no hydrogen formation and the catalyst **FeTPPUr** operates with the exclusive formation of CO with a Faradaic efficiency as high as 91% (Figure 4-23a). A stable current density of 0.77 mA cm^{-2} was achieved during the two-hour electrolysis run which confirms the good stability of the catalyst for the duration of

the electrocatalysis, as shown in Figure 4-23b. Considering a two-electron process, the rate constant (k_{cat}) was calculated to be $2.76 \times 10^3 \text{ s}^{-1}$, the TOF to be 455 s^{-1} , and the TON to be 3.28×10^6 . As shown in Figure 4-14b, this calculated TOF value fit well in the catalytic Tafel plot of **FeTPPUr** estimated by FOW analysis, indicating reliability of such quick estimation on catalytic performances. These results show that bio-inspired catalyst design for improved CO_2 reduction activity requires (i) careful choice of functional groups acting as substrate or intermediate stabilizers, (ii) specific 3D engineering of these functions within proper distances towards the active site, and (iii) careful management of proton supply within the vicinity of the active site.

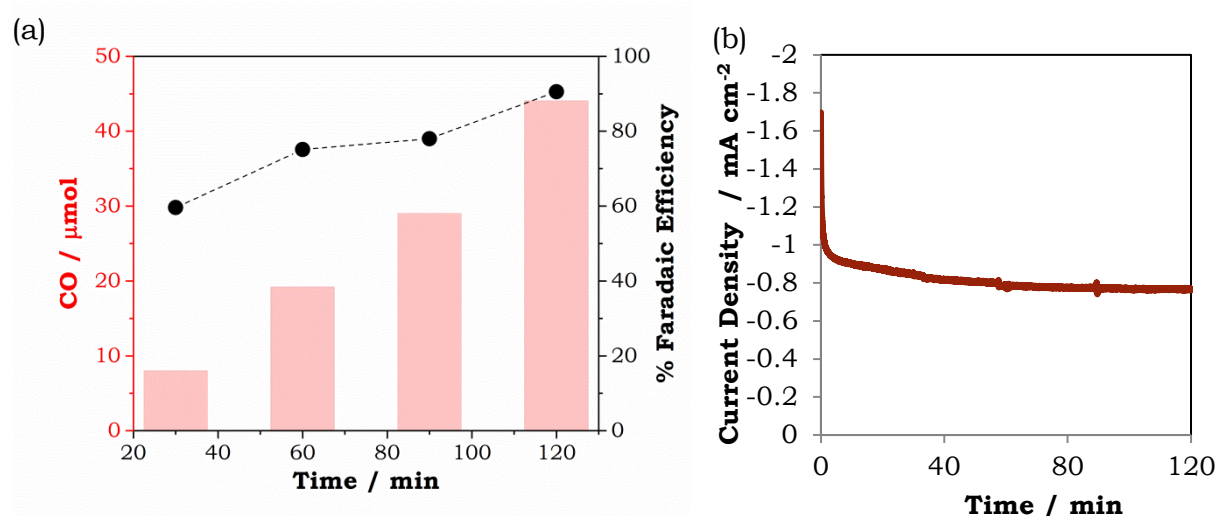


Figure 4-23. (a) Progress of CO evolution and the corresponding Faradaic efficiency and (b) current density changes during bulk electrolysis at $-1.77 \text{ V vs Fc}^{+/0}$ of a CO_2 -saturated DMF containing 0.5 mM FeTPPUr , $5.5 \text{ M H}_2\text{O}$, and 0.1 M TBAP .

4.5. Cationic Imidazolium Moieties as Intermediate Stabilizers

A closer look on the active site of CODH shows the stabilization of the metal carboxylate intermediate by the amino acid residues, histidine 93 and lysine 563. These amino acids are in hydrogen bonding distances to the oxygen atoms of the carboxylate intermediate and it has been proposed they may be in their protonated cationic forms.^[11] As such, through-space electrostatic interactions between the carboxylate intermediate and these amino acid residues might play a crucial role in the activity of the enzyme. The role of electrostatic interactions in catalysis has initially been reported by the group of Masel when the use imidazolium-based ionic liquids as electrolytes have lowered the overpotential for the electro-reduction of

CO₂ in a heterogeneous catalyst consisting of a silver cathode.^[70] It was proposed that the ionic liquid stabilizes the one-electron reduced CO₂^{•-} intermediate, thereby lowering the initial reduction barrier. Implementation of imidazolium-based ionic liquid electrolyte as cofactor in catalysis has been shown by the group of Wallace and Officer to anodically shift the reduction potential of an iron porphyrin catalyst and enhance the kinetics of CO₂ reduction.^[71] Similar substantial improvement in the overpotential and TOF were observed by the group of Costentin, Robert, and Savéant when cationic trimethylammonium groups were tethered at the periphery of an iron porphyrin catalyst.^[41] Recently, cationic methylimidazolium-functionalized Re^[45] and Mn^[46] catalysts were reported by the group of Nippe with improved electrocatalytic properties. It was proposed that the imidazolium units act to provide both hydrogen bonding and through-space electrostatic stabilization of the metal-carboxylate intermediate. Intriguingly, addition of water as a proton source resulted in a significant increase of the catalytic current at lower overpotential, but at higher concentrations of water, a drastic drop in the catalytic current together with positive potential shifts was observed.^[45]

With these recent reports, we extended the investigation of second coordination sphere approach by synthesizing an iron porphyrin derivative with methylimidazolium units attached on the periphery of the porphyrin macrocycle, denoted as FeTPPIm, as shown Figure 4-24. Inspiration for the targeted catalyst stems from the pioneering work of Collman and Boitrel where the semi-rigid “U-shaped” aryl–amide–aryl motif of the starting ligand was used to introduce coordinating or functional groups in a pre-organized fashion close to the coordination sphere of the metal ion in the center of the porphyrin ring.^[61,72-74] Iron (II) ion was inserted in the N₄ coordinating cavity of this ligand using ferrous chloride in the presence of a base. The substitution of the chloro groups at the benzylic positions was then realized upon treatment with stoichiometric amounts of N-methylimidazole at 70°C to prevent the formation of rotational isomers. Interesting features of this catalyst include the picket fence α-4-tetraimidazolium tetraphenylporphyrin ligand structure that establishes a cationic sphere on top of the active site of the catalyst, and the presence of distal NH fragments from the cationic arms, resembling the weak hydrogen bonding interactions by the previously described **FeTPPAm** with the metal carboxylate intermediate (Section 4.4). As such, this system may differentiate the extent of contribution of hydrogen

bonding and electrostatic interactions to the catalytic activity of iron porphyrin catalyst.

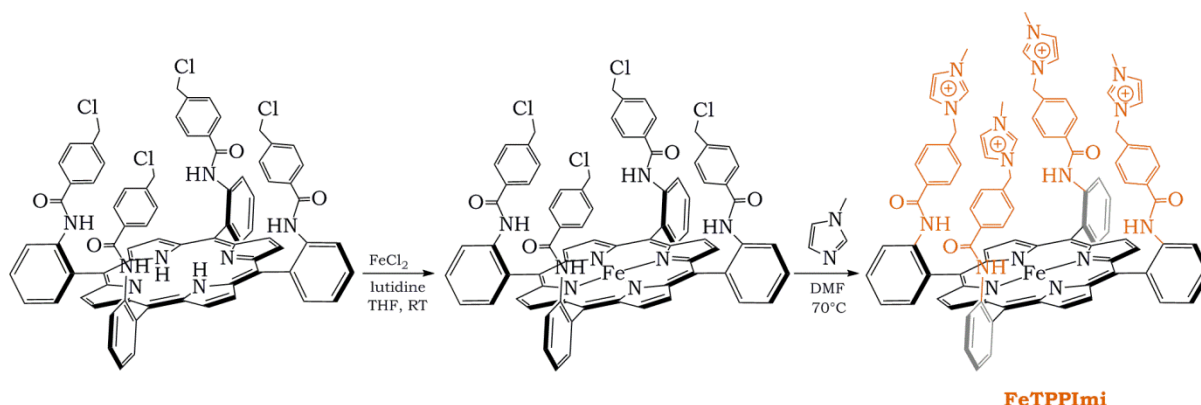


Figure 4-24. Synthesis of imidazolium-tethered iron porphyrin catalyst, **FeTPPIm**.

CV of **FeTPPIm** in an Ar-degassed DMF solution showed the typical three reversible waves in the cathodic region at -0.529 V, -1.356 V, and -1.699 V *vs* $\text{Fc}^{+/0}$ corresponding respectively to the formal $\text{Fe}^{\text{III/II}}$, $\text{Fe}^{\text{II/I}}$ and $\text{Fe}^{\text{I/0}}$ couples (Figure 4-25a). Recent reports have suggested that the second and the third redox waves mainly concern the porphyrin core acting as the locus for the addition of the two supplementary electrons and therefore can be formulated as $[\text{Fe}^{\text{II}}\text{porph}]/[\text{Fe}^{\text{II}}(\text{porph}^{\cdot})]^-$ and $[\text{Fe}^{\text{II}}(\text{porph}^{\cdot})]^-/[\text{Fe}^{\text{II}}(\text{porph}^{\cdot\cdot})]^{2-}$ couples (porph = porphyrin).^[75,76] By comparing these reduction waves to the CVs of the reference iron porphyrin catalysts (Figure 4-13), we observe that the third reduction wave of **FeTPPIm** is drastically shifted towards more positive potential in comparison with the nonfunctionalized **FeTPP** (ΔE of 415 mV), or the fluorinated analogues **FeTPPF8** (ΔE of 290 mV), **FeTPPF20** (ΔE of 100 mV), and even the **FeTPPAm** (ΔE of 310 mV). We attribute this significant shift to the stabilization of the dianionic reduced form of the iron porphyrin through a space-charge interaction with the positively charged methylimidazolium groups. This result therefore provides convincing support that the topologically pre-organized aryl-amide-aryl arms bring the methylimidazolium groups close to the porphyrin platform which helps to support charge accumulation.

Under CO_2 atmosphere and in presence of 5.5M water as a proton source, **FeTPPIm** shows the typical catalytic current on the third reduction wave but at a much lower overpotential compared to the other modified iron porphyrin catalysts. Based on the catalytic Tafel plot and linear scaling relationship in Figure 4-26,

FeTPPIIm is a much better catalyst as indicated by the upward left deviation (that is, lower overpotential and higher TOF) in comparison with the fluorinated reference catalysts **FeTPPF8** and **FeTPPF20**. Even when compared to the **FeTPPAm** having similar NH fragments that provide weak hydrogen bonding interactions in the second coordination sphere, **FeTPPIIm** is a much better catalyst. The catalyst improvement observed for **FeTPPIIm** is even more evident when compared to **FeTPPUr**, which possesses strong multi-point hydrogen bonding stabilization, indicating the great extent through-space electrostatic interactions contributed to the enhancement of the catalysis.

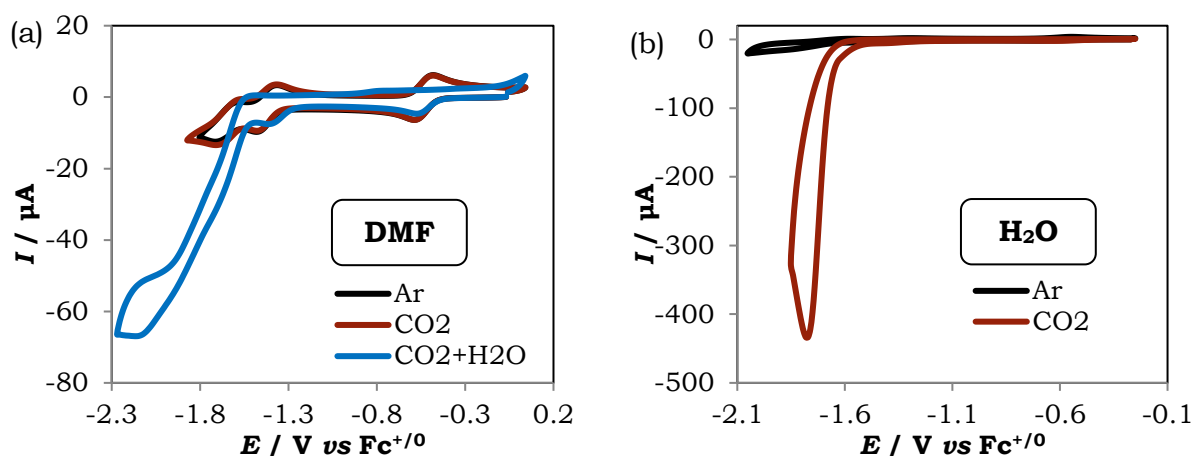


Figure 4-25. (a) CVs of 1 mM **FeTPPIIm** in DMF solution containing 0.1 M TBAP in the absence (black) and presence of CO₂ (red), and presence of CO₂ + 5.5 M H₂O (blue). (b) CVs of 0.5 mM **FeTPPIIm** in H₂O solution containing 0.1 M KCl in the absence (black) and presence of CO₂ (red). [Reference electrode for aqueous solution was SCE but potentials are converted to Fc according to Ref. [77] for better comparison].

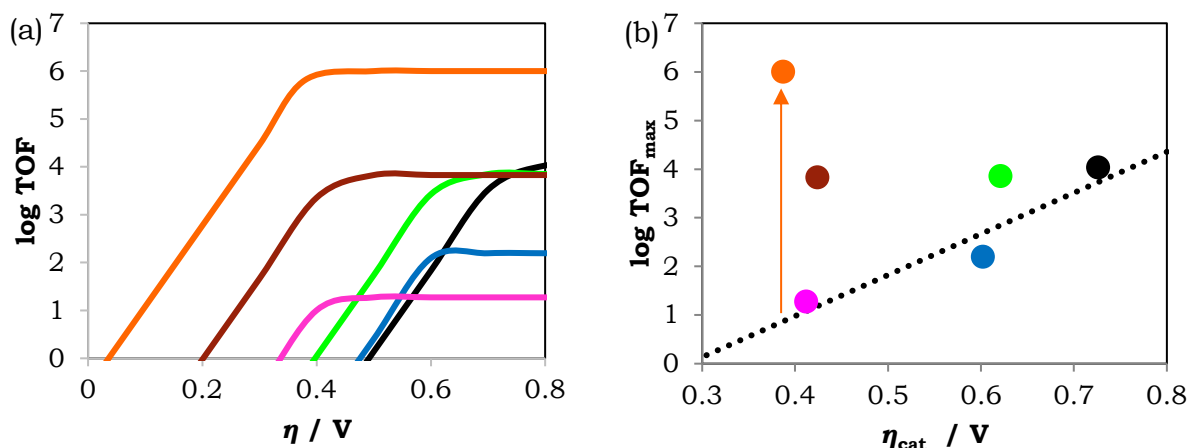


Figure 4-26. (a) Catalytic Tafel plot of **FeTPPIIm** (orange) in comparison with the modified catalysts described in Section 4.4 (black – **FeTPP**, blue **FeTPPF8**, pink – **FeTPPF20**, green – **FeTPPAm**, red - **FeTPPUr**) and (b) how **FeTPPIIm** deviates from the linear scaling relationship.

The tetracationic nature of **FeTPPIIm** renders it water-soluble hence allowing to evaluate its catalytic performance for CO₂ reduction in water as a convenient and clean solvent and proton source. The CV of **FeTPPIIm** in Ar-degassed water containing 0.1 M potassium chloride (KCl) shows three redox processes similar to those observed in DMF. However, even though CO₂ is less soluble in water (0.033 M) than in DMF (0.23 M), the CV displays a much higher catalytic current for CO₂ reduction at a potential as low as $E^{\circ}_{\text{cat}} = -1.712 \text{ V vs Fc}^{+/0}$ (Figure 4-25b). To explain this higher catalytic activity in water, we have to take into consideration the primary intermediate proposed for CO₂ reduction by iron porphyrins which is **[Fe(porph)CO₂]²⁻** described formally as a resonance of **[Fe^I(CO₂^{•-})]²⁻** and **[Fe^{II}(CO₂^{••-})]²⁻**.^[5,69,78] As described earlier, the positive deviation from the expected electrochemical reactivity as already observed in DMF may be assigned to the stabilization of this intermediate through electrostatic interactions with the positive charges of the methylimidazolium groups. In water, which has a higher relative permittivity ($\epsilon_{\text{r,H}_2\text{O}} = 78.4$) compared to DMF ($\epsilon_{\text{r,DMF}} = 36.7$),^[79] the degree of dissociation of the embarked ionic liquid (methylimidazolium⁺Cl⁻) units is greater than that in DMF,^[80] which leads to better stabilization of the **[Fe(porph)CO₂]²⁻** adduct through stronger space-charge interactions with more “free” methylimidazolium groups.

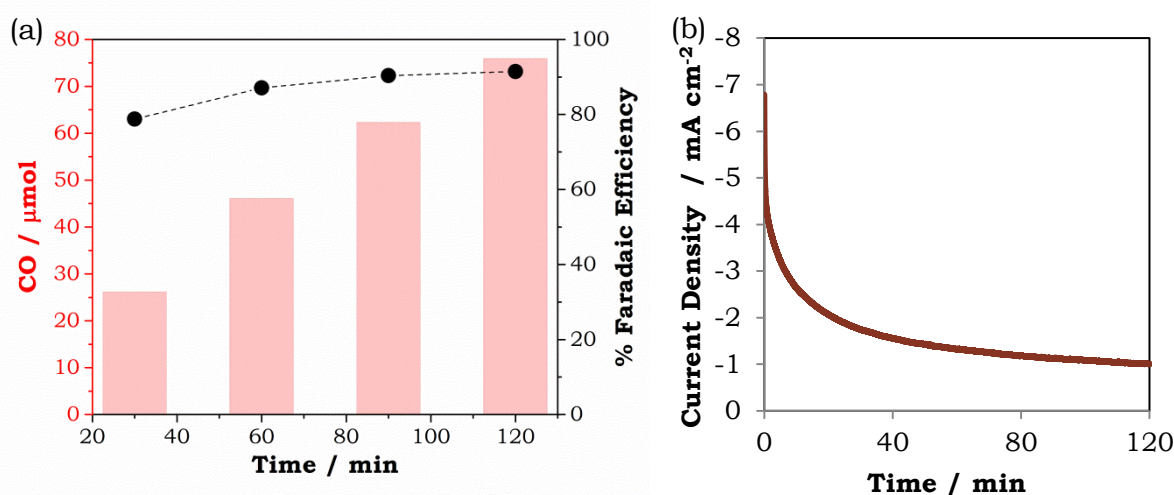


Figure 4-27. (a) Progress of CO evolution and the corresponding Faradaic efficiency and (b) current density changes during bulk electrolysis at $-1.64 \text{ V vs Fc}^{+/0}$ of a CO₂-saturated H₂O containing 0.5 mM **FeTPPIIm**, and 0.1 M KCl.

Gas chromatography analysis of the electrochemical reaction headspace during bulk electrolysis experiments was performed to examine the selectivity and the efficiency of **FeTPPIIm** for CO₂ reduction in water. As shown in Figure 4-27, two

hours of electrocatalysis at $-1.642\text{ V vs Fc}^{+/0}$, which corresponds to an overpotential of 418 mV ($E_{\text{CO}_2/\text{CO}} = -1.224\text{ V vs Fc}^{+/0}$ in H_2O), and a current density of 1.06 mA cm^{-2} , led to the exclusive formation of CO with 91% Faradaic efficiency. Considering a two-electron process, the rate constant (k_{cat}) of $2.44 \times 10^5\text{ s}^{-1}$, TOF of 14986 s^{-1} ($\log\text{ TOF} = 4.18$), and TON of 1.08×10^8 were calculated. These results show that the pre-organized ionic liquid environment confined within the active site of the catalyst promote not only significant lowering of the overpotential for CO_2 reduction but also enhance the TOF of the reaction. This gives hints that the synergy of through-space electrostatic interactions as well as hydrogen bonding stabilization of the metal carboxylate intermediate promotes improved catalytic CO_2 reduction, as observed in the comparison of the catalytic Tafel plots of the studied catalyst with notable CO_2 reduction catalysts reported in literature (Figure 4-28 and Table 4-3).

Table 4-3. Electrocatalytic performances of some notable reported catalysts for CO_2 reduction to CO in comparison with some of the modified catalysts in this work.

Catalyst	$E_{\text{cat}} / \text{V vs Fc}^{+/0}$	$\log\text{ TOF}_{\text{max}}$	Solvent	H^+	Ref
FeTPP	-2.12	4.5	DMF	PhOH	[81]
FeTPP(OH) ₈	-2.04	3.8	DMF	PhOH	[33]
FeTPP- <i>o</i> -2-amide	-2.18	6.7	DMF	PhOH	[31]
FeTPPAm	-2.01	3.9	DMF	H_2O	<i>work</i>
FeTPPUr	-1.81	3.8	DMF	H_2O	<i>work</i>
FeTPPIm	-1.78	6.0	DMF	H_2O	<i>work</i>
FeTPP- <i>o</i> -TMA	-1.64	6.0	DMF	PhOH	[41]
Ni cyclam	-1.74	1.9	ACN	H_2O	[27]
$\text{Pd}_2(\text{triphos})_2$	-1.45	1.5	DMF	HBF_4	[19]
$\text{Re}(\text{bpy})(\text{CO})_3(\text{py})$	-1.99	2.9	ACN	TFE	[82]
$\text{Mn}(\text{tbu-bpy})(\text{CO})_3\text{Br}$	-2.09	2.8	ACN	TFE	[83]
$\text{Mn}(\text{mesbpy})(\text{CO})_3\text{Br}$	-1.97	3.7	ACN	MeOH	[3]

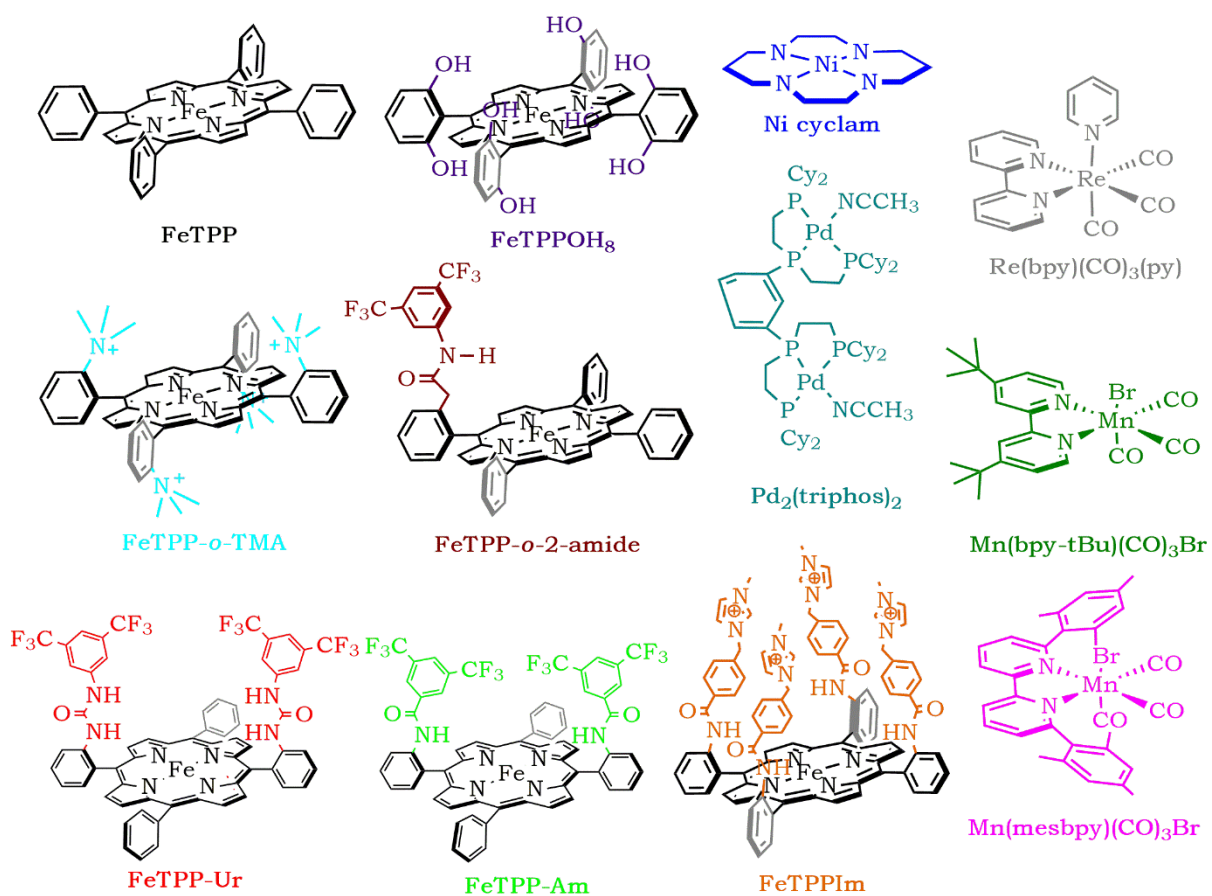
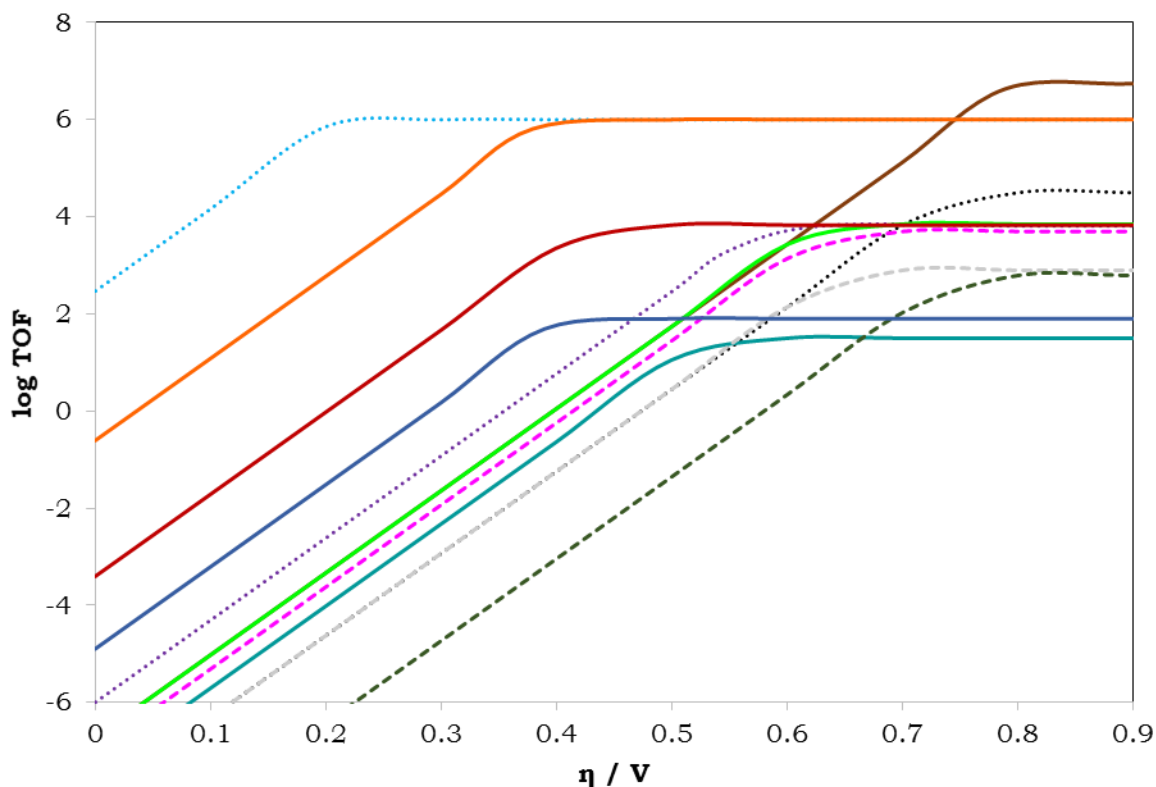


Figure 4-28. Catalytic Tafel plots comparing the electrocatalytic performances of the studied catalysts with notable reported catalysts.

4.6. Conclusions

In conclusion, we have described a bio-inspired strategy for improving the catalytic activity of well-known CO₂ reduction catalysts by applying key learnings from the structure-function studies in CO dehydrogenase enzymes, known to reversibly reduce CO₂ to CO at an exceptional efficiency and stability. Learning from the hydrogen bond stabilization of nearby lysine and histidine residues towards the metal carboxylate intermediate in the enzyme, we have systematically investigated the effect of hydrogen bond donors in the periphery of different catalysts. Introducing one or two proximal amines in the 6,6' positions of the bipyridyl ligand of the Re triscarbonyl catalyst increased the overpotential for CO₂ reduction without significant increase in the TOF. This result is attributed to the improper positioning of the hydrogen bond donors affecting both the first and second coordination spheres. Installing functions in the periphery of such Re catalysts seems complicated because of the intrinsic mechanistic pathway involving the loss of a halide ligand resulting in a pentadentate active form, requiring more sophisticated considerations in catalysts design. Improved catalytic activity by hydrogen bonding stabilization was successfully achieved when urea functions were installed in an $\alpha\beta\alpha\beta$ iron porphyrin atropisomer with significant decrease of the overpotential while maintaining a high TOF. Such a catalytic enhancement was achieved through a pre-organized positioning of the multi-point NH fragments on two urea arms within hydrogen bonding distances from the center. Our systematic study also highlighted the advantage of the multi-point hydrogen bonding from urea groups in **FeTPPUr** for CO₂ electrocatalytic reduction when compared to the single-point H-bonding from amide groups in **FeTPPAm**. More importantly, DFT calculations showed that the metal carboxylate intermediate remains in a quasi-unchanged topology while a water molecule is inserted in the second coordination sphere, explaining the synergistic effect of water as a sufficient proton source for the catalytic reduction of CO₂ in the case of the **FeTPPUr** catalyst.

We also extended our second coordination sphere approach to the introduction of cationic methylimidazolium units as local ionic liquids. This idea was inspired from a proposed role of protonated amino acids in the stabilization of **[Fe(CO₂)]²⁻** adduct in the CODH active site. Significant decrease of the overpotential and an important increase in the TOF was achieved with this system which is attributed to some extent to the weak hydrogen bonding of the proximal amide functions similar to **FeTPPAm**, but also to a larger extent to the electrostatic

interactions between the cationic arms and the metal carboxylate intermediate, leading to superior performance compared to **FeTPPUr**. Because of the cationic nature of the catalyst, it was even possible to perform CO₂ reduction in water as a convenient and clean solvent and proton source. Indeed, the careful design and systematic manipulation of the secondary coordination sphere of catalysts by applying key learnings from the structure-function studies of CODH was able to improve the catalytic activities. This serves as an important synthetic tool for scientists in developing and discovering catalysts with enhanced activities.

Bibliography

- [1] J. Hawecker, J.-M. Lehn, R. Ziessel, *Helv. Chim. Acta.* **1986**, *69*, 1990–2012.
- [2] V. S. Thoi, C. J. Chang, *Chem. Commun.* **2011**, *47*, 6578–6580.
- [3] M. D. Sampson, A. D. Nguyen, K. A. Grice, C. E. Moore, A. L. Rheingold, C. P. Kubiak, *J. Am. Chem. Soc.* **2014**, *136*, 5460–5471.
- [4] H. Takeda, C. Cometto, O. Ishitani, M. Robert, *ACS Catal.* **2017**, *7*, 70–88.
- [5] C. Costentin, J.-M. Savéant, *Nature Reviews Chemistry* **2017**, *1*, 0087.
- [6] F. Wang, *ChemSusChem* **2017**, *10*, 4393–4402.
- [7] D. Hong, Y. Tsukakoshi, H. Kotani, T. Ishizuka, T. Kojima, *J. Am. Chem. Soc.* **2017**, *139*, 6538–6541.
- [8] Y. Tamaki, O. Ishitani, *ACS Catal.* **2017**, *7*, 3394–3409.
- [9] T. Ouyang, H.-H. Huang, J.-W. Wang, D.-C. Zhong, T.-B. Lu, *Angew. Chem. Int. Ed.* **2017**, *56*, 738–743.
- [10] T. Ouyang, H.-J. Wang, H.-H. Huang, J.-W. Wang, S. Guo, W.-J. Liu, D.-C. Zhong, T.-B. Lu, *Angew. Chem. Int. Ed.* **2018**, *57*, 16480–16485.
- [11] J.-H. Jeoung, H. Dobbek, *Science* **2007**, *318*, 1461.
- [12] A. M. Appel, J. E. Bercaw, A. B. Bocarsly, H. Dobbek, D. L. DuBois, M. Dupuis, J. G. Ferry, E. Fujita, R. Hille, P. J. A. Kenis, et al., *Chem. Rev.* **2013**, *113*, 6621–6658.
- [13] M. Can, F. A. Armstrong, S. W. Ragsdale, *Chem. Rev.* **2014**, *114*, 4149–4174.
- [14] S. Ciurli, P. K. Ross, M. J. Scott, S. B. Yu, R. H. Holm, *J. Am. Chem. Soc.* **1992**, *114*, 5415–5423.
- [15] R. Panda, Y. Zhang, C. C. McLauchlan, P. Venkateswara Rao, F. A. Tiago de Oliveira, E. Münck, R. H. Holm, *J. Am. Chem. Soc.* **2004**, *126*, 6448–6459.
- [16] D. Huang, R. H. Holm, *J. Am. Chem. Soc.* **2010**, *132*, 4693–4701.
- [17] V. Artero, M. Fontecave, *Coordination Chemistry Reviews* **2005**, *249*, 1518–1535.
- [18] D. L. DuBois, A. Miedaner, R. C. Haltiwanger, *J. Am. Chem. Soc.* **1991**, *113*, 8753–8764.
- [19] B. D. Steffey, C. J. Curtis, D. L. DuBois, *Organometallics* **1995**, *14*, 4937–4943.
- [20] E. A. Mohamed, Z. N. Zahran, Y. Naruta, *Chem. Commun.* **2015**, *51*, 16900–16903.
- [21] L.-M. Cao, H.-H. Huang, J.-W. Wang, D.-C. Zhong, T.-B. Lu, *Green Chem.* **2018**, *20*, 798–803.
- [22] M. L. Helm, M. P. Stewart, R. M. Bullock, M. R. DuBois, D. L. DuBois, *Science* **2011**, *333*, 863–866.

- [23] E. B. Hulley, K. D. Welch, A. M. Appel, D. L. DuBois, R. M. Bullock, *J. Am. Chem. Soc.* **2013**, *135*, 11736–11739.
- [24] D. K. Dogutan, R. McGuire, D. G. Nocera, *J. Am. Chem. Soc.* **2011**, *133*, 9178–9180.
- [25] C. T. Carver, B. D. Matson, J. M. Mayer, *J. Am. Chem. Soc.* **2012**, *134*, 5444–5447.
- [26] S. Bhunia, A. Rana, P. Roy, D. J. Martin, M. L. Pegis, B. Roy, A. Dey, *J. Am. Chem. Soc.* **2018**, *140*, 9444–9457.
- [27] J. D. Froehlich, C. P. Kubiak, *Inorg. Chem.* **2012**, *51*, 3932–3934.
- [28] A. Chapovetsky, M. Welborn, J. M. Luna, R. Haiges, T. F. Miller, S. C. Marinescu, *ACS Cent. Sci.* **2018**, *4*, 397–404.
- [29] A. Chapovetsky, T. H. Do, R. Haiges, M. K. Takase, S. C. Marinescu, *J. Am. Chem. Soc.* **2016**, *138*, 5765–5768.
- [30] C. G. Margarit, C. Schnedermann, N. G. Asimow, D. G. Nocera, *Organometallics* **2019**, *38*, 1219–1223.
- [31] E. M. Nichols, J. S. Derrick, S. K. Nistanaki, P. T. Smith, C. J. Chang, *Chem. Sci.* **2018**, *9*, 2952–2960.
- [32] E. Haviv, D. Azaiza-Dabbah, R. Carmieli, L. Avram, J. M. L. Martin, R. Neumann, *J. Am. Chem. Soc.* **2018**, *140*, 12451–12456.
- [33] C. Costentin, S. Drouet, M. Robert, J.-M. Savéant, *Science* **2012**, *338*, 90–94.
- [34] C. Costentin, G. Passard, M. Robert, J.-M. Savéant, *Proc. Natl. Acad. Sci. USA* **2014**, *111*, 14990–14994.
- [35] C. Costentin, M. Robert, J.-M. Savéant, A. Tatin, *Proc. Natl. Acad. Sci. USA* **2015**, *112*, 6882–6886.
- [36] F. Franco, C. Cometto, F. F. Vallana, F. Sordello, E. Priola, C. Minero, C. Nervi, R. Gobetto, *Chem. Commun.* **2014**, *50*, 14670–14673.
- [37] S. E. Tignor, H.-Y. Kuo, T. S. Lee, G. D. Scholes, A. B. Bocarsly, *Organometallics* **2019**, *38*, 1292–1299.
- [38] S. A. Chabolla, C. W. Machan, J. Yin, E. A. Dellamary, S. Sahu, N. C. Gianneschi, M. K. Gilson, F. A. Tezcan, C. P. Kubiak, *Faraday Discuss.* **2017**, *198*, 279–300.
- [39] G. Neri, I. M. Aldous, J. J. Walsh, L. J. Hardwick, A. J. Cowan, *Chem. Sci.* **2016**, *7*, 1521–1526.
- [40] J. J. Walsh, G. Neri, C. L. Smith, A. J. Cowan, *Organometallics* **2018**, DOI 10.1021/acs.organomet.8b00336.
- [41] I. Azcarate, C. Costentin, M. Robert, J.-M. Savéant, *J. Am. Chem. Soc.* **2016**, *138*, 16639–16644.
- [42] H. Rao, L. C. Schmidt, J. Bonin, M. Robert, *Nature* **2017**, *548*, 74–77.
- [43] H. Rao, J. Bonin, M. Robert, *J. Phys. Chem. C* **2018**, *122*, 13834–13839.
- [44] H. Rao, C.-H. Lim, J. Bonin, G. M. Miyake, M. Robert, *J. Am. Chem. Soc.* **2018**, *140*, 17830–17834.
- [45] S. Sung, D. Kumar, M. Gil-Sepulcre, M. Nippe, *J. Am. Chem. Soc.* **2017**, *139*, 13993–13996.
- [46] S. Sung, X. Li, L. M. Wolf, J. R. Meeder, N. S. Bhuvanesh, K. A. Grice, J. A. Panetier, M. Nippe, *J. Am. Chem. Soc.* **2019**, *141*, 6569–6582.
- [47] L. Rotundo, C. Garino, E. Priola, D. Sassone, H. Rao, B. Ma, M. Robert, J. Fiedler, R. Gobetto, C. Nervi, *Organometallics* **2019**, *38*, 1351–1360.
- [48] P. Kurz, B. Probst, B. Spingler, R. Alberto, *European Journal of Inorganic Chemistry* **2006**, *2006*, 2966–2974.
- [49] A. Nakada, O. Ishitani, *ACS Catal.* **2018**, *8*, 354–363.
- [50] M. L. Clark, P. L. Cheung, M. Lessio, E. A. Carter, C. P. Kubiak, *ACS Catal.* **2018**, *8*, 2021–2029.
- [51] J. M. Smieja, C. P. Kubiak, *Inorg. Chem.* **2010**, *49*, 9283–9289.

- [52] G. J. Stor, F. Hartl, J. W. M. van Outersterp, D. J. Stufkens, *Organometallics* **1995**, *14*, 1115–1131.
- [53] J. Hawecker, J.-M. Lehn, R. Ziessel, *J. Chem. Soc., Chem. Commun.* **1984**, *0*, 328–330.
- [54] B. D. McCarthy, D. J. Martin, E. S. Rountree, A. C. Ullman, J. L. Dempsey, *Inorg. Chem.* **2014**, *53*, 8350–8361.
- [55] K. T. Ngo, M. McKinnon, B. Mahanti, R. Narayanan, D. C. Grills, M. Z. Ertem, J. Rochford, *J. Am. Chem. Soc.* **2017**, *139*, 2604–2618.
- [56] C. Costentin, S. Drouet, M. Robert, J.-M. Savéant, *J. Am. Chem. Soc.* **2012**, *134*, 11235–11242.
- [57] U. Manna, S. Kayal, S. Samanta, G. Das, *Dalton Trans.* **2017**, *46*, 10374–10386.
- [58] E. M. Nichols, C. J. Chang, *Organometallics* **2018**, *38*, 1213–1218.
- [59] C. G. Margarit, C. Schnedermann, N. G. Asimow, D. G. Nocera, *Organometallics* **2018**, DOI 10.1021/acs.organomet.8b00334.
- [60] A. Khadhraoui, P. Gotico, B. Boitrel, W. Leibl, Z. Halime, A. Aukauloo, *Chem. Commun.* **2018**, *54*, 11630–11633.
- [61] J. P. Collman, R. R. Gagne, C. Reed, T. R. Halbert, G. Lang, W. T. Robinson, *J. Am. Chem. Soc.* **1975**, *97*, 1427–1439.
- [62] J. P. Collman, R. R. Gagne, T. R. Halbert, J. C. Marchon, C. A. Reed, *J. Am. Chem. Soc.* **1973**, *95*, 7868–7870.
- [63] B. H. M. Snellink-Ruël, M. M. G. Antonisse, J. F. J. Engbersen, P. Timmerman, D. N. Reinhoudt, *Eur. J. Org. Chem.* **2000**, *2000*, 165–170.
- [64] P. R. Schreiner, *Chem. Soc. Rev.* **2003**, *32*, 289–296.
- [65] Z. Zhang, P. R. Schreiner, *Chem. Soc. Rev.* **2009**, *38*, 1187–1198.
- [66] J. Schneider, H. Jia, J. T. Muckerman, E. Fujita, *Chem. Soc. Rev.* **2012**, *41*, 2036–2051.
- [67] C. Cometto, L. Chen, P.-K. Lo, Z. Guo, K.-C. Lau, E. Anxolabéhère-Mallart, C. Fave, T.-C. Lau, M. Robert, *ACS Catal.* **2018**, *8*, 3411–3417.
- [68] J. M. Savéant, in *Elements of Molecular and Biomolecular Electrochemistry*, John Wiley & Sons, Ltd, **2006**, pp. 78–181.
- [69] C. Costentin, S. Drouet, G. Passard, M. Robert, J.-M. Savéant, *J. Am. Chem. Soc.* **2013**, *135*, 9023–9031.
- [70] B. A. Rosen, A. Salehi-Khojin, M. R. Thorson, W. Zhu, D. T. Whipple, P. J. A. Kenis, R. I. Masel, *Science* **2011**, *334*, 643–644.
- [71] J. Choi, T. M. Benedetti, R. Jalili, A. Walker, G. G. Wallace, D. L. Officer, *Chem. Eur. J.* **2016**, *22*, 14158–14161.
- [72] A. Didier, L. Michaudet, D. Ricard, V. Baveux-Chambenoit, P. Richard, B. Boitrel, *European Journal of Organic Chemistry* **2001**, *2001*, 1917–1926.
- [73] Z. Halime, M. Lachkar, T. Roisnel, E. Furet, J.-F. Halet, B. Boitrel, *Angewandte Chemie International Edition* **2007**, *46*, 5120–5124.
- [74] I. Hijazi, T. Roisnel, P. Even-Hernandez, E. Furet, J.-F. Halet, O. Cador, B. Boitrel, *J. Am. Chem. Soc.* **2010**, *132*, 10652–10653.
- [75] C. Römel, J. Song, M. Tarrago, J. A. Rees, M. van Gastel, T. Weyhermüller, S. DeBeer, E. Bill, F. Neese, S. Ye, *Inorg. Chem.* **2017**, *56*, 4745–4750.
- [76] A. J. Göttle, M. T. M. Koper, *J. Am. Chem. Soc.* **2018**, *140*, 4826–4834.
- [77] V. V. Pavlishchuk, A. W. Addison, *Inorganica Chimica Acta* **2000**, *298*, 97–102.
- [78] B. Mondal, A. Rana, P. Sen, A. Dey, *J. Am. Chem. Soc.* **2015**, *137*, 11214–11217.
- [79] K. Izutsu, in *Electrochemistry in Nonaqueous Solutions*, Wiley-Blackwell, **2003**, pp. 167–200.
- [80] W. Li, Z. Zhang, B. Han, S. Hu, Y. Xie, G. Yang, *J. Phys. Chem. B* **2007**, *111*, 6452–6456.
- [81] C. Costentin, M. Robert, J.-M. Savéant, *Acc. Chem. Res.* **2015**, *48*, 2996–3006.

- [82] K.-Y. Wong, W.-H. Chung, C.-P. Lau, *Journal of Electroanalytical Chemistry* **1998**, 453, 161–170.
- [83] J. M. Smieja, M. D. Sampson, K. A. Grice, E. E. Benson, J. D. Froehlich, C. P. Kubiak, *Inorg. Chem.* **2013**, 52, 2484–2491.

Chapter 5

Valorizing CO₂ Waste: Going Beyond CO

This Chapter includes work reported in:

- P. Gotico, A. Del Vecchio, D. Audisio, A. Quaranta, Z. Halime, W. Leibl, A. Aukauloo, *ChemPhotoChem* **2018**, 2, 715–719.

5.1. Introduction

The catalytic two-electron two-proton reduction of carbon dioxide (CO_2) to carbon monoxide (CO) is a challenging initial step that scientists have been addressing for storing renewable solar energy into chemical fuel through electro- and photo-catalytic processes. The ultimate goal is to produce high-density energy vectors (ie. C_4 - C_{12} hydrocarbons) from renewable sources to replace the currently used fossil fuels as dominant energy source. Because of the tradeoff however, between energy efficiency, electron intensity, and product selectivity, it is more economical to first produce simpler C1 building blocks from CO_2 that can be upgraded further rather than producing directly long-chain carbon products.^[1] CO for example, is used in the Fischer-Tropsch process in tandem with hydrogen gas to produce liquid fuels.^[2] Interest has also been shown for production of CO_2 -derived methanol^[3] or formic acid^[4] as alternatives to H_2 due to ease of fuel transport and handling. However, efficiency of the current systems is still not at par. Replacing the existing fossil fuels with fuels from CO_2 reduction needs major improvements in energy efficiency and overall CO_2 balance to be economically feasible and environment friendly. The current state of such CO_2 transformation technological route towards fuel source application makes it still unrealistic given the large market demand.^[5]

A variety of industrially relevant chemical transformations involves an increasing number of carbon atoms per molecule and most are still produced from fossil fuel-derived feedstocks. Envisioning a carbon-neutral emission footprint for these industries would require transforming CO_2 wastes into C1 building blocks, which becomes a more practical and cost-effective strategy. Coupling such CO_2 transformations with renewable sources of electricity or direct transformation by a renewable process (ie; direct photochemical conversions) would then result in a net zero or even net negative carbon footprint, helping to sequester CO_2 into usable valorized forms.^[6]

The diagonal transformation of CO_2 as a carbon feedstock not only for production of petrochemicals but also for other industrial reactions, as shown in Figure 5-1, seems to be promising. The concept was introduced by Cantat and colleagues with a plot showing the vertical reduction of CO_2 as a way of storing energy and the horizontal transformation representing functionalization of carbon-based products. ^[7] This perspective harmonizes the advancements both in the fields of CO_2 reduction and valorization. As such, the refinement of simple C1 products produced from catalytic reduction of CO_2 into more functionalized products is a promising approach in recycling carbon dioxide. The production scales for synthesis may be small but the added value is higher and as such the overall energy and technology requirement would not be a major issue.

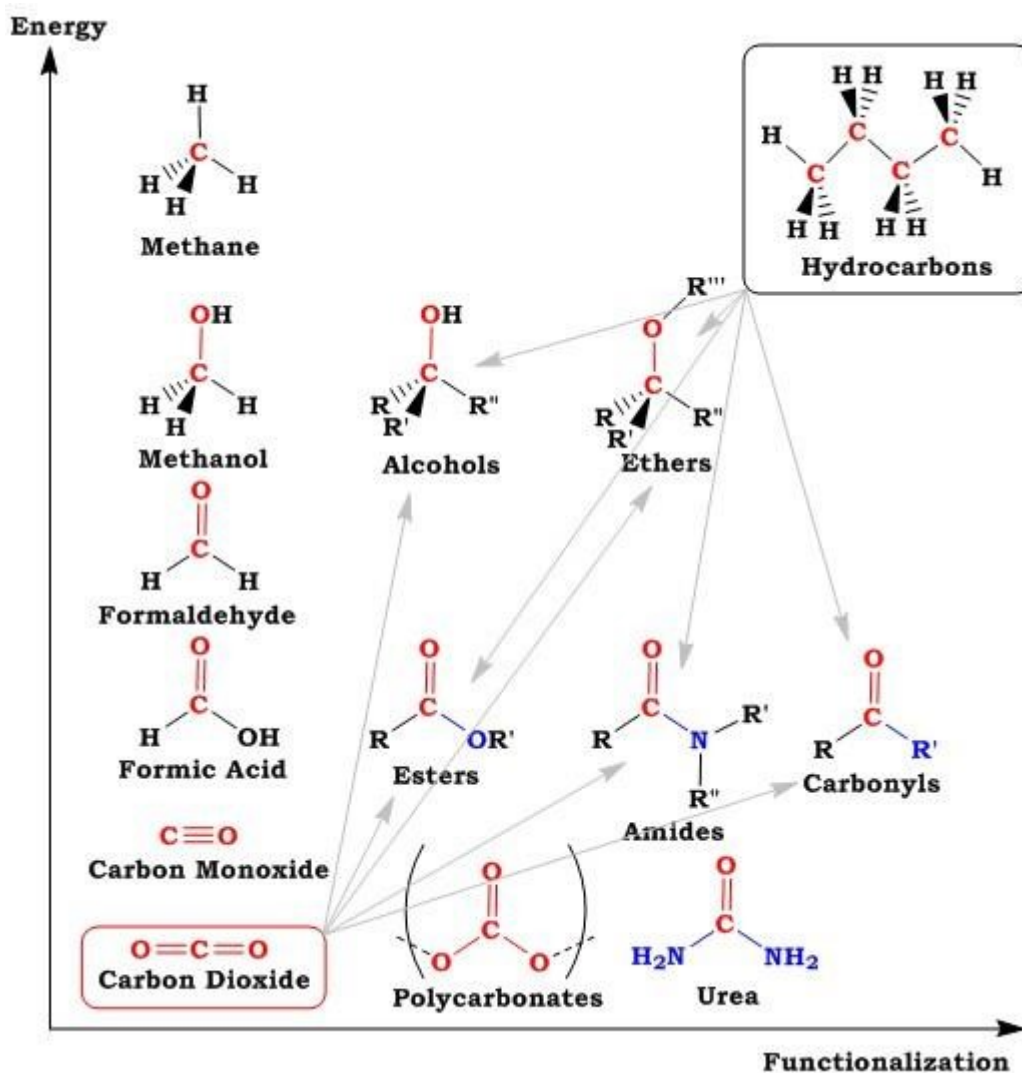


Figure 5-1. Recycling transformations of carbon dioxide.^[7]

Though most studies in the catalytic reduction of CO_2 to CO have focused on improving the efficiency, selectivity, cost, and stability of the catalyst, only little has been reported in addressing the need for capturing, storing, and valorizing the produced CO . The reduced product can be segregated from the headspace mixture of reactors by techniques such as swing adsorption,^[8] cryogenic distillation,^[9] and membrane gas separation,^[10] but these usually employ specialized equipment, and high pressure and temperature, which require extra energy input. Furthermore, the inherent toxicity and flammability of CO gas impose strict handling precautions and safety procedures. In a stepwise diagonal perspective, one can easily think of valorizing the reduced product by functionalization to produce a more useful and stable form.

5.2. Carbon Monoxide Valorization

In nature, CO dehydrogenase (CODH) enzymes transport the CO produced from the catalytic reduction of CO₂ in the C cluster site to the A cluster site of acetyl coenzyme-A (CoA) synthase via direct gas channels to insert CO in a carbonylation reaction, as shown in Figure 5-2.^[11] Inspired by this enzymatic scheme, one promising strategy is to immediately use the produced CO from photocatalytic reduction of CO₂ as a reagent in chemical transformations. This strategy is based on the significant difference in reactivity between the generally unreactive CO₂, and the reactive CO towards carbonylation reactions. Thus, the photocatalytic reduction and the carbonylation reaction can share the same atmosphere where CO₂ is transformed, and the produced CO is simultaneously consumed. This provides not only a clean way of capturing CO, but it also gives further drive towards the valorization of CO₂.

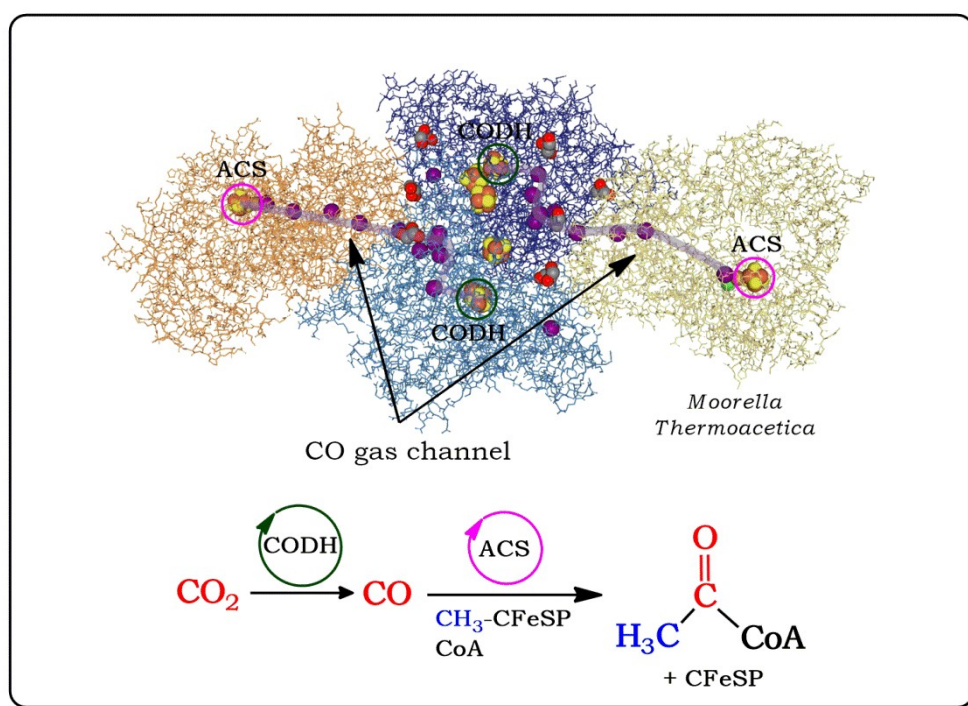


Figure 5-2. CO dehydrogenase (CODH) and Acetyl CoA Synthase (ACS) complex in *Moorella thermoacetica* showing CO gas channels between the C cluster of CODH and the A cluster of ACS. (Legend: CFeSp = corrinoid iron-sulfur protein, CoA = coenzyme A)

Carbon monoxide is an important C1 building block widely used in carbonylation reactions which is one of the industrial core processes for converting bulk chemicals into diverse products. Such transformations are pioneered by the work of Heck and co-workers in the 1970s on palladium-catalyzed reactions^[12-14]

and since then have been extensively developed.^[15–20] The introduction of CO into a molecule not only adds an extra carbon but also introduces the diversity of functionalities of carbonyl groups. It gives access to carboxylic acids, esters, amides, anhydrides, acid fluorides, aldehydes, and ketones, and the desired product is usually controlled by the nucleophile used in the reaction: water for hydroxycarbonylation, alcohols for alkoxycarbonylation, amines for aminocarbonylation, carboxylate salts, fluorides, hydrides, or organometallic reagents.^[15]

Aminocarbonylation reactions are particularly useful in forming amides which are common motifs found in bioactive compounds.^[21] The fundamental steps involved in the catalytic cycle are shown in Figure 5-3. The catalytically active species Pd^0L_2 coordinates to the π system in the electrophile (ArX) that involves the cleavage of one covalent bond to form two new bonds, resulting in the increase in the oxidation state of Pd from 0 to +2. CO then coordinates to Pd, where it undergoes a 1,1-insertion into the Pd-organyl bond. The resulting acylpalladium intermediate undergoes a nucleophilic attack by an amine releasing an amide and regenerating back the active species.

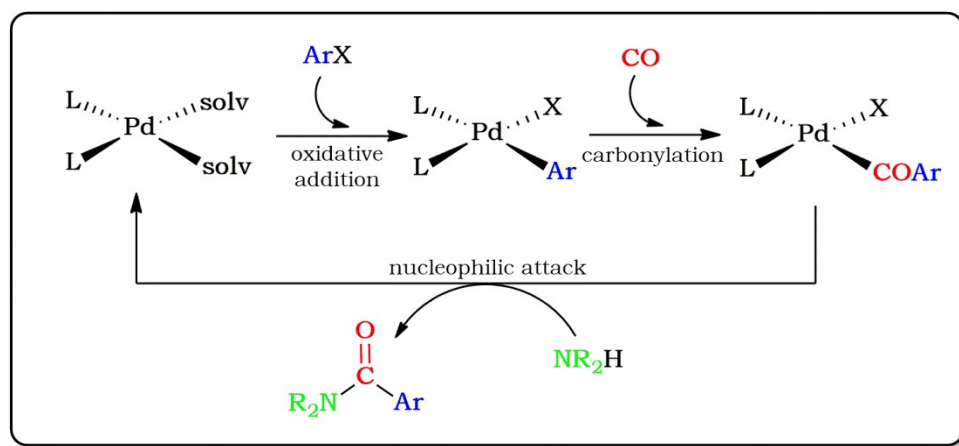


Figure 5-3. General mechanism for the Pd-catalyzed aminocarbonylation.^[16]

The use of carbon monoxide as a chemical reagent is limited by the general reluctance to use gaseous reagents, most of the time requiring high-pressure equipment, the inherent toxicity of CO and the necessary handling precautions. The group of Skrydstrup has developed a simple and efficient experimental set-up called COware®, a two-chamber system that enables safe carbonylation chemistry without the need for direct handling of gaseous CO reagent.^[21] It consists of a CO-producing chamber, where CO precursors such as 9-methylfluorene-9-carbonyl chloride or

methyldiphenyl-silacarboxylic acid were used to stoichiometrically produce CO, which was then subsequently utilized in various reactions such as amino-, alkoxy-, and thio-carbonylation, carbonylative α -arylation, Suzuki-Miyaura, Heck, Sonogashira, and C-H activation.^[22] To eliminate the use of expensive CO precursors, Skrydstrup has even investigated the use of cesium fluoride and disilane to transform CO₂ to CO and immediately utilize it in aminocarbonylation, but this approach still requires highly sensitive, difficult-to-synthesize reagents, and the utilization of a glovebox.^[23] The same group also reported the electrochemical reduction of CO₂ to CO using an iron porphyrin catalyst and its application in carbonylation chemistry.^[24]

Photoredox catalysis has already been applied in various organic synthesis including carbonylation^[25] and aminocarbonylation^[26] chemistry, but usually necessitates a reactive species, such as CO at high pressures, and high energy light sources in the UV spectral range. Photoredox activation of CO₂ for direct amino acid synthesis^[27] and hydrocarboxylation of styrenes^[28] has been investigated by the group of Jamison, but requires UV irradiation to access the CO₂^{•-} radical. Similarly, Yu et. al. reported visible-light-driven thiocarboxylation of styrenes and acrylates by accessing the reducing power of the CO₂^{•-} radical.^[29]

5.3. Objectives

In this chapter, the COware® two-chamber reactor comprising of CO-producing and CO-consuming chambers, as shown in Figure 5-4, was utilized to explore the possibility of a direct use of CO₂ in carbonylation chemistry under mild conditions. Specifically, the objectives are:

- To upscale the optimized conditions of the photocatalytic reduction of CO₂ to CO, described in Chapter 2, using a rhenium triscarbonyl bipyridyl catalyst **[Re(CO)₃(bpy)Br]**, a ruthenium trisbipyridine photosensitizer **[Ru(bpy)₃]²⁺**, and 1,3-dimethyl-2-phenylbenzimidazole (**BIH**) as sacrificial electron donors (SED) for the CO-producing chamber
- To screen and optimize a palladium-catalyzed aminocarbonylation of aryl halides for the CO-consuming chamber
- To identify the bottlenecks of applicability for such two-chamber system
- To apply such strategy in synthesizing an isotope-labeled pharmaceutically relevant drug using CO₂ as a carbon feedstock

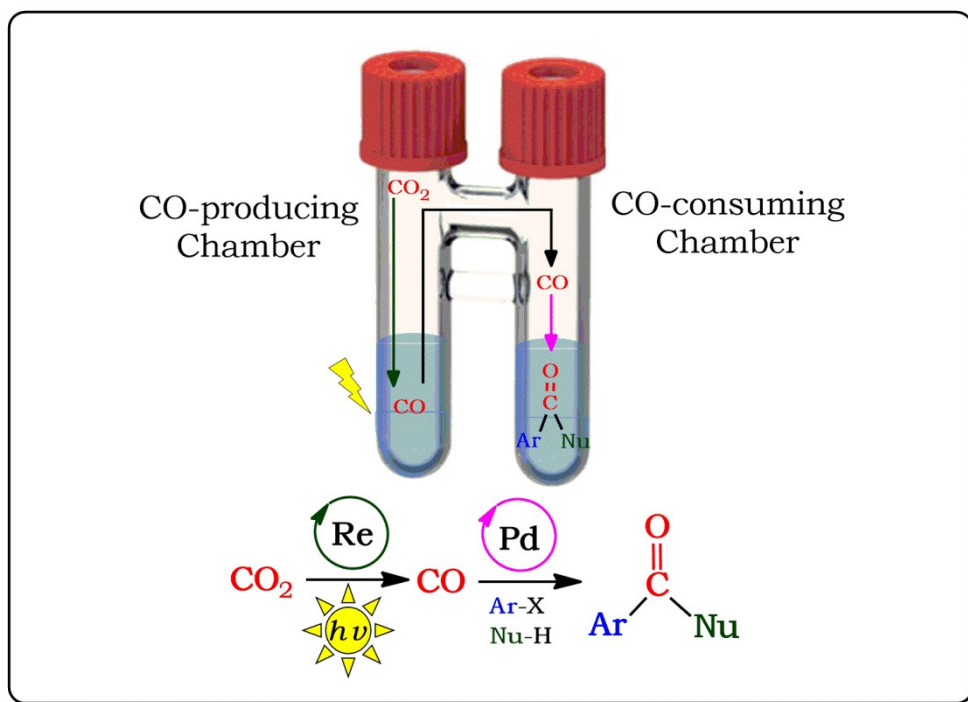


Figure 5-4. Mimicking the CODH/ACS complex for the subsequent valorization of CO produced from photocatalytic CO_2 reduction.

This proof-of-concept short circuits the need to synthesize a CO-precursor, which usually involves high pressures of CO_2 and extremely low temperatures, thereby making it a cheaper and more accessible method. Furthermore, this strategy offers a new alternative for the manipulation and use of the stable ^{13}C and radioactive ^{14}C -labeled CO_2 as labeled CO sources for its subsequent incorporation in various pharmaceutical drug preparations. This approach uses the new developments and advancements in the fields of artificial photosynthesis and carbonylation chemistry to achieve a simple, efficient, and cost-effective reduction and valorization of CO_2 .

5.4. Upscaling Optimized Photocatalytic CO_2 Reduction

The optimization of the photocatalyst system containing rhenium triscarbonyl bipyridyl catalyst $[\text{Re}(\text{CO})_3(\text{bpy})\text{Br}]$ and ruthenium trisbipyridine photosensitizer $[\text{Ru}(\text{bpy})_3]^{2+}$, and 1,3-dimethyl-2-phenylbenzimidazole (**BIH**) as sacrificial electron donors (SED), described in Chapter 2, was utilized in the CO-producing chamber of the two-chamber system. Though new catalysts were synthesized and described in Chapters 3 and 4, these catalysts, when coupled to the $[\text{Ru}(\text{bpy})_3]^{2+}$ and **BIH**, gave lower photocatalytic turnover numbers as compared

to the known **Re(CO)₃(bpy)Br**. As such, the latter was used as a catalyst in the photocatalytic runs for the CO-producing chamber.

Optimized conditions, as reported in Table 2-4 in Chapter 2, consists of 50 μM **Re(CO)₃(bpy)Br**, 50 μM **[Ru(bpy)₃]²⁺**, 90 mM **BIH** as SED, 10% (v/v) water as proton source, 10% (v/v) triethanolamine (TEOA) as Re-CO₂-adduct stabilizing additive and DMF as solvent. This optimized system produced 120 μmol of CO (turnover number of 780), within 2 hours of irradiation, until the CO production plateaus. It is to be noted that turnover numbers can easily be overestimated if lower concentrations of catalyst are used. Though TONs should ideally be constant regardless of catalyst concentration, this observation suggests: (i) that the stability of the photosensitizer is critical in the catalytic activity, (ii) degraded photosensitizer might play a non-innocent role in the production of CO and/or (iii) high margin of error handling small concentrations of catalyst (ie. nM range) can easily translate to overcalculated TON. Upscaling the photocatalytic condition into a two-chamber system requires focus on the absolute amount of CO produced, and as such a 1:1 ratio of photosensitizer:catalyst was maintained to attain a good balance between the absolute amount of CO produced and the calculated TON.

To achieve significant amounts of CO to be used in the aminocarbonylation in the second chamber, the amounts of photosensitizer, catalyst, and SED were increased. Upscaling of CO production was then investigated taking into account the effect of water (condition I), TEOA (condition II), or the combination of both (condition III) in the production of CO as shown in Figure 5-5. It can be observed that as expected, upscaling resulted in the increase of amount of CO produced, but when normalized with the amount of catalyst used (in terms of TON), both conditions II and III, where TEOA is used, decreased the TON. Though argued in

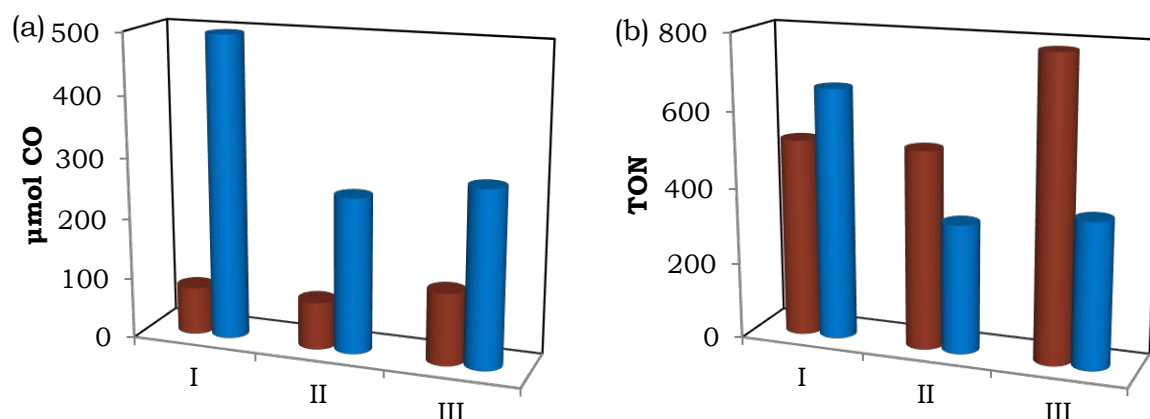


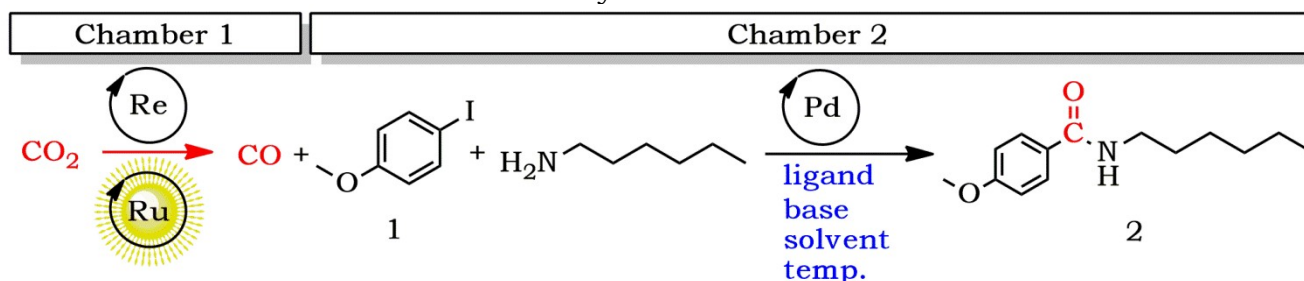
Figure 5-5. Variations in the photocatalytic performance after 2 h photo-irradiation in terms of (a) μmol of CO produced and (b) corresponding TON of different solvent conditions (I: 9:1 DMF:H₂O, II: 9:1 DMF:TEOA, III: 8:1:1 DMF:TEOA:H₂O) when both **Ru(bpy)₃Cl₂** and **Re(CO)₃(bpy)Br** were increased (red: 50 μmol , blue: 750 μmol) while maintaining the same 1:1 ratio. Details are reported in Annex.

Chapter 2 that TEOA was utilized as an additive to stabilize a Re-CO₂ adduct and works in synergy with water as a proton source, it seems that it participates in a more complicated way in the catalytic cycle because of the observed lowering of catalytic activity when conditions were simply upscaled. This merits a further investigation the role of TEOA. Interestingly, the use of DMF:H₂O solvent mixture maintained a linearly increased CO production upon upscaling, while the TON is not significantly lowered. The simplicity of such solvent condition, where water is used as a cheap source of proton, merited its use as an optimum condition for the CO-producing chamber.

5.5. Screening and Optimizing CO Valorization

Following the reactions performed by the group of Skrydstrup in their two-chamber system, aminocarbonylation reactions^[21,22] were screened to identify a reaction suitable for coupling with the mild conditions of the photocatalytic CO₂ reduction. The synthesis of n-hexyl-4-methoxybenzamide from 4-iodoanisole and n-hexylamine, as shown in Table 5-1, seemed suitable because the reaction can be performed at room temperature with low pressures (~ 1 atm) of CO.

Table 5-1. Optimizations for the synthesis of n-hexyl-4-methoxybenzamide as a model reaction for the two-chamber system.



Entry	Limiting Reagent	Ligand	Base	Solvent	T / °C	CO ₂ to CO Conversion	Yield of [2] ^[d] based on	
							CO ₂	CO
1 ^[a]	1	PPh ₃	TEA	Dioxane	80	22 %	18 %	32 %
2 ^[a]	1	P(tBu) ₃ HBF ₄	DABCO	THF	20	22 %	18 %	41 %
3 ^[b]	¹² CO	P(tBu) ₃ HBF ₄	DABCO	THF	20	22 %	18 %	83 %
4 ^[c]	¹³ CO ₂	P(tBu) ₃ HBF ₄	DABCO	THF	20	38 %	32 %	82 %

[a] Chamber 1 contains 0.19 mM Ru PS, 0.19 mM Re Cat, 0.28 M BIH, DMF + 10% H₂O producing 478 μmol CO. Chamber 2 contains 0.5 mmol of **1**, 1 mmol n-hexylamine, 0.025 mmol Pd(dba)₂, 0.05 mmol ligand, 2 mmol base, and solvent. CO₂-purged (1atm); Reaction was run for 21 hours.

[b] same as [a] except that 2.5 equivalents excess of Chamber 2 reagents in relation to CO

[c] Tritec® system was used to deliver limited amount of ¹³CO₂ (501 μmol). See Annex for details.

[d] Yield calculated as amount **[2]** isolated after column chromatography divided by either the initial amount of CO₂ or the amount of CO produced from Chamber 1.

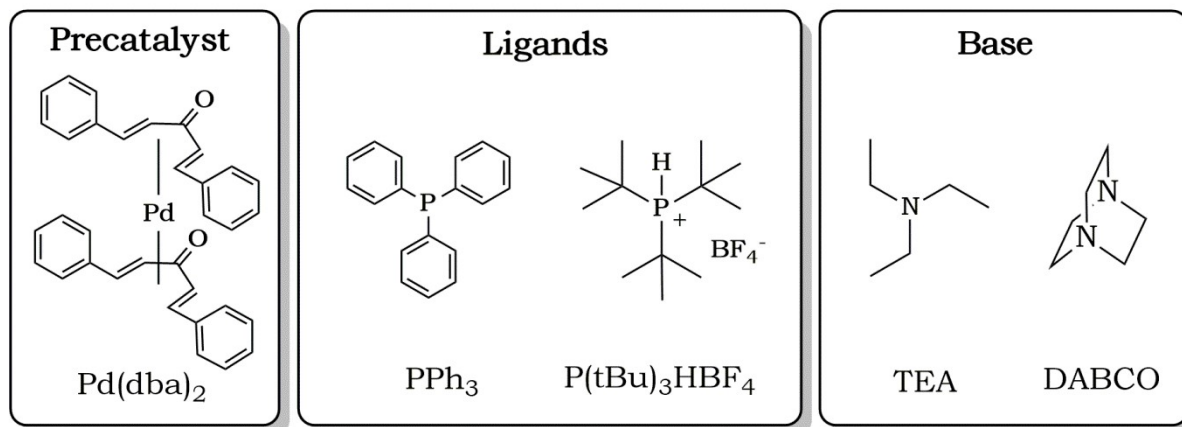


Figure 5-6. Chemical structures of the reagents used for the optimization of the CO-consuming chamber.

Bis(dibenzylideneacetone)palladium(0) (**Pd(dba)₂**) was used as a pre-catalyst for the aminocarbonylation, and the ligands, bases, and reaction conditions were optimized as each of these aspects can affect the stabilization of reaction intermediates involved in the catalytic cycle described in Figure 5-3. As shown in Table 5-1 (comparison of entries 1 and 2), the substitution with $\text{P}(\text{tBu})_3\text{HBF}_4$ as a ligand, and 1,4-diazabicyclo[2.2.2]octane (DABCO) as a base, made it possible to perform the reaction at room temperature achieving a moderate yield of 41 % using a limiting amount of CO produced from the first chamber. The observed low yield of the second chamber reaction is due to the formation of a double CO insertion product (n-hexyl-2-(4-methoxyphenyl)-2-oxoacetamide) during the Pd-catalyzed reaction, as observed by the presence of a new band in thin layer chromatography and confirmed by ^1H NMR (see supplementary information in Annex). This type of by-product is usually observed when an equimolar amount of CO is used in room temperature Pd-catalyzed carbonylation as described in the literature.^[21] Increasing the concentration of reagents in Chamber 2 prevents the double insertion of CO, and greatly improves the selectivity of the reaction in favor of the mono-insertion. Under these optimized conditions, a satisfying 83% yield was reached, based on the limiting amount of CO produced from the first chamber (Table 5-1, Entry 3).

5.6. A Change of Criterion

The photocatalytic reduction of CO_2 to CO using the Re catalyst and Ru photosensitizer (Table 5-1 Entries 1-3 and as optimized in Chapter 2) is done by saturating the DMF solution with 1 atm of CO_2 gas (by keeping an outlet to atmosphere during bubbling) and once saturated at around 10-15 min, bubbling is stopped and the closed system is prepared for photo-irradiation. As such, most

photocatalytic optimizations are done in excess amount of CO₂. Control experiments were done to quantify the initial amount of CO₂ by gas chromatography analysis of the headspace and calculations of the dissolved CO₂ based on Henry's solubility constant in DMF, and from here, the yields of n-hexyl-4-methoxybenzamide were corrected. As shown in Table 5-1, a low yield of 18% was calculated regardless of whether the reagents in the second chamber were increased (Entry 3) indicating that the reaction in the CO-producing chamber might be limiting the tandem photocatalytic-catalytic process.

The criteria for the optimizations done on the first chamber were revisited to determine the reason for the low yield. A previous criterion for optimizations was turnover number (TON) which is the amount of CO produced divided by the amount of catalyst. The use of such criterion is rationalized by the fact that the most expensive part of the system is the photocatalyst. In a two-chamber valorization of CO₂ feedstock, a perspective on atom efficiency needs to be considered as this would be a helpful parameter for segregation issues (i.e. separating unreacted ¹³CO₂ or radioactive ¹⁴CO₂ isotopes). New parameters (CO yield and CO₂ conversion) which are based on the initial amount of CO₂ were established and calculated based on the following equations:

$$\text{CO yield} = \frac{\text{amount of CO produced}}{\text{initial amount of CO}_2}$$

$$\text{CO}_2 \text{ conversion} = \frac{\text{amount of CO}_2 \text{ consumed}}{\text{initial amount of CO}_2}$$

A plot of CO yield *vs* CO₂ conversion would then give an idea on the CO₂-to-CO selectivity. In general, CO₂ conversion yield is increased by increasing the amount of photosensitizer and catalyst in the system. CO yield behaves linearly dependent on CO₂ conversion following a slope that is dependent on the selectivity of the system. As shown in Figure 5-7, it seems that the various optimizations, regardless of concentration or presence of additives, fall below the 50% selectivity line. This indicates that (i) though increasing the concentration of the reagents generally increase the CO yield and CO₂ conversion, the selectivity is intrinsic to the nature of the photocatalyst system, and (ii) this selectivity is independent of the addition of water or TEOA or PhOH or even the nature of the solvent. Though only CO and CO₂ gas was observed in the headspace, the low selectivity of the system indicates that CO₂ is transformed to another stable form in the solution. As such, ¹³C isotopic labeling was performed to identify alternative products of CO₂ reduction.

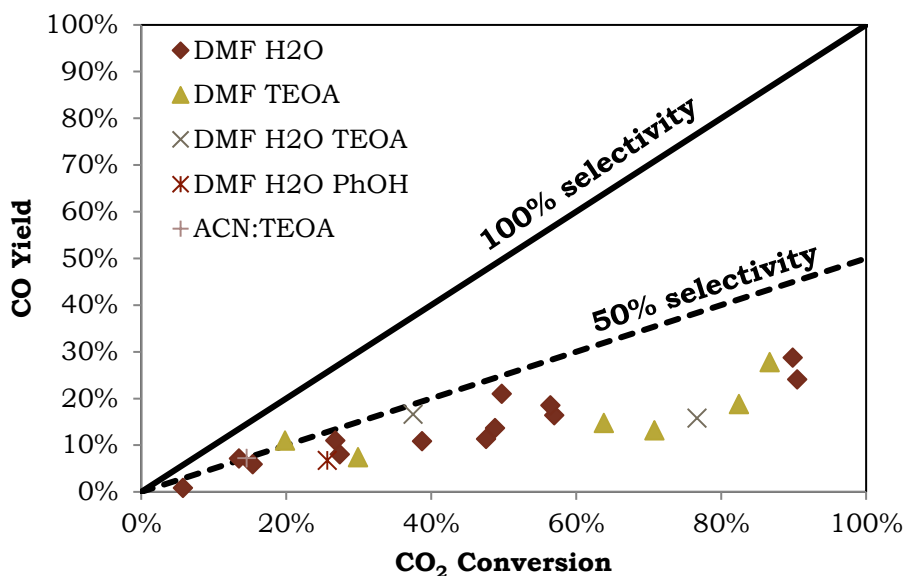


Figure 5-7. Comparison of the CO yield *vs* CO₂ conversion performance of various optimizations (concentrations, solvent conditions) done for the photocatalytic reduction of CO₂ to CO using **Ru(bpy)₃Cl₂** and **Re(CO)₃(bpy)Br** and BIH as SED.

5.7. Isotopic Labeling

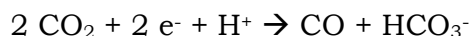
The envisioned application of the two-chamber system comprising of a visible light-induced photocatalytic reduction of CO₂ to CO and its subsequent valorization in aminocarbonylation was conceived for the isotopic labeling of amides commonly found in pharmaceutically relevant drugs. This came into fruition when collaboration was made with *Laboratoire de Marquage au Carbone 14* of *Institut des Sciences du Vivant Frederic-Joliot*, where they utilize radioactive ¹⁴carbon labeling of bioactive compounds. Carbon-14 drug radiolabeling is commonly used to study the distribution, metabolism, toxicity of a drug *in vivo*, in pre-clinical and early clinical studies (Phase 0/1). As part of the Food and Drug Administration safety assessment process, more than 80% of all drugs have used radioactive materials in their testing program.^[30] From a synthetic standpoint, ¹⁴CO₂ represents the primary ¹⁴C labeling source. The escalating price of ¹⁴C labeling building blocks, and the high costs for disposal of radioactive wastes represent major drawbacks in the field. For these reasons, the development of original, multi-catalytic procedures enabling the generation of highly functionalized molecules and advanced building blocks from carbon dioxide would be highly desirable.

Tritec® system is a state-of-the-art manifold, which enables the handling of precise amounts of carbon dioxide and is routinely used by the pharmaceutical and agrochemical industries for radiolabeling of chemicals and active pharmaceutical ingredients. This technology is particularly useful because it enables the utilization

of radioactive $^{14}\text{CO}_2$ under strict and safe working practices. As a proof-of-concept application for our newly developed two-chamber multi-catalytic system, we coupled it to a Tritec® system in order to synthesize ^{13}C -labeled pharmaceutically relevant drugs using $^{13}\text{CO}_2$. The major additional criterion to take into consideration for such an application is the elevated cost of isotope-labeled CO_2 , especially $^{14}\text{CO}_2$. For this reason, the reconsideration of criterion in the previous section was beneficial to determine the yield of the product based on the starting amount of CO_2 .

As shown in Table 5-1 entry 4, when the optimized conditions for the two-chamber system were applied to a limited amount of $^{13}\text{CO}_2$ from the Tritec® system, only 32% conversion of the $^{13}\text{CO}_2$ to ^{13}C -labeled compound was achieved even though a satisfactory yield of 83% ^{13}C -labeled product is obtained based on the amount of ^{13}CO produced. Although a slight improvement is observed using limited amount of $^{13}\text{CO}_2$ (32%, entry 4) compared to excess amount (18%, entry 3), the low yield indicates that the second chamber is efficient in transforming CO in the Pd-catalyzed aminocarbonylation, and the limitation still lies on the Ru-Re-based photocatalytic reduction of CO_2 to CO .

The course of the reaction in the first chamber was monitored by ^{13}C NMR to follow where the CO_2 is transformed as shown in Figure 5-8. It shows that after the first hour of irradiation, a partial amount of **BIH** is transformed to the oxidized **BI⁺** species, still a significant amount of unreacted CO_2 is present, and an initial significant amount of CO is formed together with some amounts of formate and bicarbonate. Completing the photocatalytic activity after 24-hr irradiation shows the complete conversion of **BIH** to **BI⁺**, and significant amounts of formate and bicarbonate present in the solution, with some unreacted CO_2 and traces of CO (as CO gas is assumed to go to the headspace because of its low solubility in DMF). The detection of formate under these reaction conditions was unprecedented inasmuch as the Re catalyst is a well-known selective catalyst towards the production of CO . Since one of the major differences in our study resides in the use of water as a proton source for CO_2 reduction, it is very likely that water could affect the selectivity pattern. As such, formate can stem from the activity of the Re catalyst] in presence of water,^[31] the activity of the degraded form of the Ru photosensitizer, and/or the hydrolysis of dimethylformamide solvent, to a minor extent. The $\text{Ru}(\text{bpy})_2(\text{solvent})_2$ complex, resulting from the loss of a bipyridine, has been shown to catalytically reduce CO_2 to formate.^[31-34] On the other hand, in the absence of water as proton source (DMF:TEOA), a large amount of bicarbonate is formed as a result of CO_2 acting as an oxygen atom acceptor,^[35] which ideally should be protons to form H_2O . As such, the overall reaction of the system is:



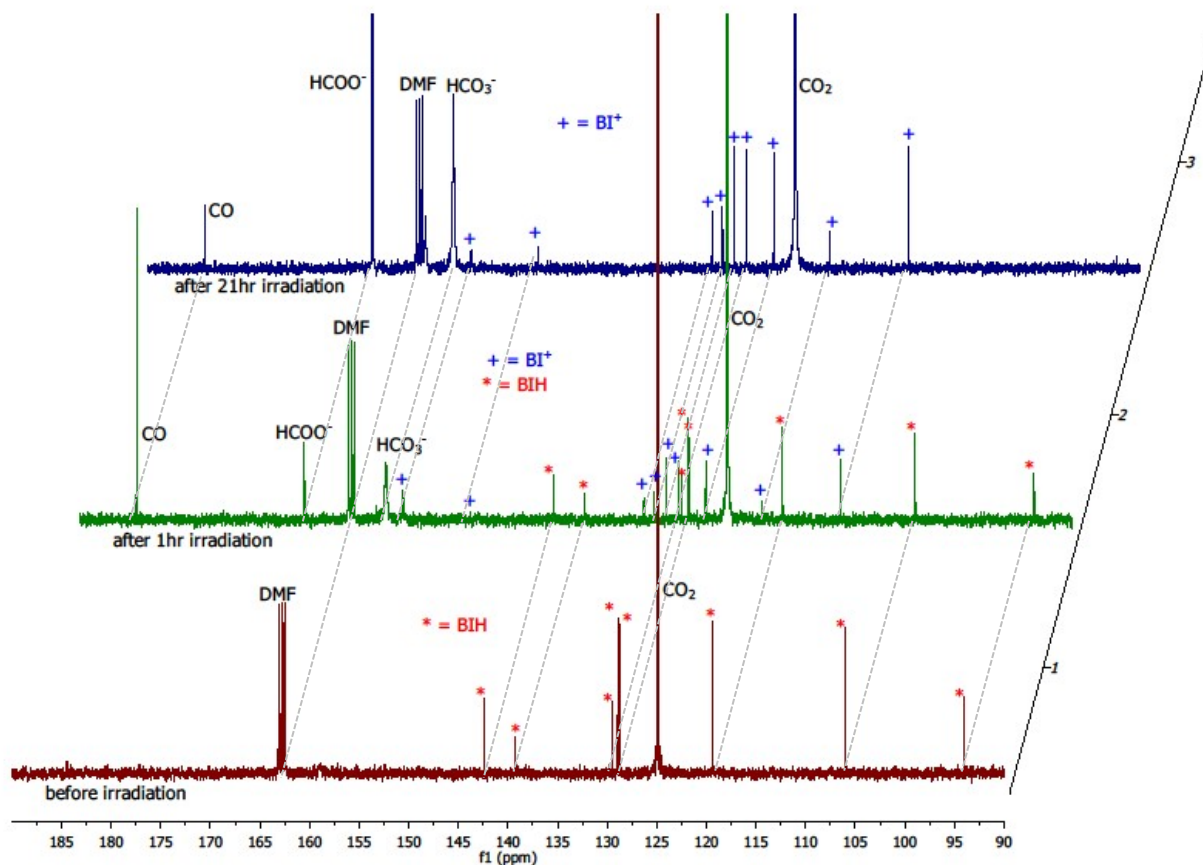
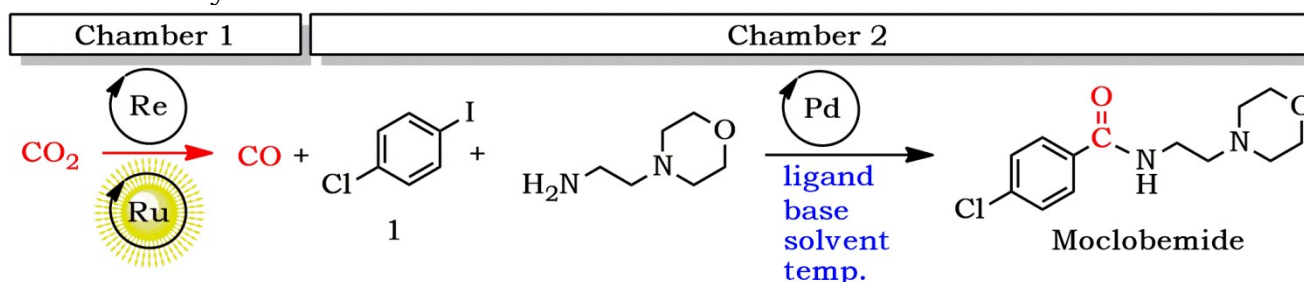


Figure 5-8. ^{13}C NMR spectra at $t = 0$ (red), $t = 1$ hour (green), and $t = 21$ hours (blue) of photocatalytic reaction of 1.4 mM $\text{Ru}(\text{bpy})_3\text{Cl}_2$, 1 mM $\text{Re}(\text{CO})_3(\text{bpy})\text{Br}$, 90 mM BIH, 145 mM TEOA in 0.77 mL 9:1 DMF- d_7 : H_2O with 422 μmol of $^{13}\text{CO}_2$ delivered using Tritec® system, showing the formation of ^{13}CO (184.35 ppm), $\text{H}^{13}\text{CO}_3^-$ (159.22 ppm), and $\text{H}^{13}\text{COO}^-$ (167.44 ppm). The weak intensity of ^{13}CO after 24 hr irradiation is due to the lower solubility of CO in the solvent.

Ongoing efforts in our group aim to address this bottleneck by using oxygen acceptors such as triphenylphosphine, and other additives/solvent conditions to re-shift the bicarbonate back to free CO_2 in the solution. Recently (about 3 months after the publication of our results), the group of He similarly used the two-chamber system for coupling CO_2 photo-reduction with Pd-catalyzed carbonylative Suzuki reaction, aminocarbonylation, and alkoxycarbonylation forming C-C, C-N, and C-O bonds respectively.^[37] They have shown that good yields can be obtained for an extended scope of carbonylation reactions, showing the applicability of such a proof-of-concept in merging photocatalytic CO_2 reduction to CO and its subsequent valorization. However, all their yields were based on the amount of CO produced. As such, further efforts should be made to address the identified limitation.

Using the current optimization of our system, the scope of this multi-catalytic strategy was expanded for the intended application of isotopic labeling of pharmaceutically relevant drugs using CO₂ as a feedstock. For proof of concept, the Moclobemide drug, a reversible inhibitor of monoamine oxidase A^[36] used to treat depression and social anxiety (but not yet approved by FDA), was prepared as shown in Table 5-2. Though the optimized condition of the reaction model in Table 5-1 was translated to the synthesis of the said drug, only a yield of 45% was achieved (entry 1). The difference comes mainly from the nature of the aryl halide and amine used in the synthesis, which requires a harsher condition for a satisfactory yield of 91% to be achieved (entry 2). Translating it to the synthesis of ¹³C-labelled drug showed similar yields, indicating the applicability of such a strategy.

Table 5-2. Optimizations for the synthesis of Moclobemide drug using the two-chamber system.



Entry	CO / mmol	Pd(dba) ₂ / mmol	Ligand / mmol	Base	solvent	T / °C	Yield based ^[c] on	
							CO ₂	CO
1[a]	0.5 [¹² C]	0.025	0.05 [P(tBu) ₃ HBF ₄]	DABCO	THF	20	11 %	45 %
2[a]	0.5 [¹² C]	0.0625	0.125 [PPh ₃]	TEA	dioxane	80	23 %	91 %
3[b]	0.2 [¹³ C]	0.0625	0.125 [PPh ₃]	TEA	dioxane	80	30 %	85 %

[a] Chamber 1 contains 0.19 mM Ru PS, 0.19 mM Re Cat, 0.28 M BIH, DMF + 10% H₂O producing 478 μmol CO. Chamber 2 contains 1.25 mmol of **1**, 2.5 mmol amine, Pd(dba)₂, ligand, 2.5 mmol base, and solvent. CO₂-purged (1 atm); Reaction was run for 21 hours.

[b] Tritec® system was used to deliver limited amount of ¹³CO₂ producing 0.2 mmol ¹³CO

[c] Yield calculated as amount Moclobemide isolated after column chromatography divided by either the initial amount of CO₂ or the amount of CO produced from Chamber 1.

5.8. Conclusion

In conclusion, the direct valorization of CO produced from the visible light-driven catalytic reduction of CO₂ by molecular photocatalysis was established towards an aminocarbonylation reaction to access amides, which are common motifs for bio-active pharmaceutically relevant compounds. CO₂ as a starting material was transformed to simple C1 building blocks which opens further opportunities not only for the valorization of products obtained by the electro- and

photo-catalytic reduction of CO₂, but also providing a cheap access to raw material for industries that use carbonylation as a core chemical process. The investigations on such an application led, however, to the finding of unexpected low selectivity of the photocatalytic system composed of Ru(**bpy**)₃Cl₂ photosensitizer and **Re(CO)₃(bpy)Br** catalyst due to the formation of significant amounts of formate and bicarbonate. This finding calls for a general precaution when revisiting reported selectivities of CO₂ reduction catalysts in the literature as the total accounting of products is often overlooked. On the other hand, this might indicate possible ways of improvement in the design of CO₂ electro- and photo-catalysts to achieve a more selective, stable, and efficient performance.

Bibliography

- [1] O. S. Bushuyev, P. D. Luna, C. T. Dinh, L. Tao, G. Saur, J. van de Lagemaat, S. O. Kelley, E. H. Sargent, *Joule* **2018**, *2*, 825–832.
- [2] P. M. Maitlis, R. Quyoum, H. C. Long, M. L. Turner, *Applied Catalysis A: General* **1999**, *186*, 363–374.
- [3] A. Hamnett, *Catalysis Today* **1997**, *38*, 445–457.
- [4] L. An, R. Chen, *Journal of Power Sources* **2016**, *320*, 127–139.
- [5] R. Francke, B. Schille, M. Roemelt, *Chem. Rev.* **2018**, *118*, 4631–4701.
- [6] P. De Luna, C. Hahn, D. Higgins, S. A. Jaffer, T. F. Jaramillo, E. H. Sargent, *Science* **2019**, *364*, eaav3506.
- [7] C. Das Neves Gomes, O. Jacquet, C. Villiers, P. Thuéry, M. Ephritikhine, T. Cantat, *Angew. Chem. Int. Ed* **2012**, *51*, 187–190.
- [8] R. Yang, in *Gas Separation by Adsorption Processes*, Elsevier Ltd, Butterworth-Heinemann, **1987**, pp. 237–274.
- [9] W. F. Castle, *Int J Refrig* **2002**, *25*, 158–172.
- [10] R. W. Baker, *Ind. Eng. Chem. Res.* **2002**, *41*, 1393–1411.
- [11] T. I. Doukov, L. C. Blasiak, J. Seravalli, S. W. Ragsdale, C. L. Drennan, *Biochemistry* **2008**, *47*, 3474–3483.
- [12] A. Schoenberg, I. Bartoletti, R. F. Heck, *J. Org. Chem.* **1974**, *39*, 3318–3326.
- [13] A. Schoenberg, R. F. Heck, *J. Org. Chem.* **1974**, *39*, 3327–3331.
- [14] A. Schoenberg, R. F. Heck, *J. Am. Chem. Soc.* **1974**, *96*, 7761–7764.
- [15] A. Brennfürer, H. Neumann, M. Beller, *Angew. Chem. Int. Ed* **2009**, *48*, 4114–4133.
- [16] C. F. J. Barnard, *Organometallics* **2008**, *27*, 5402–5422.
- [17] I. Omae, *Coord. Chem. Rev.* **2011**, *255*, 139–160.
- [18] A. Brennfürer, H. Neumann, M. Beller, *ChemCatChem* **2009**, *1*, 28–41.
- [19] M. Beller, B. Cornils, C. D. Frohning, C. W. Kohlpaintner, *J. Mol. Catal. A: Chem.* **1995**, *104*, 17–85.
- [20] I. Ryu, N. Sonoda, *Angew. Chem. Int. Ed* **1996**, *35*, 1050–1066.
- [21] P. Hermange, A. T. Lindhardt, R. H. Taaning, K. Bjerglund, D. Lupp, T. Skrydstrup, *J. Am. Chem. Soc.* **2011**, *133*, 6061–6071.
- [22] S. D. Friis, A. T. Lindhardt, T. Skrydstrup, *Acc. Chem. Res.* **2016**, *49*, 594–605.
- [23] C. Lescot, D. U. Nielsen, I. S. Makarov, A. T. Lindhardt, K. Daasbjerg, T. Skrydstrup, *J. Am. Chem. Soc.* **2014**, *136*, 6142–6147.
- [24] M. T. Jensen, M. H. Rønne, A. K. Ravn, R. W. Juhl, D. U. Nielsen, X.-M. Hu, S. U. Pedersen, K. Daasbjerg, T. Skrydstrup, *Nat. Commun.* **2017**, *8*, 489.

- [25] M. Majek, A. Jacobi von Wangelin, *Angew. Chem. Int. Ed.* **2015**, *54*, 2270–2274.
- [26] T. Kawamoto, A. Sato, I. Ryu, *Chem. Eur. J.* **2015**, *21*, 14764–14767.
- [27] H. Seo, M. H. Katcher, T. F. Jamison, *Nat. Chem.* **2017**, *9*, 453.
- [28] H. Seo, A. Liu, T. F. Jamison, *J. Am. Chem. Soc.* **2017**, *139*, 13969–13972.
- [29] J.-H. Ye, M. Miao, H. Huang, S.-S. Yan, Z.-B. Yin, W.-J. Zhou, D.-G. Yu, *Angew. Chem. Int. Ed.* **2017**, *56*, 15416–15420.
- [30] N. Penner, L. Xu, C. Prakash, *Chem. Res. Toxicol.* **2012**, *25*, 513–531.
- [31] A. Nakada, K. Koike, T. Nakashima, T. Morimoto, O. Ishitani, *Inorg. Chem.* **2015**, *54*, 1800–1807.
- [32] J. Hawecker, J.-M. Lehn, R. Ziessel, *Helv. Chim. Acta.* **1986**, *69*, 1990–2012.
- [33] J.-M. Lehn, R. Ziessel, *J. Organomet. Chem.* **1990**, *382*, 157–173.
- [34] J. Van Houten, R. J. Watts, *Inorg. Chem.* **1978**, *17*, 3381–3385.
- [35] Y. Tamaki, K. Koike, O. Ishitani, *Chem. Sci.* **2015**, *6*, 7213–7221.
- [36] I. Berlin, R. Zimmer, H. Thiede, C. Payan, T. Hergueta, L. Robin, A. Puech, *Br. J. Clin. Pharmacol.* **1990**, *30*, 805–816.
- [37] X. He, Y. Cao, X.-D. Lang, N. Wang, L.-N. He, *ChemSusChem* **2018**, *11*, 3382–3387.

Chapter 6

Conclusions and Perspectives

The way Nature uses sustainable resources to produce forms of energy which support all forms of life on earth inspires a particularly interesting learning point on how we can solve our global warming and energy crisis problems. Indeed, in these work we have shown that we can apply key insights learned from natural systems to improve artificially-designed photo- and electro-catalytic CO₂ reduction systems.

In Chapter 2, we learned how visible light is used to reduce CO₂ to CO using a photocatalyst system comprising of a rhenium triscarbonyl bipyridyl catalyst **[Re(CO)₃(bpy)Br]** and a ruthenium trisbipyridine photosensitizer **[Ru(bpy)₃]²⁺**. Mechanistic investigation through cyclic voltammetry and IR spectroelectrochemistry shows that two electrons have to be accumulated in the catalyst to form the active form that reduces CO₂. Optimized photocatalytic conditions were achieved with 1,3-dimethyl-2-phenylbenzimidazole (**BIH**) as the most efficient sacrificial electron donor because of (i) its high quenching efficiency of the excited state of the photosensitizer and (ii) the production of a non-innocent reducing **BI•** radical that thermodynamically provides the much needed two-electron accumulation in the catalyst. The limitations of the photocatalytic system points to the following considerations: (i) a precaution on leveraging the advantage of the two-electron donating ability of BIH as sacrificial electron donor, (ii) a critical need for a stable photosensitizer, and (iii) a need for a stable and efficient catalyst where the thermodynamic potentials are matched for a photo-induced electron transfer step from the photosensitizer. We address the latter limitation by developing new catalysts through the application of key concepts learned from natural systems.

In Chapter 3, inspired from the sulfur-rich uncoordinated environment found in the Ni-centered C cluster site of CO dehydrogenase (CODH) enzymes, a bio-inspired strategy was employed by modifying the first coordination sphere of a known nickel catalyst bearing a N₂S₂ ligand structure. The introduction of more thioether donors in a novel **Ni-N₂S₃** catalyst resulting to a pentadentate coordination or even replacing the pyridine donors with softer phosphine ligands in the pentadentate **Ni-P₂S₃** catalyst did indeed stabilize low oxidation states of **Ni^I** as observed in the anodic shift of the **Ni^{III/I}** redox couple. However, this extra stabilization didn't translate to an enhanced electro- and photo-catalytic reduction of CO₂ to CO. Unexpectedly, the **Ni-N₂S₃** catalyst exhibited improved electro- and photo-catalytic reduction of protons to hydrogen gas compared to the reference **Ni-N₂S₂** catalyst. Time-resolved UV-vis and X-ray absorption spectroscopic techniques were able to track down and identify the nature and environment of the

intermediates leading to the formation of a photo-induced Ni^{I} complex. This was not sufficient though to differentiate the observed experimental differences as there is a need to probe beyond the first electron transfer. This can be addressed by employing photo-accumulation studies but requires further optimization of experimental set-up and conditions to fully track the second electron accumulation.

We learned from this initial endeavor that though a strategy of modifying the primary coordination sphere of the nickel catalyst can, in most cases, shed light on the structural features of the active site of the CODH enzyme, it seems that systematic changes in such primary coordination does not necessarily translate to expected systematic improvements in the catalytic activity. This is in part due to the interplay of electronic and structural changes that might critically affect the reaction pathways of the catalyst. Furthermore, the similarity of the sulfur-rich environment to hydrogenase enzymes makes such strategy limited in controlling and preventing the competitive proton reduction activity.

In Chapter 4, another bio-inspired strategy was employed learning from the hydrogen bonding stabilization of nearby lysine and histidine residues towards the metal carboxylate intermediate in the CODH enzyme. Systematic investigation was done on the effect of hydrogen bond donors in the periphery of CO_2 reduction catalysts. Establishing one or two proximal amines in the 6,6' positions of the bipyridyl ligand of the Re triscarbonyl catalyst increased the overpotential for CO_2 reduction without significant increase in the TOF. The effect is attributed to the improper positioning of the hydrogen bond donors affecting both the properties of first and second coordination spheres. We learned that installing proximal functionalities in the periphery of such Re catalysts seems tricky because of the intrinsic mechanistic pathway involving the loss of a halide ligand resulting to a pentadentate active form. As such, further modifications for this class of catalyst require more elegant considerations in catalysts design.

We learned that improved catalytic activity by hydrogen bonding stabilization was successfully achieved when urea functions were installed in a $\alpha\beta\alpha\beta$ iron porphyrin atropoisomer with significant lowering of the overpotential while maintaining a good TOF. Such enhancement was achieved because of the pre-organized positioning of the multi-point NH fragments on both urea arms in hydrogen bonding distances towards the metal carboxylate intermediate. The systematic study showed the need for the stronger multi-point hydrogen bonding in

urea functions in **FeTPPUr** compared to the weaker single-point H-bond donors in an amide analogue in **FeTPPAm**. More importantly, DFT calculations show that the metal carboxylate intermediate remains in a quasi-unchanged topology while being put in contact with a water molecule, explaining the synergistic effect of water as a sufficient proton source for the catalytic reduction. This similarly mimics the way CODH manages its proton supply through a nearby water network, which was reported to be critical for the enzymatic activity.

In addition, we learned the advantages of establishing cationic methylimidazolium units in a picket fence iron porphyrin structure in **FeTPPIm**. Significant lowering of the overpotential and increase in the TOF was achieved which is attributed to some extent to the weak hydrogen bonding of the proximal amide functions similar to **FeTPPAm**, but to a larger extent to the electrostatic interactions between the cationic arms towards the metal carboxylate intermediate, exceeding the performance of **FeTPPUr**. Because of the cationic nature of the catalyst, it was even possible to perform CO₂ reduction in water as a convenient and clean solvent and proton source. Indeed, the careful design and systematic manipulation of the secondary coordination sphere of catalysts by applying key learnings from the structure-function studies of CODH was able to improve the catalytic CO₂ reduction activities.

In Chapter 5, we further learned on how Nature utilizes carbon monoxide as a chemical feedstock and applied it to valorize the catalytic reductions of CO₂ to CO studied in this work. The direct valorization of CO produced from the visible-light-driven catalytic reduction of CO₂ at the scale of molecular photocatalysis was established towards an aminocarbonylation reaction to access amide groups, which are common motifs for bio-active pharmaceutically-relevant compounds. As such, CO₂ as a starting material was transformed to simple C1 building blocks which open up further opportunities not only for valorizing the works done in the electro- and photo-catalytic reduction of CO₂, but also providing a cheap access to raw material for industries that uses carbonylation as a core chemical process.

This research has shown efforts to develop step-by-step strategies in improving CO₂ reduction catalysts. Some of the approaches are still crude and need further mechanistic investigations. In perspective, there are still a lot of things to improve. We observe that Nature uses almost the same elemental players (e.g. metal centers, coordinating ligands, amino acid residues, etc.) in performing efficient

processes, and the selectivity towards a certain reaction depends on how they are specifically and carefully arranged (ranging from the active sites of the enzymes to the supramolecular quaternary structures of proteins). This gives a hint that further improvement of the current molecular systems would entail a similar hyperstructuration. This may involve the synthesis of more complex ligand structures forcing an entatic state on the active site of the catalyst, or the heterogenization of the molecular catalysts in metal-organic frameworks, zeolites, and polymers, or even encapsulation on nanostructured reaction sites. A balanced decision should be made however between the complexity of the synthetic procedure, the cost of the material, and more importantly, the efficiency and stability of the system.

Harnessing solar energy and reducing carbon dioxide would, in the current state, entail the use of developments in photovoltaics to drive electrocatalytic CO₂ reduction processes. The promise and potential for a direct photoelectrocatalytic processes still rely on a fundamental need of understanding and optimizing the system. In this end, photocatalytic CO₂ reduction systems which when studied on their own rely on sacrificial electron donors should be incorporated into overall photoelectrocatalytic system where the electrons are sustainably provided by the coupled oxidation reaction, ideally using water as the substrate. Approaches may include grafting of the photosensitizers and catalyst on electrodes of a photoelectrochemical cell or grafting of supramolecular assemblies linking the photosensitizer unit and catalytic unit in a suitable directed fashion for efficient electron flow. The Z-scheme approach observed in the reaction centers in natural photosynthesis can be similarly applied by employing photoanodes and photocathodes delivering the necessary oxidizing and reducing equivalents to drive the redox reactions, eventually in tandem configuration of electrodes with complementary light absorption properties.

On a practical and scaled perspective, development and deployment of artificial photosynthesis technologies seems essential for the necessary increased use of abundant and renewable solar energy as replacement for fossil fuel resources. It can furthermore play an integral part of the global commitment for sustainable carbon capture, storage, and utilization strategy. The advancements in the field of carbon capture technologies either by direct air capture or capture from concentrated point sources will hopefully permit to use such substrate sources for photocatalytic CO₂ reduction systems. There is a need however for a techno-

economic assessment on a practical targeted product to valorize the envisioned tandem technologies. In the end, for these innovations to be globally accepted requires political, economic, and social influences to eliminate the NIMBY (“not in my backyard”) mentality.

Annex

Supplementary Information

General materials and methods	171
X-ray diffraction	171
Electrochemical characterization	172
Infrared spectroscopy and spectroelectrochemistry	173
Time-resolved optical measurements	174
Laser Flash Photolysis	174
Pump-Pump-Probe Measurements	175
Photocatalysis set-up	175
Product quantification by gas chromatography	176
Chapter 2	177
Synthesis of $\text{Re}(\text{CO})_3(2,2'\text{-bpy})\text{Br}$	177
Synthesis of 1-benzyl-1,4-dihydronicotinamide (BNAH).....	177
Synthesis of 1,3-dimethyl-2-phenyl-2,3-dihydro-1H-benzimidazole (BIH).....	177
Photo-accumulation studies.....	179
Chapter 3	180
Synthesis of N_2S_2	180
Synthesis of NiN_2S_2	180
Synthesis of N_2S_3	180
Synthesis of NiN_2S_3	181
Synthesis of P_2S_3	181
Synthesis of NiP_2S_3	182
Steady-State XANES and EXAFS Measurements.....	182
EXAFS Analysis	183
DFT Calculations	185
Optical and XANES simulations.....	185
Time-resolved XAS measurements	186

Chapter 4	188
Synthesis of ReAm1	188
Synthesis of ReAm2	188
Synthesis of TPPUr	188
Synthesis of FeTPPUr.....	189
Synthesis of TPPAm	190
Synthesis of FeTPPAm.....	190
Synthesis of FeTPPBzm.....	191
Synthesis of FeTPPIm.....	191
FOW analysis of modified iron porphyrin complexes	192
CO ₂ binding rate constants of modified iron porphyrins	194
Crystallographic data of modified iron porphyrins.....	195
DFT calculations for FeTPPAm and FeTPPUr.....	196
Bulk electrolysis of FeTPPUr in DMF.....	197
Bulk electrolysis of FeTPPIm in water.....	198
Chapter 5	199
Experimental set-up of the two-chamber system.....	199
General protocol for chamber 1	199
Control experiments for chamber 1	199
Synthesis of n-hexyl-4-methoxybenzamide using ¹² CO ₂ purging	200
Synthesis of n-hexyl-4-methoxybenzamide using ¹³ CO ₂ Tritec®	201
Synthesis of Moclobemide using ¹² CO ₂ purging.....	202
Synthesis of Moclobemide using ¹³ CO ₂ Tritec®.....	202
Bibliography	203

General materials and methods

Dimethylformamide (DMF, Aldrich 99.9%), acetonitrile (ACN, Aldrich 99.9%), tetra-*N*-butylammonium hexafluorophosphate (TBAP, Aldrich 99%) were used as received. All other chemical reagents used in the synthetic routes were obtained from commercial sources as guaranteed-grade reagents and used without further purification. The water utilized in most measurements and synthetic procedures was Milli-Q filtered (18.2 M Ω ·cm at 25 °C). Proton and carbon nuclear magnetic resonance (¹H and ¹³C NMR) spectra were recorded at room temperature on Bruker Advance 400 MHz spectrometers. Two-dimensional NMR (COSY, HSQC and HMBC) experiments were also performed in order to confirm the attribution of one-dimensional ¹H NMR signals. The electrospray ionization mass spectrometry (ESI-HRMS) experiments were performed on TSQ (Thermo Scientific, 2009) with an ESI⁺ method. Ground state absorption measurements were measured in a Specord double beam spectrophotometer (Analytik Jena), consisting of halogen and deuterium lamps as light sources, monochromator with holographic concave grating, and two photodiodes as radiation detectors. For all optical experiments sealed quartz cuvettes (1 cm x 1 cm) were used and samples purged with argon before measurements.

X-ray diffraction

X-ray diffraction data for compounds were collected by using a VENTURE PHOTON100 CMOS Bruker diffractometer with Micro-focus IuS source Cu K_{α} radiation. All crystals were mounted on a CryoLoop (Hampton Research) with Paratone-N (Hampton Research) as cryoprotectant and then flash-frozen in a nitrogen-gas stream at 100 K. For compounds, the temperature of the crystal was maintained at the selected value by means of a N-Helix cooling device within an accuracy of ± 1 K. The data were corrected for Lorentz polarization and absorption effects. The structures were solved by direct methods using SHELXS-97^[1] and refined against F^2 by full-matrix least-squares techniques using SHELXL-2018^[2] with anisotropic displacement parameters for all non-hydrogen atoms. All calculations were performed by using the Crystal Structure crystallographic software package WINGX.^[3]

Electrochemical characterization

Cyclic voltammetry (CV) measurements were performed in an electrochemical cell composed of a glassy carbon (3 mm diameter) working electrode, Ag/AgNO₃ (10⁻² M) reference electrode, and a platinum wire counter electrode. Dimethylformamide (DMF) and acetonitrile (ACN) were mainly used as solvents and solutions of samples were prepared at a concentration of 1 mM. Tertbutylammonium hexafluorophosphate (TBAP) was used as supporting electrolyte and its concentration was maintained at hundred-fold excess compared to the sample. Different proton sources (water, trifluoroethanol, phenol) were added, the solutions were purged with inert argon gas, and the cyclic voltammograms were measured at a scan rate of 100 mV/s (unless stated otherwise). Ferrocene was added to the solutions at the end of each measurement as a reference for standard comparison, and as such all potentials were reported versus the Fc⁺⁰ couple. Standard comparisons with state-of-the-art catalysts were made by converting literature values to the Fc⁺⁰ couple using reported conversion values.^[4-7]

Catalytic rates of the electrocatalytic systems were determined using the reported benchmarking strategy of foot-of-the wave (FOW) analysis of the CVs.^[8] This quick estimation technique gives the catalytic rate constant, k_{cat} and turnover frequency (TOF) preventing any contributions from side phenomena such as substrate consumption, catalyst deactivation, and/or product inhibition. The analysis is based on the linear correlation between i/i_p^0 and $1/\{1+\exp[F/RT(E - E^0_{cat})]\}$ where i is the catalytic current in the presence of CO₂, i_p^0 is the peak current in the absence of CO₂, F is the faraday constant, R is the gas constant, and T is the absolute temperature, E is the applied potential, and E^0_{cat} is the standard potential of the reversible reduction peak of the active form of the catalyst. Plotting i/i_p^0 vs. $1/\{1+\exp[F/RT(E - E^0_{cat})]\}$ gives rise to a straight line with a slope = $2.24(RT/Fv)^{1/2}(k_{cat})^{1/2}$ where v is the scan rate in Vs⁻¹ and k_{cat} is the observed catalytic rate constant.

$$\frac{i}{i_p^0} = \frac{2.24 \sqrt{\frac{RT}{Fv}} k_{cat}}{1 + \exp\left[\frac{F}{RT}(E - E^0_{cat})\right]}$$

From this value of k_{cat} , a catalytic Tafel plot can be traced by plotting $\log TOF$ vs. η :

$$\eta = E^0_{CO_2/CO} - E$$

$$TOF = \frac{k_{cat}}{1 + \exp\left[\frac{F}{RT}(E^0_{cat} - E^0_{CO_2/CO} - \eta)\right]}$$

$$\log TOF = \log k_{cat} - \frac{F}{RT \ln 10} (E_{CO_2/CO}^0 - E_{cat}^0) + \frac{F\eta}{RT \ln 10}$$

This provides a precise characterization of the performance of the catalyst as a function of the applied overpotential. Taking the TOF at zero overpotential (TOF₀) then gives the intrinsic activity of the catalyst:

$$\log TOF_0 = \log k_{cat} - \frac{F}{RT \ln 10} (E_{CO_2/CO}^0 - E_{cat}^0)$$

The maximal catalytic rate constants, TOF_{max}, asymptotically reached for large overpotentials, are also often reported which is just equal to the determined k_{cat} .^[9]

The FOW analysis has been successfully applied to the iron porphyrin catalysts with estimations close to that obtained from bulk electrolysis experiments.^[10] It has been addressed recently however, that for some catalysts, like the Re-based bipyridine catalysts, estimations using the FOW analysis yielded irreproducible k_{cat} values.^[11] The irreproducibility was attributed to the estimation of E_{cat}^0 which is sometimes beyond the reversible couple of the active form of the catalyst. There have been reports consolidating measurements of overpotential, and it was suggested that use of the half-wave potential ($E_{cat/2}$), defined as the point at which the homogeneous catalytic wave reaches half of its maximum current, is often recommended, when E_{cat} is difficult to determine.^[12,13] Because of these difficulties, most authors turn to the method of scan-rate independent catalytic plateau currents to determine the catalytic rate, where n is the number of unique electron transfer processes that occur at the electrode per catalyst and n' is the catalyst equivalents required per turnover:

$$\frac{i}{i_p^0} = 2.24 \sqrt{\left(\frac{RT}{nFv}\right) n' k_{cat}}$$

Infrared spectroscopy and spectroelectrochemistry

The IR spectra of the catalysts were determined by dropping dichloromethane solution of the samples onto the diamond prism of an attenuated total reflectance-infrared (ATR-IR) Thermo-Nicolet 6700 FTIR spectrometer equipped with a mercury-cadmium-telluride (MCT) detector. The solvent was allowed to evaporate in a stream of nitrogen gas until a dry film is deposited. 200 sample scans were recorded with a resolution of 4 cm⁻¹, in the range of 4000 cm⁻¹ to 500 cm⁻¹ with a speed of 1.89 kHz and aperture of 10 mm.

IR-spectroelectrochemistry was performed by mounting a home-made electrochemical cell on top of the ATR prism. The three-electrode cell is employed

with a glassy carbon (3 mm diameter) working electrode, Ag/AgNO₃ (10⁻² M) reference electrode, and a platinum wire counter electrode. Extra care is needed to adjust the distance between the ATR prism and the active surface of the working electrode ensuring that a thin reactive layer is immediately within the detection limit of the ATR prism. A linear sweep voltammetry (LSV) technique is used in the spectroelectrochemical measurements where the potential is swept from the start to the end potential of the reactive species being studied with a scan rate of 50 mV/s, giving an interval time of 100 s. During this interval, 80 scans of IR spectra are recorded with a resolution of 2 cm⁻¹ for the spectrum range of 4000 cm⁻¹ to 500 cm⁻¹ with a speed of 3.6 kHz and aperture of 10 mm. The IR scans take into account a background spectrum of the electrolyte solution (0.1 M TBAP in ACN), so that the resulting scans will provide the clean IR spectra related to the catalyst. As such, each potential step from the LSV corresponded to one IR spectrum. We found that this optimized set-up gives much sensitive changes in the IR signal compared to a chronoamperometric technique. It has been observed however that for some experiments, some preceding species persists on the next potential scan, resulting in observation of IR peaks from two intermediate species. The evolution of the IR spectra however is a good indication of the evolution of the intermediates during the potential sweep, with tested reference complexes agreeing with literature reports.

Time-resolved optical measurements

Laser Flash Photolysis

Excited state absorption characteristics were measured using an Edinburgh Instruments LP 920 laser flash photolysis spectrometer. Laser excitation pulses were generated from a Continuum Surelite Q-switched Nd:YAG laser coupled with a Continuum optical parametric oscillator (OPO) to produce an excitation pulse with 5 ns pulse duration at a wavelength of 460 nm (or 430 nm) and a typical laser energy of about 7-10 mJ per flash. The LP920 system is equipped with a 450 W Xenon arc lamp as the probe for the transient absorption measurements. Detection in the LP920 system is performed either via a Czerny-Turner blazed 500 nm monochromator (bandwidth: 1-5 nm) coupled with a Hamamatsu R928 photomultiplier tube (for kinetics mode), or via a 500 nm blazed spectrograph (bandwidth: 5 nm) coupled with a water-cooled ICCD camera Andor DH720 (for spectral mode). LP920 software was used for data acquisition, to calculate changes in optical density, for mathematical data treatment.

Pump-Pump-Probe Measurements

Pump-pump-probe measurements were measured in collaboration with Thu Trang Than, Dr. Minh Huong Ha Thi, and Dr. Thomas Pino from the Laboratory of Molecular Systems, Astrophysics, and Environment in Institut des Sciences Moléculaires d'Orsay (ISMO). The setup was described in a recently published report.^[14] Two Nd:YAG pumped optical parametric oscillator (OPO) lasers are used for sample excitation at 460 nm with an energy of ~ 5 mJ/pulse. The first pump operates at 20 Hz, and the second one has a repetition rate of 10 Hz. After excitation the sample is probed by a white light continuum laser (LEUKOS) with a repetition rate of 20 Hz. The probe beam is split into two arms, one for probing sample and the other for reference in order to compensate for energy fluctuation. The probing arm after passing the sample is coupled into an optical fiber bundle before being analyzed by a spectrograph SPEX 270M (Jobin Yvon). Detection of the dispersed white light is performed by an intensified CCD (ICCD) detector (PIMAX 4, Princeton Instruments). The setup is operated in online subtraction mode in which the transient absorption after the first excitation is inherently removed by running the first pump at 20 Hz which is the same as the repetition rate of the probe. Therefore, in principle we obtain a relatively pure signal from molecules that are excited twice, as the off signal then contains contributions from the singly pumped solution. It is noteworthy that the double pumped transient signal contains contributions from singly and doubly excited molecules because excitation efficiency by the first pump laser cannot reach 100%.

Photocatalysis set-up

Photocatalytic experiments were made in a modified quartz cuvette with a total volume of 6.85 mL, thermostated at 20°C, and sealed with a rubber septum. About 3.0 mL solutions of **Ru(bpy)₃Cl₂** photosensitizer, catalyst, proton source, and sacrificial electron donor were dissolved in appropriate solvents and were purged with CO₂ for 15 minutes for CO₂ reduction experiments or with Ar gas for proton reduction experiments. To excite only the ruthenium photosensitizer's MLCT band and to prevent the sample from excessive heating, a SugarCUBE high intensity LED fiber optic illuminator was utilized with a blue light output centered at 463 nm with a full width at half maximum (FWHM) characteristic of about 50 nm. The source was adjusted to produce the lowest light intensity of 180 W/m² (18 mW/cm²).

Product quantification by gas chromatography

Quantification of products during the photo- and electrocatalytic reactions was performed by withdrawing 50 μL gas aliquots from the headspace of the reaction vessel with a gas-tight syringe and injected into a gas chromatography (GC - TraceGC Ultra, ThermoScientific) equipped with a 30 m molecular sieve porous layer open tubular (PLOT) column having an internal diameter of 0.53 mm, helium carrier gas, and a thermal conductivity detector (TCD). Peak separation between H_2 , CO, and CO_2 were achieved by programming the oven temperature from an initial 40 $^\circ\text{C}$ for 2 min, ramped by 50 $^\circ\text{C}/\text{min}$ until a final temperature of 250 $^\circ\text{C}$ held for 2 min. H_2 was detected at 2.16 min, CO was detected at 3.13 min, and CO_2 was detected at 6.10 min. For more sensitive quantification of H_2 for proton reduction experiments, an argon gas was utilized as the carrier gas due to the bigger difference in the thermal conductivity between Ar and H_2 . A splitless injector line was utilized to maximize the injection volume and become sensitive to possible trace amounts. A calibration curve relating peak area and concentration of CO (or H_2) was established by injecting known amounts of pure CO (or H_2) into the reaction vessel and after 10 min equilibration time, 50 μL gas aliquots were drawn from the headspace and injected into the GC. This calibration method accounts for the headspace volume of the set-up and any CO dissolved in the solution and as such, it can be used to determine actual amounts of CO (or H_2) produced.

Chapter 2

Synthesis of $\text{Re}(\text{CO})_3(2,2'\text{-bpy})\text{Br}$

The complex was synthesized with slight modifications from literature methods.^[15] An equimolar amount of $\text{Re}(\text{CO})_5\text{Cl}$ (0.3451 g, 0.85 mmol) and 2,2'-bipyridine (0.136 g, 0.87 mmol) was dissolved in toluene (50 mL) and heated to 115 °C. The reaction mixture was stirred under reflux for 2 h. Afterwards the solution was removed from the heat source and cooled down by placing in an ice bath. The product precipitated from solution as a yellow powder and was filtered off. Pure product was isolated from the reaction with an overall yield of 92% (0.3256g). X-ray quality crystals were grown from the vapor diffusion of pentane into a chloroform solution of the complex.

$^1\text{H NMR}$ (CD_3CN , 298 K, 200 MHz): δ_{H} 7.62 (2H, t), 8.18 (2H, t), 8.41 (2H, d), 9.00 (2H, d).

ESI-HRMS: calculated $m/z = 528.9168$ $[\text{M}+\text{Na}^+]^+$ for $\text{C}_{13}\text{H}_8\text{BrN}_2\text{NaO}_3\text{Re}$, found 528.9143

Synthesis of 1-benzyl-1,4-dihydronicotinamide (BNAH)

Nicotinamide (4.88 g, 40 mmol, 1.0 eq) and benzyl bromide (5.4 mL, 50 mmol, 1.25 eq) were dissolved in a mixture of dioxane:methanol (100 mL:27 mL) and refluxed at 65 °C for 7 hours. The resulting benzyl nicotinamide precipitate was filtered, washed with dioxane and recrystallized from methanol (yield of 86 %, 7.32 g). Benzyl nicotinamide (7.0 g, 33 mmol, 1.0 eq) and Na_2CO_3 (23.0 g, 132 mmol, 4.0 eq) were mixed in 170 mL water and sodium dithionite (14.0 g, 132 mmol, 4.0 eq) was added dropwise over two hours. The resulting **BNAH** precipitate was filtered, washed with water, dried and kept in the freezer. Yield: 4.392 g (62%).

$^1\text{H NMR}$ (CDCl_3 , 300 MHz): δ_{H} 7.39-7.20 (5H, m), 7.16 (1H, d), 5.74 (1H, ap dq), 5.22 (2H, br s), 4.75 (1H, dt), 4.29 (2H, s), 3.17 (2H, dd)

ESI-HRMS: calculated $m/z = 213.1022$ $[\text{M}]^+$ for $\text{C}_{13}\text{H}_{13}\text{N}_2\text{O}$, found 213.1003

Synthesis of 1,3-dimethyl-2-phenyl-2,3-dihydro-1H-benzimidazole (BIH)

Synthesis of N-methyl-2-phenylbenzo[d]imidazole: 2.25 g of potassium hydroxide (40 mmol, 2.0 eq) was dissolved in 70 mL DMSO and was stirred at room temperature for 30 min. 4.135 g of 2-phenylbenzo[d]imidazole (21.3 mmol, 1.0 eq) was dissolved in 70 mL DMSO and was added to the previous mixture and was stirred at room temperature, closed, for 45 min. The solution turned from clear yellow to clear red. 1.4 mL of methyl iodide (22.3 mmol, 1.05 eq) was added to the

reaction mixture and stirred at room temperature, closed, for 45 min. The solution turned to yellow. The reaction mixture was then poured into a stirring solution of water (700 mL) containing potassium hydroxide (3.5 g). 200 mL of diethyl ether was then added and stirred until both layers were transparent. The organic layer was decanted, and the same process was repeated with additional diethyl ether. The combined organic layers were washed with water, brine, dried over MgSO₄, filtered, and evaporated to get yellowish oil which turned into yellow precipitate upon vacuum drying. Yield: 4.019 g (91%).

¹H NMR (DMSO-d₆, 300 MHz,) δ_H 7.86 (2H, d), 7.69 (1H, d), 7.63-7.56 (4H, m), 7.32-7.23 (2H, m), 3.88 (3H, s)

Synthesis of 1,3-dimethyl-2-phenylbenzo[d]imidazolium iodide: 3.999 g of N-methyl-2-phenylbenzo[d]imidazole (19.2 mmol, 1.0 eq) was dissolved in 30 mL dichloromethane under stirring. 3.8 mL of methyl iodide (60.5 mmol, 3.2 eq) was added to the reaction mixture and was stirred at 30°C, closed, for 17 h. The solvent was evaporated using rotary evaporator and diethyl ether was added. The solid was filtered, washed with diethyl ether, and dried under vacuum to produce off-white powder. Yield: 6.681 g (99%).

¹H NMR (DMSO-d₆, 300 MHz): δ_H 8.15 (2H, br s), 7.98 (2H, br s), 7.91-7.78 (5H, m), 3.90 (6H, s)

Synthesis of 1,3-dimethyl-2-phenyl-2,3-dihydro-1H-benzimidazole (BIH): 4.247 g of 1,3-dimethyl-2-phenylbenzo[d]imidazolium iodide (12.1 mmol, 1.0 eq) was dissolved in 160 mL methanol under inert atmosphere. 1.147 g of NaBH₄ (30.3 mmol, 2.5 eq) was slowly added to the reaction mixture in an ice-water bath. The resulting mixture was stirred under inert atmosphere at room temperature for 1 hour followed by evaporation of solvent by rotary evaporator. Water was added and the product was extracted with diethyl ether. The organic layer was treated with saturated NaCl and anhydrous MgSO₄. The solvent was evaporated, and the white solid was recrystallized with minimum amount of 5:1 (v/v) ethanol:water mixture to form white needle-like crystals. Yield: 2.185 g (81 %).

¹H NMR (CDCl₃, 300 MHz): δ_H 7.58 (2H, m), 7.41 (3H, m), 6.72 (2H, dd), 6.43 (2H, dd), 4.87 (1H, s), 2.56 (6H, s)

ESI-HRMS: calculated m/z = 223.1230 [M-H]⁺ for C₁₅H₁₅N₂, found 223.1230

Photo-accumulation studies

Photo-accumulation studies were performed by recording the spectra of the solution during photo-irradiation, in which the photocatalytic cell is directly mounted inside an Agilent Cary 60 UV-Vis spectrophotometer. A scanning kinetics mode is applied with a scanning rate of 9600 nm/min and a resolution of 1 nm, for a cycle time of 0.1 min for the duration of the desired photo-irradiation. This was performed with the same conditions and light source as previously described in the photocatalytic set-up, optimizing the concentrations and light intensity to achieve significant observable changes in the spectra.

The time-resolved spectra were then fitted with the fitting software *Kintek Global Kinetic Explorer™*. This dynamic kinetic simulation program allows for multiple data sets to be fit simultaneously to a single model based on numerical integration of the rate equations describing the reaction mechanism.^[16] The experimental spectra were input in the software as well as a proposed reaction model, based on initial kinetic studies by nanosecond pump-probe measurements and literature know-how on proposed mechanisms. The output would include the reconstruction of the experimental data, rate constants of the elementary steps proposed in the reaction model, concentration profile of the observable intermediates, and the corresponding spectra of the intermediates.

Chapter 3

Synthesis of N_2S_2

Na metal (300 mg, 13 mmol, 4.4 eq) was dissolved in absolute methanol (15 mL) under Ar. 1,2-Ethanedithiol (250 μ L, 2.97 mmol, 1.0 eq) was added to the solution and stirred at room temperature. Then, the solution of 2-picoly chloride hydrochloride (1.06 g, 6.46 mmol, 2.2 eq) in absolute methanol (7 mL) was added slowly to the mixture. The mixture was stirred for 16 h at room temperature under Ar. The solvent was removed using rotary evaporator and the residue was extracted with chloroform and H₂O. The organic layer was washed with brine solution, dried over anhydrous MgSO₄, and filtered. The volatiles of the filtrate were evaporated using rotary evaporator and further dried under vacuum to produce brown oil of bis(2-pyridylmethyl)-1,2-ethanedithiol, denoted as **N_2S_2** (811 mg, 2.95 mmol, 99% yield).

1H NMR (CDCl₃, 298 K, 360 MHz): δ_H 2.70 (4H, s), 3.85 (4H, s), 7.17 (2H, dd), 7.37 (2H, d), 7.66 (2H, dd), 8.52 (2H, d)

ESI-HRMS: calculated $m/z = 299.0647$ [M+Na⁺]⁺ for C₁₄H₁₆N₂NaS₂, found 299.0636.

Synthesis of NiN_2S_2

An equimolar solution of Ni(ClO₄)₂•6H₂O (392 mg, 1.0 mmol, 1.0 eq) in MeOH (10 mL) was added to a solution of **N_2S_2** ligand (292 mg, 1.0 mmol, 1.0 eq) in MeOH (10 mL). The mixture was stirred for 1 day at room temperature. The solvent was evaporated using rotary evaporator forming purplish oil. The oil was dissolved in acetonitrile and ethyl acetate was added to promote precipitation. X-ray quality crystals were grown by slow diffusion of ethyl acetate in the acetonitrile solution of the complex (376 mg, 0.61 mmol, 61% yield).

ESI-HRMS: calculated $m/z = 432.9588$ [M-(ClO₄)]⁺ for C₁₄H₁₆N₂S₂NiClO₄, found 432.9593.

Synthesis of N_2S_3

Na metal (2.48 g, 104 mmol, 4.0 eq) was dissolved in absolute ethanol (150 mL) under Ar atmosphere. 2,2'-Thiodiethanethiol (3.4 mL, 26.1 mmol, 1.0 eq) was added to the solution and the mixture was heated to reflux at 85 °C for 30 min. Then, a solution of 2-picoly chloride hydrochloride (8.50 g, 51.8 mmol, 2.0 eq) in absolute ethanol (100 mL) was added slowly to the mixture. The mixture was stirred and refluxed at 85 °C for 15 h under Ar. The solvent was removed using rotary

evaporator and the residue was extracted with chloroform and H₂O. The organic layer was washed with brine solution, dried over anhydrous CaCl₂, and filtered. The volatiles of the filtrate were evaporated using rotary evaporator and further dried under vacuum to produce brown oil of bis(2-pyridylmethyl)-2,2'-thiodiethanethiol, denoted as **N₂S₃** (8.743 g, 25.98 mmol, 99.5% yield).

¹H NMR (CDCl₃, 298 K, 250 MHz): δ_H 2.70 (8H, s), 3.89 (4H, s), 7.20 (2H, dd), 7.39 (2H, d), 7.70 (2H, dd), 8.56 (2H, d)

ESI-HRMS: calculated m/z = 359.0681 [M+Na]⁺ for C₁₆H₂₀N₂NaS₃, found 359.0698.

Synthesis of NiN₂S₃

An equimolar solution of Ni(ClO₄)₂•6H₂O (336 mg, 1.0 mmol, 1.0 eq) in MeOH (20 mL) was added to a solution of **N₂S₃** ligand (366 mg, 1.0 mmol, 1.0 eq) in MeOH (20 mL). The mixture was stirred for 1 hour at room temperature. The solvent was evaporated using rotary evaporator forming purplish oil. The oil was dissolved in acetonitrile and ethyl acetate was added to promote precipitation. X-ray quality crystals were grown by slow diffusion of ethyl acetate in the acetonitrile solution of the complex (438 mg, 0.69 mmol, 69% yield).

ESI-HRMS: calculated m/z = 492.9622 [M-(ClO₄)]⁺ for C₁₆H₂₀N₂S₃NiClO₄, found 492.9621.

Synthesis of P₂S₃

Synthesis of 1-chloro-2-diphenylphosphinoethane: Under an Ar atmosphere, potassium diphosphide solution (75 mL, 0.5 M in THF) was added dropwise to dichloroethane (250 mL) for 1 hour at room temperature. The mixture was stirred further for 2 h and the solvent was evaporated using rotary evaporator. The residue was extracted with dichloromethane and water. The organic layer was washed with brine solution, dried over anhydrous MgSO₄, and filtered. The volatiles of the filtrate were evaporated using rotary evaporator to produce yellow oil. The crude product was purified using column chromatography (silica gel) with chloroform as eluent, finally obtaining pure yellow oil (1.532 g, 16% yield).

¹H NMR (CDCl₃, 298 K, 250 MHz): δ_H 2.61 (2H, t), 3.63 (2H, t), 7.39-7.49 (10H, m)

Synthesis of 1,11-bis(diphenylphosphino)-3,6,9-trithiaundecane (P₂S₃): Na metal (296 mg, 12.9 mmol, 4.0 eq) was dissolved in absolute ethanol (20 mL) under

Ar atmosphere. 2,2'-Thiodiethanethiol (0.4 mL, 3.1 mmol, 1.0 eq) was added to the solution and the mixture was heated to reflux at 85 °C for 30 min. Then, a solution of 1-chloro-2-diphenylphosphinoethane (1.532 g, 6.2 mmol, 2.0 eq) in absolute ethanol (15 mL) was added slowly to the mixture. The mixture was stirred and refluxed at 85 °C for 17 h under Ar. The solvent was removed using rotary evaporator and the residue was extracted with chloroform and H₂O. The organic layer was washed with brine solution, dried over anhydrous CaCl₂, and filtered. The volatiles of the filtrate were evaporated using rotary evaporator. The residue was further purified with column chromatography (silica gel) with pentane containing 30-80% (v/v) chloroform as the eluent, finally obtaining pure yellow oil of 1,11-bis(diphenylphosphino)-3,6,9-trithiaundecane, denoted as **P₂S₃** (996 mg, 1.72 mmol, 55% yield).

¹H NMR (CDCl₃, 298 K, 250 MHz): δ_H 2.30-3.00 (20H, m), 7.35 (4H, d), 7.40-7.58 (8H, m), 7.74 (4H, dd)

ESI-HRMS: calculated m/z = 579.1527 [M+H]⁺ for C₃₂H₃₇P₂S₃, found 579.1519.

Synthesis of NiP₂S₃

An equimolar solution of Ni(ClO₄)₂•6H₂O (220 mg, 0.60 mmol, 1.1 eq) in MeOH (10 mL) was added to a solution of **P₂S₃** ligand (320 mg, 0.55 mmol, 1.0 eq) in MeOH (10 mL). The mixture was stirred for 1 hour at room temperature. The solvent was evaporated using rotary evaporator forming dark green oil. The oil was dissolved in acetonitrile and ethyl acetate was added to promote precipitation. X-ray quality crystals were grown by slow diffusion of ethyl acetate in the acetonitrile solution of the complex (202 mg, 0.24 mmol, 44% yield).

ESI-HRMS: calculated m/z = 735.0287 [M-(ClO₄)]⁺ for C₃₂H₃₆P₂S₃NiClO₄, found 735.0303.

Steady-State XANES and EXAFS Measurements

X-ray absorption measurements were performed in collaboration with Dr. Dooshaye Moonshiram from IMDEA Nanociencia in Madrid. The spectra were collected at the Advanced Photon Source (APS) at Argonne National Laboratory on bending magnet beamline 9 at electron energy 8.43 keV and average current 100 mA. The radiation was monochromatized by a Si(110) crystal monochromator. The intensity of the X-ray was monitored by three ion chambers (I₀, I₁ and I₂) filled with 70% nitrogen and 30% helium and placed before the sample (I₀) and after the

sample (I_1 and I_2). A Ni metal foil was placed between the I_1 and I_2 and its absorption recorded with each scan for energy calibration. Plastic (PEEK) EXAFS sample holders (inner dimensions of 12 mm x 3 mm x 3 mm) filled with frozen solution samples were inserted into a pre-cooled (20 K) cryostat. The samples were kept at 20 K in a He atmosphere at ambient pressure. Data were recorded as fluorescence excitation spectra using a 4-element Si drift energy-resolving detector. Solid samples were diluted with BN powder, pressed between polypropylene and mylar tape, and measured in the cryostat in transmission mode. In order to reduce the risk of sample damage by X-ray radiation, 80% flux was used in the defocused mode (beam size 1 x 10 mm) and no damage was observed to any samples scan after scan. The samples were also protected from the X-ray beam during spectrometer movements by a shutter synchronized with the scan program. No more than 5 scans were taken at each sample position in any condition. The Ni XAS energy was calibrated by the first maximum of the second derivative of the cobalt metal XANES spectrum.

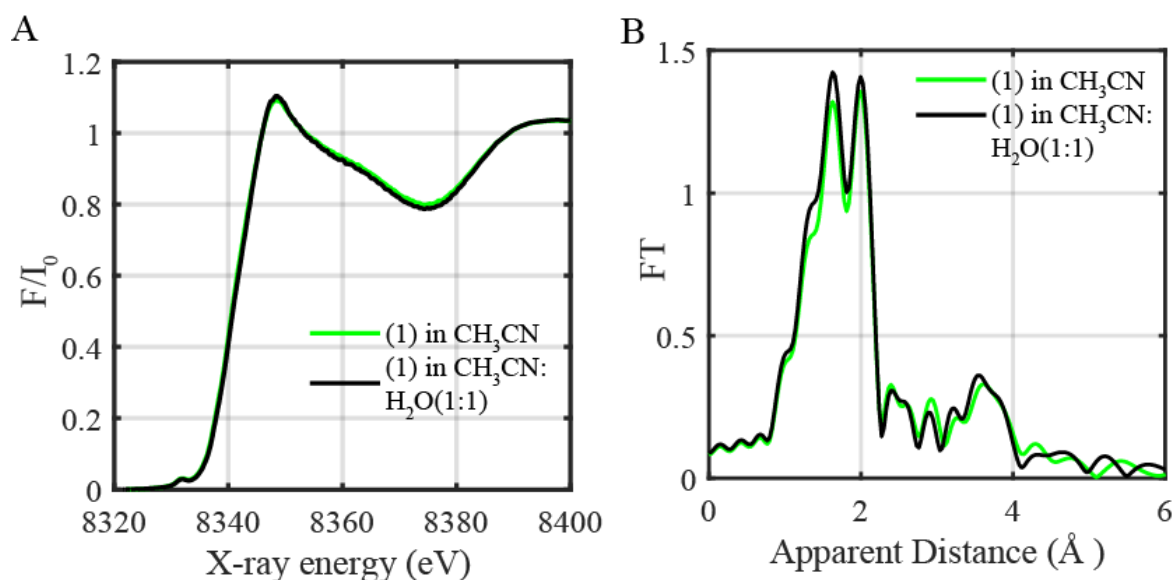


Figure 0-1. A. Normalized experimental Ni K-edge XANES of NiN_2S_3 in pure ACN (black) and in 1:1 ACN:H₂O (green) B. Fourier transforms of k^2 -weighted Ni EXAFS of NiN_2S_3 in pure ACN (black) and in 1:1 ACN:H₂O (green).

EXAFS Analysis

Athena software^[17] was used for data processing. The energy scale for each scan was normalized using copper metal standard. Data in energy space were pre-edge corrected, normalized, deglitched (if necessary), and background corrected. The processed data were next converted to the photoelectron wave vector (k) space

and weighted by k . The electron wave number is defined as $k = [2m(E - E_0)/\hbar^2]^{1/2}$, E_0 is the energy origin or the threshold energy. K-space data were truncated near the zero crossings $k = 2.486$ to 14 \AA^{-1} for the nickel-based solution complexes, in Ni EXAFS before Fourier transformation. The k-space data were transferred into the Artemis Software for curve fitting. In order to fit the data, the Fourier peaks were isolated separately, grouped together, or the entire (unfiltered) spectrum was used. The individual Fourier peaks were isolated by applying a Hanning window to the first and last 15% of the chosen range, leaving the middle 70% untouched. Curve fitting was performed using *ab initio*-calculated phases and amplitudes from the FEFF8^[18] program from the University of Washington. *Ab initio*-calculated phases and amplitudes were used in the EXAFS equation:

$$\chi(k) = S_0^2 \sum_j \frac{N_j}{kR_j^2} f_{\text{eff}_j}(\pi, k, R_j) e^{-2\sigma_j^2 k^2} e^{\frac{-2R_j}{\lambda_j(k)}} \sin(2kR_j + \phi_{ij}(k))$$

where N_j is the number of atoms in the j^{th} shell; R_j the mean distance between the absorbing atom and the atoms in the j^{th} shell; $f_{\text{eff}_j}(\pi, k, R_j)$ is the *ab initio* amplitude function for shell j , and the Debye-Waller term $e^{-2\sigma_j^2 k^2}$ accounts for damping due to static and thermal disorder in absorber-backscatterer distances. The mean free path term $e^{\frac{-2R_j}{\lambda_j(k)}}$ reflects losses due to inelastic scattering, where $\lambda_j(k)$, is the electron mean free path. The oscillations in the EXAFS spectrum are reflected in the sinusoidal term $\sin(2kR_j + \phi_{ij}(k))$, where $\phi_{ij}(k)$ is the *ab initio* phase function for shell j . This sinusoidal term shows the direct relation between the frequency of the EXAFS oscillations in k-space and the absorber-backscatterer distance. S_0^2 is an amplitude reduction factor.

The EXAFS equation^[19] was used to fit the experimental Fourier isolated data (q-space) as well as unfiltered data (k-space) and Fourier transformed data (R-space) using N , S_0^2 , E_0 , R , and σ^2 as variable parameters (Table 0-1). N refers to the number of coordination atoms surrounding Ni for each shell. The quality of fit was evaluated by R-factor and the reduced Chi² value. The deviation in E_0 ought to be less than or equal to 10 eV. R-factor less than 2% denotes that the fit is good enough. R-factor between 2 and 5% denotes that the fit is correct within a consistently broad model. The reduced Chi² value is used to compare fits as more absorber-backscatter shells are included to fit the data. A smaller reduced Chi² value implies a better fit. Similar results were obtained from fits done in k, q, and R-spaces.

DFT Calculations

DFT optimization calculations were performed using the ORCA program package developed by Neese and co-workers^[20] The DFT optimizations reported here were carried out using ORCA, B3LYP^[21,22] as functional, the Zeroth Order Regular Approximation (ZORA) as previously reported^[23] with def2-TZVP triple-zeta basis sets,^[24] and the atom-pairwise Grimme dispersion correction with the Becke-Johnson damping scheme (D3BJ).^[25,26]

Optical and XANES simulations

Optical and time-dependent DFT (TD-DFT) calculations for the UV-Visible absorption spectra and XANES spectra of the proposed **Ni^{III}** and **Ni^I** geometries were performed using the same functional, basis sets and dispersion correction effects with dense integration grids, and the fully decontracted def2-TZVP/J^[24] auxiliary basis set. Up to 150 roots were calculated. A broadening of 2500 cm⁻¹ was applied to all calculated optical spectra whereas that of 2.0 eV was applied to all calculated XANES spectra. The donor orbitals for XAS calculations were chosen as Ni 1s and all virtual orbitals were selected as acceptor orbitals. The calculated Ni XANES spectra contain contributions from electric quadrupole, electric dipole, and magnetic dipole transitions.

Table O-1. EXAFS fit parameters for modified nickel complexes.

Sample	Fit	Peak	Shell, N	R, Å	E ₀	ss. ² / 10 ⁻³	R-factor	Red. Chi ²
NiN ₂ S ₃	1	1	Ni-N,3	2.13	-0.9	4.1	0.0213	538
in ACN	2	1,2	Ni-N,3 Ni-S,3	2.04 2.40	-5.3	4.8 5.9	0.0048	123
NiN ₂ S ₃	3	1	Ni-N,3	2.13	-0.9	3.4	0.0223	235
in 1:1 ACN:H ₂ O	4	1,2	Ni-N,3 Ni-S,3	2.05 2.41	-4.7	3.9 5.7	0.0030	20
NiN ₂ S ₂	5	1	Ni-N,3	2.10	-1.6	3.6	0.0098	103
in 1:1 ACN:H ₂ O	6	1,2	Ni-N,4 Ni-S,2	2.06 2.40	-4.1	4.0 5.0	0.0002	1.3

Table 0-2. DFT calculated parameters: charge, spin state, bond distances and Ni Mulliken charge of all calculated models for **NiN₂S₃**.

	Charge	Spin	Ni-N ₁	Ni-N ₂	Ni-N ₃ / Ni-O ₃	Ni-S ₁	Ni-S ₂	Ni-S ₃
[Ni^{III}(CH₃CN)]²⁺	2	1	2.075	2.117	2.094	2.417	2.454	2.467
[Ni^{III}(OH₂)²⁺	2	1	2.081	2.102	2.199	2.405	2.435	2.440
					(Ni-O)			
[Ni^{II}]²⁺	2	1	2.046	2.061		2.358	2.364	2.433
[Ni^I(CH₃CN)]⁺	1	½	2.070	2.113	2.911	2.366	2.387	2.766
[Ni^I(OH₂)]⁺	1	½	2.090	2.099	4.302	2.347	2.370	2.749
					(Ni-O)			
[Ni^I]⁺	1	½	2.069	2.078		2.347	2.374	2.564

Table 0-3. DFT calculated parameters: charge, spin state, bond distances and Ni Mulliken charge of all calculated models for **NiN₂S₂**.

	Charge	Spin	Ni-N ₁	Ni-N ₂	Ni-N ₃	Ni-N ₄ /O ₄	Ni-S ₁	Ni-S ₂
[Ni^{III}(CH₃CN)₂]²⁺	2	1	2.094	2.095	2.120	2.123	2.424	2.428
[Ni^{III}(CH₃CN)(OH₂)²⁺	2	1	2.076	2.096	2.109	2.220	2.391	2.413
[Ni^{III}(CH₃CN)]²⁺	2	1	2.024	2.079	2.084		2.331	2.395

Time-resolved XAS measurements

Time-resolved X-ray absorption spectra were collected at 11 ID-D¹ beamlines at the Advanced Photon Source using undulator radiation at electron energy 8.43 keV. The experiments were carried out using the 24-bunch timing mode of APS (in top up mode with a constant 102 mA ring current) which consists of a train of X-rays separated by 153 ns. This mode easily allows for gateable detectors that selects X-ray pulses. This timing mode was suitable for this type of experiments in which a fresh sample was required for every incoming X-ray pulse as well as for the time resolution of the avalanche Photodiode (APD) detectors.

The samples were pumped at 400 nm wavelength using a regenerative amplified laser with 10 kHz repetition rate 5ps-FWHM pulse length and laser power of 630 mW. The sample was circulated through a stainless-steel nozzle into a free-flowing 550 μm cylindrical jet inside an airtight aluminium chamber, and continuously degassed with nitrogen. The X-ray and laser beams were spatially

overlapped with an X-ray spot size of $100\ \mu\text{m(V)} \times 450\ \mu\text{m(H)}$ and laser spot size of $170\ \mu\text{m(V)} \times 550\ \mu\text{m}$. With a liquid flow speed of around $3\ \text{m/s}$, the pumped laser volume was calculated to move out of the FWHM region in around $24\ \mu\text{s}$. This temporal range ensured that the excited state volume was probed more at the center and less at the edges where the excitation fraction would be less, due to movement of the sample. Beamline 11 ID-D has an automated data digitization system which allows for all X-ray pulses after laser excitation to be collected. Such a system, together with the larger X-ray beam spot size, was very useful for our experiments, as multiple X-ray pulses after laser excitation were averaged to monitor the dynamics for the formation and decay of Ni^{I} transient species in the ns- μs time regime. In addition, by averaging multiple pulses, we obtained a better resolution of the main features in the pre-edge and edge regions of the transient signals.

The delay between the laser and X-ray pulses was adjusted by a programmable delay line (PDL-100A-20NS, Colby Instruments) and the X-ray fluorescence signals were collected with two APDs positioned at 90° on both sides of the liquid jet. Moreover, a combination of Z-1 filters and soller slits with conical geometry were used to reduce the background from elastically scattered X-rays. A Ni metal foil was placed between two ionization chambers downstream to the X-ray beam, and its transmission recorded with each scan for energy calibration.

Chapter 4

Synthesis of ReAm1

An equimolar amount of $\text{Re}(\text{CO})_5\text{Cl}$ (64.2 mg, 0.37 mmol) and 6-amino-2,2'-bipyridine (150 mg, 0.37 mmol) was dissolved in toluene (30 mL) and heated to 115 °C. The reaction mixture was stirred under reflux for 1 h. Afterwards the solution was removed from the heat source and cooled down by placing in an ice bath. The product precipitated from solution as a yellow powder and was filtered off. Pure product was isolated from the reaction with an overall yield of 68% (131 mg). X-ray quality crystals were grown from the vapor diffusion of pentane into a chloroform solution of the complex.

^1H NMR (CD_3CN , 298 K, 200 MHz): δ_{H} 6.00 (2H, br s), 6.97 (1H, d), 7.55 (1H, t), 7.64 (1H, d), 7.75 (1H, t), 8.10 (1H, t), 8.25 (1H, d), 9.00 (1H, d).

ESI-HRMS: calculated $m/z = 543.9259$ $[\text{M}+\text{Na}^+]^+$ for $\text{C}_{13}\text{H}_9\text{BrN}_3\text{NaO}_3\text{Re}$, found 543.9257

Synthesis of ReAm2

An equimolar amount of $\text{Re}(\text{CO})_5\text{Cl}$ (70.3 mg, 0.38 mmol) and 6,6'-diamino-2,2'-bipyridine (150 mg, 0.37 mmol) was dissolved in toluene (30 mL) and heated to 115 °C. The reaction mixture was stirred under reflux for 1 h. Afterwards the solution was removed from the heat source and cooled down by placing in an ice bath. The product precipitated from solution as a yellow powder and was filtered off. Pure product was isolated from the reaction with an overall yield of 53% (106 mg). X-ray quality crystals were grown from the vapor diffusion of pentane into a chloroform solution of the complex.

^1H NMR (CD_3CN , 298 K, 250 MHz): δ_{H} 5.99 (4H, br s), 6.87 (2H, d), 7.50 (2H, d), 7.70 (2H, t)

ESI-HRMS: calculated $m/z = 558.9386$ $[\text{M}+\text{Na}^+]^+$ for $\text{C}_{13}\text{H}_{10}\text{BrN}_4\text{NaO}_3\text{Re}$, found 558.9355

Synthesis of TPPUr

3,5-Bis(trifluoromethyl)phenyl isocyanate (215 μL , 1.245 mmol) were added to a solution of $\alpha\beta\alpha\beta$ -5,10,15,20-tetrakis (2-aminophenyl)porphyrin (**TAPP $\alpha\beta\alpha\beta$**) (200 mg, 0.296 mmol) in dry dichloromethane under argon. After an overnight stirring at room temperature, the solvent was removed under vacuum. Finally, the residue was chromatographed on a silica gel and eluted with chloroform. The expected compound was precipitated by dissolving it in a minimum amount of dichloromethane and adding a large amount of pentane. After a filtration, washing

with pentane and drying under vacuum, compound **TPPUr** was obtained as purple solid with 89 % yield (447 mg). Single crystals suitable for X-ray diffraction analysis were obtained by a slow evaporation of a **TPPUr** saturated solution in a 1:5 mixture of acetone:H₂O. Due to the D_{2d} symmetry of **TPPUr** porphyrin, the four urea arms are magnetically equivalent. 2D NMR (COSY, HSQC and HMBC) experiments were also performed in order to confirm the attribution of 1D ¹H NMR signals.

¹H NMR ((CD₃)₂CO, 298 K, 400 MHz): δ_H 8.92 (8H, s), 8.48 (4H, d, *J* = 8.0 Hz), 7.91 (12H, m), 7.59 (8H, s), 7.56 (4H, td, *J*₁ = 7.6 Hz, *J*₂ = 0.8 Hz), 7.40 (4H, s), 7.31 (4H, s), -2.72 (2H, s)
¹³C NMR ((CD₃)₂CO, 298 K, 100 MHz): δ_c 152.2, 141.3, 139.1, 134.8, 132.4, 131.2 (q, *J* = 32 Hz), 129.6, 123.2 (q, *J* = 269.7 Hz), 123.1, 122.9, 117.53, 115.5, 114.5.

ESI-HRMS: calculated *m/z* = 1695.3455 [M+H]⁺ for C₈₀H₄₇F₂₄N₁₂O₄, found 1695.3455;
 calculated *m/z* = 1717.3274 [M+Na]⁺ for C₈₀H₄₆F₂₄N₁₂O₄Na, found 1717.3236.

UV-Vis (CHCl₃): λ_{max} / nm (ε, in M⁻¹cm⁻¹): 423 (159900), 517 (8800), 553 (4500), 590 (6100), 647 (4400)

Synthesis of FeTPPUr

A solution of porphyrin **TPPUr** (200 mg, 0.188 mmol) and lutidine (273 μL, 2.360 mmol) in dry THF was degassed by argon bubbling for 30 min. Then, FeBr₂ (178 mg, 0.826 mmol) was added and the reaction mixture was stirred overnight at room temperature under argon. The reaction mixture was then filtered to remove the excess of iron salts and the solvent was evaporated under vacuum. The reaction crude was dissolved in 50 mL of CHCl₃ and 50 mL aqueous solution of 0.5 M HCl was added. After, 3 hours stirring the two phases were separated and the organic phase containing the iron complex was evaporated under vacuum. Chromatographic purification on a silica gel using a mixture of methanol:CHCl₃ (from 0:100 to 3:97) gives **FeTPPUr** (with a Cl⁻ as axial coordinating anion) in 80 % yield (165 mg). Single crystals suitable for X-ray diffraction analysis were obtained by a slow evaporation of a **FeTPPUr** saturated solution in a 1:6 mixture of methanol:H₂O, resulting in a crystal structure having a methoxide axial ligand.

ESI-HRMS: calculated *m/z* = 1802.2654 [M-Cl+MeO+Na]⁺ for C₈₁H₄₇F₂₄FeN₁₂NaO₅, found 1802.2644.

UV-Vis (CHCl₃): λ_{max} / nm (ε, in M⁻¹cm⁻¹): 417 (52700), 517 (7500), 591 (2100), 652 (1700), 684 (1800)

IR wavenumber in cm⁻¹: NH stretching at 3352, C=O stretching at 1713 and 1683.

Synthesis of TPPAm

To a solution of **TAPP** $\alpha\beta\alpha\beta$ in a dry mixture 1:1 of CHCl_3 and THF was added 3,5-bis(trifluoromethyl)benzoyl chloride (240 μL , 1.304 mmol) in presence of triethylamine (400 μL , 2.964 mmol) at room temperature under an argon atmosphere. After an overnight stirring, the solvent was removed under vacuum and the crude was chromatographed on a silica gel and a mixture methanol:dichloromethane from 0:100 to 0.5:99.5. The expected compound was precipitated by dissolving it in a minimum amount of dichloromethane and adding a large amount of pentane. After a filtration, washing with pentane and drying under vacuum, compound **TPPAm** was obtained as purple solid with 85 % yield (412 mg). Due to the D_{2d} symmetry of **TPPAm** porphyrin, the four amido arms are magnetically equivalent. 2D NMR (COSY, HSQC and HMBC) experiments were also performed in order to confirm the attribution of 1D ^1H NMR signals.

^1H NMR (CDCl_3 , 298 K, 400 MHz): δ_{H} 8.97 (8H, s), 8.73 (4H, d, $J = 8.4$ Hz), 8.12 (4H, dd, $J_1 = 7.6$ Hz, $J_2 = 1.2$ Hz), 7.96 (4H, td, $J_1 = 7.6$ Hz, $J_2 = 1.2$ Hz), 7.69 (4H, td, $J_1 = 7.6$ Hz, $J_2 = 1.2$ Hz), 7.31 (4H, s), 7.09 (4H, s), 6.81 (8H, s), -2.58 (2H, s).

^{13}C NMR (CDCl_3 , 298 K, 100 MHz): δ_{C} 162.3, 137.9, 136.4, 134.25, 131.8, 131.2 (q, $J = 32$ Hz), 130.5, 127.4, 124.4, 124.2, 121.6 (q, $J = 272$ Hz), 121.5, 114.7.

ESI-HRMS: calculated $m/z = 1657.2838$ [$\text{M}+\text{Na}^+$] $^+$ for $\text{C}_{80}\text{H}_{42}\text{F}_{24}\text{N}_8\text{NaO}_4$, found 1657.2918.

UV-Vis (CHCl_3): λ_{max} / nm (ϵ , in $\text{M}^{-1}\text{cm}^{-1}$): 423 (202700), 456 (26400), 516 (12700), 549 (3800), 590(4800), 654 (4000)

Synthesis of FeTPPAm

A solution of porphyrin **TPPAm** (200 mg, 0.188 mmol) and lutidine (546 μL , 4.720 mmol) in dry CHCl_3 was degassed by argon bubbling for 30 min. Then, FeBr_2 (356 mg, 1.652 mmol) was added and the reaction mixture was stirred overnight at 50° C under argon. The reaction mixture was then filtered to remove the excess of iron salts and the solvent was evaporated under vacuum. The crude was dissolved in 50 mL of CHCl_3 and 50 mL aqueous solution of 0.5 M HCl was added. After, 3 hours stirring the two phases were separated and the organic phase containing the iron complex was evaporated under vacuum. Chromatographic purification on a silica gel using a mixture of methanol: CHCl_3 (from 0:100 to 3:97) gives **FeTPPAm** (with a Cl^- as axial coordinating anion) in 78 % yield (165 mg). Single crystals suitable for X-ray diffraction analysis were obtained by a slow evaporation a **FeTPPAm** saturated solution in a 1:6 mixture of methanol: H_2O , resulting to a crystal structure having a methoxide axial ligand.

ESI-HRMS: calculated $m/z = 1742.2218$ $[M-Cl+MeO+Na]^+$ for $C_{81}H_{43}F_{24}FeN_8NaO_5$, found 1742.2201; calculated $m/z = 1756.2010$ $[M-Cl+HCO_2+Na]^+$ for $C_{81}H_{41}F_{24}FeN_8NaO_6$, found 1756.2005.

UV-Vis ($CHCl_3$): λ_{max} / nm (ϵ , in $M^{-1}cm^{-1}$): 357 (32700), 422 (72100), 508 (9100), 575 (3100), 646 (2800), 673 (2400)

IR wavenumber in cm^{-1} : NH stretching at 3411 and 3298, C=O stretching at 1689 and 1678

Synthesis of FeTPPBzm

The starting ligand, *meso*-tetra (*o*-(2-chloromethyl)benzamidephenyl) porphyrin with an $\alpha\alpha\alpha\alpha$ configuration (500 mg, 0.389 mol), was dissolved in 10 mL of Ar degassed THF then 2,6-lutidine (0.9 mL, 7.781 mol) and $FeCl_2$ (345 mg, 2.723 mol) were added to the reaction mixture. After an overnight stirring at room temperature, the solvent was evaporated, and the crude material was dissolved in 100 mL of $CHCl_3$ then extracted with 100 mL of 0.25 M solution of HCl. The organic phase was filtered through a small plug of silica gel then the solvent was evaporated to **FeTPPBzm** as a dark purple solid (470 mg, yield = 88 %).

ESI-HRMS: calculated $m/z = 1336.2270$ $[M]^+$ for $C_{76}H_{52}C_{14}FeN_8O_4$, found 1336.2213.

UV-vis (MeOH): λ_{max} / nm (ϵ , in $M^{-1}cm^{-1}$): 341 (29800), 419 (95900), 593 (6400), 656 (3500).

Synthesis of FeTPPIIm

FeTPPBzm complex (100 mg, 73 μ mol) was dissolved in 5 mL of dry DMF under Ar atmosphere, then 1-methylimidazole was added (23 μ L, 291 μ mol) to the reaction mixture at room temperature. After 24 hours stirring at 70° C, the reaction mixture was brought to room temperature then approximately 200 mL of diethylether were added. The obtained purple precipitate was filtered and washed with 2 x 50 mL of diethylether to give **FeTPPIIm** (114 mg, yield = 92 %).

The $\alpha\alpha\alpha\alpha$ geometry (the four arms in the same side with regard to the porphyrin plane) of the porphyrin ligand is maintained at room temperature due to the blocked rotation of the aryl groups on the *meso* positions of the macrocycle. At higher temperature, this rotation becomes possible and can induce the formation of a mixture of four possible atropoisomers ($\alpha\alpha\alpha\alpha$, $\alpha\beta\alpha\beta$, $\alpha\alpha\beta\beta$ and $\alpha\beta\beta\beta$). To confirm the retention of the $\alpha\alpha\alpha\alpha$ geometry during the synthesis of **FeTPPIIm**, we performed a control experiment using the starting porphyrin ligand. In this experiment, a solution of the $\alpha\alpha\alpha\alpha$ porphyrin in DMF was heated at 70° C for more than 24 hours

then TLC and ^1H NMR monitoring of this solution showed no modification of the porphyrin geometry.

ESI-HRMS: calculated $m/z = 381.1370$ $[\text{M}]^{4+}$ for $\text{C}_{92}\text{H}_{76}\text{FeN}_{16}\text{O}_4$, found 381.1392.

ESI-HRMS: calculated $m/z = 305.1101$ $[\text{M}]^{5+}$ for $\text{C}_{92}\text{H}_{76}\text{FeN}_{16}\text{O}_4$, found 305.1118.

UV-vis (MeOH): λ_{max} /nm (ϵ , in $\text{M}^{-1}\text{cm}^{-1}$): 344 (29400), 421 (102800), 594 (5400), 640 (3100).

FOW analysis of modified iron porphyrin complexes

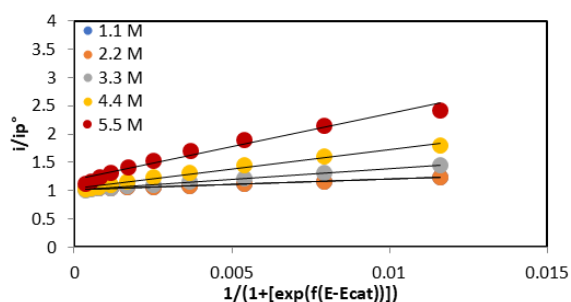


Figure 0-2. FOW analysis of 1 mM **FeTPP** in CO_2 -saturated DMF as a function of H_2O concentration.

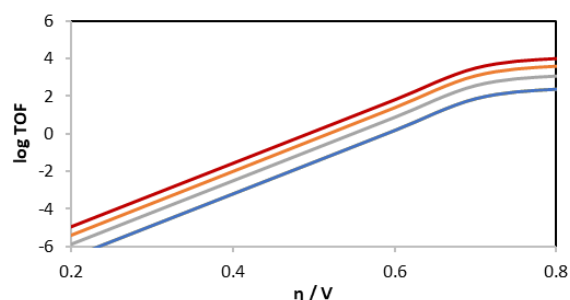


Figure 0-3. Catalytic Tafel plots of **FeTPP** in CO_2 -saturated DMF at various concentrations of H_2O (1.11 M to 5.55 M).

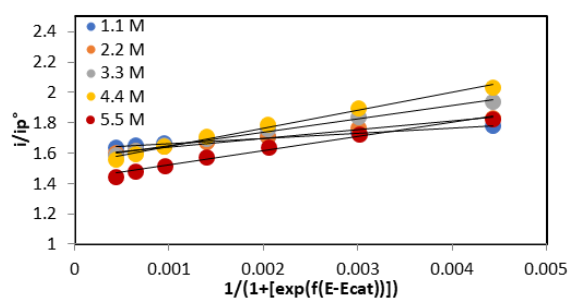


Figure 0-4. FOW analysis of 1 mM **FeTPPAm** in CO_2 -saturated DMF as a function of H_2O concentration.

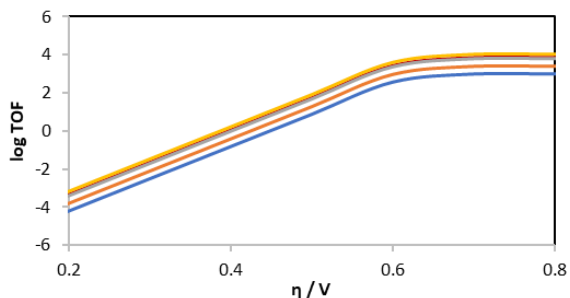


Figure 0-5. Catalytic Tafel plots of **FeTPPAm** in DMF at various concentrations of H_2O (1.11 M to 5.55 M).

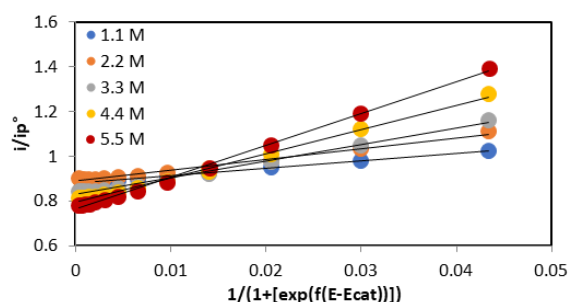


Figure 0-6. FOW analysis of 1 mM **FeTPPF₈** in CO_2 -saturated DMF as a function of H_2O concentration.

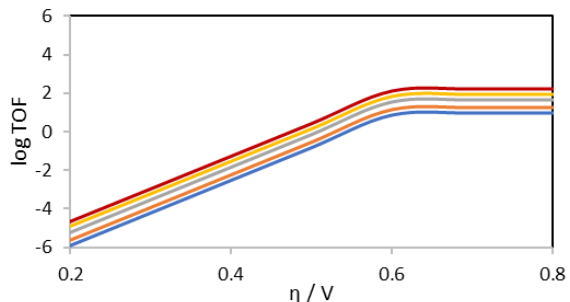


Figure 0-7. Catalytic Tafel plots of **FeTPPF₈** in CO_2 -saturated DMF at various concentrations of H_2O (1.11 M to 5.55 M).

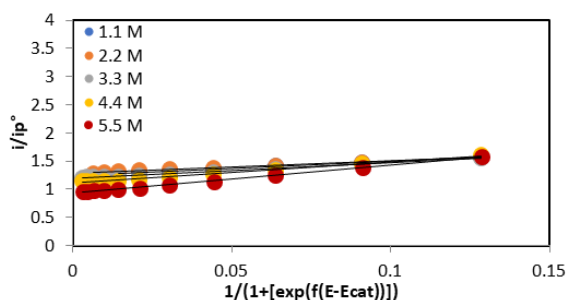


Figure 0-8. FOW analysis of 1 mM **FeTPPF₂₀** in CO₂-saturated DMF as a function of H₂O concentration.

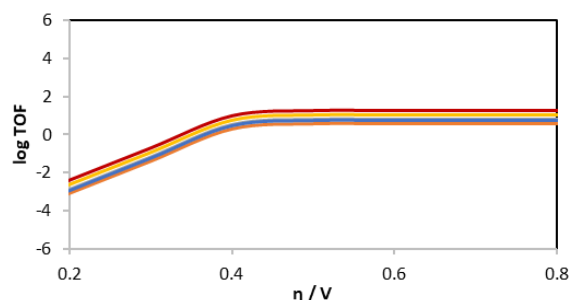


Figure 0-9. Catalytic Tafel plots of **FeTPPF₂₀** in CO₂-saturated DMF at various concentrations of H₂O (1.11 M to 5.55 M).

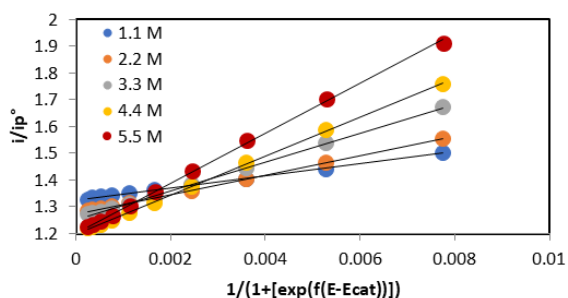


Figure 0-10. FOW analysis of 1 mM **FeTPPUr** in CO₂-saturated DMF as a function of H₂O concentration.

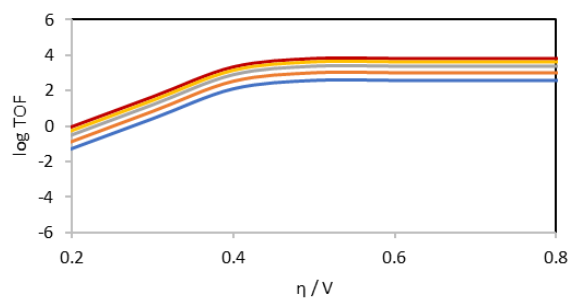


Figure 0-11. Catalytic Tafel plots of **FeTPPUr** in CO₂-saturated DMF at various concentrations of H₂O (1.11 M to 5.55 M).

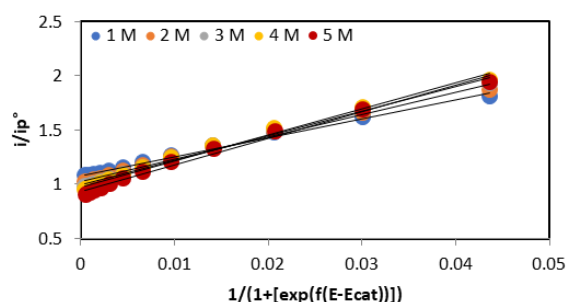


Figure 0-12. FOW analysis of 1 mM **FeTPPUr** in CO₂-saturated DMF as a function of TFE concentration.

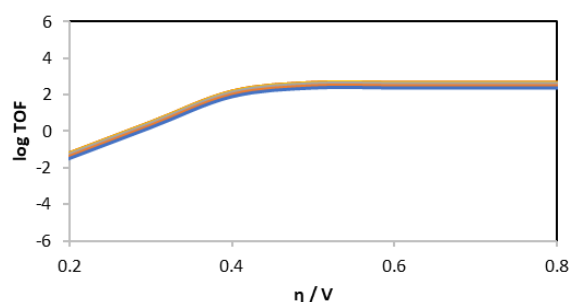


Figure 0-13. Catalytic Tafel plots of **FeTPPUr** in CO₂-saturated DMF at various concentrations of TFE (1 M to 5 M).

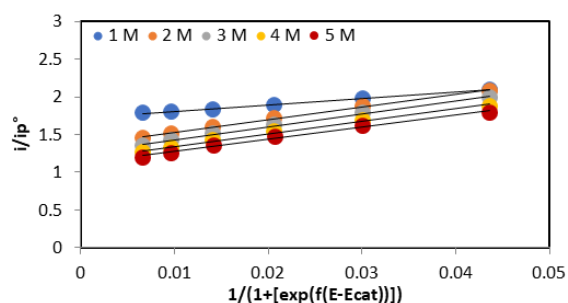


Figure 0-14. FOW analysis of 1 mM **FeTPPUr** in CO₂-saturated DMF as a function of PhOH concentration.

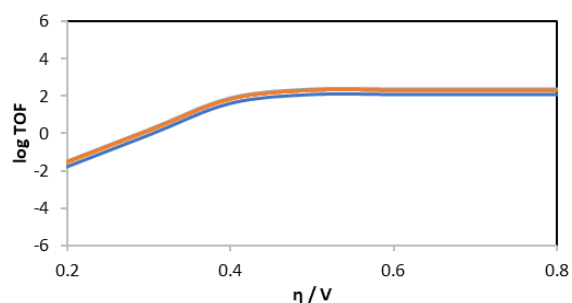


Figure 0-15. Catalytic Tafel plots of **FeTPPUr** in CO₂-saturated DMF at various concentrations of PhOH (1 M to 5 M).

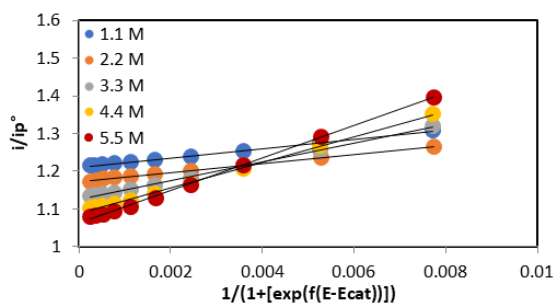


Figure 0-16. FOW analysis of 1 mM **FeTPPUr** in CO₂-saturated DMF as a function of D₂O concentration.

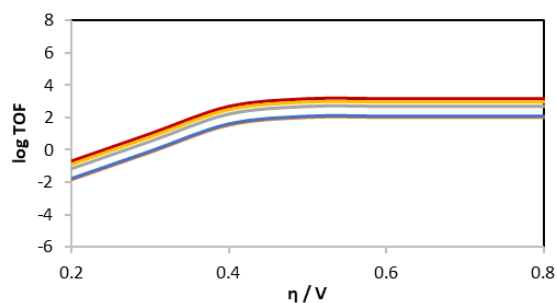
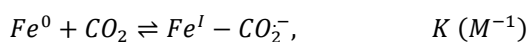
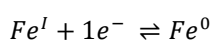


Figure 0-17. Catalytic Tafel plots of **FeTPPUr** in DMF at various concentrations of D₂O as proton source (1.11 M to 5.55 M).

CO₂ binding rate constants of modified iron porphyrins

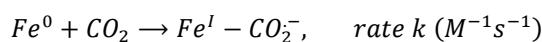
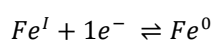
The CO₂ binding constant (K_{CO_2}) or binding rate constant (k_{CO_2}) was calculated based on procedures reported in literature by analysis of the CVs under Ar and CO₂ in dry DMF (to avoid any catalytic turnover in the presence of proton source). For a reversible peak after CO₂ binding, the method proposed by Ingle^[27-29] is widely used. This has been applied for **FeTPP**, **FeTPPF₈** and **FeTPPF₂₀** to determine CO₂ binding constant (K_{CO_2} in M⁻¹), with increased scan rate (1 V/s) helping to achieve reversible kinetics. However, for **FeTPPUr** and **FeTPPAm**, reversibility was not achieved even by increasing the scan rate indicating that the electron transfer and CO₂ binding reaction are rapid, but the reverse reaction is slow. For such a condition, the method proposed by the group of Savéant^[30,31] is used, assuming all the complexes follow an EC mechanism. A plot E_p as a function of $\ln v$ would give an intercept, where k (in M⁻¹s⁻¹) is calculated. The calculated slope from E_p vs. $\ln v$ is 0.0275 which is different from the supposed $RT/2F$ (0.0128), possibly indicating a different mechanism. The equation was then modified accounting for the experimental slope and from here the CO₂ binding rate constant was estimated for the catalysts. The solubility of CO₂ in DMF at 25 °C is 0.23 M.^[32]

Reversible kinetics upon CO₂ binding:



$$E^{0'} = E^0 + \left(\frac{RT}{F}\right) \ln(1 + K[CO_2]), \quad Eq. 1$$

Irreversible kinetics upon CO₂ binding:



$$E_p = E^0 - 0.78 \frac{RT}{F} + \left(\frac{RT}{2F}\right) \ln \frac{RTk[CO_2]}{Fv}, \quad Eq. 2$$

Table 0-4. Calculated values for CO₂ binding constants (K_{CO_2}) and rate constants (k_{CO_2}) for the modified iron porphyrin complexes.

Complex	$K_{\text{CO}_2} / \text{M}^{-1}$	$k_{\text{CO}_2} / \text{M}^{-1}\text{s}^{-1}$
FeTPP	0.92	7.6
FeTPPF8	0.92	-
FeTPPF20	0.92	-
FeTPPAm	-	6.8
FeTPPUr	-	58.0

Crystallographic data of modified iron porphyrins**Table 0-5.** Crystallographic data and structure refinement details.

Complexes	TPPUr (CCDC 1884363)	FeTPPUr (CCDC 1884364)	FeTPPAm (CCDC 1884362)
Crystal size, mm ³	0.21 x 0.21 x 0.08	0.23 x 0.04 x 0.01	0.24 x 0.24 x 0.10
Space group	<i>P</i> 2 ₁ / <i>c</i>	<i>I</i> 4 ₁ / <i>a</i>	<i>I</i> 4 ₁ / <i>a</i>
a, Å	24.9021(10)	54.7237(15)	23.3404(9)
b, Å	15.1441(6)	54.7237(15)	23.3404(9)
c, Å	24.5639(9)	14.7337(5)	15.4763(7)
$\alpha = \gamma, \beta$ °	90, 94.649(2)	90, 90	90, 90
Cell volume, Å ³	9 233.1(6)	44 123(3)	8 431.1(8)
Z ; Z'	4; 1	20; 5/4	4; 1/4
T, K	100(1)	100(1)	100(1)
F ₀₀₀	4 072	19 027	3916
μ , mm ⁻¹	1.098	2.370	2.513
θ range, °	3.419 - 66.830	2.283 - 50.546	3.426 - 67.067
Reflection collected	136 091	175 687	50 153
Reflections unique	16 355	11 589	3 761
R _{int}	0.0253	0.0669	0.0198
GOF	1.041	1.592	1.158
Refl. obs. ($I > 2\sigma(I)$)	14 357	7 621	3 352
Parameters	1 271	1 350	298
wR ₂ (all data)	0.2288	0.4153	0.2665
R value ($I > 2\sigma(I)$)	0.0806	0.1451	0.0981

Table 0-6. Selected bond distances for the modified iron porphyrins.

Complexes	FeTPP-Ur	FeTPP-Am	
Fe-N	2.050(8)		
	2.041(9)	2.045(8)	2.076(4)
	2.020(8)		
	2.044(9)		
Fe-O	1.852(8)	1.87(2)	1.863(11)

DFT calculations for FeTPPAm and FeTPPUr

DFT calculations were performed using the Gaussian 09 program package.^[33] Unrestricted BP86 functional was selected based on previous calculations.^[34] Def2-SVP and 6-31G(d,p) polarized basis sets were chosen for Fe and main group atoms, respectively. Diffuse basis functions were added to p-type orbitals of main group elements to take into account the dianionic character of the molecules. Geometries of all Fe porphyrin models were optimized in the gas phase based on experimental X-ray structures. To speed up the calculations, CF₃ substituents and urea arms opposite to the CO₂ coordination side were replaced with protons. Optimizations were followed by vibrational frequency calculations to confirm the nature of all computed stationary points as minima. Free enthalpy energies were calculated at 298 K, 1 atm. Figures and mapped electrostatic potential were generated using ChemCraft program.^[35]

The geometry of the triply reduced [FeTPPUr-CO₂]²⁻ active species was optimized as singlet, triplet, and quintuplet states under unrestricted open-shell calculation. The singlet state was found as the ground state, while triplet and quadruplet state lie 8 and 23 kcal mol⁻¹ higher in energy. Consequently [FeTPPAm-CO₂]²⁻ was only optimized as a singlet.

Table 0-7. Comparison of the relative energies of the model of [FeTPPUr-CO₂]²⁻ depending on the spin state envisioned.

Spin State	Thermal free energy (H)	ΔG (kcal/mol)
S=0	- 4273.16955	0
S=1	- 4273.156722	8.05
S=3	- 4273.133128	22.85

Bulk electrolysis of FeTPPUr in DMF

Bulk electrolysis was performed in CO₂-saturated 9:1 DMF:H₂O containing 0.1 M TBAP as supporting electrolyte. A gas-tight two-compartment cell was used for this experiment, each cell having a volume of 43 mL. The first compartment was filled with 20 mL electrolyte solution containing 0.5 mM catalyst and the working electrode (glassy carbon rod, effective surface area 1.60 cm²) and reference electrode (Ag/AgNO₃), while the second compartment was filled with 20 mL electrolyte solution and contained the counter electrode (10 cm x 3 cm titanium grid with nominal spacing of 0.19 mm and wire diameter of 0.23 mm).

Faradaic efficiency (FE) for the 2-electron reduction of CO₂ to CO was calculated using the following:

$$FE = \frac{Q_{exp}}{Q_{theo}} = \frac{2 * F * mol\ CO}{Q_{theo}}$$

where $F = 96485\ C\ mol^{-1}$, $mol\ CO$ is the amount of CO detected by GC and Q_{theo} is the total charge passed, calculated by integrating the current *vs.* time curve.

Scan rate-dependence experiments show a linear correlation between the peak currents and (scan rate)^{1/2} indicating that the complexes are freely-diffusing under non-catalytic conditions.

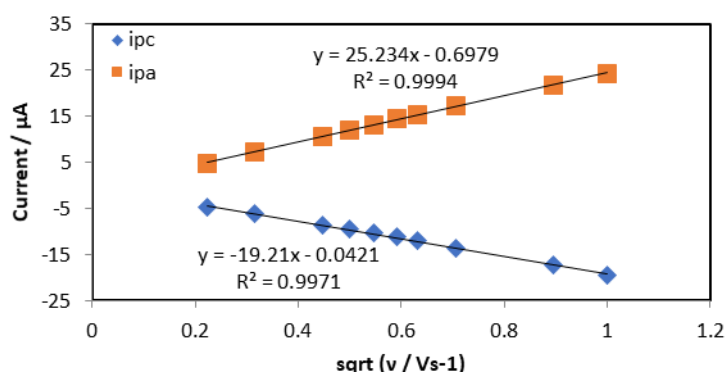


Figure 0-18. Diffusion current peak (Fe^{II/I}) as a function of square root of scan rate.

The diffusion coefficient of catalyst **FeTPPUr** was determined by plotting peak current as a function of square root of scan rate, following Randles-Sevcik equation:

$$i_p = 0.4463nFAC \left(\frac{nFvD}{RT} \right)^{\frac{1}{2}}$$

The following parameters were used: n (electron transferred) = 1, $F = 96485\ C\ mol^{-1}$, $R = 8.314\ J\ K^{-1}\ mol^{-1}$, $T = 298\ K$, $A = 0.07065\ cm^2$ (glassy carbon electrode with diameter of 3 mm), $C = 1 \times 10^{-6}\ mol\ cm^{-3}$. The calculated average diffusion coefficient of catalyst **FeTPPUr** in DMF (0.1 M TBAP) is $1.40 \times 10^{-6}\ cm^2\ s^{-1}$.

The electrolysis is described by the equation^[8,36]:

$$\frac{i}{FA} = \frac{C_{cat}^0 \sqrt{2k_{cat}D_{cat}}}{1 + \exp\left[\frac{F}{RT}(E_{electrolysis} - E_{cat})\right]}$$

$$k_{cat} = \frac{i^2 \left[1 + \exp\left[\frac{F}{RT}(E_{electrolysis} - E_{cat})\right]\right]^2}{2F^2 A^2 C_{cat}^0{}^2 D_{cat}} = 2.76 \times 10^3 \text{ s}^{-1}$$

Calculations were made from $i = -1.12$ mA (taking into account 91% FE for CO production) and the following parameters: A (electrode surface) = 1.60 cm^2 , C_{cat}^0 (catalyst concentration) = $5 \times 10^{-7} \text{ mol cm}^{-3}$, D_{cat} (catalyst diffusion coefficient) = $1.40 \times 10^{-6} \text{ cm}^2 \text{ s}^{-1}$, $E_{electrolysis} = -1.076 \text{ V vs. NHE}$, $E_{cat} = -1.118 \text{ V vs NHE}$, and t (electrolysis time) = 7200 s . The turnover frequency (TOF) and turnover number (TON) were then calculated using:

$$TOF = \frac{k_{cat}}{1 + \exp\left[\frac{F}{RT}(E_{electrolysis} - E_{cat})\right]} = 455 \text{ s}^{-1}$$

$$TON = TOF \times t = 3.28 \times 10^6$$

Bulk electrolysis of FeTPPI_m in water

Bulk electrolysis was performed in a CO₂-saturated water containing 0.1 M KCl as supporting electrolyte at pH = 6.3. A gas-tight two-compartment cell was used for this experiment, each cell having a volume of 43 mL. The first compartment was filled with 20 mL water containing KCl and 0.5 mM catalyst and the working electrode (glassy carbon rod, effective surface area of 1.41 cm^2) and reference electrode (Ag/AgCl), while the second compartment was filled with 20 mL water containing KCl and contains the counter electrode ($10 \text{ cm} \times 3 \text{ cm}$ titanium grid with nominal space of 0.19 mm and wire diameter of 0.23 mm). Scan rate-dependence experiments show a linear correlation between the peak currents and (scan rate)^{1/2} indicating that the complexes are freely-diffusing under non-catalytic conditions with a calculated average diffusion coefficient of $2.64 \times 10^{-7} \text{ cm}^2 \text{ s}^{-1}$ in water. Calculations for catalytic activity were similarly performed using $i = -1.5$ mA (taking into account 91% FE for CO production) and the following parameters: A (electrode surface) = 1.41 cm^2 , C_{cat}^0 (catalyst concentration) = $5 \times 10^{-7} \text{ mol cm}^{-3}$, D_{cat} (catalyst diffusion coefficient) = $2.64 \times 10^{-7} \text{ cm}^2 \text{ s}^{-1}$, $E_{electrolysis} = -0.948 \text{ V vs NHE}$, $E_{1/2} = -1.018 \text{ V vs NHE}$, $F = 96485 \text{ C mol}^{-1}$, $R = 8.314 \text{ J K}^{-1} \text{ mol}^{-1}$, $T = 298 \text{ K}$, and t (electrolysis time) = 7200 s . The turnover frequency (TOF) was calculated to be 14986 s^{-1} and turnover number (TON) to be 1.08×10^8 .

Chapter 5

Experimental set-up of the two-chamber system

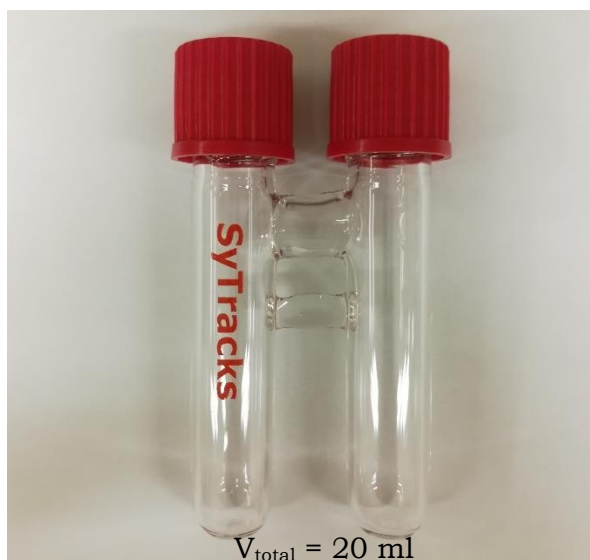


Figure 0-19. COware® two-chamber system used for the valorization of photocatalytic reduction of CO₂ to CO in aminocarbonylation using ¹²CO₂ source.

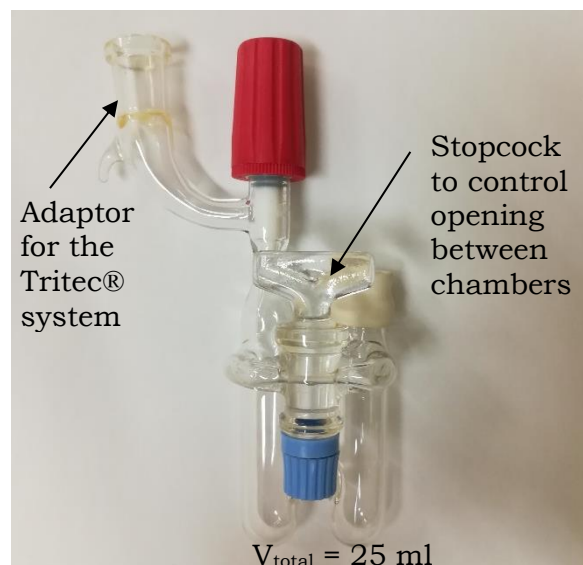


Figure 0-20. Modified COware® two-chamber system for manipulations using ¹³CO₂ source.

General protocol for chamber 1

Stock solution of 1.34 mM **Ru(bpy)₃Cl₂** was prepared by dissolving 1 mg in 1 ml DMF. Stock solution of 1.98 mM **Re(CO)₃(bpy)Br** was prepared by dissolving 1 mg in 1 mL DMF. Optimized condition for Chamber 1 consists of adding 0.57 ml of **Ru(bpy)₃Cl₂** stock solution (0.19 mM), 0.38 ml of **Re(CO)₃(bpy)Br** stock solution (0.19 mM), 0.40 mL deionized water, 2.65 mL DMF, and 250 mg **BIH** (0.28 M). This chamber is photo-irradiated in the photocatalytic reaction with a blue LED lamp (463 nm, FWHM 50 nm, 180 W/m²).

Control experiments for chamber 1

Control experiments on Chamber 1 were done to determine the amount of ^{12/13}CO produced using the two-chamber system. For ¹²CO₂ manipulations, the COware® system in Figure 0-19 was utilized. Chamber 1 was loaded according to “General protocol for chamber 1” and Chamber 2 was loaded with 4 mL DMF. The chambers were sealed with a screwcap fitted with a Teflon® seal. Chamber 2 solution was purged with argon gas for 10 minutes (keeping 1 atm pressure by putting an outlet syringe), after which Chamber 1 was purged with carbon dioxide gas for 15 minutes (keeping 1 atm pressure by putting an outlet syringe). From this

set-up, CO₂ content was estimated to be 1987 μmol based on the solubility of CO₂ in the solvents and the amount in the headspace determined by gas chromatography. Chamber 1 was photo-irradiated with a blue LED lamp while Chamber 2 was covered with aluminium foil to avoid any illumination. The two-chamber system was then held at room temperature for 21 hours under constant stirring. 50 μL gas aliquots were then withdrawn from the headspace of chamber 1 and subjected to gas chromatography and showed an amount of 440 μmol ¹²CO in the headspace. Estimated amount of ¹²CO dissolved in the solvents were minimal (39 μmol) because of its poor solubility.

For ¹³CO₂ manipulations using the Tritec® system, the modified two-chamber system in Figure 0-20 was utilized. Chamber 1 was loaded according to “General protocol for chamber 1” and Chamber 2 was loaded with 4 mL DMF. The chambers were sealed with a screwcap fitted with a Teflon® seal. Chamber 1 was sealed by tightening the red knob while Chamber 2 was sealed by placing a rubber septum. The adaptor was then connected to the Tritec® system. The chambers were degassed three times using freeze-thaw method. 500 μmol of ¹³CO₂ was then injected to the chambers using the Tritec® system keeping the stopcock open between the two chambers. The loaded chambers were then removed from the Tritec® system and the solutions were left to thaw to room temperature. Once thawed, Chamber 1 was photo-irradiated with a blue LED lamp while Chamber 2 was covered with aluminium foil to avoid any illumination. The two-chamber system was then held at room temperature for 21 hours under constant stirring. 50 μL gas aliquots were then withdrawn from the headspace of chamber 1 and subjected to gas chromatography and showed an amount of 192 μmol ¹³CO in the headspace. Estimated amount of ¹³CO dissolved in the solvents were minimal because of its poor solubility.

Synthesis of n-hexyl-4-methoxybenzamide using ¹²CO₂ purging

COware® two-chamber system shown in Figure 0-19 was used. Chamber 1 was loaded according to “General protocol for Chamber 1” and Chamber 2 was loaded with Pd(dba)₂ (14.5 mg, 0.025 mmol), P(tBu)₃HBPf₄ (14.5 mg, 0.05 mmol), 4-iodoanisole (293 mg, 1.25 mmol), tetrahydrofuran (3.7 mL), n-hexylamine (0.33 mL, 2.5 mmol), and DABCO (280 mg, 2.5 mmol). The chambers were sealed with a screwcap fitted with a Teflon® seal. Chamber 2 solution was purged with argon gas

for 10 minutes (keeping 1 atm pressure by putting an outlet syringe), after which, Chamber 1 was purged with carbon dioxide gas for 15 minutes (keeping 1 atm pressure by putting an outlet syringe). Chamber 1 was photo-irradiated with a blue LED lamp while Chamber 2 was covered with aluminium foil to avoid any illumination. The two-chamber system was then held at room temperature for 21 hours under constant stirring. After the reaction, the crude mixture in Chamber 2 was filtered and the solvent evaporated using rotary evaporator. It was then subjected to column chromatography (30% ethyl acetate in cyclohexane) and isolated as a yellowish solid (85.5 mg, 364 μmol , 83% based on CO, 18% based on CO₂).

¹H NMR (CDCl₃, 298 K, 300 MHz): δ_{H} 7.77 (2H, d), 6.91 (2H, d), 6.06 (1H, br s), 3.84 (3H, s), 3.43 (2H, td), 1.60 (2H, q), 1.32 (6H, m), 0.89 (3H, t)

¹³C NMR (CDCl₃, 298 K, 250 MHz): δ_{C} 167.0, 162.0, 128.6 (2C), 127.2, 113.7 (2C), 55.4, 40.0, 31.5, 29.7, 26.7, 22.6, 14.0

ESI-HRMS: calculated $m/z = 258.1464$ [M+Na⁺] for C₁₄H₂₁NO₂, found 258. 1466

Synthesis of *n*-hexyl-4-methoxybenzamide using ¹³CO₂ Tritec®

Modified two-chamber system shown in Figure 0-20 was used. Chamber 1 was loaded according to “General protocol for Chamber 1” and Chamber 2 was loaded with Pd(dba)₂ (14.5 mg, 0.025 mmol), P(tBu)₃HBPf₄ (14.5 mg, 0.05 mmol), 4-iodoanisole (293 mg, 1.25 mmol), tetrahydrofuran (3.7 mL), *n*-hexylamine (0.33 mL, 2.5 mmol), and DABCO (280 mg, 2.5 mmol). Chamber 1 was sealed by tightening the red knob while Chamber 2 was sealed by placing a rubber septum. The adaptor was then connected to the Tritec® system. The chambers were degassed three times using freeze-thaw method. 501 μmol of ¹³CO₂ was then injected to the chambers using the Tritec® system keeping the stopcock open between the two chambers. The loaded chambers were then removed from the Tritec® system and the solutions were left to thaw to room temperature. Once thawed, Chamber 1 was photo-irradiated with a blue LED lamp while Chamber 2 was covered with aluminium foil to avoid any illumination. The two-chamber system was then held at room temperature for 21 hours under constant stirring. After the reaction, the crude mixture in Chamber 2 was filtered and the solvent evaporated using rotary evaporator. It was then subjected to column chromatography (30% ethyl acetate in cyclohexane) and isolated as a yellowish solid (37 mg, 159 μmol , 82% based on ¹³CO, 32% based on ¹³CO₂).

¹H NMR (CDCl₃, 298 K, 400 MHz): δ_H 7.77 (2H, d), 6.91 (2H, d), 5.96 (1H, br s), 3.78 (3H, s), 3.37 (2H, td), 1.53 (2H, q), 1.26 (6H, m), 0.82 (3H, t)

¹³C NMR (CDCl₃, 298 K, 400 MHz): δ_C 166.0 (¹³C-enriched), 161.0, 127.6 (2C), 126.3, 112.7(2C), 54.4, 39.0, 30.5, 28.7, 25.7, 21.6, 13.0

LC-MS: calculated m/z = 237.2 [M+H⁺] for C₁₃¹³CH₂₁NO₂, found 237.4

Synthesis of Moclobemide using ¹²CO₂ purging

COware® two-chamber system shown in Figure 0-19 was used. Chamber 1 was loaded according to “General protocol for Chamber 1” and Chamber 2 was loaded with Pd(dba)₂ (36 mg, 0.0625 mmol), PPh₃ (33 mg, 0.125 mmol), 1-chloro-4-iodobenzene (298 mg, 1.25 mmol), dioxane (3.4 mL), 4-(2-aminomethyl)morpholine (0.33 ml, 2.5 mmol), and triethylamine (0.34 ml, 2.5 mmol). The chambers were sealed with a screwcap fitted with a Teflon® seal. Chamber 2 solution was purged with argon gas for 10 minutes (keeping 1 atm pressure by putting an outlet syringe), after which, Chamber 1 was purged with carbon dioxide gas for 15 minutes (keeping 1 atm pressure by putting an outlet syringe). Chamber 1 was photo-irradiated with a blue LED lamp and was held at room temperature while Chamber 2 was covered with aluminium foil to avoid any illumination and was held at 80°C (immersed in an oil bath) for 21 hours under constant stirring. After the reaction, the crude mixture in Chamber 2 was filtered and the solvent evaporated using rotary evaporator. It was then subjected to column chromatography (2% methanol in dichloromethane) and isolated as a brownish solid (122.4 mg, 455 μmol, 91% based on CO, 23% based on CO₂).

¹H NMR (CDCl₃, 298 K, 300 MHz): δ_H 7.68 (2H, d), 7.36 (2H, d), 6.84 (1H, br s), 3.68 (4H, t), 3.48 (2H, q), 2.54 (2H, t), 2.45 (4H, t)

¹³C NMR (CDCl₃, 298 K, 300 MHz): δ_C 166.5, 137.7, 133.1, 128.9 (2C), 128.5 (2C), 67.1 (2C), 57.0, 53.4 (2C), 36.2.

ESI-HRMS: calculated m/z = 269.1051 [M+H⁺] for C₁₃H₁₈ClN₂O₂, found 269.1055

Synthesis of Moclobemide using ¹³CO₂ Tritec®

Modified two-chamber system shown in Figure 0-20 was used. Chamber 1 was loaded according to “General protocol for Chamber 1” and Chamber 2 was loaded with Pd(dba)₂ (36 mg, 0.0625 mmol), PPh₃ (33 mg, 0.125 mmol), 1-chloro-4-iodobenzene (298 mg, 1.25 mmol), dioxane (3.4 mL), 4-(2-aminomethyl)morpholine (0.33 ml, 2.5 mmol), and triethylamine (0.34 ml, 2.5 mmol). Chamber 1 was sealed

by tightening the red knob while Chamber 2 was sealed by placing a rubber septum. The adaptor was then connected to the Tritec® system. The chambers were degassed three times using freeze-thaw method. 530 μmol of $^{13}\text{CO}_2$ was then injected to the chambers using the Tritec® system keeping the stopcock open between the two chambers. The loaded chambers were then removed from the Tritec® system and the solutions were left to thaw to room temperature. Once thawed, Chamber 1 was photo-irradiated with a blue LED lamp and was held at room temperature while Chamber 2 was covered with aluminium foil to avoid any illumination and was held at 80°C (immersed in an oil bath) for 21 hours under constant stirring. After the reaction, the crude mixture in Chamber 2 was filtered and the solvent evaporated using rotary evaporator. It was then subjected to column chromatography (2% methanol in dichloromethane) and isolated as a brownish solid (43.3 mg, 161 μmol , 85% based on ^{13}CO , 30% based on $^{13}\text{CO}_2$).

^1H NMR (CDCl_3 , 298 K, 300 MHz): δ_{H} 7.70 (2H, d), 7.38 (2H, d), 6.78 (1H, br s), 3.70 (4H, t), 3.5 (2H, q), 2.58 (2H, t), 2.48 (4H, t)

^{13}C NMR (CDCl_3 , 298 K, 300 MHz): δ_{C} 166.5 (^{13}C -enriched), 137.8, 133.5, 128.9 (2C), 128.5 (2C), 67.1 (2C), 57.0, 53.5 (2C), 36.2.

ESI-HRMS: calculated $m/z = 270.1085$ [$\text{M}+\text{H}^+$] for $\text{C}_{12}^{13}\text{CH}_{18}\text{ClN}_2\text{O}_2$, found 270.1084

Bibliography

- [1] G. M. Sheldrick, *SHELXS 97, Program for the Solution of Crystal Structure*, University Of Göttingen, Germany, **1997**.
- [2] G. M. Sheldrick, *Acta Cryst. A* **2008**, *64*, 112–122.
- [3] L. J. Farrugia, *J. Appl. Crystallogr.* **1999**, *32*, 837–838.
- [4] N. G. Connelly, W. E. Geiger, *Chem. Rev.* **1996**, *96*, 877–910.
- [5] D. T. Sawyer, A. Sobkowiak, J. L. Roberts, *Electrochemistry for Chemists*, Wiley, **1995**.
- [6] N. Elgrishi, M. B. Chambers, X. Wang, M. Fontecave, *Chem. Soc. Rev.* **2017**, *46*, 761–796.
- [7] V. V. Pavlishchuk, A. W. Addison, *Inorganica Chimica Acta* **2000**, *298*, 97–102.
- [8] C. Costentin, S. Drouet, M. Robert, J.-M. Savéant, *J. Am. Chem. Soc.* **2012**, *134*, 11235–11242.
- [9] I. Azcarate, C. Costentin, M. Robert, J.-M. Savéant, *J. Phys. Chem. C* **2016**, *120*, 28951–28960.
- [10] C. Costentin, J.-M. Savéant, *Nature Reviews Chemistry* **2017**, *1*, 0087.
- [11] M. L. Clark, P. L. Cheung, M. Lessio, E. A. Carter, C. P. Kubiak, *ACS Catal.* **2018**, *8*, 2021–2029.
- [12] E. S. Rountree, B. D. McCarthy, T. T. Eisenhart, J. L. Dempsey, *Inorg. Chem.* **2014**, *53*, 9983–10002.
- [13] A. M. Appel, M. L. Helm, *ACS Catal.* **2014**, *4*, 630–633.
- [14] S. Mendes Marinho, M.-H. Ha-Thi, V.-T. Pham, A. Quaranta, T. Pino, C. Lefumeux, T. Chamailé, W. Leibl, A. Aukauloo, *Angew. Chem. Int. Ed.* **2017**, *56*, 15936–15940.

- [15] E. Portenkirchner, K. Oppelt, C. Ulbricht, D. A. M. Egbe, H. Neugebauer, G. Knör, N. S. Sariciftci, *Journal of Organometallic Chemistry* **2012**, 716, 19–25.
- [16] K. A. Johnson, Z. B. Simpson, T. Blom, *Analytical Biochemistry* **2009**, 387, 20–29.
- [17] B. Ravel, M. Newville, *J Synchrotron Rad* **2005**, 12, 537–541.
- [18] J. J. Rehr, S. I. Zabinsky, R. C. Albers, *MRS Proceedings* **1993**, 307, 3.
- [19] D. C. Koningsberger, R. Prins, *X-Ray Absorption: Principles, Applications, Techniques of EXAFS, SEXAFS, and XANES*, John Wiley And Sons, **1988**.
- [20] F. Neese, *Wiley Interdisciplinary Reviews: Computational Molecular Science* **2012**, 2, 73–78.
- [21] A. D. Becke, *J. Chem. Phys.* **1993**, 98, 5648–5652.
- [22] P. J. Stephens, F. J. Devlin, C. F. Chabalowski, M. J. Frisch, *J. Phys. Chem.* **1994**, 98, 11623–11627.
- [23] P. Coppens, I. V. Novozhilova, *International Journal of Quantum Chemistry* **2005**, 101, 611–623.
- [24] F. Weigend, R. Ahlrichs, *Phys. Chem. Chem. Phys.* **2005**, 7, 3297–3305.
- [25] S. Grimme, J. Antony, S. Ehrlich, H. Krieg, *J. Chem. Phys.* **2010**, 132, 154104.
- [26] S. Grimme, S. Ehrlich, L. Goerigk, *Journal of Computational Chemistry* **2011**, 32, 1456–1465.
- [27] E. M. Nichols, J. S. Derrick, S. K. Nistanaki, P. T. Smith, C. J. Chang, *Chem. Sci.* **2018**, 9, 2952–2960.
- [28] R. R. Gagne, J. L. Allison, D. M. Ingle, *Inorg. Chem.* **1979**, 18, 2767–2774.
- [29] M. D. Sampson, A. D. Nguyen, K. A. Grice, C. E. Moore, A. L. Rheingold, C. P. Kubiak, *J. Am. Chem. Soc.* **2014**, 136, 5460–5471.
- [30] J. M. Savéant, in *Elements of Molecular and Biomolecular Electrochemistry*, John Wiley & Sons, Ltd, **2006**, pp. 78–181.
- [31] C. Cometto, L. Chen, P.-K. Lo, Z. Guo, K.-C. Lau, E. Anxolabéhère-Mallart, C. Fave, T.-C. Lau, M. Robert, *ACS Catal.* **2018**, 8, 3411–3417.
- [32] I. Bhugun, D. Lexa, J.-M. Saveant, *J. Am. Chem. Soc.* **1994**, 116, 5015–5016.
- [33] M. J. Frisch, G. W. Trucks, H. B. Schlegel, G. E. Scuseria, M. A. Robb, J. R. Cheeseman, G. Scalmani, V. Barone, B. Mennucci, G. A. Petersson, *Gaussian Inc. Wallingford CT* **2009**.
- [34] C. Römel, J. Song, M. Tarrago, J. A. Rees, M. van Gastel, T. Weyhermüller, S. DeBeer, E. Bill, F. Neese, S. Ye, *Inorg. Chem.* **2017**, 56, 4745–4750.
- [35] “Chemcraft - Graphical program for visualization of quantum chemistry computations,” can be found under <https://www.chemcraftprog.com/index.html>
- [36] C. Costentin, M. Robert, J.-M. Savéant, *Acc. Chem. Res.* **2015**, 48, 2996–3006.

Titre : Stratégies bio-inspirées pour la réduction catalytique et la valorisation du dioxyde de carbone

Mots clés : photosynthèse artificielle, réduction de CO₂, bio-inspiré, photocatalyse, électrocatalyse, valorisation

Résumé : La criticité du réchauffement climatique incite à chercher des solutions pour réduire les émissions de dioxyde de carbone (CO₂). Le développement de catalyseurs qui peuvent aider à capturer, activer, réduire et valoriser le CO₂ est au cœur de ce défi. Cette thèse a répondu à cet appel en développant des mimétismes moléculaires inspirés de la Nature, dans le cadre plus large de la photosynthèse artificielle.

Au début il s'agissait de suivre le parcours d'un photon de lumière visible et de déterminer comment il peut réduire la molécule de CO₂.

Ensuite afin de réaliser des catalyseurs plus efficaces, de nouvelles molécules ont été synthétisées en s'inspirant de l'enzyme CO déshydrogénase (CODH) qui présente des performances exceptionnelles pour la réduction du CO₂.

Enfin, une autre propriété du CODH a conduit à une validation de principe pour la valorisation immédiate du CO photo-produit dans la synthèse des liaisons amides marqués, une caractéristique courante des médicaments.

Title : Bio-inspired Strategies for the Catalytic Reduction and Valorization of Carbon Dioxide

Keywords : artificial photosynthesis, CO₂ reduction, bio-inspired, photocatalysis, electrocatalysis, valorization

Abstract : The criticality of global warming urges for the advancement of science to reduce carbon dioxide (CO₂) emissions in the atmosphere. At the heart of this challenge is the development of sustainable catalysts that can help capture, activate, reduce, and eventually valorize CO₂. This PhD work tried to respond to this call by developing molecular mimics inspired by natural systems in the larger scheme of artificial photosynthesis.

Firstly, it involved tracking the journey of a photon of visible light and how it is transformed to a reducing power able to reduce CO₂.

Secondly, in search for more efficient and stable catalysts, new mimics were synthesized inspired by the exceptional performance of CO dehydrogenase enzymes (CODH) in reducing CO₂.

Lastly, further understanding of CODH also led to a proof-of-concept that directly valorizes the photo-produced CO for the synthesis of isotopically-labelled amide bonds, a common motif in pharmaceutically-relevant drugs.

